Search for Fourth Generation down-type quarks in the same-sign dilepton channel with ATLAS at a centre-of-mass-energy, sqrt(s) = 7 TeV.

D I S S E R T A T I O N

zur Erlangung des akademischen Grades

doctor rerum naturalium
(Dr. rer. nat.)
im Fach Physik

eingereicht an der
Mathematisch-Naturwissenschaftlichen Fakultät I
Humboldt-Universität zu Berlin

von
Dipl. Phys. Rocco Mandrysch

Präsident der Humboldt-Universität zu Berlin:
Prof. Dr. Jan-Hendrik Olbertz

Dekan der Mathematisch-Naturwissenschaftlichen Fakultät I:
Prof. Stefan Hecht, Ph.D.

Gutachter:
1. Prof. Dr. Heiko Lacker
2. Prof. Dr. Thomas Lohse
3. Jun.-Prof. Dr. Arno Straessner

eingereicht am: 03.05.2012
Tag der mündlichen Prüfung: 19.07.2012

Abstract

The model of a fourth generation is currently not excluded by theoretical arguments. In this thesis a search for a fourth generation down-type quark is presented with the decay hypothesis:

$$pp \rightarrow b'\bar{b}' + X \rightarrow t + W^- + \bar{t} + W^+ + X \rightarrow b\bar{b} + W^+ + W^- + W^+ + W^- + X.$$

The search is performed with an integrated luminosity of $2.05\,\mathrm{fb}^{-1}$, obtained with the ATLAS experiment at the Large Hadron Collider running proton-proton collisions at a center-of-mass energy of $\sqrt{s} = 7\,\mathrm{TeV}$. Events for the analysis are selected with a search signature of two same-sign charged leptons (e or μ) in the final state, which is a rare Standard Model signature. Beside using the standard event selection from ATLAS top analyses, the event selection criteria are optimized with a multivariate analysis in order to maximize the significance. Furthermore, systematic uncertainties are studied coming from the parton distribution function as well as the initial and final state radiation. With the selected events in the signal region of two same-sign leptons, the signal is extracted via a counting method. The extracted signal is used for the determination of the mass limit of the fourth generation down-type quark with a modified frequentist method. Assuming a branching ratio of $100\,\%$ for the decay $b' \rightarrow t + W$, b' masses below $461\,\mathrm{GeV}$ are excluded at $95\,\%$ confidence level.

Zusammenfassung

Das Modell einer vierten Familie konnte bis heute aufgrund von theoretischen Argumenten nicht ausgeschlossen werden. In dieser Arbeit wird die Suche nach einem Down-artigen Quark der vierten Familie mit dem folgenden angenommenen Zerfall:

$$pp \rightarrow b'\bar{b}' + X \rightarrow t + W^- + \bar{t} + W^+ + X \rightarrow b\bar{b} + W^+ + W^- + W^+ + W^- + X$$

vorgestellt. Für diese Analyse wird eine integrierte Luminosität von $2.05\,\text{fb}^{-1}$ verwendet, aufgenommen mit dem ATLAS Experiment bei einer Schwerpunktsenergie von $\sqrt{s} = 7\,\text{TeV}$ für die Proton-Proton Kollisionen am Large Hadron Collider. In der Analyse werden Ereignisse mit zwei gleich geladenen Leptonen (e oder μ) in den Endzuständen selektiert, was eine seltene Signatur im Standard Modell darstellt. Neben einer verwendeten Standardselektierung für die Ereignisse, entnommen aus der ATLAS Top-Quark Analyse, wird eine Optimierung der Schnitte mit einer multivariaten Analyse durchgeführt. Des Weiteren werden systematische Unsicherheiten studiert, die durch die Partonendichteverteilungsfunktion sowie durch Abstrahlung von Teilchen wie Gluonen im Anfangs- und im Endzustand bei der Simulation mit dem Monte Carlo Generator entstehen. Mit den selektierten Ereignissen in der Signalregion von zwei gleich geladenen Leptonen wird durch eine Zählanalyse die Anzahl gemessener Signalereignisss extrahiert. Mit diesen Signalereignissen wird dann die untere Massenausschlussgrenze des b'-Quarks mit einer modifizierten Frequentistmethode bestimmt. Das Ergebnis zeigt, dass mit einem angenommenem Verzweigungsverhältnis von $100\,\%$ für den Zerfall $b' \rightarrow t + W$ alle Massen unterhalb einer Grenze von $461\,\text{GeV}$ mit einem $95\,\%$ Konfidenzintervall ausgeschlossen sind.

Contents

Contents

1. Introduction

The Standard Model [1],[2],[3],[4],[5],[6],[7] of particle physics describes the elementary particles and their interactions between each other successfully and has been verified with an increasing accuracy by several collider experiments. However, the Higgs mechanism [8], [9], [10], [11], [12], which describes the electroweak symmetry breaking in the Standard Model, and the corresponding Higgs particle have not been discovered yet. Recently accomplished experiments were able to exclude certain mass ranges.

To finally exclude or confirm the Higgs particle the Large Hadron Collider (LHC), a proton-proton accelerator, has been built together with the setup of several experiments. The LHC produces a larger data set with a higher energy than any collider before. One main experiment is the ATLAS detector for probing the electroweak symmetry breaking and discovering the Higgs boson along with the measuring of its properties.

In nature there are phenomena, which cannot be described by the Standard Model like the asymmetry between baryons and antibaryons in the early beginning of the universe. This asymmetry can be generated by the CP violation caused by the phase in the CKM matrix, which was postulated by Andrei Sakharov [13]. Nevertheless, the CP violation introduced by the CKM matrix in the Standard Model is too small to explain that effect [14]. This points to an extension of the Standard Model, which provides a possibility to solve the problem.

The simple extension of the Standard Model with the model of a fourth generation leads to an alternative ansatz for the generating of the baryon asymmetry [14]. Furthermore, the fourth generation can play an important role in the electroweak symmetry breaking. If the new quarks have a very high mass, $m \approx 550 \, \text{GeV}$, the quarks could form a condensate, which could appear as a scalar field and could be responsible for the electroweak symmetry breaking [15], [16]. In the Standard Model of three generations only a light Higgs is allowed. Adding the fourth generation particles in the electroweak precision fit, a higher Higgs mass up to $750 \, \text{GeV}$ is compatible with the Standard Model at $95 \, \%$ confidence level [17].

The number of generations in the Standard Model is a free parameter and allows then the extension to an additional family containing two quarks and one charged and

one neutral lepton. Furthermore, the uncertainties of the measured Cabibbo-Kobayashi-Maskawa-Matrix (CKM matrix), which describe the mixing among the quarks, provides space for an additional quark family. Direct searches at experiments like CDF, L3, CMS and ATLAS have not been discovered the fourth generation yet and lower mass bounds have been determined.

By the beginning of the year 2011 ATLAS started to measure the produced particles coming from the proton-proton collisions at a center-of-mass energy of $\sqrt{s} = 7\,\text{TeV}$ provided by the LHC. The data sets taken from March till August are used for this analysis.

For the search for the fourth generation of quarks a signature is needed, for which the Standard Model background is expected to be small. Assuming a pair production of the down-type quark b' and a branching ration of $100\,\%$ for the decay $b' \to t + W$ the decay channel is as follows:

$$pp \to b'\bar{b}' + X \to t\bar{t} + W^+ + W^- + X \to b\bar{b} + W^+ + W^- + W^+ + W^- + X$$

With the requirement of a leptonic decay into electrons and muons of two same-sign W boson the final state provides the search signature of two same-sign leptons with any flavor combination. This search signature is rare Standard Model signature. Requiring a hadronic decay of the other two W bosons in addition to the b quarks the jet multiplicity is very high in the final state. With a high jet multiplicity the background suppression in events with two same-sign leptons can be improved. In this signal region the counted number of events, the signal, is extracted via a method for a lower mass bound determination. For the signal event selection, standard analysis criteria optimized for the top analysis inside ATLAS are used in this analysis due to similar properties of the final state. Moreover, the event selection is optimized to improve the background suppression and the results are compared with the standard event selection. Furthermore, uncertainties on event selection are studied coming from parton density function as well ass the initial state and final state radiation.

The structure of this thesis is the following: In the beginning (chapter two) the Standard Model with its main fundamental ingredients is briefly introduce followed by the discussion of the motivation of the fourth generation model and the used search signature. Chapter three contains technical aspects of the LHC and the ATLAS detector. Then in chapter four the Monte Carlo samples and data set used for this analysis are described. In chapter five a brief description of the particle reconstruction is given following by the discussion of the physical object and event selection. Chapter seven covers the systematic studies on the event selection coming from the generator setup. The

introduction of the method used for counting the events and signal extracting is done in chapter eight together with the mass limit calculation. A summary and onclusion are given in the last chapter.

2. The Standard Model and the Fourth Generation extension

The Standard Model of particle physics (SM) describes the fundamental particles of matter together with their interactions (except gravitation). Many phenomena in nature can be described successfully by the SM. Nevertheless, the Standard Model can not explain the generation of the baryogenesis. This points to the requirement of an extension of the model and a possible candidate for this is the model of a fourth generation of fermions.

In this chapter, I discuss the main ingredients and some problems of the Standard Model. First, I introduce the elementary particles and then the basic properties of the their interactions together with the Higgs mechanism. Secondly, I present the simple extension of the SM with a fourth family of leptons and quarks. Finally, I introduce the search signature for the search of these quarks at the LHC, which is used in this thesis.

2.1. The Standard Model

The Standard Model of particle physics describes all known elementary particles and their interactions. The basic theory is a relativistic quantum field theory, which is usually formulated within the Lagrangian formalism together with the Lagrangian density $\mathcal{L}$. Generally, the SM is based on the idea that the matter is described by fermion fields and the interactions between the particles are interceded by gauge bosons. The particles are grouped into particles with half-integer and integer, called fermions and bosons, respectively. The gauge bosons mediate the different forces between the fermions. Finally, the masses of the particles in the SM are generated by the Higgs mechanism.

2.1.1. Fermions

All fermions of the SM have a half-integer spin and are divided into two groups: leptons and quarks. Both categories are split into three families. For each lepton family there is one electrically charged lepton (e, μ, τ) and one electrically uncharged lepton (ν_e, ν_μ,

2. The Standard Model and the Fourth Generation extension

ν_τ). Each quark family contains an up-type (up, charm and top) and a down-type quark (down, strange and bottom).

The electrical charge of the e, μ, τ is integer-numbered, while the charge of the up-type quark is $+\frac{2}{3}e$ and the charge of the down-type quark is $-\frac{1}{3}e$. Additionally, these particles have a weak isospin and only the quarks have a further color charge.

Quarks interact electromagnetically, weakly and strongly. The electrically charged leptons interact only electromagnetically and weakly, while the electrically uncharged leptons interact only weakly.

Figure 2.1 shows the observed masses of the Standard Model fermions (except neutrinos) and gauge bosons. The basic properties of the leptons and quarks are summarized in Table 2.1.
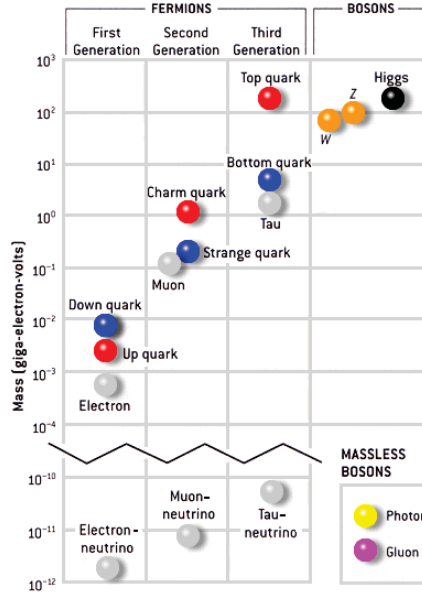

Figure 2.1.: The masses of the Standard Model particles [18]. The Higgs particle is not discovered yet but is presented in this figure with the supposed mass.

	First family	Second family	Third family	Elm. charge [e]
Charged lepton	e	μ	τ	-1
Neutrino	ν_e	ν_μ	ν_τ	0
Up type quark	u (up)	c (charm)	t (top)	$+\frac{2}{3}$
Down type quark	d (down)	s (strange)	b (bottom)	$-\frac{1}{3}$

Table 2.1.: The fermions of the Standard Model separated into their different families.

2.1.2. Gauge bosons

As mentioned before, bosons have an integer spin. The bosons of the electromagnetic and strong interaction, called the photon and the gluon, respectively, do not have a mass and are electromagnetically uncharged. The weak interaction is different. The $W^\pm$ bosons are electrically charged with charges of $\pm e$ and have a mass of $m_{W^\pm} \sim 80\,\text{GeV}$, while the Z boson has a similar mass ($m_Z \sim 91\,\text{GeV}$) but is electromagnetically uncharged.

Table 2.2 presents the gauge bosons of the Standard Model elementary forces and their properties.

	Boson(s)	El. charge [e]	Mass	Range	Coupling constants
Electromagn.	Photon γ	0	0	∞	$\alpha(M_Z^2) \approx 1/127$
Weak	$W^\pm$	± 1	$\sim 80\,\text{GeV}$ [19]	$\sim 10^{-18}\,\text{m}$	$\alpha_W(M_Z^2) \approx 1/29$
	Z	0	$\sim 91\,\text{GeV}$ [19]		
Strong	8 Gluons g	0	0	$\sim 10^{-15}\,\text{m}$	$\alpha_s(M_Z^2) \approx 0.119$

Table 2.2.: The elementary forces by the Standard Model and their properties.

2.1.3. Interactions

The several interactions are mediated by their corresponding gauge bosons. The interactions between the particles in the SM can be described mathematically with the theory of the local gauge invariance. The symmetry group of this theory is as follows:

$$SU(3)_C \otimes SU(2)_L \otimes U(1)_Y \tag{2.1}$$

The $SU(3)_C$ describes the strong interaction via the gluons between quarks, where the index C stands for color charge. The theory of quantum chromodynamics is based on this group. The symmetry group of the electroweak interaction $SU(2)_L \otimes U(1)_Y$ contains the combination of quantum electrodynamics and the weak interaction. The charged weak bosons couple to the left handed fermions. Y is the conserved charge of the group $U(1)_Y$, called hypercharge, and is connected to the third component of the weak isospin T_3 and the electromagnetic charge Q by:

$$Q = T_3 + \frac{Y}{2} \tag{2.2}$$

Quantum electrodynamics

The electromagnetic interaction is mediated by the photon. This gauge boson has zero mass and no charge. The electromagnetic interaction is based on the theory of quantum

electrodynamic and the corresponding Lagrangian is defined as follows:

$$\mathcal{L} = -\frac{1}{4} F_{\mu\nu} F^{\mu\nu} + \sum_n \bar{\psi}_n (i\gamma^\mu D_\mu - m_n)\psi_n \, ,$$

(2.3)

where the fermion field ψ is invariant under a local $U(1)$ transformation:

$$\psi_i \to e^{ie\alpha(x)}\psi_i \, .$$

(2.4)

$D_\mu = \partial_\mu + ieA_\mu$ is the minimal covariant derivative and γ^μ are the Dirac-matrices. e and m describe the electric charge and the mass of the fermion field ψ_i, respectively, and $F_{\mu\nu} = \partial_\mu A_\nu - \partial_\nu A_\mu$ stands for the electromagnetic field tensor. With the Lorentz gauge $\partial_\mu A^\mu = 0$ in $U(1)$ the potential of the electromagnetic field $A_\mu(x)$ is not completely defined. One is free to add the derivative of an additional function $\partial_\mu \alpha(x)$ to the current field, A_μ, without changing the electrical and magnetic fields and the physical observables:

$$A_\mu(x) \to A'_\mu(x) = A_\mu(x) + \partial_\mu \alpha(x)$$

(2.5)

These are the properties of the photon field. Additionally, the requirement of local gauge invariance of the $U(1)$ enforces the introduction of the electromagnetic gauge field A_μ.

Together with the definition of the electromagnetic current of the electron $j^\mu = -e\bar{\psi}\gamma^\mu\psi$ the Lagrangian in equation 2.3 results in

$$\mathcal{L} = -\frac{1}{4} F_{\mu\nu} F^{\mu\nu} + \bar{\psi}(i\gamma^\mu \partial_\mu - m)\psi_n - j^\mu A_\mu.$$

(2.6)

This Lagrangian is defined as the sum of the photon part, the electron part and the interaction part.

As mentioned above the photon field couples to the electrically charged fermion fields and the relation between the coupling constant and the electromagnetic charge is defined as follows:

$$\alpha = \frac{e^2}{4\pi} \approx \frac{1}{137}$$

(2.7)

The coupling constant shows a dependence on the momentum transfer q^2 due to pertubative corrections as presented in Figure 2.2. In the theory with one loop correction, the running coupling constant is given by:

$$\alpha(q^2) = \frac{\alpha(\mu^2)}{1 - \frac{\alpha(\mu^2)}{3\pi} \log\left(\frac{q^2}{\mu^2}\right)}$$

(2.8)

with $\alpha(\mu^2)$ the constant at a reference energy μ. With increasing values of Q^2 the denominator in equation (2.8) becomes smaller, while α becomes larger. At a certain energy α is infinite, which is called *Landau-Pole*.
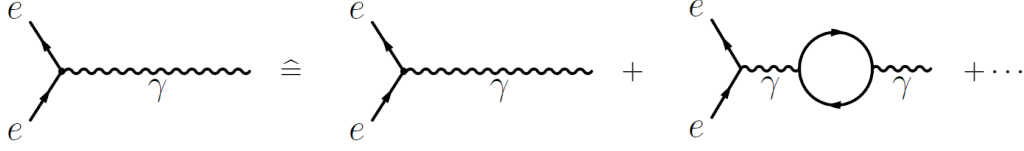

Figure 2.2.: The measured charge is not the same as it appears in equation (2.7) and is not explained by the left graph. It is given by an infinite number of higher order loop graphs [20].

Electroweak interaction

The electroweak interaction is based on the symmetry group $SU(2)_L \otimes U(1)$ and is a combination of the QED and weak interaction. The $SU(2)_L$ symmetry provides a gauge boson triplet $W_\mu^{1,2,3}$, while from the $U(1)$ symmetry a gauge boson singlet B_μ arise. The electroweak symmetry breaking leads to rotation of the mass eigenstates, which are the physically fields, to form the weak eigenstates:

$$\begin{pmatrix} W_\mu^+ \\ W_\mu^- \end{pmatrix} = \frac{1}{\sqrt{2}} \begin{pmatrix} 1 & -i \\ i & 1 \end{pmatrix} \begin{pmatrix} W_\mu^1 \\ W_\mu^2 \end{pmatrix} \tag{2.9}$$

$$\begin{pmatrix} Z_\mu^0 \\ A_\mu \end{pmatrix} = \begin{pmatrix} \cos\theta_W & -\sin\theta_W \\ \sin\theta_W & \cos\theta_W \end{pmatrix} \begin{pmatrix} W_\mu^3 \\ B_\mu \end{pmatrix} \tag{2.10}$$

The Weinberg angle θ_W ($\sin\theta_W = 0.23116 \pm 0.00013$ [1] [19]) describes the strength of the mixing of the fields W_μ^3 and B_μ. W_μ^+ and W_μ^- are the fields of the physically observed charged W-bosons, while the mixing of the neutral fields B_μ and W_μ^3 provides the physically particles of the photon A_μ and the Z-boson Z_μ. The coupling in the electroweak theory is described by two parameters: g and g'. g characterizes the coupling of the vector fields $W_\mu^{1,2,3}$ and g' the coupling to the vector field B_μ. The relation between both coupling constants via the Weinberg angle θ_W is as follows:

$$g \sin\theta_W = g' \cos\theta_W = e \tag{2.11}$$

---

[1] Measured value is the effective mixing angle.

2. The Standard Model and the Fourth Generation extension

In the electroweak interaction the fermions are grouped in multiplets due to the $SU(2)_L$ gauge symmetry: the left-handed fermions of each family are weak-isospin doublets, which contain a charged lepton and a neutrino while the right-handed fermions form singlets. Only the left-handed fermions and the right-handed anti-fermions couple to the $W^{\pm}$ bosons.

The quark mass eigenstates are not identical to their weak eigenstates due to the symmetry breaking. The bosons of the weak interaction couple only to the weak eigenstates of the quarks, which are rotated states. The relation between the mass and weak eigenstates is described by the *Cabibbo-Kobayashi-Maskawa* or CKM matrix:

$$V_{CKM} = \begin{pmatrix} V_{ud} & V_{us} & V_{ub} \\ V_{cd} & V_{cs} & V_{cb} \\ V_{td} & V_{ts} & V_{tb} \end{pmatrix} \tag{2.12}$$

The CKM matrix causes flavor changing charged current interaction with the $W^{\pm}$-bosons, while flavor changing neutral currents are absent on tree level in the Standard Model by the *GIM* mechanism. The neutral currents with flavor conservation via the Z/γ are allowed in the electroweak interaction. In the case of a 2×2 matrix only one parameter θ_C is used, which describes the mixing between the weak (d' and s') and the mass eigenstate (d and s), and is called Cabibbo angle:

$$\begin{pmatrix} d' \\ s' \end{pmatrix} = \begin{pmatrix} \cos\theta_C & \sin\theta_C \\ -\sin\theta_C & \cos\theta_C \end{pmatrix} \cdot \begin{pmatrix} d \\ s \end{pmatrix} \tag{2.13}$$

The value of this angle is $\theta_C \approx 13°$ and due to its small value the flavor changing charged currents are suppressed or Cabibbo disfavored, which is also called *GIM* mechanism. Thus, flavor changing neutral currents can only appear at level of quantum loop corrections with a very small branching fractions.

For three generation the CKM matrix can be parametrized by:

$$V_{CKM} = \begin{pmatrix} c_{12}c_{13} & s_{12}c_{13} & s_{13}e^{-i\delta_{13}} \\ -s_{12}c_{23} - c_{12}s_{23}s_{13}e^{i\delta_{13}} & c_{12}c_{23} - s_{12}s_{23}s_{13}e^{i\delta_{13}} & s_{23}c_{13} \\ s_{12}s_{23} - c_{12}c_{23}s_{13}e^{i\delta_{13}} & -c_{12}s_{23} - s_{12}c_{23}s_{13}e^{i\delta_{13}} & c_{23}c_{13} \end{pmatrix} \tag{2.14}$$

with $c_{ij} = \cos\theta_{ij}$, $s_{ij} = \sin\theta_{ij}$, three angles θ_{12}, θ_{13}, θ_{23} and the phase δ_{13}. This parametrization indicates how strong the mixing among the families is. The consequence of the phase is the introduction of the charge-parity (CP) violating effects in the Standard Model. The amplitude $\mathcal{M}$ of flavor changing processes like $t \rightarrow b + W$ is proportional to

the corresponding element of the CKM matrix: $\mathcal{M} \propto V_{tb}^*$.

Quantum chromodynamics

Quantum chromodynamics (QCD) is the quantum field theory of the strong interaction and is based on the gauge group $SU(3)_C$. This theory describes the interaction via gluons. The Lagrangian is formed in this way:

$$\mathcal{L} = \bar{\psi}_i(i\gamma^\mu(D_\mu)_{ij} - m\delta_{ij})\psi_j - \frac{1}{4}G^a_{\mu\nu}G^{\mu\nu}_a \ , \tag{2.15}$$

where ψ_i are the quark fields and $G^a_{\mu\nu}$ are the gluon fields. $D_\mu = \partial_\mu + ig_sG^a_\mu T^a$ is the covariant derivate with the eight generators T^a of the $SU(3)$ gauge group. The charge of the QCD is called color: red, green and blue. Due to the non-abelian character of the $SU(3)$, the color charge of the gluons is composed of a color and a anti-color and couple among each other.

In QCD the coupling constant $\alpha_s = g_s^2/4\pi$ depends on q^2 due to the additional loop diagrams of gluons or quark-antiquark-pairs. The coupling constant is given by:

$$\alpha_s(q^2) = \frac{\alpha_s(\mu^2)}{(1 + \frac{\alpha_s(\mu^2)}{12\pi})(33 - 2n_f)\log\left(\frac{q^2}{\mu^2}\right)} \ , \tag{2.16}$$

where n_f is the number of quark flavors.

With equation (2.16) the strong coupling constant gets smaller at higher energies or at shorter distances and approaches zero for very large q^2. This situation is called *asymptotic freedom*. On the other hand it means that the coupling gets stronger at higher distances. At a sufficient high potential energy a new quark-antiquark-pair can be created. Therefore quarks do not appear isolated due to the *confinement*.

Higgs mechanism

From precise measurements one know that the fermions and the bosons of the weak interaction have a mass. In the Standard Model the mass is generated in a gauge invariant dynamical way by the interaction of the particles with a scalar field, which is called Higgs mechanism and is based on the idea of spontaneous $SU(2)_L \times U(1)_Y$ symmetry breaking.

The Lagrangian of a scalar field ϕ with a mass term is defined as follows:

$$\mathcal{L} = \frac{1}{2}(\partial_\mu\phi)(\partial^\mu\phi) - \left(\frac{1}{2}\mu^2\phi^2 + \frac{1}{4}\lambda\phi^4\right) \tag{2.17}$$

with the definition

$$V(\phi) = \frac{1}{2}\mu^2\phi^2 + \frac{1}{4}\lambda\phi^4 + ... \tag{2.18}$$

for the potential $V(\phi)$ together with the real parameters μ and λ. The potential is developed as a Taylor series up to the second term of a generic potential. The main requirement for the potential $V(\phi)$ is a symmetrical property: $V(\phi) = V(-\phi)$. The parameter λ has to be positive due to $V \to \infty$ for $\phi \to \pm\infty$ and with the requirement of the bare minimum. With the choice of $\mu^2 < 0$ the minimum of the potential moves from $\phi = 0$ to

$$|\phi_0| = \sqrt{\frac{-\mu^2}{\lambda}} = \nu \;. \tag{2.19}$$

The value of the new minimum is then the vacuum expectation value v. With the development of this new minimum every possible ground state breaks the $SU(2)_L$ symmetry, which is known as *spontaneous symmetry breaking*.

The scalar field itself can be defined as an isospin doublet with complex components due to the local gauge symmetry of the $SU(2)_L$:

$$\phi = \begin{pmatrix} \phi_{+1/2} \\ \phi_{-1/2} \end{pmatrix} = \frac{1}{\sqrt{2}}\begin{pmatrix} \phi_1 + i\phi_2 \\ \phi_3 + i\phi_4 \end{pmatrix} \tag{2.20}$$

The field ϕ is described by real field components ϕ_i and the factor $1/\sqrt{2}$ is convention. With the definition $\phi_1 = \phi_2 = \phi_4 = 0$ and $\phi_3 = \nu + h(x)$ the field around the minimum can be calculated as

$$\phi = \frac{1}{\sqrt{2}}\begin{pmatrix} H_1(x) + iH_2(x) \\ \nu + h(x) + iH_4(x) \end{pmatrix}. \tag{2.21}$$

The field component $h(x)$ can be discovered as a particle with the name Higgs boson (H). The mass of the Higgs boson is defined in the Lagrangian density as $m_H = \sqrt{2}\mu$. The other components $H_i(x)$ are massless and are called *Goldstone bosons*.

In the Standard Model the ground state is chosen such that the photon is massless. In the case of the W boson mass, the Lagrangian in equation (2.17) is modified with the field ϕ in equation (2.20):

$$\mathcal{L} = (\partial_\mu\phi)^\dagger(\partial^\mu\phi) - \mu^2\phi^\dagger\phi - \lambda(\phi^\dagger\phi)^2 \;. \tag{2.22}$$

The first term describes the kinetic energy of the field and the other two describe the potential. To make the equation local gauge invariant in $SU(2)$ the rotation in the

isospin space can be used:

$$\phi'(x) = e^{i\alpha_a(x)J_a}\phi(x) \; , \tag{2.23}$$

where $J_a(a = 1, 2, 3)$ are the Pauli matrices τ_a with an additional factor of $\frac{1}{2}$: $J_a = \frac{1}{2}\tau_a$. Then the derivative in the kinetic term has to be updated as follows:

$$\partial_\mu \Rightarrow D_\mu = \partial_\mu + igJ_aW_\mu^a \; , \tag{2.24}$$

which also introduces the gauge fields W_μ^a of $SU(2)$ with the following transformation properties:

$$W'_\mu = W_\mu^a - \frac{1}{g}\partial_\mu\alpha_a - f_{abc}\alpha_bW_\mu^c \; . \tag{2.25}$$

f_{abc} is the structure constant of the $SU(2)$ and is defined by the total antisymmetric tensor: $f_{abc} = \epsilon_{abc}$. This fixes the commutation relation of J_a: $[J_a, J_b] = i\epsilon_{abc}J_c$. With the next step the following term

$$\frac{1}{4}W_{\mu\nu}^aW_a^{\mu\nu} \tag{2.26}$$

needs to be added to equation (2.17), which describes the kinematics of the gauge fields with the field tensor W_μ^a. With the commutation relation $[D_\mu, D_\nu] = igJ_aW_\mu^a$ the field tensor can be described as follows

$$W_{\mu\nu}^a = \partial_\mu W_\nu^a - \partial_\nu W_\mu^a - g\epsilon_{abc}W_\mu^bW_\nu^c \; . \tag{2.27}$$

The updated Lagrangian, introduced in equation (2.22), is now given by:

$$\mathcal{L} = \left((\partial_\mu + igJ_aW_\mu^a)\phi\right)^\dagger \left((\partial^\mu + igJ_bW_b^\mu)\phi\right) - \mu\phi^\dagger\phi - \lambda(\phi^\dagger\phi)^2 - \frac{1}{4}W_{\mu\nu}^aW_a^{\mu\nu} \; . \tag{2.28}$$

With the definition of ϕ in equation (2.20) and using $\phi_1 = \phi_2 = \phi_4 = 0$, the first term of this new Lagrangian can be transformed to the following equation:

$$\frac{1}{2}(\partial_\mu h(x))(\partial^\mu h(x)) + \frac{g^2}{8}\nu^2 W_\mu^aW_a^\mu + \frac{g^2}{4}\nu^2 h(x)W_\mu^aW_a^\mu + \frac{g^2}{8}h(x)^2W_\mu^aW_a^\mu \; . \tag{2.29}$$

The first term describes the kinematics of the scalar field while the second term describes the mass of the gauge fields W_μ^a:

$$\frac{g^2}{8}\nu^2 W_\mu^aW_a^\mu = \frac{1}{2}m_W^2 W_\mu^aW_a^\mu \tag{2.30}$$

This defines the mass of the W boson: $m_W = \frac{1}{2}g\nu$. The third and the fourth term

in equation (2.29) describe the coupling of the Higgs field to the gauge fields W_μ^a. In the Standard Model, $SU(2) \times U(1)$ gauge invariance is required, which extends the covariant derivative 2.24 by an additional $U(1)$ gauge field. The physical gauge bosons are the massive $W^\pm$ and Z bosons, and the massless photon. The $W^\pm$ fields are a linear combination of the W^1 and W^2, while Z boson and photon are a mixing of the W^3 field and the $U(1)$ gauge field. As discussed in [21] the mass of the Z boson is $m_Z = \frac{1}{2}\nu\sqrt{g^2 + g'^2}$. Both boson masses relate to each other in such a way: $m_W = m_Z \cos\theta_W$. The fermions get their mass via the Yukawa coupling. Local gauge invariance does not allow a bare mass term for the fermion in the SM Lagrangian density. The Yukawa coupling is the connection between the mass term of the fermion fields and the Higgs field.

The Higgs boson has not been discovered yet. Currently, only exclusion limits for the mass exists. LEP II sets a lower limit for the mass of the Standard Model Higgs of $m_H = 114\,\text{GeV}$ at $95\,\%$ confidence level (CL) [22]. Figure 2.3 shows the observed and expected $95\,\%$ CL upper limit on the ratio to the Standard Model cross section as a function of the Higgs boson mass [23]. This result is based on the combined CDF and D0 search and the green areas represent the excluded mass regions. The results by ATLAS experiment are presented in Figure 2.4 and 2.5 [24]. Here, the observed (full line) and expected (dashed line) $95\,\%$ CL combined upper limits on the SM Higgs boson production cross section divided by the Standard Model expectation as a function of the Higgs mass are shown in the low mass region (Figure 2.4) and full mass range (Figure 2.5). The red area in Figure 2.4 displays the observed exclusion at $95\,\%$ CL. As displayed in Figure 2.5 the mass is excluded for the values: $110.0\,\text{GeV}$ to $117.5\,\text{GeV}$, $118.5\,\text{GeV}$ to $122.5\,\text{GeV}$, and $129\,\text{GeV}$ to $539\,\text{GeV}$ at $95\,\%$ CL. ATLAS used several Higgs decay channels for the search like $H \to ZZ^{(*)} \to l^+l^-l^+l^-$, $H \to WW^{(*)} \to l^\pm\nu_l l^\mp\nu_l$ and $H \to \gamma\gamma$. An excess is observed in these channels by the ATLAS experiment at $m_H \approx 126\,\text{GeV}$ with a local significance of 2.5σ, where the expected significance in the presence of a Standard Model Higgs boson for that mass hypothesis is 2.9σ. The CMS experiments applied similar decay channels. The results are shown in Figure 2.6 and 2.7 [25]. The largest excess by the CMS experiment with a local significance of 3.1σ, is observed for a mass hypothesis of $m_H = 124\,\text{GeV}$ in the channels $H \to ZZ^{(*)} \to l^+l^-l^+l^-$ and $H \to \gamma\gamma$.
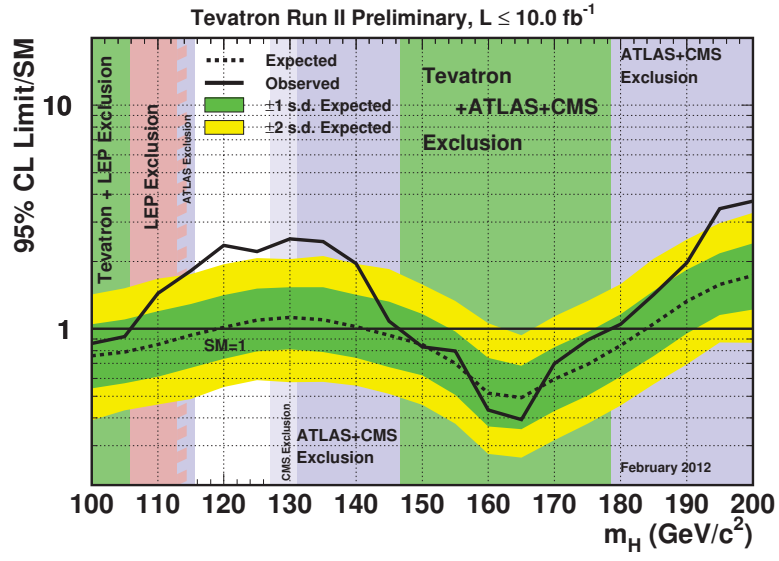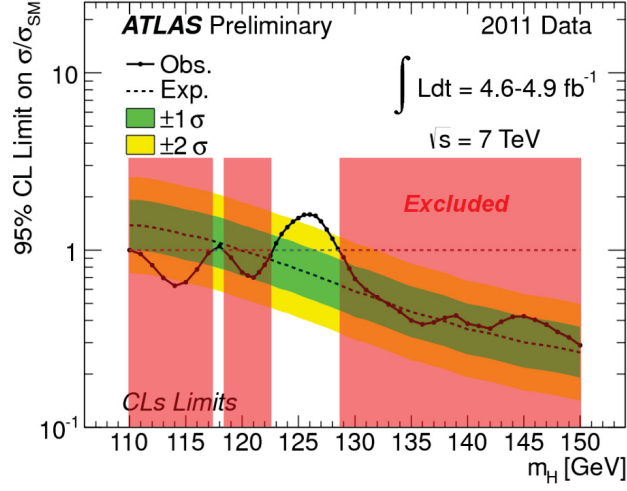
Figure 2.3.: Observed and expected (median, for the background-only hypothesis) 95 %
CL upper limits on the ratios to the SM cross section, as functions of the
Higgs boson mass for the combined CDF and D0 analyses. The bands
indicate the 68 % and 95 % probability regions where the limits can fluctuate,
in the absence of signal [23].

Figure 2.4.: The observed (full line) and expected (dashed line) 95 % CL combined up-
per limits on the SM Higgs boson production cross section divided by the
Standard Model expectation as a function of m_H in the low mass rang. The
dotted curves show the median expected limit in the absence of a signal
and the green and yellow bands indicate the corresponding 68 % and 95 %
intervals [26], [24].
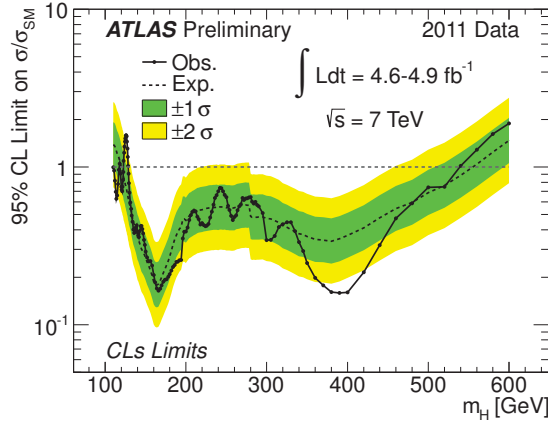
Figure 2.5.: The observed (full line) and expected (dashed line) 95 % CL combined up-
per limits on the SM Higgs boson production cross section divided by the
Standard Model expectation as a function of m_H in the full mass rang. The
dotted curves show the median expected limit in the absence of a signal
and the green and yellow bands indicate the corresponding 68 %and 95 %
intervals [24].
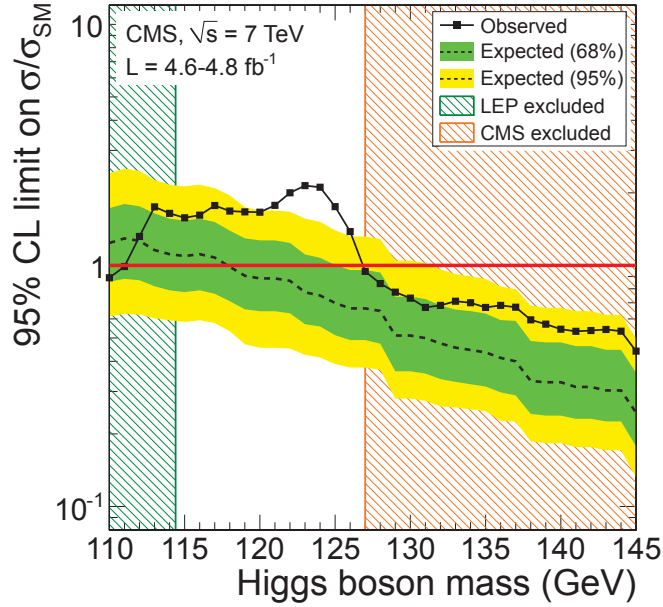
Figure 2.6.: The 95 % CL upper limits on the signal strength parameter $\mu = \sigma/\sigma_{SM}$ for the SM Higgs boson hypothesis as function of the Higgs boson mass in the low mass rang with the measurements at the CMS experiment. The observed values are shown by the solid line. The dashed line indicates the expected median of results for the background only hypothesis, while the green (dark) and yellow (light) bands indicate the ranges that are expected to contain 68 % and 95 % of all observed excursions from the median, respectively. The mass regions, which are first excluded by LEP, Tevatron and this measurement, are shown as hatched areas. [25].
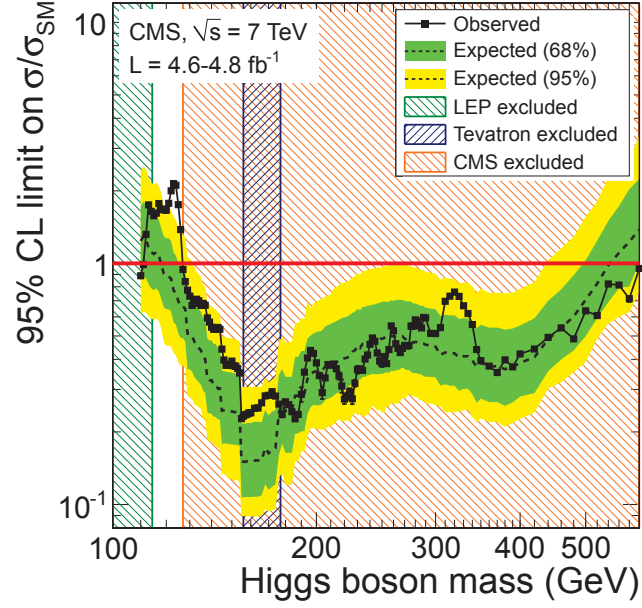
Figure 2.7.: The 95 % CL upper limits on the signal strength parameter $\mu = \sigma/\sigma_{SM}$ for the SM Higgs boson hypothesis as function of the Higgs boson mass in the full mass rang with the measurements at the CMS experiment.. The observed values are shown by the solid line. The dashed line indicates the expected median of results for the background only hypothesis, while the green (dark) and yellow (light) bands indicate the ranges that are expected to contain 68 % and 95 % of all observed excursions from the median, respectively. The mass regions, which are first excluded by LEP, Tevatron and this measurement, are shown as hatched areas [25].

2.1.4. Problems of the Standard Model

As I already discussed in the chapters before, the Standard Model can provide an explanation for many phenomena in the universe. However, as an example, the asymmetry between the matter and antimatter in the universe, which arose directly after the big bang, cannot be explained. This asymmetry, calling Baryogenesis, can be generated by three conditions, which are defined by Andrei Sakharov [13]. One of these conditions is the C and CP violation. Then the Jarlskog parameter [27] can be used for the calculation of the asymmetry parameter value, which is the ratio of the number of baryons to the number of photons. The calculated value is then by a factor of 10^{10} smaller [28] than the Wilkinson Microwave Anisotropy Probe (WMAP) [29] and COBE [30] measurement [14].

Due to the energy dependence of the coupling constants one can see that at a higher energies the three coupling constants are almost equal as shown in Figure 2.8 (dashed lines). At this energy a new symmetry group is possible with a new coupling constant describing the coupling constants of the $U(1)$, $SU(2)$ and $SU(3)$ and the Standard Model as a low energy approximation. The supersymmetric extension of the Standard Model is such a candidate to provides the possibility of the coupling constant unification. Another possible ansatz is the fourth generation model, which is discussed in chapter 2.2.
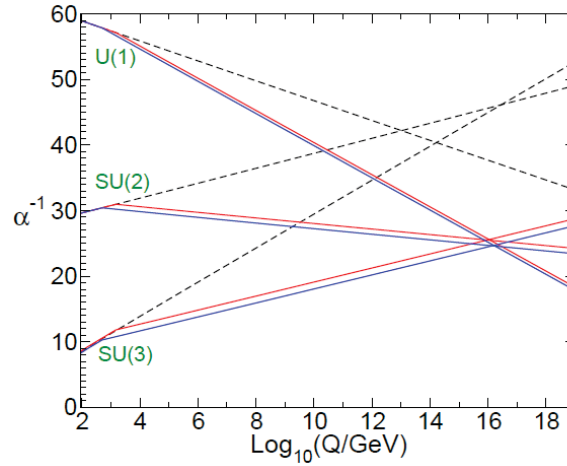
Figure 2.8.: Running of the coupling constants of $U(1)$, $SU(2)$ and $SU(3)$ in the Standard Model (dashed lines) and in the minimal supersymmetric extension of the Standard Model as the function of the energy scale [31].

2.2. The Fourth Generation

ATLAS and CMS observed an excess of events at a Higgs mass of $m_H \approx 126\,\text{GeV}$ [24] and $m_H = 124\,\text{GeV}$ [25], respectively. The channel with the highest sensitivity is $H \to \gamma\gamma$. In a case of a fourth generation model the channel $H \to gg$ [32] has the highest branching fraction. With a Higgs mass above than $150\,\text{GeV}$ the dominant decay channel is $H \to W^+W^-$ [32]. If the Higgs boson will be discovered at a mass of $m_H \approx 125\,\text{GeV}$ then many fourth generation mass scenarios are excluded.

As described in the chapter 2.1.4 with the CP violation it is possible to explain the baryon asymmetry in the beginning of the universe. But the CP violation introduced by the CKM matrix in the case of three generation is too small. Introducing an additional family of quarks involves an extension of the CKM matrix into a 4×4 matrix, which introduce two more phases. The three phases supported by a sufficient high mass of the new quarks ($m \geq 300\,\text{GeV}$) would enhance the CP violation [14].

Another interesting property of this extension of the Standard Model is the gauge couplings unification, which can be generated at a scale of order $10^{15}-10^{18}\,\text{GeV}$ in the simplest non-supersymmetric Grand Unification model $SU(5)$ [33]. Here, the function, which describes the evolution of the gauge coupling, contains contributions from Yukawa couplings. With fourth generation particles, which are sufficiently heavy, the Yukawa coupling grows with higher energies and can affect the evolution of the coupling constants.

The fourth generation quarks, if they have a higher mass than $550\,\text{GeV}$, can play an important role in electroweak symmetry breaking [15], [16]. Above this mass the particles can form a condensate state due to a strong coupling of the Goldstone bosons at the heavy quarks as discussed by the classical analysis of partial wave unitarity in [34]. This condensate can be described as a *pseudo-Goldstone boson* which can cause a global symmetry breaking.

The extension of the Standard Model with a fourth family also influences the oblique electroweak corrections [17] derived from electroweak observables like the decay width and the mass of the Z boson. The oblique correction is definition by three parameters: S, T and U, which are also known as the Peskin-Takeuchi parameters [35]. The definition is based on a reference point at $(S, T) = (0, 0)$. At this point the Standard Model is defined together with the assumption for a Higgs mass of $m_H = 115\,\text{GeV}$ and for a top mass of $m_t = 170.9\,\text{GeV}$. Due to a small value of the parameter U in every calculation the value can be set to zero and will not be considered in the following. The introduction of the fourth generation particles causes a shift of the parameters due to their masses

differences in the calculation. The shifts ΔS and ΔT of the parameter S and T are defined as follows [17], [36] :

$$\Delta S = \frac{1}{6\pi} \left(1 - 2Y \left[N_c \cdot \ln \frac{m_{t'}^2}{m_{b'}^2} - \ln \frac{m_{\nu_4}^2}{m_{\ell_4}^2} \right] \right) \tag{2.31}$$

$$\Delta T = \frac{1}{12\pi(\sin\theta_W)^2(\cos\theta_W)^2} \left[N_c \cdot \left(\frac{m_{t'} - m_{b'}}{m_Z} \right)^2 + \left(\frac{m_{\nu_4} - m_{\ell_4}}{m_Z} \right)^2 \right] . \tag{2.32}$$

The parameter N_C is the color factor. As an example Table 2.3 provides a few masses of the fourth generation particles together with the yield contribution to the S and T parameter with the 68 % confidence level ellipse of the electroweak precision constraints. This applies the following constraints on the lepton masses:

$$m_{\ell_4} - m_{\nu_4} \simeq 30 - 60 \,\text{GeV} \tag{2.33}$$

and in the case of the quark masses:

$$m_{t'} - m_{b'} \simeq \left(1 + \frac{1}{5} \ln \frac{m_H}{115 \,\text{GeV}} \right) \cdot 50 \,\text{GeV} . \tag{2.34}$$

The effect of increasing the Higgs mass and the shifts of S and T are illustrated in figure 2.9 with blue lines. The red line in figure 2.9 shows the effect of increasing the Higgs mass. For example, with a Higgs mass of $m_H = 200 \,\text{GeV}$ the value of the recalculated S and T parameter would be outside the 95 % confidence level ellipse. This confirms the incompatibility of higher Higgs masses with the Standard Model. The shifts of the S and T parameter, due to the fourth generation, move the point back into the 68 % CL ellipse. This provides allowed Higgs masses up to 315 GeV (750 GeV) for 68 % (95 %) CL.

Parameter set	$m_{t'}$ [GeV]	$m_{b'}$ [GeV]	m_H [GeV]	ΔS	ΔT
(a)	310	260	115	0.15	0.19
(b)	320	260	200	0.19	0.20
(f)	400	325	300	0.21	0.25

Table 2.3.: Parameter sets for the shifts in the (S, T) parameter space (figure 2.9), due to a 4th family. The lepton masses are fixed to $m_{\ell_4} = 155 \,\text{GeV}$ and $m_{\nu_4} = 100 \,\text{GeV}$ [17].
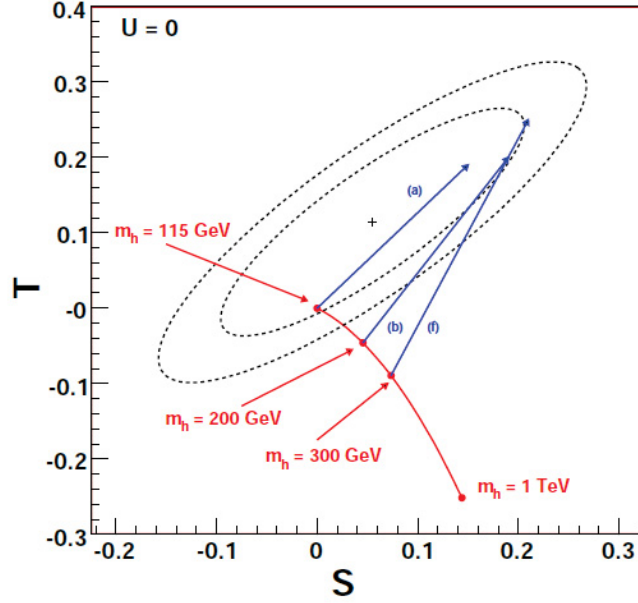
Figure 2.9.: Illustration of the shift in S,T by adding 4th generation fermions with different mass combinations (blue arrow lines), which are listed in table 2.3, and increasing Higgs boson mass (red soline line). Both, the 68% and the 95% confidence level ellipses are shown.[17].

2.2.1. Searches

Generally, the mass differences of the fourth family particles are constrained by electroweak precision data and searches at experiments could only determine mass limits. In the following, I describe the relevant searches for the quarks and leptons, which provides the highest mass constraints.

Leptons

The results for the leptons are from searches at the LEP experiments, where data from electron-positron collisions were used for the analysis. Figure 2.10 illustrates the measurement of the hadronic production cross section around the Z resonance (dots) together with the prediction for two, three and four families of light neutrinos (curves) [37]. This shows a very good agreement with the calculation of three families of light neutrinos. The precise result is: $N_\nu = 2.991 \pm 0.007$ [19]. However, this does not exclude a fourth generation neutrino but gives a lower mass limit of $m_{\nu_4} \geq m_Z/2$ for the neutrino.
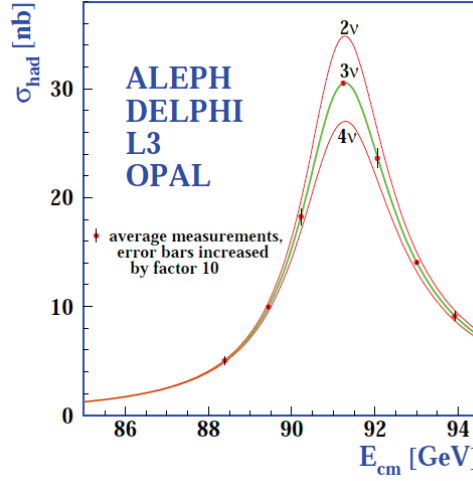
Figure 2.10.: The measurements of the hadronic production cross section around the
Z resonance done at the LEP experiments [37]. The curves describe the
theoretical Standard Model prediction for two, three and four light neutrino
families.

For the search of the charged lepton l_4 at L3 [38] a pair production via the decay of
a directly produced Z-boson or photon was assumed and it was distinguished between
two scenarios:

- The l_4 lepton has a short lifetime and decays into a W-boson and a neutrino (ν_e,
  ν_μ, ν_τ or ν_4). The W-boson can decay into every possible channel. For the searches
  the mass range $5\,\text{GeV} < \Delta m < 60\,\text{GeV}$ with $\Delta m = m_{\ell_4} - m_{\nu_4}$ is applied.

- The l_4 lepton has a long lifetime and passes the whole detector without a de-
  cay. In this case the search signature is the observation of two back-to-back high
  momentum tracks.

With an integrated luminosity of $\mathcal{L} = 450\,\text{pb}^{-1}$ the lower limit was set to $100.8\,\text{GeV}$ at
$95\,\%$ confidence level [39].

With searches at L3 a lower mass limit for the neutrino ν_4 was set and a pair production
$\nu_4\bar{\nu}_4$ via the decay of the Z-boson was assumed. The analysis was accomplished with the
assumption that ν_4 is either a Dirac- or a Majorana neutrino. To ensure a high detection
and reconstruction efficiency this search was restricted to decay lengths below $1\,\text{cm}$. The
neutrinos are assumed to decay into electrons, muons and taus with an additional W-
boson. The lowest mass limit was set for the Dirac neutrino to $m_{\nu_4}^{Dirac} > 90.3\,\text{GeV}$ [39]
and for the Majorana neutrino $m_{\nu_4}^{Majorana} > 62.1\,\text{GeV}$ [40].

2. The Standard Model and the Fourth Generation extension

Quarks

Currently. the highest mass limit for the fourth generation quarks was set by the CMS collaboration with the assumption of a short life time of the quarks. Additionally a $100\,\%$ branching fraction for the selected decay channel were assumed. Other searches for fourth generation quarks were done by the CDF collaboration [41], [42].

For the search of the t' quark at the CMS experiment the decay channel $t'\bar{t}' \to WbW\bar{b} \to l\nu bq\bar{q}\bar{b}$ was required and was done in lepton-plus-jets events [43]. A single charged and isolated lepton ($e^{\pm}$ or $\mu^{\pm}$), missing transverse momentum and at least four jets with high transverse momenta were used as the search signature. For the electron channel a luminosity of $\mathcal{L} = 4683\,\mathrm{pb}^{-1}$ and for the muon channel of $\mathcal{L} = 4601\,\mathrm{pb}^{-1}$ were available. In the electron channel electrons were selected with the requirements on the transverse momentum $p_T > 35\,\mathrm{GeV}$ and on the pseudorapidity $|\eta| < 2.5$. The criteria for the four jets is $|\eta| < 2.45$ and $p_T > 120$ for the leading jet, $90\,\mathrm{GeV}$ for the second leading jet and $35\,\mathrm{GeV}$ and $30\,\mathrm{GeV}$ for the last two jets. At least one jet had to fulfill the *b-jet* identification criteria. Every event had a missing transverse momentum of $p_T > 20\,\mathrm{GeV}$. The Muons in the muon channel were selected with $p_T > 35\,\mathrm{GeV}$ and $|\eta| < 2.1$ and for the jets and the missing transverse energy the same criteria were applied as for the electron channel. The mass of the t' was calculated with a kinematic fit and together with H_T the presence of this quark was tested via a likelihood fit. H_T is the sum of the transverse energies of the leptons, the jets and the magnitude of missing p_T. Masses for the t' below $557\,\mathrm{GeV}$ at $95\,\%$ confidence level were excluded [43].

For the search for the heavy bottom like quark at the CMS experiment the decay channel $b' \to tW$ with a branching fraction of $100\,\%$ was assumed with the search signature of trileptons or same-sign charged dileptons and at least one *b-jet* in the final state. The integrated luminosity for the analysis was $\mathcal{L} = 1.14\,\mathrm{fb}^{-1}$. The criteria for the isolated muons and isolated electrons were $p_T > 20\,\mathrm{GeV}$ and $|\eta| < 2.4$. Every same-sign dilepton (trilepton) event should have at least four (two) jets with $p_T > 25\,\mathrm{GeV}$ and $|\eta| < 2.5$. Events with the invariant mass of $|M_{ll} - M_Z| < 10\,\mathrm{GeV}$ for same-sign electron or muon pairs were rejected in order to suppress the background from the Z decays. The scalar variable $S_T = \sum p_T(jets) + \sum p_T(leptons) + \not{E}_T$ should be higher than $500\,\mathrm{GeV}$ in every event. With the background yields and observed data events the lower mass limit was calculated with the Bayesian method [44] to $611\,\mathrm{GeV}$ at $95\,\%$ confidence level [45].

Searches for the t' and b' were done at the ATLAS experiment as well. Masses for the b' with less than $m_{b'} = 495\,\mathrm{GeV}$ were excluded at $95\,\%$ confidence level [46]. Here, a pair production of the b' and a decay $b'\bar{b}' \to t\bar{t} + W^+W^- \to b\bar{b}W^+W^+W^-W^- \to l\nu_l qqqqqq$

were assumed in the lepton-plus-jet channel. For the analysis exactly one lepton, large missing transverse momentum and at least six jets were applied. In the case of the t' the lepton-plus-jets channel were also used. As for the b' a pair production were assumed and the decay channel of the t' was $t'\bar{t}' \to b\bar{b} + W^+W^- \to b\bar{b}l\nu_l qq$. An isolated electron or muon, high missing transverse momentum and at least three jets were used in this analysis. Here, masses below $m_{t'} = 495\,\text{GeV}$ were excluded at $95\,\%$ confidence level [47].

If the CKM matrix has tiny mixing angles between the fourth and the other three families the fourth generation quarks could have a long lifetime. In this situation the quarks can escape the acceptance of the analysis cuts and lower mass limits are possible again [48]. A lower mass limit is also possible if the quarks have a smaller branching ratio as the requirement of $100\,\%$. Thus, searches for quarks with a mass, which is lower than the mass limit, are motivated again.

2.2.2. CKM matrix

In the case of a fourth family the CKM matrix becomes:

$$V_{CKM}^{4x4} = \begin{pmatrix} V_{ud} & V_{us} & V_{ub} & V_{ub'} \\ V_{cd} & V_{cs} & V_{cb} & V_{cb'} \\ V_{td} & V_{ts} & V_{tb} & V_{tb'} \\ V_{t'd} & V_{t's} & V_{t'b} & V_{t'b'} \end{pmatrix} \tag{2.35}$$

In this case $V_{nb'}$ with $n = u, c, t$ and $V_{t'm}$ with $m = d, s, b$ describe the quark mixing of the new family with the other three know families. For the extension of the parametrized V_{CKM}^{3x3} matrix, introduced in equation (2.14), into V_{CKM}^{4x4}, the matrix has to be multiplied with three new matrices. These new matrices describe the mixing of the fourth family with the other three SM families. The parametrized V_{CKM}^{4x4} is given by:

$$V_{CKM}^{4x4} = \begin{pmatrix} & & & 0 \\ & V_{CKM}^{3x3} & & 0 \\ & & & 0 \\ 0 & 0 & 0 & 1 \end{pmatrix} \times \begin{pmatrix} 1 & 0 & 0 & 0 \\ 0 & 1 & 0 & 0 \\ 0 & 0 & c_{34} & s_{34} \\ 0 & 0 & -s_{34} & c_{34} \end{pmatrix} \times \tag{2.36}$$

$$\begin{pmatrix} 1 & 0 & 0 & 0 \\ 0 & c_{24} & 0 & s_{24}e^{-i\delta_2} \\ 0 & 0 & 1 & 0 \\ 0 & -s_{24}e^{i\delta_2} & 0 & c_{24} \end{pmatrix} \times \begin{pmatrix} c_{14} & 0 & 0 & s_{14}e^{-i\delta_3} \\ 0 & 1 & 0 & 0 \\ 0 & 0 & 1 & 0 \\ -s_{14}e^{i\delta_3} & 0 & 0 & c_{14} \end{pmatrix}$$

The phase angles are described by δ_1, δ_2 and δ_3 and the parameters c_{i4} and s_{i4} ($i = 1, 2, 3$) are the cosine and the sine of the Euler angles θ_{14}, θ_{24} and θ_{34}. These angles denote the mixing between the fourth family and the other three families.

Table 2.4 shows the measured values of the CKM matrix elements with their uncertainties taken from the *Particle Data Group* [19]. With the assumption of a unitary

CKM matrix element	Value [19]
V_{ud}	0.97425 ± 0.00022
V_{us}	0.2252 ± 0.0009
V_{cd}	0.230 ± 0.011
V_{cs}	1.023 ± 0.036
V_{cb}	$(40.6 \pm 1.3) \times 10^{-3}$
V_{ub}	$(3.89 \pm 0.44) \times 10^{-3}$

Table 2.4.: The most precisely measured CKM matrix elements with their uncertainties. Further details on how these elements have been measured are described in chapter 11 of ref. [19].

$V_{CKM}^{4\mathrm{x}4}$ it is possible to calculate the value ranges of the new fourth generation elements in $V_{CKM}^{4\mathrm{x}4}$. Further constraints on the values of the CKM parameters, which describes the mixing of the fourth families with the other three know Standard Model families, are discussed in [49] and [50].

2.2.3. Search strategy for down-type quarks with same-sign charged leptons

The LHC is a proton-proton collider (for more information see chapter 3.1) and the pair production channels of fourth generation quarks are the following:

1. $gg \rightarrow g \rightarrow Q\bar{Q}$

2. $q\bar{q} \rightarrow g \rightarrow Q\bar{Q}$

3. $q\bar{q} \rightarrow \gamma/Z \rightarrow Q\bar{Q}$

The cross section for the pair production of the heavy quark is calculated with the software tool HATHOR [51] including NNLO$^{\mathrm{approx}}$ cross sections [52], [53]. For the calculation of the NNLO$^{\mathrm{approx}}$ cross section only terms, which are dominating the results, are taken into account for the next-to-next-to-leading order (NNLO) QCD correction. The neglecting terms are not calculated without changing the result significantly. Figure 2.11 shows the NNLO$^{\mathrm{approx}}$ cross section as a function of the heavy quark mass for proton-anti-proton collisions at a center-of-mass energy of $\sqrt{s} = 1.96\,\mathrm{TeV}$ (Tevatron)

and for proton-proton collisions at a center-of-mass energy $\sqrt{s} = 7\,\text{TeV}$, $10\,\text{TeV}$ and $14\,\text{TeV}$ (LHC). For the calculation, all possible production channels are included. The cross section for $\sqrt{s} = 7\,\text{TeV}$ is one order of magnitude higher as for the Tevatron and provides an analysis for which less luminosity is needed. The cross section for proton-proton collisions do not decrease as strongly with higher masses as for proton-anti-proton collisions.
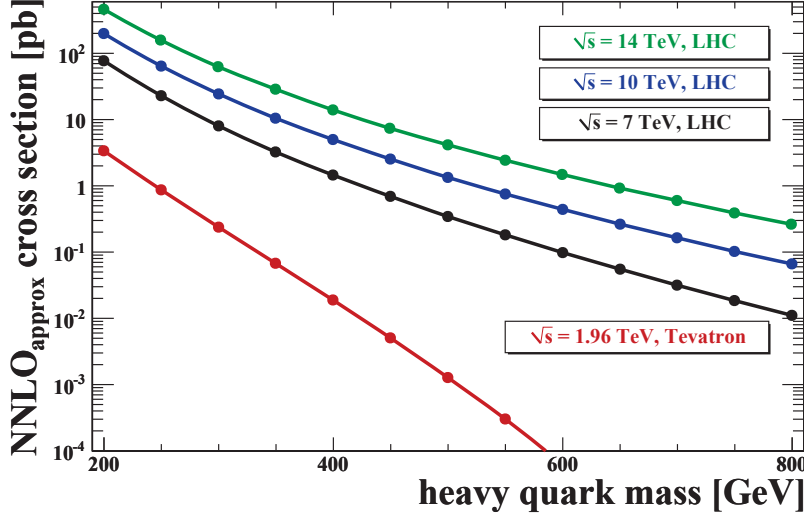
Figure 2.11.: Approximate next-to-next-to-leading order cross sections [52], [53] for heavy quark pair production as a function of the heavy quark mass and for different center-of-mass energies [51].

In the case of a single quark production, the channels are the same as for single top production introduced in Figure 4.6 (chapter 4.1.4).

Generally, the decay channel depends on the masses of the heavy quarks and the CKM matrix elements. With the assumption of a unitary V_{CKM}^{4x4} matrix many scenarios are possible inside the uncertainties of the V_{CKM}^{3x3} elements. The electroweak precision fit prefer $m_{t'} > m_{b'}$ and $|m_{t'} - m_{b'}| < m_W$ [17]. Adding the CKM mixing in the calculation of the oblique parameters S, T and U shows that the probability of mass scenario, $m_{b'} > m_{t'}$, is higher as without the CKM mixing [54]. In the case of $m_{t'} > m_{b'}$, the b' cannot decay into a t' and W. With the assumption $m_{b'} > m_{t'}$, two scenarios are possible: With $|m_{t'} - m_{b'}| > m_W$ the b' prefers to decay either in $b'\bar{b}' \rightarrow t\bar{t} + W^+W^-$ or in $b'\bar{b}' \rightarrow t'\bar{t}' + W^+W^-$. If one assume a smaller mass difference between b' and t' than the W boson mass, the b' cannot decay into t' and a W, but it prefers the decay

$b' \rightarrow t + W$. In all possible mass scenarios one can see that every scenario contains the decay $b' \rightarrow t + W$ and a final state of $b\bar{b} + 2W^+2W^-$ listed in table 2.5. This shows that

$m_{t'} > m_{b'}$	$m_{t'}$-$m_{b'} > m_W$	$b'\bar{b}' \rightarrow tW^-\bar{t}W^+ \rightarrow b\bar{b} + 2W^+2W^-$
		$t'\bar{t}' \rightarrow b'\bar{b}' + 2W \rightarrow b\bar{b} + 3W^+3W^-$
	$m_{t'}$-$m_{b'} < m_W$	$b'\bar{b}' \rightarrow t\bar{t} + W^-W^+ \rightarrow b\bar{b}2W^+2W^-$
		$t'\bar{t}' \rightarrow bW^+\bar{b}W^-$
$m_{b'} > m_{t'}$	$m_{b'}$-$m_{t'} > m_W$	$b'\bar{b}' \rightarrow t'W^-\bar{t}'W^+ \rightarrow b\bar{b} + 2W^+2W^-$
		$b'\bar{b}' \rightarrow tW^-\bar{t}W^+ \rightarrow b\bar{b} + 2W^+2W^-$
		$t'\bar{t}' \rightarrow bW^+\bar{b}W^-$
	$m_{b'}$-$m_{t'} < m_W$	$b'\bar{b}' \rightarrow tW^-\bar{t}W^+ \rightarrow b\bar{b}2W^+2W^-$
		$t'\bar{t}' \rightarrow bW^+\bar{b}W^-$

Table 2.5.: Possible final states of t' and b' decays as a function of the mass scenarios between t' and b' with the assumption of $|m_{b'} - m_t| > m_W$.

the decay and the final state are independent of the mass scenarios of the b' and t'. The complete decay channel is the following:

$$pp \rightarrow b'\bar{b}' + X \rightarrow t\bar{t} + W^+ + W^- + X \rightarrow b\bar{b} + W^+ + W^- + W^+ + W^- + X \quad (2.37)$$

With the assumption of a leptonic decay of two same-sign charged W bosons, this leads to a possible final state of same-sign leptons, which can be an electron or muon pair and also a combination of an electron and a muon. This final state is a rare Standard Model signature and be used as an search signature for suppressing the Standard Model background efficiently. With the hadronic decay of the other W bosons and the presence of the two b-quarks the jet multiplicity is very high. Further, neutrinos coming from the W decay, which cannot be measured in the detector, lead to a missing transverse energy. Requiring a high jet multiplicity and a high missing transverse energy, this can support the background suppression. Figure 2.12 shows the complete decay channel. It is still possible that other effects like the charge misidentification of the leptons can fake this search signature. A detailed discussion of this is provided in chapter 4.1.4.
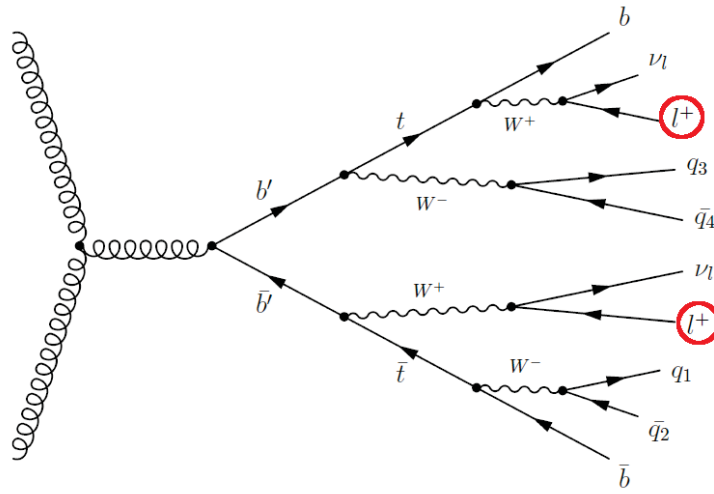
Figure 2.12.: The pair production of $b'\bar{b}'$ and the complete decay channel with two same-sign leptons (red) in the final state [20].

3. The LHC and the ATLAS Detector

The LHC[55] is a machine for proton-proton collisions designed for a maximum center-of-mass energy of $\sqrt{s} = 14$ TeV. At the four collision points of the LHC the following detectors are located: ATLAS [56], CMS [57], ALICE [58] and LHCb [59].

ATLAS and CMS are multi-purpose detectors for the discovery of new particles, while ALICE and LHCb have been built for special physics projects. ALICE is used for the study of the quark-gluon plasma, especially in heavy ion collisions, to understand the situation of the universe a few minutes after the big bang. LHCb investigates b-hadron physics for a better understanding of CP violation. In the following, I briefly describe the LHC and the ATLAS detector in detail.

3.1. The Large Hadron Collider

The LHC has been built in the former LEP tunnel at CERN with a circumference of 27 km. The current setup of the LHC provides a center-of-mass energy of $\sqrt{s} = 7$ TeV. It will increase up to $\sqrt{s} = 14$ TeV after the upgrade of the LHC during the technical stop in 2013/2014. Before the protons enter in the LHC, they have to pass several pre-accelerators (see Figure 3.1). In the first step, the protons are accelerated by a linear accelerator (LINAC) to an energy of 50 MeV. Then in the *PS* and the *SPS* the particles are accelerated up to 25 GeV and 450 GeV, respectively. Finally, in the LHC itself the protons reach their final energy. In the LHC, they gain their energy from superconductive radio frequency cavities and stay on track with the magnetic fields provided by a total of 1232 superconductive dipole magnets. These magnets have a length of 15 m and a working temperature of 1.7 K. Both beams are deflected inside these magnets.

The design luminosity of the LHC at $\sqrt{s} = 14$ TeV is $L = 10^{34}$ cm^{-2}s^{-1}. The luminosity is defined as

$$\mathcal{L} = f \cdot \frac{n_1 \cdot n_2}{4\pi\sigma_x\sigma_y}, \tag{3.1}$$

where f is the collision frequency, n_1 and n_2 are the numbers of particles in the two proton beams. σ_x and σ_y are the widths of the beam in the x and y direction, respectively. The
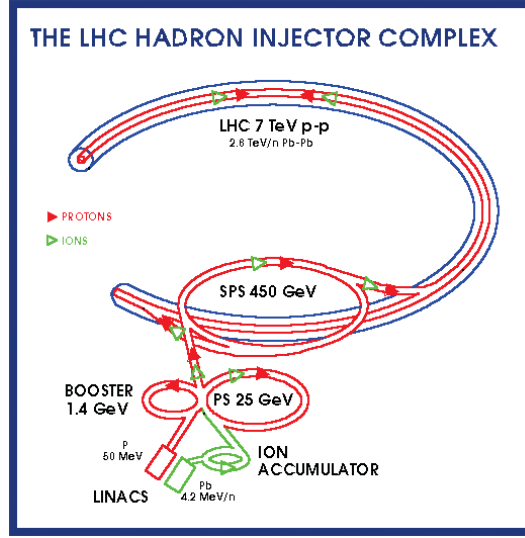
Figure 3.1.: Schematic overview of the various stages of acceleration of both protons and ions on their way to injection into LHC [60].

determination of the luminosity is presented briefly in chapter 4.2.

3.2. ATLAS Detector

As mentioned above, the ATLAS experiment (A Toroidal LHC ApparatuS) is a multi-purpose detector and has been built to study a variety of physics topics at the LHC. For this purpose, the detector has been assembled in a series of superposed concentric cylinders for the measurement of electrons, photons, muons and jets (for the jet reconstruction see chapter 5.3) around the beam to cover a wide range of η and ϕ [see Figure 3.2]. More information about the coordinate system can be found in chapter 3.2.1.

The central part is the inner detector (ID) for the reconstruction of the tracks of charged particles with a high precision. It consists of the pixel detector, the semiconductor tracker (SCT) and the transition radiation tracker (TRT). All these components are surrounded by a superconductive solenoid with a magnetic field of 2 T. The ID with the solenoid magnet is followed by the calorimeter system, which measures the energy of electromagnetically and strongly interacting particles. It contains the electromagnetic calorimeter (ECAL) and hadronic calorimeter (HCAL). The outermost system is the muon spectrometer (MS) for the muon reconstruction together with the toroid Magnet system which provides a field up to 1 T. The detector has a mass of around 7000 t, a length of 44 m and a height of 25 m.
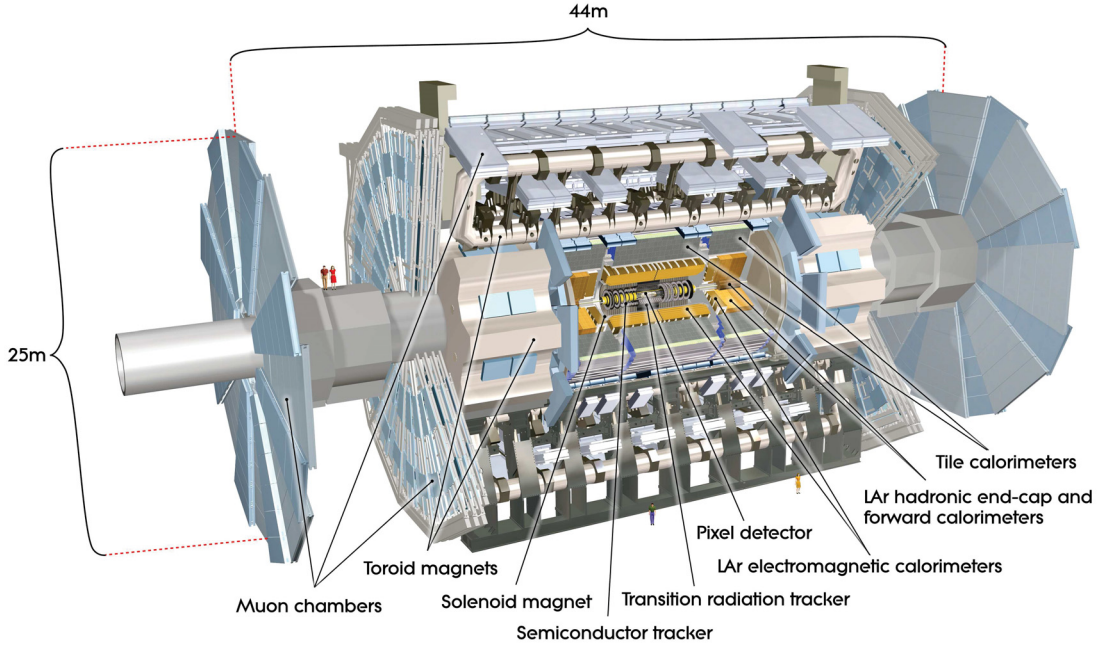
Figure 3.2.: Overview of the ATLAS detector [56].

3.2.1. Coordinate system

ATLAS has a symmetric structure with the nominal interaction point in the center of the detector. Due to this, a cylindrical coordinate system can be used, whose point of origin is situated in the center of the detector. The x-axis of this system points towards the center of the accelerator, while the y-axis is directed upwards. For the definition of the right-handed coordinate system the z-axis points along the beam pipe of the LHC in the clockwise direction. Using the polar angle Θ, which is measured from the positive z-axis, the pseudorapidity η is defined as follows:

$$\eta = -\ln\left(\tan\frac{\Theta}{2}\right) \; . \tag{3.2}$$

In the case of massless particles, η equals the rapidity y:

$$y = \frac{1}{2}\ln\left(\frac{E + p_z}{E - p_z}\right) \; , \tag{3.3}$$

where E is the energy of the particle and p_z is the z component of the momentum. The x- and y-axis determine the azimuthal angle ϕ by $\tan\phi = \frac{x}{y}$ varying between $-\pi$ and π. Due to the Lorentz invariance of the rapidity, the distance between two particles is

defined in terms of their distances in η and ϕ:

$$\Delta R = \sqrt{(\Delta\eta)^2 + (\Delta\phi)^2} \ . \tag{3.4}$$

3.2.2. The magnet system

In ATLAS two magnet systems have been implemented for the measurement of the track momenta of charge particles. Figure 3.3 shows a drawing of the geometry of the magnet windings and the tile calorimeter steel. The solenoid winding lies inside the calorimeter volume. In total, both systems together store an energy of 1.6 GJ.

The magnet, which provides the magnetic field for the ID, has solenodial shape and is placed between the ID and the ECAL. It produced an axial field of 2 T. In order to reach a good energy resolution in the calorimeter, this magnet was designed to have a relatively law material budget of 0.66 X_0. The radiation length X_0 of a material designates the average distance. A particle in their case an electron has to migrate for a reduction of its energy to $\frac{1}{e}$ of the original value. The solenoid magnet has an axial length of 5.8 m and an inner and outer radius of 2.46 m and 2.56 m, respectively.

The toroid magnet system is split into the barrel and the endcap part with a field of 0.5 T and 1 T, respectively. Every system contains coils assembled radially and symmetrically around the beam axis. To provide an overlap between the barrel and the endcap magnetic field, the endcaps are rotated by 22.5° with respect to the barrel system.

3.2.3. The Inner detector

The innermost detector is the inner detector, which is split into three parts: the pixel detector, the semiconducting tracker and the transition radiation tracker. The detector was designed for the identification of the tracks and the sign of charged particles and the vertex reconstruction with a very high precision. In the ID only the transverse momentum p_T can be measured via the bending of the track in the $R-\phi$ plane caused by the Lorentz force in the magnetic field of the solenoid magnet. This is due to the magnetic field being aligned parallel to the z-axis. The other components of the momentum are calculated by a fit of the track. The relevant information is provided by the hits in the different components of the ID. Via the primary and the secondary vertex reconstruction it is possible to calculate the life-time of particles which decay directly in the ID. For example *b-tagging* [61], an algorithm for the identification of b-jets, can be realized with the ID. Figure 3.4 shows a drawing of an overview of the ID with the separate components displayed. Figure 3.5 presents a drawing of the sensors and structural elements of the
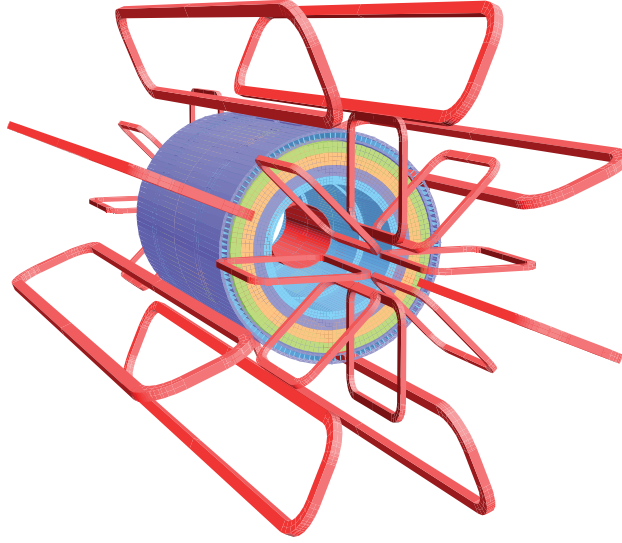
Figure 3.3.: Geometric overview of the eight barrel toroid coils and the magnet windings of both endcaps with the tile calorimeter steel. The tile calorimeter consists of by four layers with different magnetic properties and an outside return yoke. [56].

ID. The momentum resolution of the ID containing all components is [56]:

$$\sigma_{p_T}/p_T = 0.05\,\%p_T \oplus 1\,\% \ . \tag{3.5}$$

The pixel detector

The innermost part of the ID is the pixel detector which provides an excellent primary and secondary vertex reconstruction. The pixel detector is built using three layers in the barrel region (layer 0, layer 1 and layer 2) and three discs on each end. The first layer in the barrel region is constructed for the identification of b-hadron decays and is therefore called the b-layer. The high precision of the pixel detector also provides the possibility to distinguish the primary from the secondary vertices. The detector is built up of 1500 barrel modules and 1000 disc modules. Every disc module consists of 60000 pixel modules with a size of $50\,\mu\text{m} \times 400\,\mu\text{m}$. As a result, the pixel detector provides three points for the determination of the position of every charged track. The resolution of this detector is $10\,\mu\text{m}$ in the $R - \phi$ plane and $115\,\mu\text{m}$ in the z-direction. Each layer has a thickness of $1\,\%$ of the radiation length and covers an η range of $|\eta| < 2.5$.
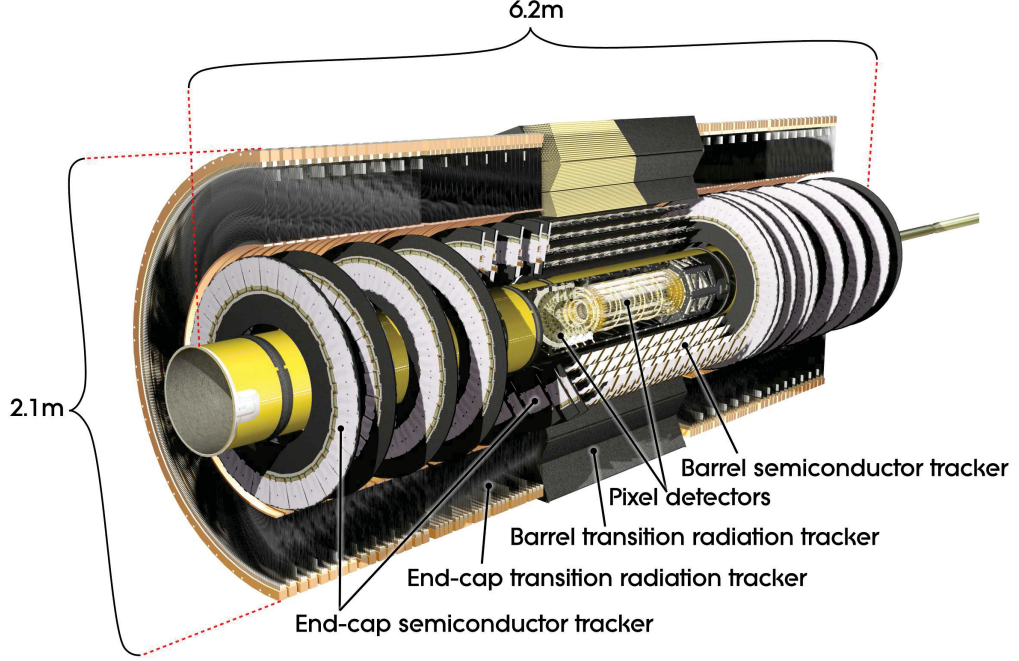
Figure 3.4.: Overview of the ATLAS inner detector [56].

The semiconductor tracker

The detector enclosing the Pixel detector is the semiconductor tracker, which is build up of silicon sensors segmented in strips. With the SCT the position of the track in the azimuthal $R - \phi$ plane is measured together with the transverse impact parameter d_0, which is the distance between the point of closest approach (PCA) of a track and the reconstructed primary vertex (defined in 6.2). This parameter is calculated as follows:

$$d_0 = (\overrightarrow{x}_{PrimVertex} - \overrightarrow{x}_{PCA}) \cdot (\overrightarrow{p} \times \overrightarrow{e}_z)), \tag{3.6}$$

where $\overrightarrow{p}$ is the reconstructed momentum of the track and $\overrightarrow{e}_z$ is the unit vector in z-direction in the PCA. $\overrightarrow{x}_{PrimVertex}$ is defined as the vector from the interaction point, which is the center of the coordinate system, to the primary vertex. The vector between the PCA and the interaction point is $\overrightarrow{x}_{PCA}$. The distance in the z-coordinate is given by the longitudinal impact parameter (z_0), which is also determined by the SCT. In the barrel part of the detector the strips are wire bonded together to 12.8 cm long strips and glued together in 4 mrad stereo angle back-to-back to form a module. The modules in the forward area are similar ordered, while the stripes have a tapered shape. The
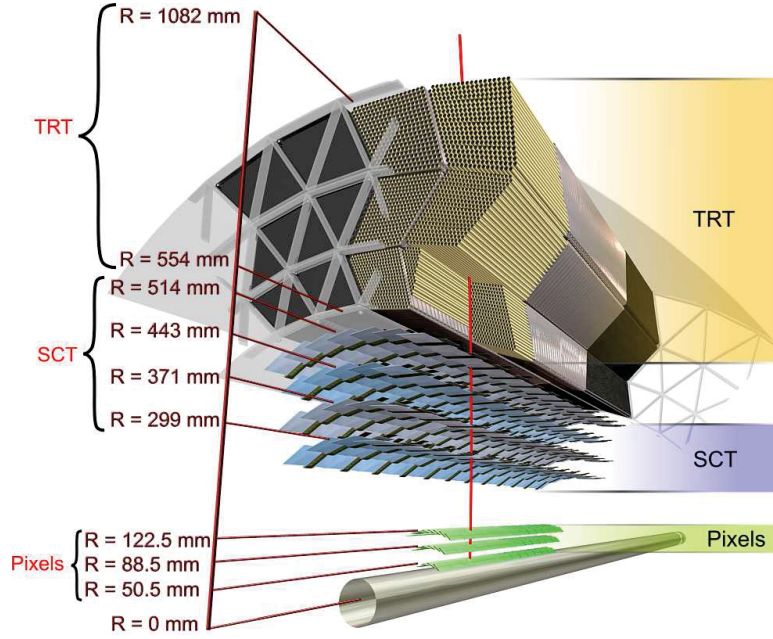
Figure 3.5.: The diagram shows the sensors and structural elements of the ID traversed by a charged track of $p_T = 10\,\text{GeV}$ in the barrel part of the ID ($\eta = 0.3$). The track crosses the beryllium beam pipe, the three cylindrical silicon-pixel layers, the four cylindrical double layers of the SCT and the transition radiation tracker [56].

SCT has 4088 modules and a resolution of $17\,\mu\text{m}$ in the $R - \phi$ plane and $580\,\mu\text{m}$ in the z-direction. The tracks can be distinguished, if they are at least $200\,\mu$ metre away from each other. One segment has a surface of $6.6\,\text{cm}^2 \times 6.40\,\text{cm}^2$.

The transition radiation tracker

The outermost part of the ID is the transition radiation tracker. This is a drift chamber, which is built up of 370 000 straw tubes. These tubes contain $70\,\%$ Xe, $27\,\%$ CO_2 and $3\,\%$ O_2. The diameter of each tube is $4\,\text{mm}$. The barrel part of the detector consists of 50 000 straws with a length of $144\,\text{cm}$ and each of the endcaps have 320 000 radial straws in 20 wheels. The resolution of the TRT is $130\,\mu\text{m}$ in the $R - \phi$ plane due to the transition radiation fibers, which are interleaved between the straws. Low energy transition radiation photons are then absorbed in the Xenon gas and produce larger signal amplitudes than minimum-ionizing charged particles. With the low and high threshold it is possible to distinguish between transition radiation signals and normal track signals. This provides the possibility to discriminate between electrons and charged

pions.

3.2.4. The Calorimeter system

The task of the calorimeter is to measure the energy of the particles by absorbing the particles completely. When the particles pass the calorimeter system they interact with the material and produce a shower of secondary particles. These particles can be measured and the information is used by the algorithm for the particle identification. The ATLAS calorimeters are a sampling calorimeters, which contain layers of absorber and a passive materials. The absorber material induces the shower of particles, which are then measured by the passive material. Unlike the ID the calorimeter can detect neutral particles as they interact electromagnetically or hadronically. The ATLAS calorimeter system has a high granularity and due to this it provides the possibility to measure the shape and the position of the shower. This is needed for the discrimination between pions and electrons. Figure 3.6 shows the ATLAS calorimeter system. It consists of four subsystems: the hadronic tile calorimeter, the electromagnetic calorimeter, the hadronic endcap calorimeter, forward calorimeter.
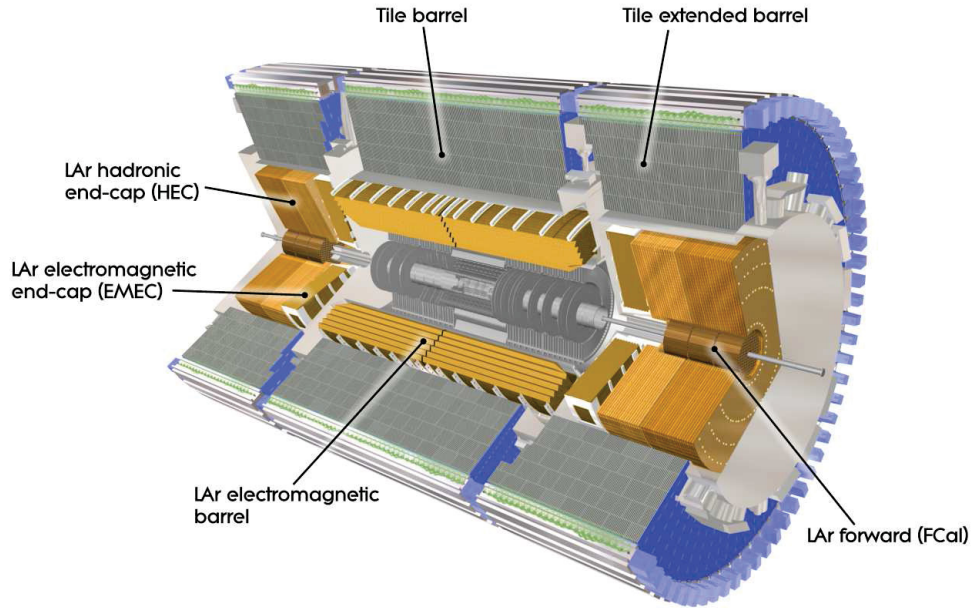
Figure 3.6.: Overview of the ATLAS calorimeter system [56].

The electromagnetic calorimeter

The inner part of the calorimeter system is the electromagnetic calorimeter (ECAL). It is a liquid-argon calorimeter (LAr) with an accordion structure as shown in Figure 3.7. In this sampling calorimeter lead layers are used as absorber and the liquid argon for the detection of the particles. The ECAL is segmented into the barrel ($\eta < 1.475$) and the two endcaps ($1.375 < |\eta| < 3.2$). The barrel itself is divided in two parts of $3.5\,\text{m}$ length with a gap of $4\,\text{mm}$ at $z = 0$. Both endcaps are segmented into two wheels. The inner wheels cover the η-range $1.375 < |\eta| < 2.5$ and the outer wheels cover the η-range $2.5 < |\eta| < 3.2$. With the accordion geometry the calorimeter has a symmetric structure in ϕ without any gaps. Its main task is to measure and identify electrons and photons of a broad energy spectrum. An important requirement of the calorimeter is the sufficient thickness. It has to be at least several radiation length X_0 thick so that the electrons and photons do not punch through. Therefor, the barrel has a diameter of 22 X_0 and both endcaps a length of 24 X_0. Between the calorimeter system and the ID, in the range of $|\eta| < 1.8$, the LAr presampler is installed for the correction of the energy loss of electrons and photons due to their passing through the ID, solenoid and cyrostat. The first sampling of the calorimeter is made by fine strips for a precise measurement of the particle η position to distinguish from each other. The second sampling is the longest and absorbs the largest part of the energy. The resolution of this part is better than that of the third one, which is mainly used for definition of the leakage into the hadronic calorimeter. The resolution σ_E of the ECAL is defined by [56]:

$$\sigma_E/E = 10\,\%/\sqrt{E} \oplus 0.7\,\% \tag{3.7}$$

The tile hadronic calorimeter

The main task of the tile calorimeter (HCAL) is the measurement of the energy of the jets. Here, steel is used for the absorbing layers and scintillating tiles for the detection layers. The barrel covers the range of $|\eta| < 1.0$. From $|\eta| = 0.8$ till $|\eta| = 1.7$ two wheels take care of the energy measurement. The resolution σ_E of the HCAL is defined by [56]:

$$\sigma_E/E = 50\,\%/\sqrt{E} \oplus 3\,\% \ . \tag{3.8}$$

LAr hadronic endcap and forward calorimeter

For the η-range $1.5 < |\eta| < 3.2$ the hadronic endcap calorimeter (HEC) was built in two wheels, which use parallel copper plates to cause the particle shower.
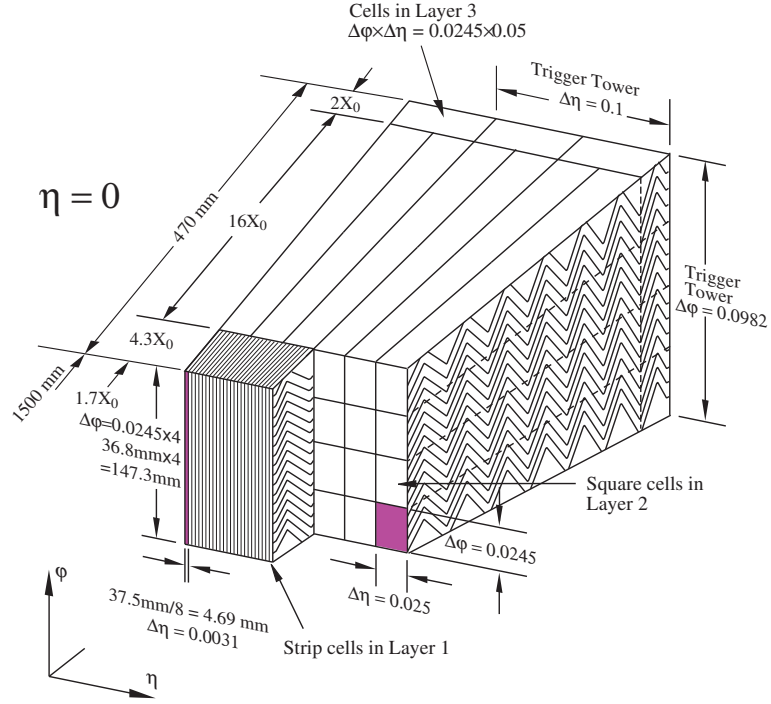
Figure 3.7.: Sketch of a barrel module where the different layers are clearly visible. The granularity in η and ϕ of the cells in the three layers and the trigger towers is also shown. [56].

The forward calorimeter (FCAL) covers the region $3.1 < |\eta| < 4.9$. In this system liquid argon is the active material and two different materials are used for the absorption: For the first of the three modules copper is used for the electromagnetic measurement and for the other two tungsten is used for the hadronic measurement.

The resolution of the HEC is [56]:

$$\sigma_E/E = 50\,\%/\sqrt{E} \oplus 3\,\% \, , \tag{3.9}$$

while for FCAL the resolution is [56]:

$$\sigma_E/E = 100\,\%/\sqrt{E} \oplus 10\,\% \, . \tag{3.10}$$

3.2.5. The Muon Spectrometer

The outermost detector is the muon spectrometer (MS), which was built for the identification of muons. Muons are minimal ionizing particles and pass the other components

of the ATLAS detector almost without any interaction. The magnetic field for the track reconstruction is provided by the Toroid magnetic system. This system consists of the barrel range ($|\eta| < 1.4$) and the forward region ($1.6 < |\eta| < 2.7$). As described above for the transition area both systems are used. The MS is built up of different components: monitored drift tubes (MDT), cathode strip chambers (CSC), thin gap chambers (TGC) and resistive plate chambers (RPC).

Over most of the η range the MDTs are used for the precision measurement of tracks. These contain three to eight layers of drift tubes made up of aluminum and have a diameter of 30 mm. The gas inside the tubes is 93 % Ar and 7 % CO_2. Based on this construction the resolution is 35 µm per chamber and 80 µm per tube. The muon spectrometer contains 1088 monitored drift tubes.

In the region $2.0 < |\eta| < 2.7$ the cathode strip chambers are used for the innermost tracking layer. These are multiwire proportional chambers with cathode plane segments and provide a resolution of 5 mm in the transverse plane and 40 µm in the bending plane. The CSCs have a higher rate capability and time resolution as the MDT due to the gas mixture of 30 % Ar, 50 % CO_2 and 20 % CF_4 in the CSCs.

Another task of the MS is to efficiently trigger the muon tracks and to identify the corresponding bunch crossing. In the barrel region ($|\eta| < 1.5$) resistive plate chambers are used with a time resolution of 1.5 ns. In the endcaps ($1.05 < |\eta| < 2.4$) the TGCs are chosen for this task with a time resolution of 4 ns. The RPCs are built up of two resistive plates which are parallel oriented with a distance of 2 mm between each other. The thin gap chambers are multi wire proportional chambers with a functionality comparable to the cathode strip chambers. These chambers have a better time resolution than the RPCs due to a different gas mixture and a smaller distance between the anode and the cathode.

As a result of the layout of the monitored drift tubes the thin gap chambers are needed to determine the azimuthal coordinate of a muon track for the completion of the measurement. For the inner layers of the MDT two layers of the TGCs are used while the middle layer is completed by seven TGC layers. The resolution of the MS is [56]:

$$\sigma_{p_T}/p_T = 10\,\% \text{ at } \mathrm{u}p_T = 1\,\text{TeV} . \tag{3.11}$$
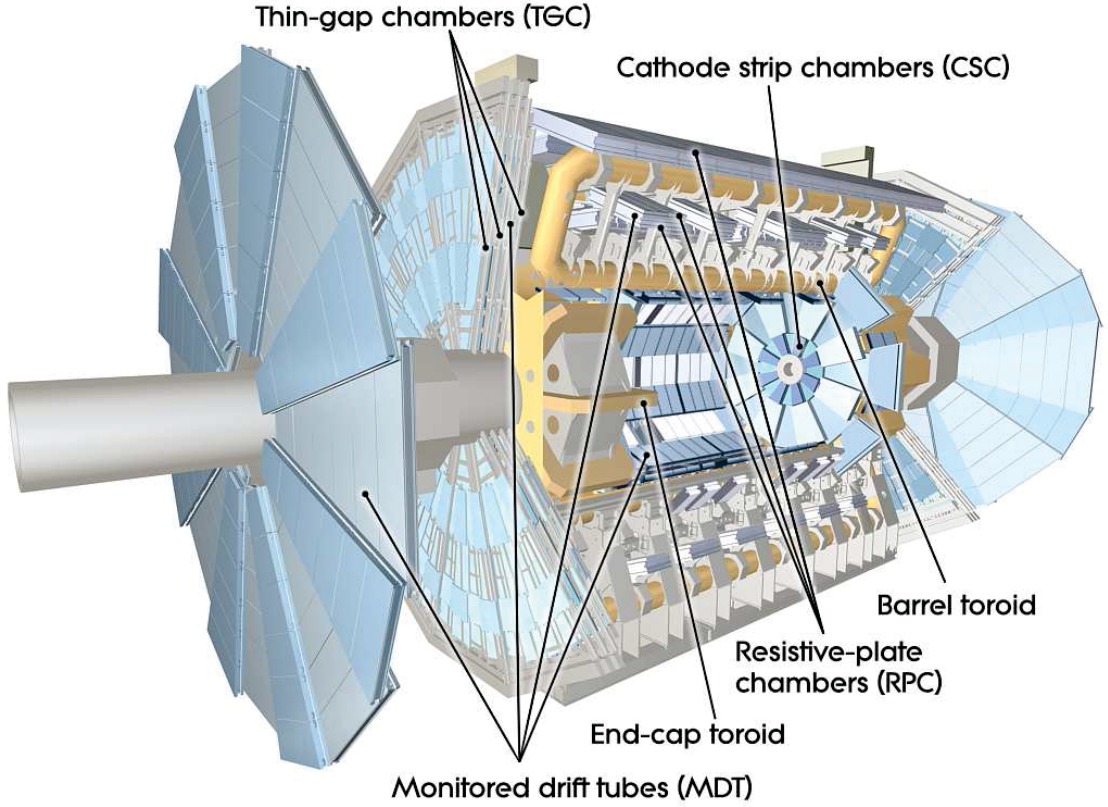
Figure 3.8.: Overview of the Muon Spectrometer [56].

3.2.6. Trigger and data acquisition

The LHC provides an approximate interaction rate of $1\,\mathrm{GHz}$ at the design luminosity of $\mathcal{L} = 10^{34}\,\mathrm{cm^{-2}s^{-1}}$ [56]. This is higher than the maximum rate of $100\,\mathrm{Hz}$ for writing out to the permanent storage elements. The ATLAS trigger system provides the facility with high detection efficiency of several physical objects to reduce the rate and thus with an enrichment of physical interesting events (see Figure 3.9).

This trigger system organizes the event selection in three levels, where the rate is reduced by few orders of magnitude at each level providing more time for a more precise decision at the next level. The decision at the first level (Level-1) is hardware based and reduces the rate to $75\,\mathrm{kHz}$ in less than $2.5\,\mathrm{\mu s}$. The next two levels (Level-2 and Event Filter) are combined to the High-Level-Trigger (HLT) system. Level-2 cuts down the rate to $1\,\mathrm{kHz}$ and takes $40\,\mathrm{ms}$ for each decision. At the last step the events pass the system with a maximum rate of $100\,\mathrm{Hz}$. There the decision can take up to seconds.
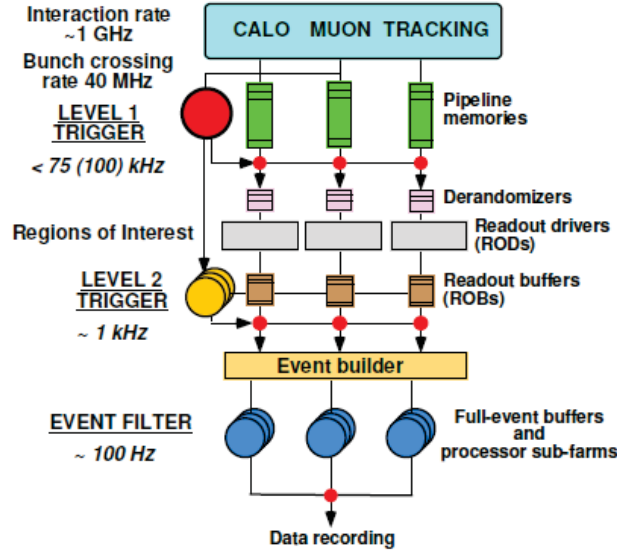
Figure 3.9.: Overview of ATLAS trigger and data acquisition system. [62].

Level-1 Trigger

For a fast decision the muon trigger chambers RPC and CSC are used for the selection of muons. The electron, photon and jet selection is based only on the calorimeter information with a reduced granularity to save time for the decision. The information from the ID are not used due to the high number of read out channels. Applying the information leads to an increase of the time for the decision.

During the processing of the Level-1 decision the information from all sub detectors is retained in pipeline memories. Also the data of the corresponding bunch crossing is stored in these memories, because the calorimeter signal extends over several bunch crossings and the time-of-flight of the particles can be larger than the time between two bunch crossings. Events with a very high cross section like minimum bias events can be suppressed with an additional prescale factor. With the prescale factor x, the trigger selects only every x-th event which passes the trigger requirement.

The Level-1 calorimeter decision is based on towers with a size of 0.1×0.1 in $\eta \times \phi$ in the central region and larger in the forward region. This result is sent to the central trigger (CTP) within $1.5\,\mu s$ after the event occurs (see Figure 3.10). The next step is the digitalization of the signal which is done in the pre-preprocessor. Another task of this component is to identify the bunch crossing. For the identification of the transverse energy values of each object a look-up table is used. Afterwards the information passes

the cluster processor (CP) for the identification of electrons, photons and τ-leptons candidates. At the same time the *Jet/Energy-sum* processor reconstructs the jets and calculate the globals sum of (missing) transverse energy from 0.2×0.2 trigger elements in $\eta \times \phi$.
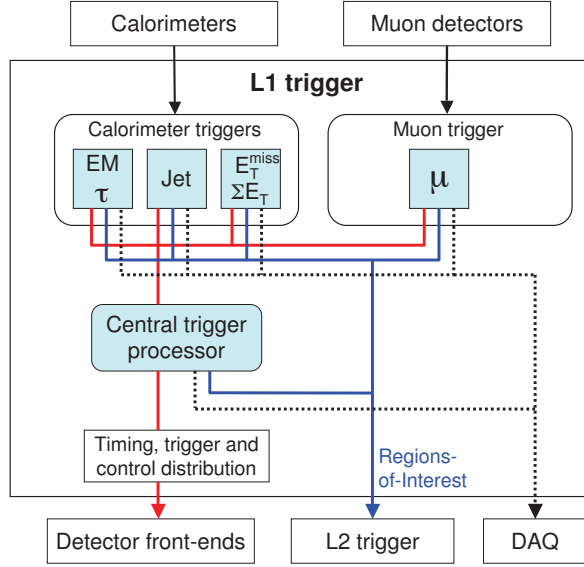
Figure 3.10.: Block diagram of the Level-1 trigger. The overall Level-1 decision is made by the central trigger processor taking input from calorimeter and muon trigger results. The paths to the detector front-ends, Level-2 trigger, and data acquisition system are shown from left to right in red, blue and black, respectively. [56].

Electrons and photons are identified using a 2×2 cluster of trigger towers if at least one of the four possible sums of towers 1×2 or 2×1 exceeds a given threshold (see Figure 3.11). The isolation energy is calculated with the twelve towers around the core and with the sum of the additional 2×2 hadronic tower to suppress the jet background. The algorithm searches over all windows until a candidate is found. The coordinates of the corresponding tower are the location of the region of interest (ROI).

The Level-1 trigger decision by itself is made by the central trigger processor (CTP) with the information from the calorimeter and the muon system. The decision is based on the multiplicity of the trigger object and the corresponding energy threshold. After a positive decision the information about the location and threshold are sent as the ROI to the Level-2 system. At the same time the data from the front-end is transfered over 1574 readout links (ROLs) into 1574 readout buffers (ROBs) contained in the readout

system units (ROSs), where they are temporarily stored for later usage.
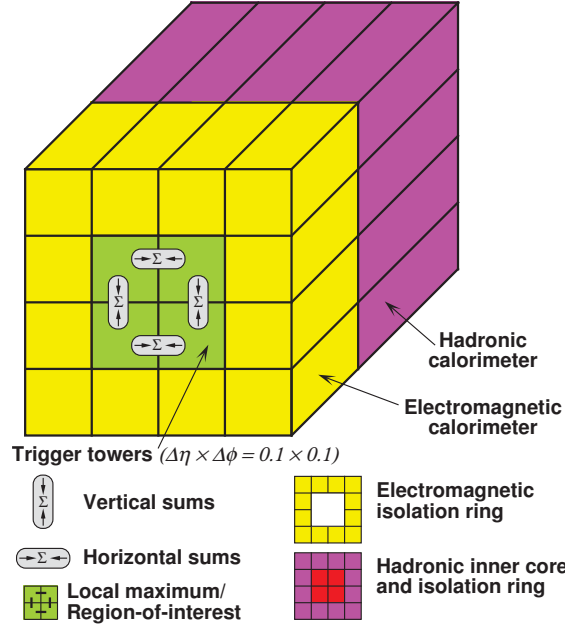
Figure 3.11.: Sketch of the electron and photon Level-1 trigger algorithm. [56].

The High-Level Trigger

The high level trigger system is divided into Level-2 and EF. After the Level-2 has received the data about the region of interest the ROI builder assembles the information to an integrated data together with the corresponding ID information. The ROI builder is a sub system of the Level-2 trigger system and collects the information from eight dedicated ROLs. In the next step the Level-2 supervisor assigns the data to one of the Level-2 processing units. After a positive decision the data is forwarded to the data flow manager (DFM), which manages the event building. The outcome is a single event data structure, which is given to the Event Filter (EF).

The EF uses the complete detector information from all subsystems. Events, which passed the selection criteria, are sent to the output notes (SFO) of the data acquisition system. All rejected events are removed from the system. Also the EF is a processing farm like the Level-2 with a selection algorithm based on standard event reconstruction.

4. Monte Carlo simulation and ATLAS data

Monte Carlo generators play a major role in particle physics analyses as they are needed for many purposes to perform the analysis. In this chapter, I introduce the different steps necessary to produce Monte Carlo samples suitable for analysis of ATLAS data (generation, detector simulation, digitization and reconstruction). Furthermore, I describe the different generators which were used in this analysis. At the end, I give a description of the ATLAS data taken in 2011, which this analysis is based on.

4.1. Monte Carlo simulation

Monte Carlo samples provide the possibility to study and to optimize the particle identification and the event selection efficiencies. Furthermore, the topology of signal and background events can be studied. This is important if both have a similar topology. For these studies a detailed detector simulation is needed, which describes the particle interactions with the detector very well.

The production and the decay of the fourth generation quarks are generated with Pythia6 [63]. For the background production AlpGen [64] at matrix element level and Herwig [65] for the shower calculation are mainly use. The decay of the τ and the photon radiation is simulated with Tauola [66] and Photos [67], respectively.

4.1.1. Generation of simulated events

The generation of Monte Carlo events is split into perturbatively calculable and non-perturbative parts to allow an exact as computationally possible description of the different physical processes. The steps are:

- **Hard scattering:** This is the primary parton-parton or "hard" interaction, which produces the desired particles like fourth generation quarks described by the matrix element. Figure 4.1 describe schematically the interaction of two partons (a and b) with the momentum $p_1 = x_1 \cdot P_1$ and $p_2 = x_2 \cdot P_2$ coming from the protons with the momentum P_1 and P_2. This is described by a calculation on matrix element

level and the cross-section of the hard scattering is given by [68]:

$$\sigma(P_1, P_2) = \sum_{i,j} \int dx_1 dx_2 f_i(x_1, \mu^2) f_j(x_2, \mu^2) \hat{\sigma}_{i,j}(p_1, p_2, \alpha_s(\mu^2), q^2/\mu^2) \, . \quad (4.1)$$

The scale of the hard scattering is defined by q, which could be the mass of a boson or an heavy quark. The function $f_{i,j}(x_{1,2}, \mu^2)$ in equation (4.1) is the *Parton distribution function* (PDF), which is defined at a factorization scale μ and determine the probability density of finding a parton of type i with the momentum fraction x_i in the hadron at q^2. It cannot be calculated by perturbation theory and have to be determined from experimental results, which were collected at deep-inelastic scattering experiments at HERA and direct photon production measurements. Further sources for the determination are W, Z and jet production measurements at hadron colliders [69]. Different groups provide a set of PDFs, which differ by the used data set. The uncertainties of the PDFs are obtained with a linear propagation of the experimental uncertainties from the input data and the uncertainties are given by a set of one sigma orthogonal error eigenvectors. $\hat{\sigma}_{i,j}(p_1, p_2, \alpha_s(\mu^2), q^2/\mu^2)$ in equation (4.1) denotes the *short-distance* cross-section, also called partonic cross-section, for the scattering of the partons of types i and j. The partonic cross-section can be calculated with perturbative QCD and electroweak theories.
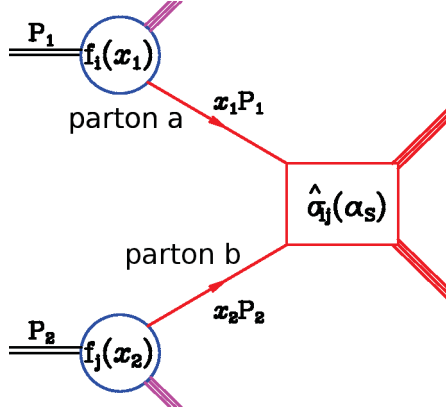
Figure 4.1.: Illustration of the hard scattering via the interaction of the partons a and b of a proton-proton collision. [68].

- **Initial and final state radiation:** Quarks and gluons can radiate additional gluons while photons can be emitted by electrons, muons, taus, quarks and charged

hadrons. The radiation of a gluon or a photon from partons before the hard scattering is called initial state radiation (ISR) (Figure 4.2(a)) and the radiation in the final state is called final state radiation (FSR) (Figure 4.2(b)). The model for the description of the radiation is different in the several Monte Carlo generators. For example, Pythia6 uses for the modeling of the initial (final) state radiation a space-like (time-like) shower algorithm. Herwig calculates the initial (final) state radiation with a backward (coherent) branching algorithm. For more information see [63] and [65].

(a) Initial state radiation [70].　　(b) Final state radiation [70].
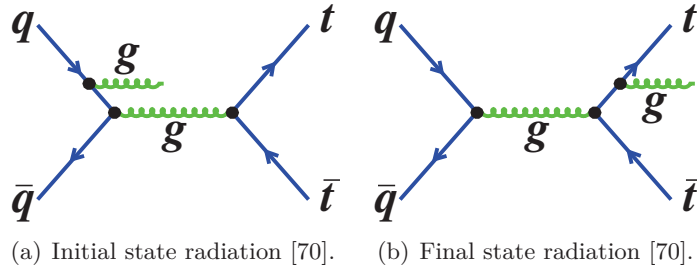
Figure 4.2.: Schematic illustration of initial state (4.2(a)) via a gluon radiation from incoming quark. The final state radiation (4.2(b)) is illustrated via a gluon radiation from the outgoing top quark.

- **Underlying event:** A proton contains valence quarks, sea quarks and gluons, commonly labeled as partons, hence hadron-hadron interactions are inherently many-body problems. "Everything" besides the hard interaction is usually called underlying event. The main contribution are interactions of those partons not involved in the hardest scatter (multiple parton interactions). Also the radiation of a quark, gluon or a photon from these particles contribute to the underlying event. These processes cannot be calculated perturbatively. Thus, phenomenological models are used in large parts, which need to be tuned to data.

- **Hadronization:** Quarks and gluons carry color charge. Due to the confinement only colorless hadron systems can exist isolated requiring a mechanism that combines colored objects into color-singlet hadrons. This can be only calculated by phenomenological models. One example is the *Lund string fragmentation model*, which is used in Pythia6. Herwig is based on a cluster hadronization model [65]. More information about these models in the chapters below.

Pythia6

As a leading order (LO) generator Pytia6[63] provides all relevant subprocesses of event generation which are described above. Besides the available Standard Model theory it can calculate processes of the fourth generation model. For the simulation of the fragmentation it uses the Lund string fragmentation model. In this model the partons are connected via massless and relativistic color strings. Each string has color charge at one end and its anti-color at the other. When the quark (q) and anti-quark ($\overline{q}$) move away from each other, the potential energy stored in the strings increases. If the invariant mass of these string pieces becomes large enough the string breaks resulting in the production of a new quark anti-quark ($q'\overline{q}'$) pair, so that the system splits into two color-singlet systems $q\overline{q}'$ and $q'\overline{q}$. The color strings directly or color-singlet system via these strongs can interact among each other and new color systems can be created, which is called color reconnection.

Every parton is characterized by a "virtuality scale" q^2, which is used for the ordering to the cascade radiations and decays. In the time-like model for the final state radiation the maximum for this virtuality q^2_{max} is set by the hard-scattering process. Thereafter the virtuality is decreased down to the cut-off scale q^2_0. In general, this cut-off scale is used to regulate divergences in the emission probabilities caused by adding higher leading order correction for gluon emission. The algorithm for the initial state radiation based on a "backwards evolution", in which the hard scattering is selected first and then the preceded parton shower is subsequently reconstructed. This reconstruction is started at the hard interaction scale, where q^2 has its maximum. Then the algorithm moves "backwards"in "time" towards smaller q^2 till the parton-shower initiator. There the cut-off scale q^2_0 is defined as well.

MadGraph/MadEvent

MadGraph/MadEvent [71] is typically used for multiple electroweak bosons with associated jets. It's a matrix element generator and applies Pythia6 for the parton shower calculation, both for ISR and FSR as well as hadronization. A matrix element generator simulate the process on parton-level.

AlpGen & Jimmy

AlpGen is a generator for standard model processes, which is used mainly for the production of electroweak bosons in associations with jets. It profits from the implementation of the MLM parton-showering and the matrix element matching technique [72]. For the

shower simulation itself Herwig is used. To get better description of the underlying event the generator Jimmy [73] has been added.

MC@NLO

With MC@NLO [74] Standard Model processes can be calculated on tree level with NLO QCD corrections. The output is compatible with generators like Herwig.

Herwig

Herwig [65] is a LO generator, but it calculates the physical steps using a different model to the Pythia6 generation concept. The cluster hadronization model is based on the pre-confinement property of the angular-ordered parton shower. All outgoing gluons are split non-perturbatively into light quark anti-quark pairs. With the pre-confinement these clusters have a distribution of mass and spatial size which peaks at low values and then falls rapidly for large cluster masses and sizes. This is asymptotically independent of the hard subprocess type and scale. Generally massive clusters decay into lighter clusters until they are too light to decay further. evolution" type as in Pythia6 but with a different setup.

4.1.2. Detector Simulation

For the detector simulation step Geant4 [75] is used. Geant4 simulates the passage of particles through matter and their interactions with the material. It also includes the decay of the newly produced particles caused by the interactions. Furthermore, it calculates the energy loss of particles due to their interactions and uses a geometrically detailed material map of the ATLAS detector as an input. The detector simulation takes into account the calculation of bremsstrahlung and photon conversion as well.

4.1.3. Digitization and Reconstruction

After the detector simulation the digitization step is applied. It formats the output of the detector simulation into a data format, which is identical to the data streaming from the detector. Further tasks are the simulation of the noise due to the deficient hardware of the detector and the pileup production. The protons are grouped in packets called bunches. During the collision of two bunches, more than one proton from each beam can collide. The pileup simulation of the *MC10b* Monte Carlo production is a mixture of *in-time* and *out-of-time* pileup. The effect of several proton-proton collisions

during one bunch crossing is called *in-time* pileup and takes into account effects like the increasing track multiplicity. With *out-of-time* pileup the effect of detector signals from earlier bunch collisions are simulated. This is done technically with an overlay of the physics signal, such as the production and decay of fourth generation quarks, and simulated low-energy proton-proton collisions called *minimun bias* events. Figure 4.3(a) shows the average number of interactions per bunch crossing in the Monte Carlo samples. The maximum is between six and eleven. The recorded luminosity as a function of the average number of bunch crossing in data is presented in Figure 4.3(b). Here, the maximum is at seven and is similar with the maximum in the Monte Carlo samples. In the pileup setup for *MC10b* 36 bunches are collected to a bunch train with a distance of 50 ns between the bunches, which follows a gap of 225 ns and then another bunch train with 36 bunches. This setup is similar to the beam configuration used at the LHC in the beginning of 2011.
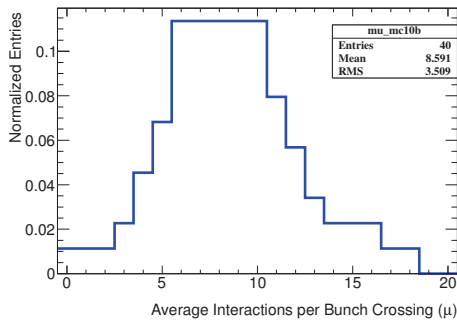
(a) The average number of interaction for one bunch crossing used for the Monte Carlo pileup production [76]. The distribution is normalized to one.
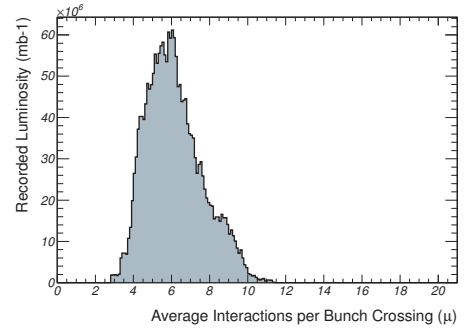
(b) The recorded luminosity for the average number of interactions per bunch crossing with data from the period B, D-K (for more information about the periods see chapter 4.2).

Figure 4.3.:

maximum of this distribution is between six and seven. The bunch spacing is 50 ns in the bunch train of 36 bunches which follows a gap of 225 ns and then another bunch train with 36 bunch crossings. This setup is similar to the beam configuration used at the LHC in the beginning of 2011.

In the last step of the Monte Carlo sample production the reconstruction algorithm identifies the physical objects which is also done with the data from the detector. The result is a data format with all relevant information of these objects. In chapter 5 the reconstruction algorithms are discussed in detail.

4.1.4. Signal and background Monte Carlo samples

In the following I introduce the signal and main background processes relevant for this analysis. Further, I discuss the possible processes responsible for faking the search signature of two same-sign leptons.

b' signal samples

The signal events are generated with Pythia6 and a b' pair production is applied. Furthermore, a $100\,\%$ branching ratio for the decay $b' \to t + W$ is required in order to get four W-bosons in the final state, where two of them have the same-sign:

$$pp \to b'\bar{b}' \to t\bar{t} + W^+ W^- \to b\bar{b} + 2W^+ 2W^-. \tag{4.2}$$

To get a higher numbers of events with a leptonic decay of the W boson a filter selecting generated events with the following parameters is used:

- At least one lepton $(e^{\pm}, \mu^{\pm})$ from a W-boson decay
- $p_T^{\mathrm{lepton}} > 10\,\mathrm{GeV}$
- $|\eta^{\mathrm{lepton}}| < 2.7$

This filter selects $70\,\%$ of the originally generated events. Monte Carlo samples with masses of the b' between $300\,\mathrm{GeV}$ and $600\,\mathrm{GeV}$ in steps of $50\,\mathrm{GeV}$ are available. The NNLO$^{\mathrm{approx}}$ cross-section [52], [53], which were calculated with HATHOR [51], are presented in Table 4.1 including the branching ratio and the generator filter efficiency ε. The values in Table 4.1 are used in the analysis.

Mass [GeV]	NNLO$^{\mathrm{approx}}$ cross-section $\times$ BR $\times$ ε [pb]
300	5.944
350	2.4318
400	1.0677
450	0.5132
500	0.26233
550	0.13569
600	0.039588

Table 4.1.: The NNLO$^{\mathrm{approx}}$ cross-section [51], [52], [53] for the signal process including the branching ratio of $100\,\%$ for the decay $b' \to t + W$ and the generator filter efficiency of $70\,\%$.

Background samples

The search signature of two same-sign leptons is a rare Standard Model signature. Nevertheless, background processes can still contribute to the signal region, which contains beside the two same-sign leptons additional leptons (e.g. $pp \to ZZ \to l^+l^-l^+l^-$). Then it is possible that not every lepton is reconstructed or pass the selection criteria for the analysis. A source for a faked search signature is the production of additional leptons by another lepton due to bremsstrahlung and events with this final state are called trilepton events. Figure 4.4 shows such a process, where a Z decays in an electron-positron pair (e_1^+ & e_4^-). Due to the interaction with the detector material e_4^- radiates a high energy photon, which decays then in a electron-positron pair (e_2^+ & e_3^-). This is also possible with processes like $pp \to W^\pm \to l^\pm + \nu_l$.

Another source of faked leptons are hadron decays into leptons inside a jet. For example, an event with a b-jet besides a leptonic W decay can produce a final state with same-sign dileptons.

Jets pass firstly the electromagnetic calorimeter before they interact with the material in the hadronic calorimeter. Thus, jets can produce a signature in the electromagnetic calorimeter similar to the electron, which can be misidentified as an electron by the corresponding algorithm.

Monte Carlo samples with directly produced pairs of light or b-quarks are not used in this analysis due to the small statistics after the event and object selection. This results in single entries in few bins in the final histograms, which does not allow a serious discussion of the results. The effects caused by these jets and bremsstrahlung are taken into account by using a data driven estimation, which is discussed in chapter 6.3.
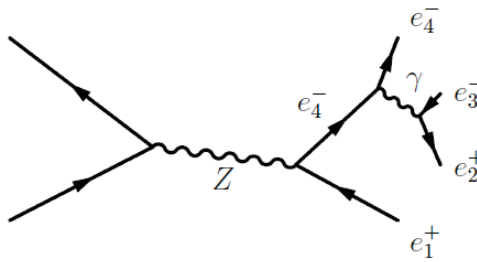
Figure 4.4.: Feynman graph showing the production of a Z-boson and the decay into two oppositely charged leptons (here electrons). One of the electrons radiates a photon, which converts into another lepton-antilepton pair as it interacts with the detector material. [20].

The following processes can fake the search signature of two same-sign leptons and can contribute to the signal region. All corresponding cross-sections are taking from *Top Monte Carlo working group* [76] and are used in the analysis. Mainly all used generator are leading order generators. The leading order cross-section is then multiplied with a *k*-factor, which to correct the leading-order cross-section for next to leader order (NLO) contributions

t$\bar{\text{t}}$+jets: For the production of the $t\bar{t} + jets$ sample AlpGen is used for the tree-level calculation and Herwig for the shower calculation. Monte Carlo samples are generated, in which both W bosons decay leptonically. Further samples, in which one decays leptonically and the other one decays hadronically, are also used. The additional partons are produced together with the top pair on tree level via processes like a gluon radiation. Table 4.2 shows the next to leading order cross-section for the samples with several numbers of additional partons.

Process	NLO Cross Section [pb]
$t\bar{t}$ $(WW \to l\nu l\nu)$ + Np0	5.788
$t\bar{t}$ $(WW \to l\nu l\nu)$ + Np1	5.676
$t\bar{t}$ $(WW \to l\nu l\nu)$ + Np2	3.547
$t\bar{t}$ $(WW \to l\nu l\nu)$ + Np3	2.251
$t\bar{t}$ $(WW \to l\nu qq)$ + Np0	24.087
$t\bar{t}$ $(WW \to l\nu qq)$ + Np1	23.814
$t\bar{t}$ $(WW \to l\nu qq)$ + Np2	14.731
$t\bar{t}$ $(WW \to l\nu qq)$ + Np3	9.387

Table 4.2.: The NLO cross-section of samples with a top pair with several additional numbers of partons.

Z+jets: In this process a Z-boson is generated directly, which then decays into e^+e^-, $\mu^+\mu^-$, $\tau^+\tau^-$ or $\nu\bar{\nu}$. All decay channels are produced without and with several additional partons streaming from gluon radiation from the initial parton. Another process is a gluon decaying into a quark anti-quark pair, where one quark contributes to the Z-boson production as shown in Figure 4.5. Then the additional parton can be reconstructed as a jet. Monte Carlo samples, in which an additional $b\bar{b}$ pair beside a light quark is produced, are also applied. The generator for this process is AlpGen together with Herwig. The NLO cross-sections are listed in Table 4.3 and 4.4.

W+jets: Similar to the $Z + jets$ the W-boson is produced directly due to quark an-
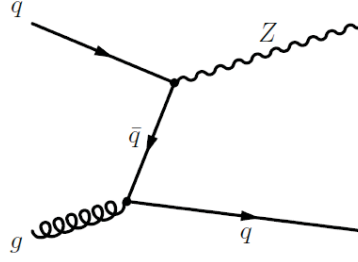
Figure 4.5.: Feynman graph showing the production of a Z-boson together with an additional parton. This occurs, if the initial gluon splits into a quark-antiquark pair before the scattering process [20].

nihilation and then decays only leptonically. Several additional partons are produced for this sample varying between one and five per event on tree level. AlpGen is applied for the tree level calculation and for the parton shower simulation Herwig is used. In Table 4.5 the NLO cross-sections for the $W^{\pm} \to l^{\pm}\nu_l + jets$ are listed. Also in this case produced Monte Carlo samples with an additional $b\bar{b}$ pair beside the light quark jets are implemented in the analysis and the corresponding cross-sections are presented in Table 4.6. In this case, the leptonic decay channels of the W boson are not divided.

Diboson+jets The diboson samples contain a pair production of W^+W^-, W^+Z or ZZ with and without additional partons. The decay of the bosons include all leptonic decay channels and the additional parton is streaming from processes like gluon radiation on tree level. These samples are produced with AlpGen and Herwig for the tree level and the parton shower calculation, respectively. Table 4.7 presents the NLO cross-section for the diboson+jets samples.

Single top: In single top events only one top is produced via the s- and t-channel and Wt associated production. Figure 4.6 shows the different possibilities for single top production in proton proton collisions. For the s- and t-channel there are separate samples for every leptonic decay channel of the W boson, while for the Wt-channel all leptonic decay channel are included. MC@NLO is used for the tree level calculation and Herwig for the parton shower simulation. Table 4.8 shows the NLO cross-section for every single top channel, which are calculated directly with MC@NLO.

Drell-Yan: Drell-Yan is a process, in which a virtual photon or Z-boson is produced

Process	NLO Cross Section [pb]
$Z \to e^+e^- + \text{Np0}$	830.125
$Z \to e^+e^- + \text{Np1}$	166.237
$Z \to e^+e^- + \text{Np2}$	50.282
$Z \to e^+e^- + \text{Np3}$	13.922
$Z \to e^+e^- + \text{Np4}$	3.616
$Z \to e^+e^- + \text{Np5}$	0.942
$Z \to \mu^+\mu^- + \text{Np0}$	830.125
$Z \to \mu^+\mu^- + \text{Np1}$	166.237
$Z \to \mu^+\mu^- + \text{Np2}$	50.282
$Z \to \mu^+\mu^- + \text{Np3}$	13.922
$Z \to \mu^+\mu^- + \text{Np4}$	3.616
$Z \to \mu^+\mu^- + \text{Np5}$	0.942
$Z \to \tau^+\tau^- + \text{Np0}$	830.125
$Z \to \tau^+\tau^- + \text{Np1}$	166.237
$Z \to \tau^+\tau^- + \text{Np2}$	50.282
$Z \to \tau^+\tau^- + \text{Np3}$	13.922
$Z \to \tau^+\tau^- + \text{Np4}$	3.616
$Z \to \tau^+\tau^- + \text{Np5}$	0.942
$Z \to \nu^+\nu^- + \text{Np0}$	3571.9
$Z \to \nu^+\nu^- + \text{Np1}$	737.84
$Z \to \nu^+\nu^- + \text{Np2}$	223.89
$Z \to \nu^+\nu^- + \text{Np3}$	61.825
$Z \to \nu^+\nu^- + \text{Np4}$	15.746
$Z \to \nu^+\nu^- + \text{Np5}$	4.1721

Table 4.3.: The NLO cross-section of $Z \to e^+e^-$, $\mu^+\mu^-$, $\tau^+\tau^-$ and $\nu^+\nu^-$ with several numbers of additional partons.

directly with Pythia6. For efficiency reasons the generator is required to simulate decays into a pair of electrons or muons only. An additional criterion for this process is the invariant mass between $15\,\text{GeV}$ and $60\,\text{GeV}$ well below the ATLAS invariant mass window of the Z boson. In this case no additional k-factor is used and Table 4.1.4 presents the LO cross cross-section calculated directly with Pythia6.

Process	NLO Cross Section [pb]
$Z \to e^+e^- + b\bar{b} + \text{Np0}$	6.52
$Z \to e^+e^- + b\bar{b} + \text{Np1}$	2.47
$Z \to e^+e^- + b\bar{b} + \text{Np2}$	0.808
$Z \to e^+e^- + b\bar{b} + \text{Np3}$	0.387
$Z \to \mu^+\mu^- + b\bar{b} + \text{Np0}$	6.52
$Z \to \mu^+\mu^- + b\bar{b} + \text{Np1}$	2.47
$Z \to \mu^+\mu^- + b\bar{b} + \text{Np2}$	0.808
$Z \to \mu^+\mu^- + b\bar{b} + \text{Np3}$	0.387
$Z \to \tau^+\tau^- + b\bar{b} + \text{Np0}$	6.52
$Z \to \tau^+\tau^- + b\bar{b} + \text{Np1}$	2.47
$Z \to \tau^+\tau^- + b\bar{b} + \text{Np2}$	0.808
$Z \to \tau^+\tau^- + b\bar{b} + \text{Np3}$	0.387
$Z \to \nu^+\nu^- + b\bar{b} + \text{Np0}$	32.823
$Z \to \nu^+\nu^- + b\bar{b} + \text{Np1}$	14.487
$Z \to \nu^+\nu^- + b\bar{b} + \text{Np2}$	5.2435
$Z \to \nu^+\nu^- + b\bar{b} + \text{Np3}$	1.5562

Table 4.4.: The NLO cross-section of $Z \to b\bar{b} + e^+e^-$, $\mu^+\mu^-$, $\tau^+\tau^-$ and $\nu^+\nu^-$ with several numbers of additional partons.

Process	NLO Cross Section [pb]
$W^\pm \to e^\pm\nu_e + \text{Np0}$	8296.0
$W^\pm \to e^\pm\nu_e + \text{Np1}$	1551.6
$W^\pm \to e^\pm\nu_e + \text{Np2}$	452.5
$W^\pm \to e^\pm\nu_e + \text{Np3}$	121.1
$W^\pm \to e^\pm\nu_e + \text{Np4}$	30.4
$W^\pm \to e^\pm\nu_e + \text{Np5}$	8.3
$W^\pm \to \mu^\pm\nu_\mu + \text{Np0}$	8284.2
$W^\pm \to \mu^\pm\nu_\mu + \text{Np1}$	1561.6
$W^\pm \to \mu^\pm\nu_\mu + \text{Np2}$	453.25
$W^\pm \to \mu^\pm\nu_\mu + \text{Np3}$	121.66
$W^\pm \to \mu^\pm\nu_\mu + \text{Np4}$	31.01
$W^\pm \to \mu^\pm\nu_\mu + \text{Np5}$	8.32
$W^\pm \to \tau^\pm\nu_\tau + \text{Np0}$	8284.2
$W^\pm \to \tau^\pm\nu_\tau + \text{Np1}$	1561.6
$W^\pm \to \tau^\pm\nu_\tau + \text{Np2}$	453.25
$W^\pm \to \tau^\pm\nu_\tau + \text{Np3}$	121.66
$W^\pm \to \tau^\pm\nu_\tau + \text{Np4}$	31.01
$W^\pm \to \tau^\pm\nu_\tau + \text{Np5}$	8.32

Table 4.5.: The NLO cross-section of $W^\pm \to e^\pm\nu_e$, $\mu^\pm\nu_\mu$ and $\tau^\pm\nu_\tau$ with several numbers of additional partons.

Process	NLO Cross Section [pb]
$W^{\pm} \to l^{\pm}\nu_l + b\bar{b} + \text{Np0}$	3.2
$W^{\pm} \to l^{\pm}\nu_l + b\bar{b} + \text{Np1}$	2.6
$W^{\pm} \to l^{\pm}\nu_l + b\bar{b} + \text{Np2}$	1.4
$W^{\pm} \to l^{\pm}\nu_l + b\bar{b} + \text{Np3}$	0.6

Table 4.6.: The NLO cross-section of $W^{\pm} \to +b\bar{b} + l^{\pm}\nu_l$ with several numbers of additional partons. The decay of the W boson implicates all decays into leptons.

Process	NLO Cross Section [pb]
$W^+W^- \to l^+\nu_l l^- \bar{\nu}_l + \text{Np0}$	2.6397
$W^+W^- \to l^+\nu_l l^- \bar{\nu}_l + \text{Np1}$	1.2552
$W^+W^- \to l^+\nu_l l^- \bar{\nu}_l + \text{Np2}$	0.5729
$W^+W^- \to l^+\nu_l l^- \bar{\nu}_l + \text{Np3}$	0.2215
$W^{\pm}Z \to l^{\pm}\nu_l l^+l^- + \text{Np0}$	0.8599
$W^{\pm}Z \to l^{\pm}\nu_l l^+l^- + \text{Np1}$	0.5297
$W^{\pm}Z \to l^{\pm}\nu_l l^+l^- + \text{Np2}$	0.2879
$W^{\pm}Z \to l^{\pm}\nu_l l^+l^- + \text{Np3}$	0.1216
$ZZ \to l^+l^-l^+l^- + \text{Np0}$	0.6612
$ZZ \to l^+l^-l^+l^- + \text{Np1}$	0.3045
$ZZ \to l^+l^-l^+l^- + \text{Np2}$	0.1152
$ZZ \to l^+l^-l^+l^- + \text{Np3}$	0.0408

Table 4.7.: The NLO cross-section for $W^+W^- \to l^+\nu_l l^- \bar{\nu}_l$, $W^{\pm}Z \to l^{\pm}\nu_l l^+l^-$ and $ZZ \to l^+l^-l^+l^-$ with and without several numbers of additional partons.

Process	NLO Cross Section [pb]
$W\pm \to e^{\pm}\nu_e$ (t-channel)	7.152
$W\pm \to \mu^{\pm}\nu_{\mu}$ (t-channel)	7.176
$W\pm \to \tau^{\pm}\nu_{\tau}$ (t-channel)	7.128
$W\pm \to e^{\pm}\nu_e$ (s-channel)	0.4685
$W\pm \to \mu^{\pm}\nu_{\mu}$ (s-channel)	0.4684
$W\pm \to \tau^{\pm}\nu_{\tau}$ (s-channel)	0.4700
$W\pm \to l^{\pm}\nu_l$ (Wt channel)	14.581

Table 4.8.: The NLO cross-section of all single top channels calculated directly with MC@NLO.

Process	LO Cross Section [pb]
$Z/\gamma \to e^+e^-$	1253.0
$Z/\gamma \to \mu^+\mu^-$	1252.9

Table 4.9.: LO cross-section of DrellYan samples with the decay into e^+e^- and $\mu^+\mu^-$.

(a) s-channel

(b) Wt associated production

(c) t-channel

(d) Wt associated production
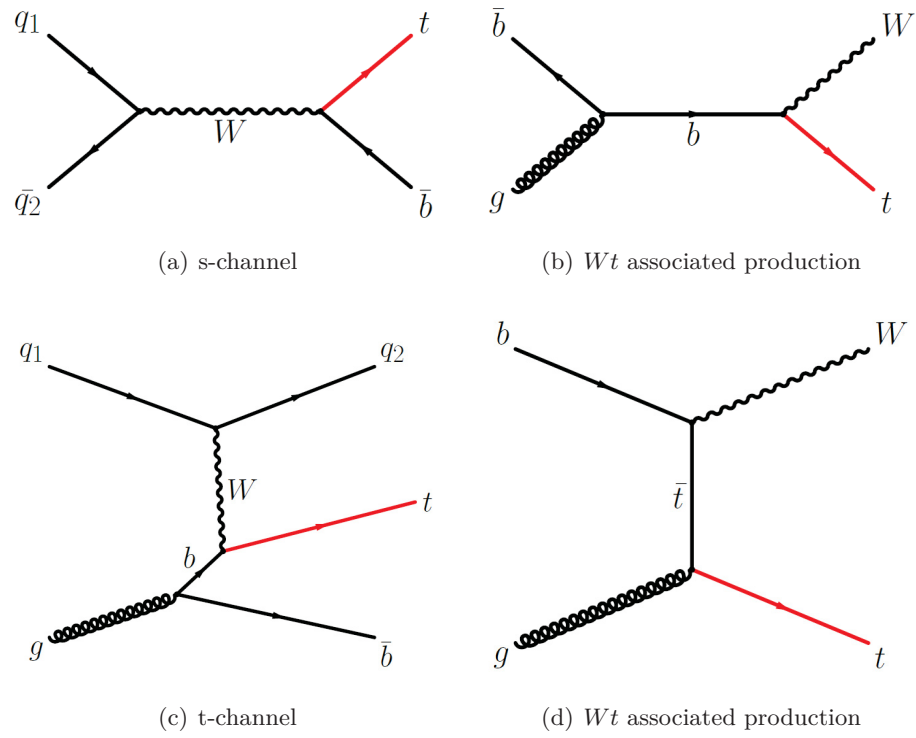
Figure 4.6.: Single top production processes in the s-channel (a), t-channel (c) and in Wt associated production ((b) and (d)) [20].

4.2. Data

For this analysis ATLAS data are used, which was taken in 2011 from April until August, and was stored in streams: egamma and muon stream. If an event passed the requirement of an electron or photon trigger it was saved in the egamma stream. For the muon stream the events had to pass the criteria of the muon trigger. Then, the reconstruction algorithms were running for the identification of physical objects like electrons, muons and jets.

During the data taking the configuration of the LHC beams was updated to allow for increased luminosity, which caused an upgrade of the detector configuration as well. Due to this, the data was divided into periods and one period presents recorded data with a consistent detector configuration. The periods B and D - K are used for this analysis.

Not every event is usable for the analysis. For example, non collision background can produce a signal in the detector, which can be identified as an event [77]. Non collision background events are inelastic or elastic interactions of protons with the residual gas inside the beam pipe producing particles like pions or muons, which travel in the beam halo and can deposit their energy in the calorimeter. Simulation studies have shown that inelastic interaction from a distance greater than $550\,\mathrm{m}$ from the interaction point can still produce a significant contribution in the detector. It is also possible that a fraction of protons of a bunch can leak into the neighboring bucket and can leads to collisions called satellite collisions. These backgrounds depend on the operational conditions of the LHC like machine optics, collimator settings, gas density and the filling scheme. Cosmic muons are counted as beam background too. These particles can cause a trigger to fire via a large energy loss in the calorimeter. The overlap with a standard collision event could leads to a false trigger decision.

For the analysis in this thesis electrons, muons and jets are essential and require a high data quality and well understood detector calibration. Therefore, only data events are used, which were taken, when the detector operated under nominal conditions. For example, the read-out error for all channels for the whole inner detector has to be lower than $2\,\%$ and for the calorimeter system less than $1\,\%$. Additionally, a stable beam needs to be declared by the LHC. The selection of the events is done via applying a *good run list* [78], where all usable events are registered.

The absolute luminosity is calculated via equation (3.1) in chapter 3.1. The size of the bunches σ_x and σ_x can be determined with *van der Meer* scans [79], [80] or called beam-separation or luminosity scans. The observed event rate is measured while scanning the two beams across each other. This is done first in the horizontal (x) and then in the

vertical direction (y). With the *van der Meer* method in Atlas the absolute luminosity is calibrated. The measurement of the luminosity during the data taking is mainly done with LUCID, a gas-filled (C_4F_{10}) Cherenkov detector, which covers the η range $5.6 < |\eta| < 6.0$. LUCID is installed surrounding the beam pipe at each side $17\,\text{m}$ away from the interaction point.

Together with the *good run list* the luminosity is calculated to be $2.05\,\text{fb}^{-1}$ with an uncertainty of $\pm 3.7\,\%$. The main part of this uncertainty is coming from the *van der Meer* scans with $\pm 3.4\,\%$ [81].

5. Reconstruction of physical objects in ATLAS

In chapter 2.2.3, I introduced the search strategy, which is based on two same-sign leptons, a high jet multiplicity and missing transverse energy. The reconstruction algorithms for electrons, muons and jets are described in the following chapter. Here, I concentrate on the identification of the objects, which are used in the analysis and are recommended by the corresponding physics performance groups. The calculation of the missing transverse energy is discussed in chapter 6.1.4 due to the dependence of the final selection criteria of the electrons, muons and jets, which are described in chapter 6.1.

5.1. Electrons

In ATLAS, special electron[1] reconstruction algorithms are based on the detector regions and on the available data of the calorimeter and the inner detector. For the region $|\eta| < 2.5$, in which the information from the electromagnetic calorimeter and the inner detector are available, there are two different types of algorithms: the standard, also called *HighPt*, algorithm and the soft electron algorithm. Outside this region, namely $2.5 < |\eta| < 4.9$, only the information from the calorimeter can be used for the reconstruction. Due to the similar shower shape of electrons and photons in the calorimeter it is impossible to distinguish between these objects.

The HighPt algorithm selects isolated objects with a high transverse momentum and is recommended for this search strategy. In the first step it identifies a cluster candidate with the sliding window algorithm. In the second step a corresponding track is reconstructed. Generally, every electron candidate without an associated track is tagged as a photon. The *sliding window* algorithm works in three steps: the tower building, the pre-cluster (seed) finding, and the cluster filling. First, the electromagnetic calorimeter is divided into a grid in the η - ϕ plane of $N_\eta \times N_\phi = 200 \times 256$ elements with the size of $\Delta\eta = \Delta\phi = 0.025$. Then the pre-cluster algorithm looks for a window of five towers in

---

[1]This also takes into account positrons.

η and ϕ, in which the sum of the deposited transverse energy of every tower is greater than $3\,\text{GeV}$. After that the pre-cluster algorithm computes the position of the window. If another window is identified, which is closer than $\Delta R = \sqrt{(\Delta\eta)^2 + (\Delta\phi)^2} < 0.3$, the window with the higher transverse energy is chosen. With the cluster filling step the final electromagnetic cluster is built by using all cells inside and outside the above defined window. After the identification of a cluster candidate a corresponding track is selected by the calculation of the distance between the position of the cluster in the second layer of the electromagnetic calorimeter and the position of the track. If the distance is smaller than 0.05 in η and 0.1 in ϕ the track is chosen. Finally, the electron four-momentum is computed with the deposited energy in the cluster and with the η and ϕ value of the track.

The soft electron or track-based algorithm chooses a track candidate and selects a corresponding cluster in the second step. This provides the possibility to identify electrons close to or inside a jet with a low transverse momentum. If an electron is tagged by the *HighPt* and the soft algorithm the reconstructed information from the *HighPt* algorithm is stored.

Beside the reconstruction step every electron has to pass several quality criteria and is flagged as *loose*, *medium* or *tight*. This *IsEM* flag is based on the information from the hadronic and the electromagnetic calorimeter and from the inner detector and uses the following variables:

- *The lateral shower shape R_η:* The lateral shower shape is given by the ratio of the energy in the cluster with the size of 3×7 cells and the energy in a 7×7 window in $\eta \times \phi$. Both energies are reconstructed in the second layer of the electromagnetic calorimeter. Electrons deposit their energy mainly in a 3×7 window due to their small lateral leakage, while jets and other hadrons produce a larger tail. The variable peaks ideally at $R_\eta \approx 1$ for electrons as shown in Figure 5.1.

- *The lateral width ω:* This width in η is calculated with the deposit energy from the cells (E_{cell}) in the second layer of the electromagnetic calorimeter in a window of 3×7 cells in $\eta \times \phi$.

$$\omega = \sqrt{\frac{\sum_{cell} E_{cell} \times \eta_{cell}^2}{\sum_{cell} E_{cell}} - \left(\frac{\sum_{cell} E_{cell} \times \eta_{cell}}{\sum_{cell} E_{cell}}\right)^2} \,, \qquad (5.1)$$

  where η_{cell} is the η position of the cell. Generally, hadrons produce a broader shape than electrons.
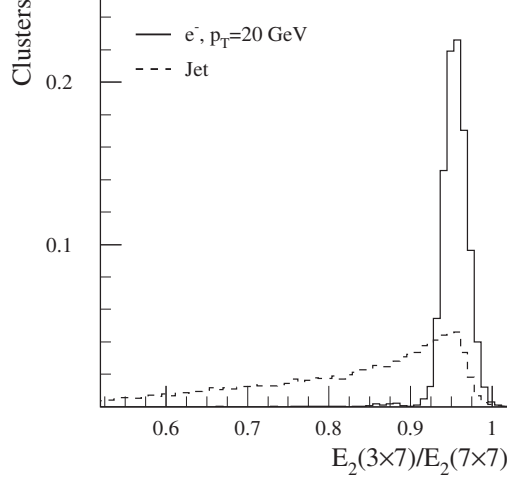
Figure 5.1.: The lateral shower shapes in the second layer of the electromagnetic calorimeter for electrons and jets are shown. Both distributions are normalized to unit area [82].

- $\Delta E = E^{2nd} - E^{min}$: This energy difference is calculated with the value of the second maximum E^{2nd} and the energy reconstructed in the strip with the minimal value E^{min} between the first and the second maximum. Decays like $\pi^0 \rightarrow \gamma\gamma$ lead to two maxima in the shower. Figure 5.2 shows the ΔE distribution for electrons and jets with a transverse momentum of $p_T = 20\,\mathrm{GeV}$. Both distributions are normalized to unit area. The electron distribution ends at a value of $\Delta E \approx 0.15$, while the jet distributions has also entries at higher values. A high jet supression can be realized with a cut at $\Delta E \approx 0.1$.

- *The total shower width $\omega_{tot/3strips}$:* This variable uses the information of the first layer of the electromagnetic calorimeter. The parameter i stands for the number of strips and i_{max} is the number of strips until the first local maximum:

$$\omega_{tot} = \sqrt{\frac{\sum E_i \times (i - i_{max})^2}{\sum E_i}} \quad (5.2)$$

In case of $\omega_{3strips}$ the same formula is used but only 3 strips around the local maximum are used instead of 40 as for ω_{tot}.

- $R_{max_2} = E_{max_2}/(1+9(5)\times10^{-3}E_T)$: E_T is the transverse energy from the cluster in the whole electromagnetic calorimeter and E_{max_2} stands for the second maximum. The constant 5 (9) is for a low (high) luminosity.

65
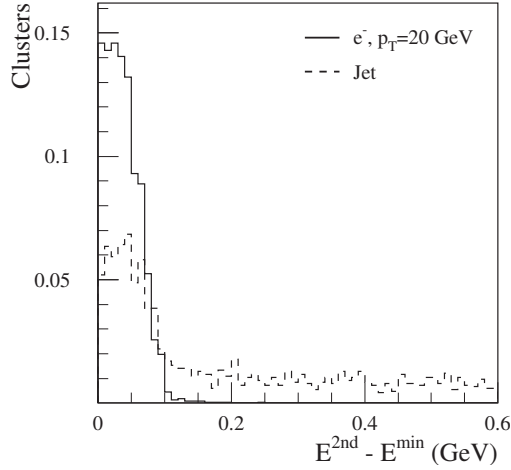
Figure 5.2.: The distribution of difference between the energy of the second maximum E^{2nd} and the minimum (E^{min}) value of electrons and jets is shown in the layer of the electromagnetic calorimeter. Both distributions are normalized to the unit area [82].

- F_{side}: This fraction describes the relation of the energy inside a core ($E(\pm 3)$) and around the core ($E(\pm 1)$). The core has a size of 3 strips and the energy around the core is taken from one strip. The shower core is defined by the strip with the highest deposited energy.

$$F_{side} = \frac{E(\pm 3) - E(\pm 1)}{E(\pm 1)} \tag{5.3}$$

- *The hadronic leakage*: This is defined as the ratio of the energy deposit in the first sampling of the hadronic calorimeter and the reconstructed transverse energy of the cluster in the electromagnetic calorimeter. For electrons the ratio is small while for hadrons it peaks around one. Electrons deposit a small amount of their energy ($\approx 2\,\%$) in the hadronic calorimeter.

- *Track quality cuts:*
  - At least nine precision hits altogether in the pixel and semiconductor tracker are required
  - At least two hits in all pixel layers with one in the b-layer.
  - A transverse impact parameter $|d_0| < 0.1\,\mathrm{cm}$ is needed (For determination see chapter 3.2.3).

The different quality categories are defined as follows:

Loose: In this category only limited information from the calorimeters are used like the hadronic leakage and the shower-shape variables which are derived from the middle layer of the electromagnetic calorimeter (lateral shower shape and lateral shower width). These cuts provide an excellent identification efficiency but a low rejection of fake electrons.

Medium: In the medium category the quality is improved by adding selection criteria with the information of the strips in the first layer of the electromagnetic calorimeter and on the track variables. For example, the rejection of processes like $\pi \rightarrow \gamma\gamma$ can be suppressed, because the pion decay produces two maxima in the shower, while an electron causes one maximum. Further calorimeter criteria are R_{max_2}, w_{tot}, $w_{3strips}$ and F_{side} due to the broader shower width of the pions than for the electrons. The tracking criteria include the number of hits in the pixel detector, the number of silicon hits and the transverse impact parameter. In this category the jet rejection increases by a factor of 3-4 with respect to the loose cuts, while the identification efficiency is reduced by $\sim 10\%$.

Tight: The criteria of this category are based on the medium selections with more additional cuts on the track and the isolation in the calorimeter. Finally, all quality criteria have to be passed. Here, the track needs to have a hit in the b-layer for the rejection of electrons coming from photon conversion processes. Figure 5.3(a) shows the radiation length of the material in the ID as a function of η and Figure 5.3(b) displays the probability of a photon conversion depending on the distance from the vertex for several η values. The overall conversion probability is around 50% and makes the cut for the suppression of these photons an important requirement. To reject the background from charged hadrons, further criteria for the tracks are the ratio of high-threshold hits and the number of hits in the TRT. The distance between the cluster and the track in η and ϕ has to be smaller than for the basic candidate selection. For a better agreement between the track and the cluster a cut on E/p is required.
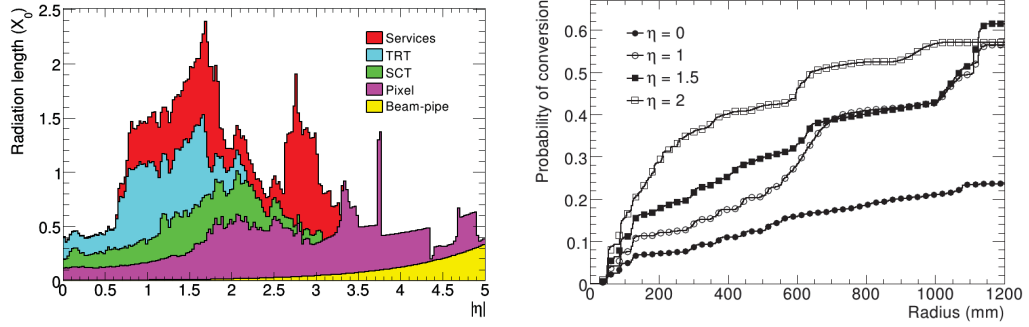
(a) Amount of material in the inner detector (b) Probability of a photon to have converted as given in radiation length as a function of $|\eta|$ [83]. a function of the radius for different values of pseudorapidity [83].

Figure 5.3.:

5.2. Muons

In ATLAS there are three collections of muon reconstruction algorithms: *MuIdCollection* and *StacoCollection* and for the identification in the Calorimeter: *Calorimeter Muon Collection*. The algorithms in the *MuIdCollection* and *StacoCollection* are working similarly to reconstruct the different components of the muon track in the inner detector and in the muon spectrometer. The *MuIdCollection* is the mainly used one and is applied for this analysis. It contains the following algorithms:

Moore and Muid Standalone: The Moore algorithm identifies the track in the muon spectrometer. Then the Muid Standalone algorithm uses this information for the extrapolation to the vertex and the determination of the track parameters at the vertex.

MuTagIMO: This algorithm identifies muons with the reconstructed track in the inner detector together with a segment in the muon spectrometer. A segment is a short track, which is identified only in one of the subcomponents of the muon spectrometer.

MuGirl: It performs the search for a track in the muon spectrometer and uses an inner detector track as an input. If the full track is refitted successfully this muon is flagged as a Combined Muon (CB) called Muid combined, otherwise the muon is defined as a Tagged Muon.

The muons in the *MuIdCollection* can be divided into four quality levels: Tight, Medium, Loose and Very Loose. The definition of these levels is inclusive. For example, all tight muons are included in the medium quality selection. The four categories are determined as follows:

Tight All Muid combined and MuGirl muons which have a successfully combined fit and at least two monitored drift tubes and cathode strip chambers hits or less than six holes on the track. Outside the influence of the inner detector ($|\eta| > 2.5$) Standalone muons need at least three monitored drift tubes and cathode strip chambers hits.

Medium: All standalone muons.

Loose: All muons, which are found by the tagging algorithms and have an inner detector track with silicon hits.

Very Loose: MuTagIMO muons, which only have tracks in the TRT.

After running all algorithms, an overlap removal between standalone and combined muons is made. Standalone muons are removed if they are also identified as combined muons.

The muon candidates with the highest purity are provided by the combined muon algorithm. Figure 5.4 shows a detailed schematic drawing of the different muon spectrometer components and Figure 5.5 presents the corresponding reconstruction efficiency. In Figure 5.6 and 5.7 the reconstruction efficiencies are presented as a function of the muon transverse momentum and η, respectively. The overall efficiency is around 95% with the 2010 data at $\sqrt{s} = 7\,\mathrm{TeV}$ and for Monte Carlo as well. All efficiencies are obtained with the tag and probe method with $Z \to \mu^+\mu^-$ events. For more information about this method see [84]. The efficiencies depend on the reconstructed muon spectrometer track, which varies with η. In the two following regions the efficiency is very low:

- At $\eta \sim 0$ the detector is only partially equipped with muon chambers to provide space for services of the ID and the calorimeters.

- In the transition region between the barrel and the end caps at $|\eta| \sim 1.2$ only one chamber is traversed by muons due to staged end-cap chambers. Therefor, no stand-alone momentum measurements are available and the combined muon efficiency decreases in this region.

The scale factors, which are presented in Figure 5.6 and 5.7, are calculated with the ratio of the reconstruction efficiency of the muons in data and Monte Carlo. They are used in the analysis for the correction of the discrepancy of the reconstruction efficiency between data and Monte Carlo (for more information see chapter 6.1.2).
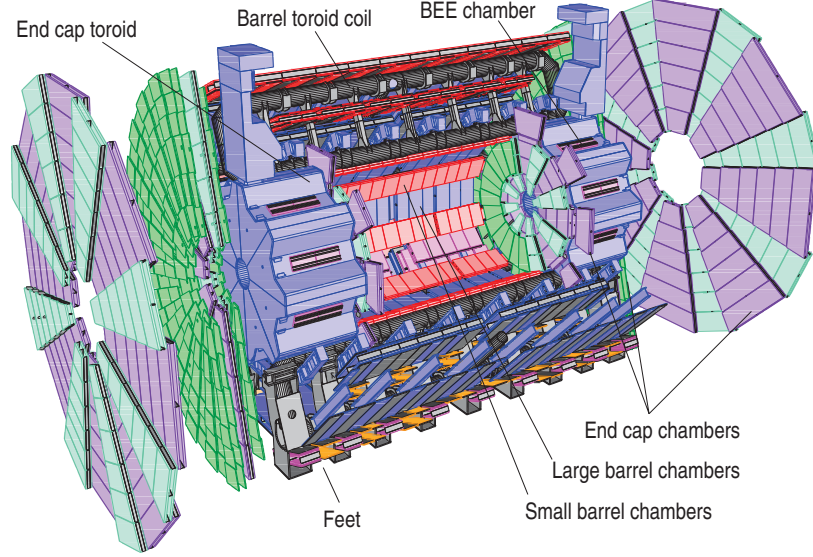
Figure 5.4.: Schematic drawing of the ATLAS muon spectrometer [84].
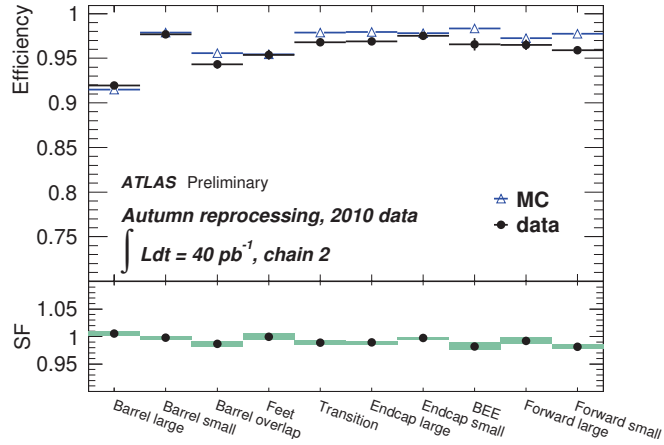
Figure 5.5.: Reconstruction efficiencies and scale factors for CB muons for the different detector regions. The efficiencies are obtained from data (dots) without background correction and Monte Carlo simulation (open triangles) including backgrounds. The corresponding scale factors are shown in the lower part. [84].
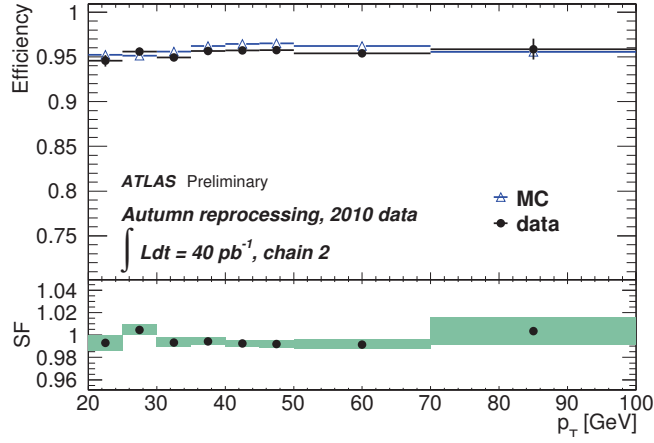
Figure 5.6.: Reconstruction efficiencies and scale factors for CB muons as a function of the muon p_T. The efficiencies are obtained from data (dots) without background correction and Monte Carlo simulation (open triangles) including backgrounds. The corresponding scale factors are shown in the lower part [84].
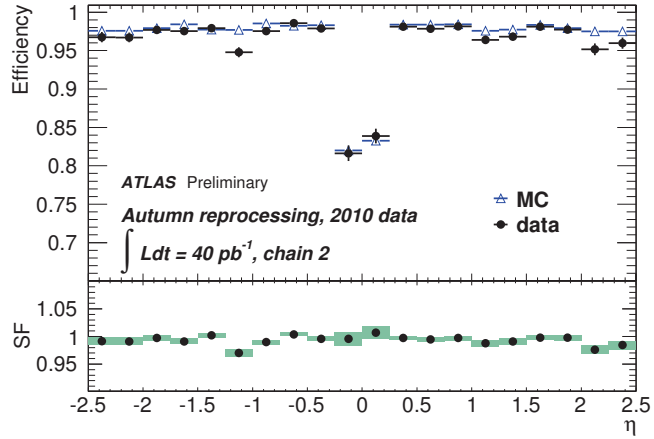
Figure 5.7.: Reconstruction efficiencies and scale factors for CB muons as a function of muon η. The efficiencies are obtained from data (dots) without background correction and Monte Carlo simulation (open triangles) including backgrounds. The corresponding scale factors are shown in the lower part [84].

5.3. Jets

The LHC is a hadron collider and due to that it produces many quarks and gluons which can be reconstructed as jets. Jets are widespread objects and the jet multiplicity and the properties depend on the algorithm which is used for the identification. The two main favored categories are the *Cone-* [85] and the *Cluster*-algorithm [86], [87], [88]. The Cone algorithm reconstructs a jet via the collection of the energy deposited in every cell in a cone around a cluster. The cluster algorithm has been used at lepton colliders and electron-proton colliders like HERA and is recommended for the physics analysis by the *Jet/EtMiss performance group* [76]. It is based upon pair-wise clustering of the initial constituents. In the first step the algorithm defines a distance, which is measured between several objects. The distance d_{ij} between two objects and the distance d_{iB} between an object and the beam are defined as follows:

$$d_{ij} = min(k_{Ti}^{2p}, k_{Tj}^{2p}) \frac{(\Delta R)_{ij}^2}{R^2} \tag{5.4}$$

$$d_{iB} = k_{Ti}^{2p} \ , \tag{5.5}$$

where

$$(\Delta R)_{ij}^2 = (\eta_i - \eta_j)^2 + (\phi_i - \phi_j)^2 \tag{5.6}$$

and η_i is the pseudorapidity of the object i. k_T is the transverse moment of the object i. After the calculation of all possible d values the objects i and j are combined and removed from the list if the smallest entry is d_{ij}. If the smallest entry is d_{iB} this object is defined as a complete jet and will be removed from the list. The parameter R defines the resolution at which jets are distinguished from each other. If the values for R are large the distance d_{ij} will be smaller and thus more objects will be combined into a jet. For small values of R less objects will be merged to a jet. Depending on the value of p, which can be 0, -1 or $+1$, three different sub cluster algorithms have been defined: k_T [86], Cambridge/Aachen [87] and Anti-k_T [88].

The k_T algorithm uses $p = +1$ in equation (5.5). Hence, objects with a relative low k_T are merged first. Therefore, objects with the highest k_T are combined at the end and due to this it is easier to study the substructure of jets. The value $p = 0$ is used in the Cambridge/Aachen algorithm, for which the k_T value is irrelevant, and objects near to each other in ΔR are formed first. Moreover, the final merge is the one with the largest distance and thus provides the possibility to study the substructure of jets.

For the cluster the Anti-k_T algorithm $p = -1$ is used in equation (5.5). This entails $\Delta R < R$ and all softer objects are merged with a harder object, which is the closest in ΔR. Thus, soft radiation cannot affect the jet boundary. If $\Delta R < R$ is for two objects a single jet is formed together with their soft objects in the vicinity. But if the distance of those objects are within $R < \Delta R < 2R$ the energy is shared among them. For this algorithm the ordering of the clustering is not relevant. The Anti-k_T is the recommended algorithm for the jet reconstruction [76].

In ATLAS this jet algorithm uses clusters, which are identified in the electromagnetic and in the hadronic calorimeter system with the TopoCluster algorithm [76]. In general, cells are ordered by the significance of their deposited energy. Cells are tagged as *seeds*, *neighbors* or *others* depending on their significance above the noise level. Cells with a deposited energy value higher than 4σ above the noise level are flagged as *seed*. All directly neighboring cells with 2σ over the noise level are tagged as *neighbor* and with 0σ over the noise level as *other*. More detailed information about the Topological Clustering are explained in [76].

For the jet finding algorithm also the four momentum vector of the cluster is necessary. The cluster is defined as massless and the energy of the jet is the sum of the deposited energy in every cluster i:

$$E_{jet} = \sum_i E_i. \tag{5.7}$$

The position in η and ϕ is measured for every cluster in the calorimeter. The η and ϕ value of the jet, weighted by the energy of the jet, is defined as follows:

$$\eta_{jet} = \frac{1}{E_{jet}} \sum_i E_i \eta_i \tag{5.8}$$

$$\phi_{jet} = \frac{1}{E_{jet}} \sum_i E_i \phi_i . \tag{5.9}$$

Various sources, ranging from hardware problems, LHC beam conditions, cosmic ray showers to noise bursts [76], can fake a jet. Thus, jets have to pass a set of quality criteria in order to suppress the fakes, which are the following: bad, ugly and good [76].

In general physical objects like electrons or photons are also reconstructed as a jet, which implies the need of an overlap removal between the object and the jets in the analysis. More information about this in chapter 6.1.1.

6. Object and event selection

In chapter 5, the reconstruction algorithm for electrons, muons and jets are described. Based on this the object selection and the calculation of the missing transverse energy are introduced in this section together with the event selection criteria for an efficient background suppression. The definition of the electrons, muons, jets and missing transverse energy depend on the *Top Common Objects* [76], which are optimized for the top analyses by the *ATLAS Top Group*. The reason for applying these criteria is the similar event topology between the decays of fourth generation quarks and the top quarks. This is also done for the event selection criteria. The final agreement in the distributions between the Monte Carlo samples and the data are presented in this chapter as well. At the end of this chapter a method and the results for a further event selection optimization for this signal channel is discussed.

6.1. Object selection

6.1.1. Electrons

Reconstructed object

The electron in this analysis has to be reconstructed by the HighPt algorithm and pass the tight quality selection criteria. Using the tight quality criteria results in a low fake rate of the electrons. Every electron is selected with a transverse energy of $E_T \geq 25\,\mathrm{GeV}$, because with this energy the trigger efficiency reach its highest efficiency (Figure 6.2(a)). The energy is calculated as follows:

$$E_T = E^{\mathrm{cluster}}/cosh(\eta_{\mathrm{track}}) \tag{6.1}$$

where E^{cluster} is the calorimeter cluster energy and η_{track} is the direction of the electron track. This is done for the case $N_{\mathrm{SCT}} + N_{\mathrm{Pix}} \geq 4$. In the case of $N_{\mathrm{SCT}} + N_{\mathrm{Pix}} < 4$ the transverse energy is then used directly from the cluster (E_T^{cluster}), which is recommended by the *ATLAS egamma performance group* [76]. For the calculation of the transverse energy of the cluster the measured deposited energy, η, ϕ are used and for

the mass of the cluster the value $m_{\text{cluster}} = 0\,\text{GeV}$ is applied. The electrons, which are reconstructed in the pseudorapidity range $1.37 < |\eta^{\text{cluster}}| < 1.52$, are not used in the analysis. There, the resolution of the detector is worse than in the other regions of the electromagnetic calorimeter due to the gap between the barrel and endcaps of the electromagnetic calorimeter.

In chapter 2.2.3 the search strategy of two same-sign leptons is discussed, for which a leptonic decay into electrons and muons of the W boson is assumed. To select only prompt electrons from the W boson decay these electrons have to pass the following isolation criteria: The sum of the deposited energy in every calorimeter cell in a cone of $\Delta R < 0.2$ around the cluster has to be lower than $E_T^{cone20} < 3.5\,\text{GeV}$. Due to the pileup this energy needs to be corrected depending on the transverse momentum and the position of the corresponding electron and the number of vertices in the event. The factors for the correction are measured with $Z \to e^+e^-$ data events with a systematic uncertainty of $2\,\%$, which covers a possible unmeasured data and Monte Carlo discrepancy introduced by the used cuts [89].

The energy scale of the electron cluster is corrected in data as a function of the cluster position $\eta_{cluster}$ via $E_{new} = \frac{E}{1+\alpha}$ [76]. Figure 6.1 shows the α values depending on the pseudorapidity. In the η range $|\eta| < 1$ the scale factors are smaller than zero and lead to a higher corrected energy, while for $1 < |\eta| < 2.5$ and excluding the region $1.37 < |\eta^{\text{cluster}}| < 1.52$ the factor are positive. The systematic uncertainties are within $1 - 1.5\,\%$ dominated by the detector material and the presampler energy scale. For the electrons in the Monte Carlo samples a randomised Gaussian resolution function is applied for the energy correction together with the statistical and systematic uncertainties [76].

During the data taking read-out modules of the electromagnetic calorimeter were broken and due to this it is impossible to measure the electron energy in this region of the calorimeter. If an electron is reconstructed very close to this region it is possible that a wrong energy is measured. Thus, it cannot be considered in the analysis [76].

Trigger object

At least one electron in every event of the egamma stream passing the reconstruction selection criteria has to match with an electron trigger object. A match is successfully if the distance is $\Delta R < 0.15$ between the trigger and the reconstructed object. For the periods B - I the chain *e20_medium* is used and for the period K *e22_medium* is applied. Both trigger chains are unprescaled and use the same quality selection criteria excluding the E_T requirement, which is increased for *e22_medium*. The reason for changing the
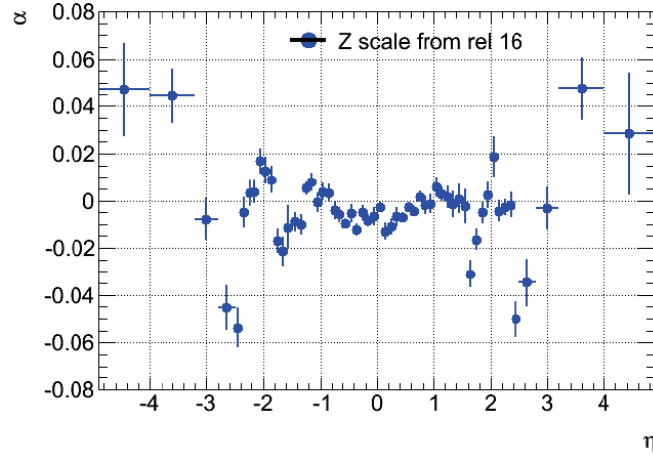
Figure 6.1.: Energy scale correction factors versus the pseudorapidity determined in $Z \rightarrow e^+e^-$ events [76].

threshold is a higher event rate provided by an improved proton beam setup. For the Monte Carlo events the chain *e20_medium* is used.

The variables, which are used for the trigger decision, are the same as for the *IsEM* selection (chapter 5.1).

The criteria on Level-1 of the electron trigger is a simple requirement on the transverse energy (E_T) of the cluster in the calorimeter which is in detail for each of the two chains:

- e20_medium: $E_T > 14\,\text{GeV}$

- e22_medium: $E_T > 18\,\text{GeV}$

The more complex decision on Level-2 is based on the hadronic leakage, the lateral shower shape R_η and $E_T > 19\,\text{GeV}$ for the cluster in the calorimeter.

On Event Filter level the hadronic leakage is also used for the trigger decision together with the total shower width (ω_{tot}) and E_{ratio}. The track of the electron trigger object has to pass the following criteria:

- Number of pixel hits $N_{Pixel} \geq 1$.

- Number of hits in the pixel and SCT $N \geq 7$.

- Transverse impact parameter $d_0 < 5\,\text{mm}$.

and a track matching with $\Delta\eta < 0.01$ between the cluster and the track is made. On this trigger level the requirement for the cluster is $E_T > 20\,\text{GeV}$ [90].

6. Object and event selection

Figure 6.2 shows the efficiencies for *e20_medium* at each trigger level (Level-1, Level-2 and Event Filter), which are measured with $Z \to e^+ e^-$ events using the tag and probe method [91]. These efficiencies are determined as a function of the reconstructed electron transverse energy for the candidates satisfying the tight identification requirements with $|\eta_{cluster}| < 2.47$. The invariant mass of both electrons with the opposite-sign is in the range of $80\,\mathrm{GeV} < M_{e^+e^-} < 100\,\mathrm{GeV}$. The luminosity for this measurement is $\mathcal{L} = 206\,\mathrm{pb}^{-1}$. The efficiencies rise up fast and are close to one for all three levels with $E_T \gtrsim 25\,\mathrm{GEV}$ as expected.

(a)   (b)
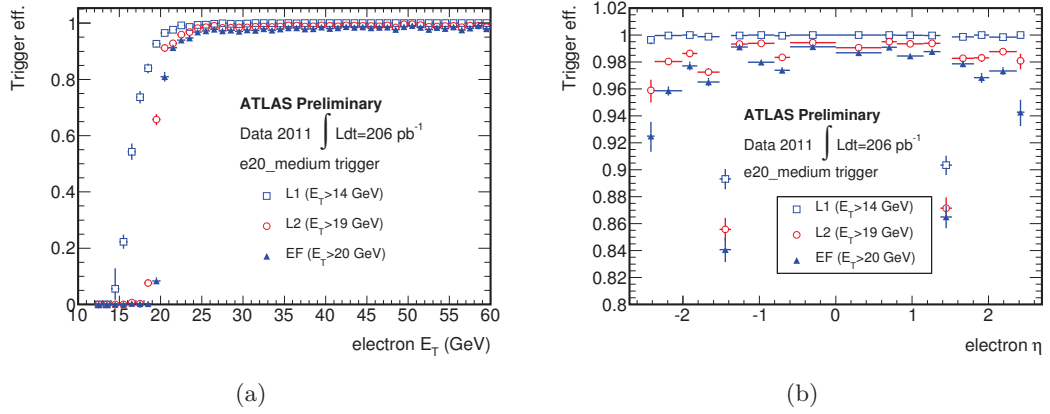
Figure 6.2.: Trigger efficiencies for *e20_medium* at each trigger level (Level-1, Level-2 and Event Filter) measured with $Z \to e^+ e^-$ events using the tag-and-probe method [91].

6.1.2. Muons

Reconstructed object

All muons, which are reconstructed with the combined muon algorithm, are used with the following additional requirements: $p_T > 20\,\mathrm{GeV}$ and $|\eta| < 2.5$. These muons also have to pass the quality criteria for the tight category.

Further the selection criteria for the quality of the inner detector track, which are recommended by the muon performance group [76], are applied as follows [76]:

- At least one hit in the b-layer

- Number of pixel hits + number of crossed dead pixel sensors > 1

- Number of SCT hits + number of crossed dead SCT sensors >= 6

- Number of pixel holes + number of SCT holes < 3

- TRT (define n = number of TRTHits + number of TRTOutliers):
  - for $|\eta| < 1.9$: require $n > 5$ and $n_{\text{TRTOutliers}}/n < 0.9$
  - for $|\eta| >= 1.9$: if n>5 then require $n_{\text{TRToutliers}}/n < 0.9$ (this means for $n <= 5$ and $|\eta| >= 1.9$: no additional cut)

These cuts take into account the current detector conditions like dead modules and reject muons coming from hadron decays.

The muons for the analysis should be isolated to use only prompt muons from W boson decays. The sum of the p_T of all tracks in a cone of $\Delta R = 0.3$ around the track of the muon has to be lower than $4\,\text{GeV}$. All tracks for this isolation criteria are reconstructed in the inner detector. For the isolation requirement in the calorimeter the deposited transverse energy E_T^{cone20} in all clusters in a cone of $\Delta R < 0.3$ around the muon cluster is used and has to fulfill $E_T^{cone20} < 4\,\text{GeV}$. The clusters are build in the the electromagnetic and hadronic calorimeter.

The third requirement is the overlap removal with jets. All muons are removed if the distance ΔR to the next jet with $p_T > 20\,\text{GeV}$ is smaller than $\Delta R < 0.4$. To reduce the muon charge misreconstruction the track in the inner detector has to have the same charge as the track in the muon spectrometer. Fake muons can be produced also by cosmic ray events. These muons can be suppressed by a cut on the extrapolated transverse impact parameter ($|d_0| < 0.5\,\text{mm}$), because then the tracks of the cosmic muons are more away from the interaction point. Additionally, a cut on the distance in ϕ is required, $\Delta\phi < 3.1$, because comic muons have a back-to-back track in both hemisphere of the detector and the distance between both track in ϕ is $\Delta\phi \approx 3.14$. The track of a cosmic muon, which goes through the whole detector, can be reconstructed as two tracks. Then, a cosmic muon is identified as two muons. The momentum vectors of these two tracks point to opposite directions. The vector between the primary vertex and the PCA ($\overrightarrow{x}_{PrimVertex} - \overrightarrow{x}_{PCA}$ in Equation 3.6) is the same for both tracks. Due to this, the scalar product in Equation 3.6 is $sign\ d_0 > 0$ for one track and $sign\ d_0 < 0$ for the other. In the case of two prompt muons, $sign\ d_0$ will be positive or negative for both tracks as long as the vector between the primary vertex and the PCA is not the same for both tracks. The vectors are not the same when the distance in ϕ for both tracks is $\Delta\phi \lesssim 3$, which is mostly the case. However, requiring $sign\ d_0 > 0$ or $sign\ d_0 < 0$ for both tracks in order to suppress cosmic muons has a low influence on the cosmic rejection. Hence, the criteria for both muon tracks $\Delta\phi < 3.1$ is applied as before.

The differences in the muon momentum resolution between data and Monte Carlo were corrected by applying a Gaussian function on the transverse momentum of the muons in the Monte Carlo. For the correction of the reconstruction discrepancy between Monte Carlo and data scale factors as function of the transverse momentum and the pseudorapidity are applied (Figure 5.6 - 5.7 in chapter 5.2). These scale factors were determined with a tag and probe method on $Z \rightarrow \mu^+\mu^-$ events on data and were compared with Monte Carlo events [76]. The trigger efficiency of the muon trigger chain is corrected as well and the scale were measured with the same method.

Trigger object

In the case of the *muon stream* at least one reconstructed muon has to match to a trigger object with the requirement $\Delta R < 0.15$, which passed the trigger item *EF_mu18* (for period B-I) or *EF_mu18_medium* (for period J-K). Both trigger items are recommended and the update to the second one is needed due to a higher instant luminosity in the periods J-K than in the periods B-I [76]. In the case of Monte Carlo events the chain *EF_mu18* is used.

On Level 1 the requirement is based only on the transverse momentum of the muon in the muon spectrometer. The corresponding item on Level-1 for *EF_mu18* is *L1_MU10*, for which a $p_T > 10$ GeV is required. *L1_MU11* is the item on Level-1 for *EF_mu18_medium* and $p_T > 11$ GeV is applied. Further, with *L1_MU10* a hit in two inner RPC layers are required, while for *L1_MU11* a hit in three RPC layers is needed.

On Level-2 and Event Filter the selection are the same. Beside a requirement on the transverse momentum a fit between the track in the inner detector and the muon spectrometer is made.

6.1.3. Jets

The recommended jets for this analysis are *AntiKt4TopoEMJets*. These jets are reconstructed with the Anti-kt algorithm with $R = 0.4$ and use topological clusters in the calorimeter system as an input. The calibration is based on the electromagnetic scale with a jet energy scale factor depending on the transverse momentum and the pseudorapidity. These jets were calibrated with a Monte Carlo sample which was produced with an pileup event average $< \mu >= 8$ and a bunch spacing of 75 ns. Further, a transverse momentum of 20 GeV for every jet is required. As mentioned in chapter 5.3 an overlap removal between electrons and jets needs to be applied. Every jet is removed from the analysis if there is an electron closer than $\Delta R < 0.2$, because for this distance the

whole cluster of the electron is inside the reconstruction area of the jet. For the overlap removal all electrons are used, which pass the selection criteria in chapter 6.1.1. Due to the overlap removal only jets with $|\eta| < 2.5$ are selected. The jet energy resolution is determined with the data from 2010 and then extrapolated to the data of 2011 [92]. It shows a agreement between Monte Carlo and data within 2%. The disagreement is corrected via a smearing of the jet energy [76]. Another source of the jet energy scale uncertainty is the pile up which is 5% for jets with $p_T > 30\,\text{GeV}$ [76].

6.1.4. Missing transverse energy

The missing transverse energy is calculated with the vectorial negative sum of all deposited energy in the calorimeter and reconstructed energy of the muons in the muon spectrometer [93], [94]:

$$\not{E}_x = -\sum_i E_i \sin\theta_i \cos\phi_i \ , \tag{6.2}$$

$$\not{E}_y = -\sum_i E_i \sin\theta_i \sin\phi_i \ , \tag{6.3}$$

$$\not{E}_T = \sqrt{\not{E}_x{}^2 + \not{E}_y{}^2} \ . \tag{6.4}$$

With the missing transverse energy it is possible to determine the transverse energy of the neutrinos, which do not interact with the detector.

In ATLAS the deposited energy in the calorimeter is associated with reconstructed physical objects like electrons ($e^\pm$), muons ($\mu^\pm$), photons (γ), taus ($tau^\pm$) and jets. $\not{E}_{x(y)}$ is defined as follows [93], [94]:

$$\not{E}_{x(y)} = \not{E}_{x(y)}{}^e + \not{E}_{x(y)}{}^\mu + \not{E}_{x(y)}{}^\gamma \ \not{E}_{x(y)}{}^\tau \ \not{E}_{x(y)}{}^{jets} + \not{E}_{x(y)}{}^{softjets} + \not{E}_{x(y)}{}^{CellOut} \ , \tag{6.5}$$

where $\not{E}_{x(y)}{}^{jets}$ contains reconstructed jets with $p_T > 20\,\text{GeV}$ and $\not{E}_{x(y)}{}^{softjets}$ summarize all jets with $7\,\text{GeV} < p_T < 20\,\text{GeV}$. The reason for the distinction is the different calibration. The energy of reconstructed muons in the muon spectrometer and in the calorimeter are combined in the term $\not{E}_{x(y)}{}^\mu$. $\not{E}_{x(y)}{}^{CellOut}$ contains the deposited energy in the calorimeter, which cannot be associated to a reconstructed physical object. For the term $\not{E}_{x(y)}{}^e$ electrons with $p_T > 10\,\text{GeV}$ are used, which pass the tight quality selection criteria.

In general, the missing transverse energy follows an approximately stochastic be-

haviour and the resolution can be defined as follows [93], [94]:

$$\sigma[GeV] = k \cdot \sqrt{\sum_i E_T^i} \ , \tag{6.6}$$

where $\sum_i E_T^i$ is the sum of the reconstructed transverse energy in the muon spectrometer and the deposited transverse energy in the calorimeter. The parameter k depends on the physical channel in the event and is $k = 0.42 \, \mathrm{GeV}^{1/2}$ for $Z \to l^+l^-$ events and $k = 0.51 \, \mathrm{GeV}^{1/2}$ for di-jets events.

6.2. Event selection

6.2.1. Top Event Selection

This analysis is running on the egamma and on the muon stream separately and at least one trigger object has to pass the corresponding trigger item.

In addition, a vertex with at least five tracks is required in order to suppress non collisions background [95]. A vertex is reconstructed in two steps: With the first step the associated tracks of a vertex candidate are identified. In the second step the position of the vertex is determined by a fit. The requirements for the tracks are the following:

- $p_T > 400 \, \mathrm{MeV}$.

- $|d_0| < 4 \, \mathrm{mm}$

- At least four hits in the SCT detector.

- At least six hits in the pixel and SCT detectors.

The primary vertex is then defined as the vertex with the highest sum of the transverse momentum of all track [96].

Then at least two jets with $p_T > 20 \, \mathrm{GeV}$ and at least one electron with $E_T > 25 \, \mathrm{GeV}$ or at least one muon with $p_T > 20 \, \mathrm{GeV}$ are required. The cut on the transverse momentum for the electron is higher as for muons due to a non negligible fake rate for electrons in the p_T range below $25 \, \mathrm{GeV}$.

The missing transverse energy in every event has to be higher than $\not{E}_T > 40 \, \mathrm{GeV}$. Jets near the dead modules of the electromagnetic calorimeter can effect the calculation of the missing transverse energy caused by a mis-reconstructed jet energy. Thus, on data every event is removed if at least one jet is inside the area $-0.1 < \eta < 1.5$ and $-0.9 < \phi < -0.5$. Furthermore, events are rejected if there is at least one jet passing

the bad quality criteria. The calculation of $\not{E}_T$ can be affected by a *LAr noise burst* as well. In this case every event with a *LAr noise burst*, which is caused by calorimeter defects, is not used.

Besides the basic top event selection requirements a cut on H_T, which is the scalar sum of the transverse energy momenta of all leptons and jets in every event, of $H_T > 350\,\text{GeV}$ is applied. The value for this cut is optimized for two same-sign lepton events to reach the maximum sensitivity for a b' mass of $m(b') = 400\,\text{GeV}$ [97].

In events with two electrons or muons with any sign combination a cut on the invariant mass of $M_{l^\pm l^\pm, l^\pm l^\mp} > 15\,\text{GeV}$ is applied due to a cut on generator level for the Drell Yan Monte Carlo sample. A further criterion for these events is the "Z-veto". Here, the invariant mass of two electrons or muons has to be outside the Z mass window: $m_{l^\pm l^\pm, l^\pm l^\mp} < 86\,\text{GeV}$ or $m_{l^\pm l^\pm, l^\pm l^\mp} > 96\,\text{GeV}$.

Table 6.1 presents separately the event selection efficiency for above mentioned event selection for the b' signal sample with $m(b') = 400\,\text{GeV}$ and all background categories described in chapter 4.1.4. The cut called "Trigger" includes the efficiency of the generator filter and the efficiency of the trigger item *EF_e20medium*, which presents the real trigger efficiency for Monte Carlo samples. The efficiencies, where the muon trigger *EF_mu18* is required, are presented in table A.1 in the Appendix A. The cut efficiency for the b' and for every single background sample (separate for every number of additional partons and every decay into lepton) is calculated as follows:

$$\epsilon_i = \frac{n_i}{n_{i-1}}, \tag{6.7}$$

where n_i present the number of events passing the criteria i and all previous ones and n_{i-1} stands for the number of events fulfilling the applied cuts before. The corresponding errors for the cut efficiencies are determined with the following equations [19]:

$$\epsilon_{lo} = \frac{n_i F_F^{-1}[\alpha_{lo}; 2n_i, 2(n_{i-1}-n_i+1)]}{n_{i-1}-n_i+1+n_i F_F^{-1}[\alpha_{lo}; 2n_i, 2(n_{i-1}-n_i+1)]} \tag{6.8}$$

$$\epsilon_{up} = \frac{(n_i+1) F_F^{-1}[1-\alpha_{up}; 2(n_i+1), 2(n_{i-1}-n_i)]}{(n_{i-1}-n_i)+(n_i+1) F_F^{-1}[1-\alpha_{up}; 2(n_i+1), 2(n_{i-1}-n_i)]} , \tag{6.9}$$

where ϵ_{lo} and ϵ_{up} are the upper and lower limit for the efficiency at confidence level $1 - \alpha_{lo}$ and $1 - \alpha_{up}$, respectively. These equation are based on the frequentist approach for binomial distributed data and results in asymmetric errors for efficiencies close to zero or one. The situation for very low efficiency is realistic for tights cuts. In equation (6.9), F_F^{-1} is the quantile of the Fisher-Snedecor distribution and $\alpha_{lo} = \alpha_{up} = 0.16$ is used for a $68\,\%$ confidence level. For more details see [19]. In Table 6.1 the several

6. Object and event selection

Monte Carlo background samples are summarize in categories. For example, the category
"W+jets" contains the processes: $W \to e\nu_e$, $\mu\nu_\mu$ and $\tau\nu_\tau$ and each with different numbers
of additional partons. The efficiency is then calculated via the sum of the weighted
efficiency $w_i \cdot \epsilon_i$ of every subsample:

$$\epsilon = \sum_i w_i \cdot \epsilon_i \tag{6.10}$$

$$w_i = \frac{n_i}{\sum_j n_j} \ , \tag{6.11}$$

where $n_{i/j}$ stands for the number of events passing the cuts of the subsample i/j. With
the following equation:

$$\sigma^\pm = \sqrt{\sum_i w_i^2 \left(\sigma_i^\pm\right)^2} \ , \tag{6.12}$$

the upper (σ^+) and lower (σ^-) limit for the combined efficiency is computed with the
corresponding upper (σ_i^+) and lower (σ_i^-) limit of the subsample i.

The requirement of a single electron trigger chain has for some samples like the signal
sample a large effect as shown in Table 6.1. For example, for the signal sample the
efficiency is $\epsilon \approx 0.39$, while for the $Z + b\bar{b} + jets$ sample the efficiency is $\epsilon \approx 0.74$.
In the following, the requirement of at least one lepton (e or μ) almost all events are
selected, which is the same for the criteria $P_T^{LeadLep}$ and $P_T^{2ndLeadLep}$. When applying the
cut on the missing transverse energy background samples without $\not{E}_T$ in the final state
($Z + jets$, $Z + b\bar{b} + jets$ and Drell-Yan) are suppressed very well. As already described,
the criteria on $H_T > 350\,\mathrm{GeV}$ is optimized for the signal sample and shows in this case in
Table 6.1 for this signal sample the highest efficiency. With the event selection criteria
on the variables N_{Jets} and M_{inv} and a Z mass veto the efficiencies for the signal and
all backgrounds are very high, $\epsilon \approx 0.99$. The signal sample has the highest total event
selection efficiency, while for the background samples the efficiency is $\epsilon \lesssim 0.05$, which is
mainly caused by the $\not{E}_T$ and H_T requirement.

The event selection efficiencies when using a muon trigger chain are listed in Table
A.1 in the Appendix A. There, the efficiency for the trigger requirement is very high,
$\epsilon \approx 0.99$, while applying at least one muon with and without an additional lepton (e
or μ) the efficiency for the signal is $\epsilon \approx 0.24$ and for background samples like $Z + jets$,
$t\bar{t} + jet$ very high, $\epsilon \approx 0.9$. As shown in Table 6.1 the requirement on the variables
$P_T^{LeadLep}$, $P_T^{2ndLeadLep}$, N_{Jets} and M_{inv} and a Z mass veto do not show a difference in
the efficiency between the signal and the background. Using a cut on $\not{E}_T$ and H_T the

background is suppressed well. The total event selection efficiency for the signal in every is $\epsilon \approx 0.17$, while for the background it is less than 0.05.

Sample	Generated events	Trigger	$N_{lepton} \geq 1$	$P_T^{LeadLep}$	$P_T^{2ndLeadLep}$	E_T^{Miss}
b' (400 GeV)	9.99×10^4	$0.39792^{+0.00155}_{-0.00154}$	$0.91602^{+0.00139}_{-0.00141}$	$0.99563^{+0.00034}_{-0.00037}$	$1.00000^{+0.00000}_{-0.00005}$	$0.53337^{+0.00262}_{-0.00262}$
$t\bar{t} + jets$	8.79×10^5	$0.30840^{+0.00051}_{-0.00050}$	$0.94929^{+0.00043}_{-0.00044}$	$0.99688^{+0.00011}_{-0.00012}$	$1.00000^{+0.00000}_{-0.00002}$	$0.43838^{+0.00101}_{-0.00101}$
$Z + jets$	2.55×10^7	$0.39655^{+0.00015}_{-0.00015}$	$0.98574^{+0.00951}_{-0.00951}$	$0.99932^{+0.00001}_{-0.00023}$	$1.00000^{+0.00000}_{-0.00023}$	$0.05557^{+0.00020}_{-0.00016}$
$Z + b\bar{b} + jets$	1×10^6	$0.74409^{+0.00068}_{-0.00069}$	$0.97916^{+0.00028}_{-0.00035}$	$0.99924^{+0.00005}_{-0.00021}$	$1.00000^{+0.00000}_{-0.00020}$	$0.06738^{+0.00074}_{-0.00067}$
$W + jets$	2.46×10^7	$0.45918^{+0.00021}_{-0.00021}$	$0.99467^{+0.00004}_{-0.00004}$	$0.99993^{+0.00000}_{-0.00000}$	$1.00000^{+0.00000}_{-0.00000}$	$0.19727^{+0.00022}_{-0.00022}$
$W + b\bar{b} + jets$	1.65×10^4	$0.21197^{+0.00326}_{-0.00320}$	$0.96902^{+0.00288}_{-0.00344}$	$0.99997^{+0.00003}_{-0.00106}$	$1.00000^{+0.00000}_{-0.00105}$	$0.27304^{+0.00806}_{-0.00779}$
$Single\ Top$	1.65×10^6	$0.46526^{+0.00070}_{-0.00070}$	$0.97299^{+0.00035}_{-0.00035}$	$0.99859^{+0.00008}_{-0.00009}$	$1.00000^{+0.00000}_{-0.00002}$	$0.36848^{+0.00105}_{-0.00105}$
$Diboson + jets$	2.47×10^5	$0.38865^{+0.00129}_{-0.00129}$	$0.98036^{+0.00056}_{-0.00062}$	$0.99262^{+0.00035}_{-0.00041}$	$1.00000^{+0.00000}_{-0.00011}$	$0.35415^{+0.00202}_{-0.00201}$
$Drell - Yan$	1.59×10^6	$0.04733^{+0.00028}_{-0.00027}$	$0.98066^{+0.00082}_{-0.00085}$	$0.99988^{+0.00005}_{-0.00009}$	$1.00000^{+0.00000}_{-0.00008}$	$0.00649^{+0.00052}_{-0.00048}$

Sample	H_T	N_{Jets}	M_{inv}	$Z-Veto$	Total ϵ
b' (400 GeV)	$0.96436^{+0.00133}_{-0.00138}$	$0.99953^{+0.00016}_{-0.00022}$	$0.99981^{+0.00010}_{-0.00016}$	$0.99341^{+0.00059}_{-0.00064}$	$0.18531^{+0.00123}_{-0.00122}$
$t\bar{t}+jets$	$0.48751^{+0.00165}_{-0.00166}$	$0.99839^{+0.00020}_{-0.00027}$	$0.99994^{+0.00003}_{-0.00015}$	$0.99867^{+0.00018}_{-0.00026}$	$0.05682^{+0.00032}_{-0.00031}$
$Z+jets$	$0.25289^{+0.00269}_{-0.00269}$	$0.96549^{+0.00185}_{-0.00215}$	$1.00000^{+0.00000}_{-0.00090}$	$0.87481^{+0.00388}_{-0.00418}$	$0.01260^{+0.00024}_{-0.00023}$
$Z+b\bar{b}+jets$	$0.31504^{+0.00689}_{-0.00688}$	$0.98606^{+0.00260}_{-0.00433}$	$1.00000^{+0.00000}_{-0.00317}$	$0.85431^{+0.00825}_{-0.00931}$	$0.01852^{+0.00073}_{-0.00069}$
$W+jets$	$0.14376^{+0.00068}_{-0.00068}$	$0.95910^{+0.00111}_{-0.00136}$	$1.00000^{+0.00000}_{-0.00105}$	$1.00000^{+0.00000}_{-0.00105}$	$0.02480^{+0.00015}_{-0.00015}$
$W+b\bar{b}jets$	$0.21932^{+0.02181}_{-0.02055}$	$1.00000^{+0.00000}_{-0.03313}$	$1.00000^{+0.00000}_{-0.03313}$	$1.00000^{+0.00000}_{-0.03313}$	$0.01250^{+0.00158}_{-0.00135}$
$Single\ Top$	$0.14175^{+0.00146}_{-0.00145}$	$0.98876^{+0.00111}_{-0.00133}$	$0.99973^{+0.00024}_{-0.00057}$	$0.99910^{+0.00035}_{-0.00064}$	$0.01260^{+0.00014}_{-0.00013}$
$Diboson+jets$	$0.29785^{+0.00480}_{-0.00473}$	$0.93847^{+0.00463}_{-0.00604}$	$0.99842^{+0.00067}_{-0.00384}$	$0.93059^{+0.00533}_{-0.00656}$	$0.03846^{+0.00084}_{-0.00081}$
$Drell-Yan$	$0.04014^{+0.02056}_{-0.01448}$	$1.00000^{+0.00000}_{-0.22614}$	$1.00000^{+0.00000}_{-0.22614}$	$1.00000^{+0.00000}_{-0.22614}$	$0.00001^{+0.00001}_{-0.00000}$

Table 6.1.: Event selection efficiency for the signal b' with $m(b') = 400\,\mathrm{GeV}$ and all used background categories. For the trigger selection the item EF_e20_medium is used. Top event selection cuts are applied. The number of generated events are scaled to a luminosity of $2.05\,\mathrm{fb}^{-1}$.

6.2.2. Optimized event selection

The event selection in the chapter before is optimized for the $t\bar{t}$ analysis to suppress the background efficiently. To improve the event selection criteria in order to get an optimal significance for the fourth generation signal the *Toolkit for Multivariate Data Analysis with ROOT* (TMVA) [98] is used. Due to the search signature of two same-sign leptons the optimization is done in such events.

The choice of the input variables are based on the top event selection criteria.Figure 6.3 presents the input distributions, after requiring two same-sign leptons, for the signal (blue) and for the combination of every background sample (red). The W bosons from heavy quark decays have a larger boost transverse to the beam direction than the W boson in the Standard Model processes. Thus, the leptons from W decay in the signal samples mainly move along the central direction ($|\eta| \lesssim 1.5$) as shown in Figure 6.3(e) and 6.3(f). The background distribution has its maximum in the eta range $1.5 \lesssim |\eta| \lesssim 2.5$. Due to this the variables $|\eta^{LeadLep}|$ and $|\eta^{SecondLeadLep}|$, which is the pseudorapidity of the lepton with the highest and second highest transverse momentum, respectively, are also applied for the optimization. For other variables like N_{Jets}, H_T or $E_T^{LeadJet}$ the signal distribution has its maximum at higher values than the background distribution.

The TMVA package provides several algorithms for performing the multivariate analysis. For this case the "Cuts" method with the "Genetic algorithm" (GA) as minimization algorithm is chosen for the optimization. In this method the signal efficiency ε_S is set to a specific value and then the background rejection $r = 1 - \varepsilon_B$, with ε_B as the background efficiency, is maximized. The algorithm iterates over signal efficiencies between $0\,\%$ and $100\,\%$ and for each signal efficiency it varies the cuts on the input variables until the background rejection reaches its maximum. For a given signal efficiency the result are an optimal minimal and maximal cut value for each input variable. Figure 6.4 shows the background rejection as a function of the signal efficiency, which presents the correlation between an increase of the signal efficiency and a decrease of the background rejection. The distribution fluctuates for values of the signal efficiency between the 0.4 and 0.9, which can be caused by low statistics of background samples like W+jets. The background rejection is very high for low signal efficiencies, but for a signal efficiency of $\varepsilon_S \approx 0.6$ the background rejection decreases.

The signal (ε_S) and background (ε_B) efficiency as a function of the obtained cut value for every input variable is presented in Figure 6.5. The signal efficiencies after the cut optimization have their maximum at lower cut values for every variable and decrease with
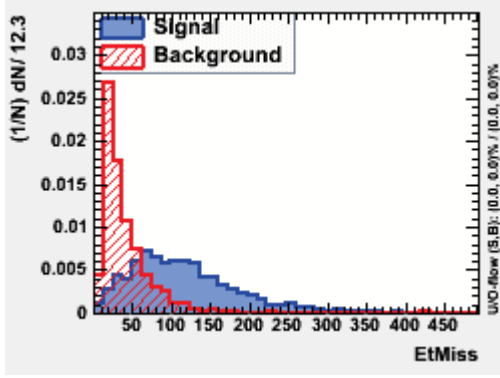
(a) $E\!\!\!/_T$
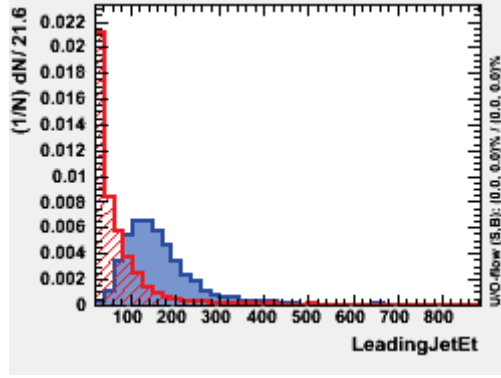
(b) $E_T^{LeadJet}$
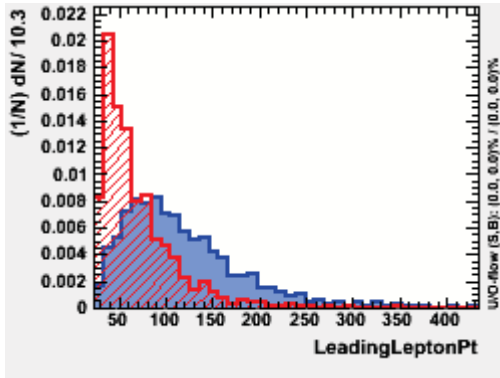
(c) $p_T^{LeadLep}$
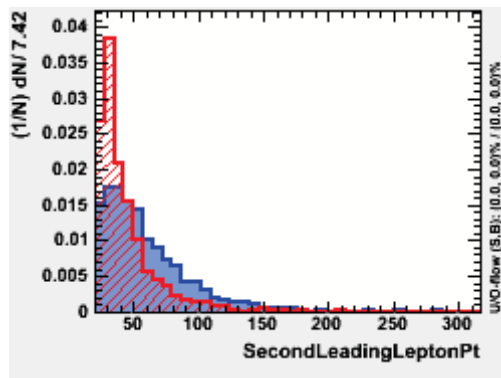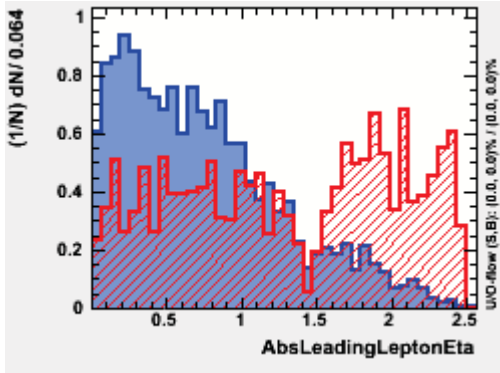
(d) $p_T^{SecondLeadLep}$
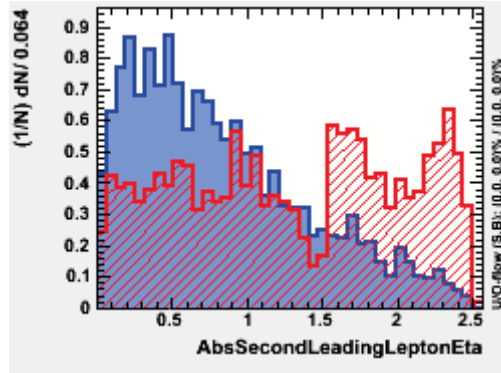
(e) $|\eta^{LeadLep}|$

(f) $|\eta^{SecondLeadLep}|$
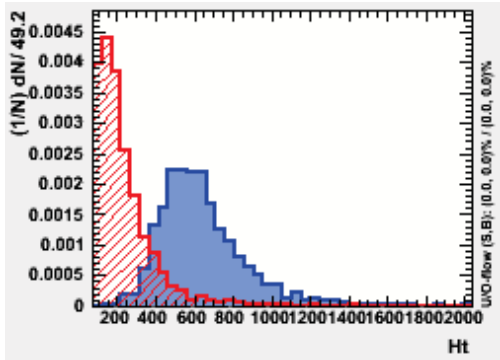
(g) H_T
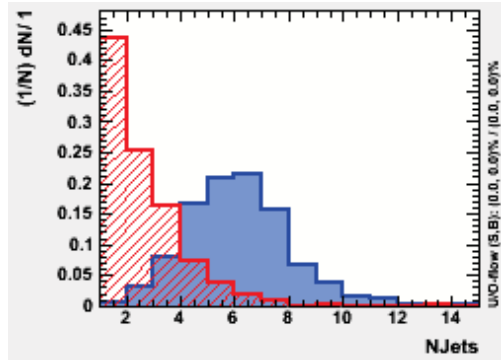
(h) N_{Jets}

Figure 6.3.: Input variables for the cut optimization with TMVA. The red distribution present the sum over all background samples and the blue one shows the signal distribution with a b' mass $m_{b'} = 400\,\mathrm{GeV}$

89
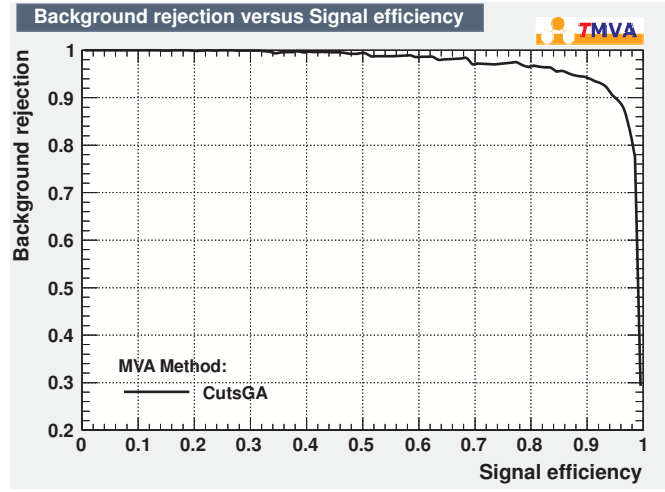
Figure 6.4.: Background rejection depending on the signal efficiency after the cut optimization.

higher values, except in the case of H_T, where the highest efficiency is at $H_T \approx 400\,\text{GeV}$. The same behavior is visible the background efficiencies, but their decrease is very sharp and is lower than 0.05 for every variable.

TMVA produces a set of cuts to a corresponding signal and background efficiency. For the optimization of the selection criteria a cut value has to be choose, for which the significance reaches its maximum. With following definition of the significance [99]:

$$Sign = \frac{S}{\sqrt{B}} \tag{6.13}$$

the standard deviation between signal and and expected background is measured, where S and B are the signal background yields after applying the optimized cuts, respectively, and scaled to a available data luminosity of $\mathcal{L} = 2.05\,\text{fb}^{-1}$ for this analysis. The significance in equation (6.13) is plotted in Figure 6.8 as a function of the optimized cut values and in Figure 6.6 as a function of the signal efficiency. In Figure 6.6 the significance is zero for efficiency values between 0.0 and 0.2, and has then its maximum for $\varepsilon_S \approx 0.25$ and finally decrease for higher efficiencies. The significance as a function of the optimized cut values (Figure 6.8) fluctuates between 5 and 25 for all distributions, which can be caused by low statistics of the background samples. For H_T and N_{Jets}, the significance increase with higher values of H_T and N_{Jets}.

Another definition of a significance is the following [99]:

$$Sign' = \frac{S}{\sqrt{S+B}}. \tag{6.14}$$

If one measure a signal, $1/Sign'$ describe the relative uncertainty of the measure number of events. The significance as a function of the signal efficiency and the optimization cut values for the input variables are plotted in Figure 6.7 and 6.9, respectively. The significance in Figure 6.7 increase with higher signal efficiencies and has its maximum at $\varepsilon_S \approx 0.95$. The significances for the input variables $\not{E}_T$, $E_T^{LeadJet}$, $p_T^{LeadLep}$ and $p_T^{SecondLeadLep}$ fluctuate, between one and five for low values of the input variables, but they reach their maximum at certain values, which are chosen as their new cut values for this analysis. In Figure 6.9(e) and 6.9(f) the significance is plotted for $|\eta^{LeadLep}|$ and $|\eta^{SecondLeadLep}|$, respectively, and has its maximum at $|\eta| \approx 0$ and becomes smaller for higher $|\eta|$ values. A cut on $|\eta| \approx 0$ cannot be chosen and due to that $|\eta| < 1.37$, where the gap appears between the barrel and endcap of the electromagnetic calorimeter, is applied in this analysis. In the case of H_T and N_{Jets} the significance increase first and then decrease again. The values, for which the behavior changes, are used for the new selection criteria as well. The following list shows the summary of the chosen cut values for every variable:

- $\not{E}_T > 50\,\text{GeV}$

- $E_T^{LeadJet} > 70\,\text{GeV}$

- $p_T^{LeadLep} > 40\,\text{GeV}$

- $p_T^{SecondLeadLep} > 20\,\text{GeV}$

- $\eta^{LeadLep} < 1.37$

- $\eta^{SecondLeadLep} < 1.37$

- $H_T > 400\,\text{GeV}$

- $N_{Jets} \geq 4$

After applying the optimized cut the event selection efficiencies change. The new values are listed in Table 6.2 using an egamma trigger chain. In the case of a muon trigger chain the efficiencies are presented in Table A.2 in the Appendix A. With a higher cut value on $p_T^{LeadLep}$ than for the top event selection the efficiency for the background is

lower than for the signal sample. The new criteria for the transverse energy and H_T shows a very small improvement, while the cut on $E_T^{LeadJet}$ suppresses all background samples very well, except $t\bar{t}+jets$. Applying $\eta^{LeadLep} < 1.37$ also suppresses the background well, but with $\eta^{SecondLeadLep} < 1.37$ no effect is visible. The total event selection efficiency for the background samples is lower than with the top event selection efficiency, but for the signal the value is lower as well.

(a) $\not{E}_T$

(b) $E_T^{LeadJet}$

(c) $p_T^{LeadLep}$

(d) $p_T^{SecondLeadLep}$

(e) $|\eta^{LeadLep}|$

(f) $|\eta^{SecondLeadLep}|$

(g) N_{Jets}

(h) H_T
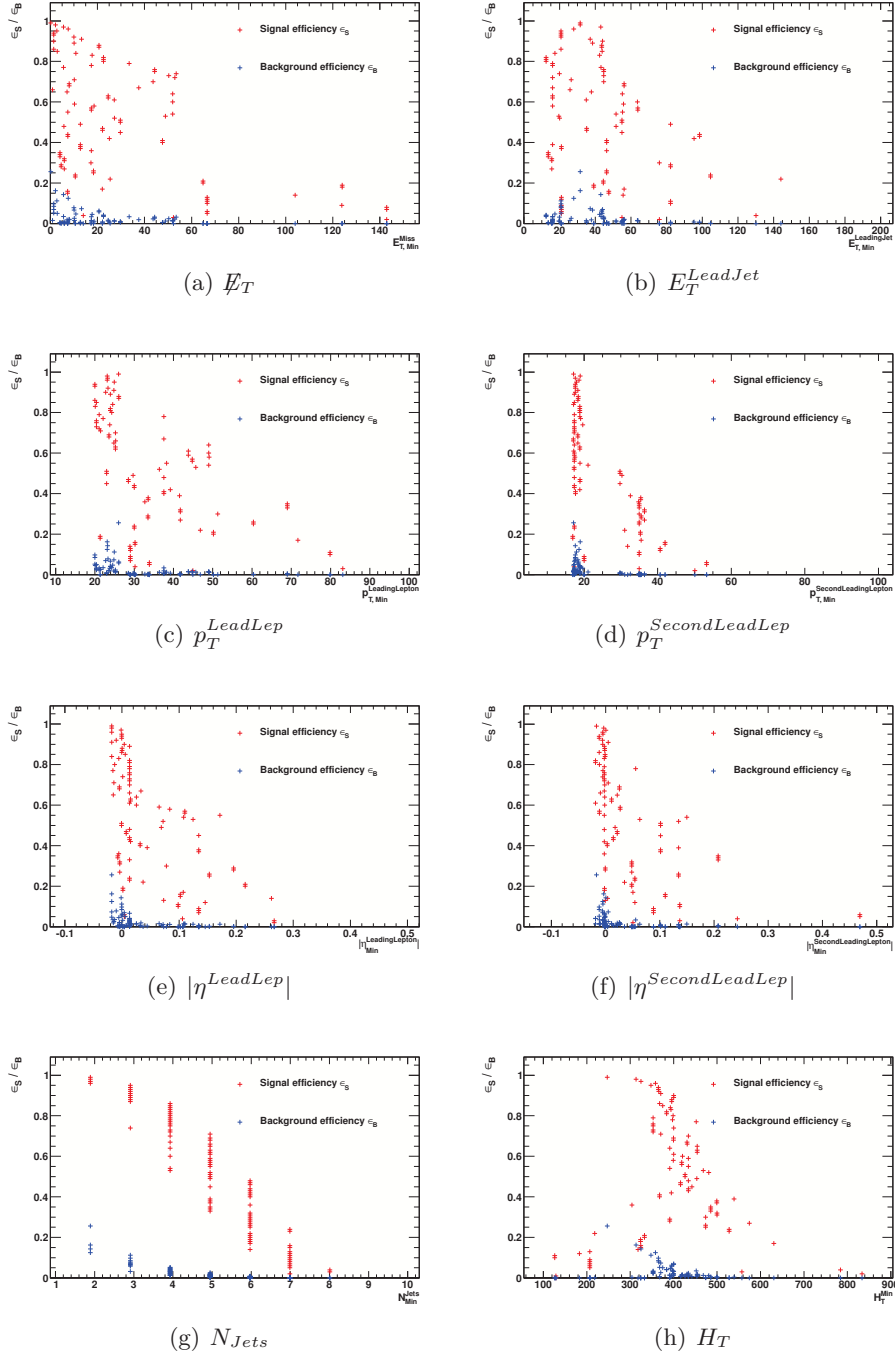
Figure 6.5.: Signal (ε_S, red) and background efficiency (ε_B, blue) as a function of the the cut values after the optimization with TMVA. The mass of the b' is $m_{b'} = 400 \, \text{GeV}$.
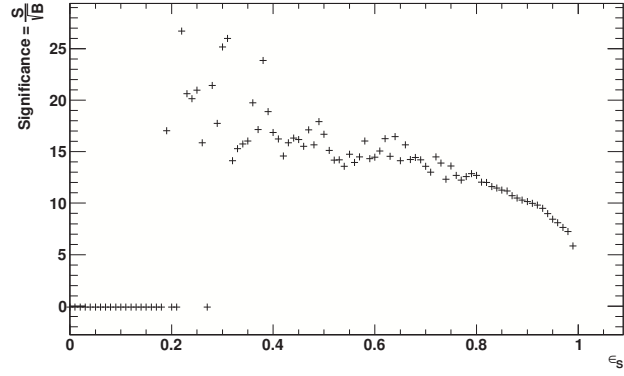
Figure 6.6.: Significance $S/\sqrt{B}$ as a function of the signal efficiencies after the optimization with TMVA.

Figure 6.7.: Significance $S/\sqrt{S+B}$ as a function of the signal efficiencies after the optimization with TMVA.

(a) $\not{E}_T$

(b) $E_T^{LeadJet}$

(c) $p_T^{LeadLep}$

(d) $p_T^{SecondLeadLep}$

(e) $|\eta^{LeadLep}|$

(f) $|\eta^{SecondLeadLep}|$

(g) H_T

(h) N_{Jets}

Figure 6.8.: Significance $S/\sqrt{B}$ as a function of the cut values for the input variables optimized with TMVA.

(a) $\not{E}_T$

(b) $E_T^{LeadJet}$

(c) $p_T^{LeadLep}$

(d) $p_T^{SecondLeadLep}$

(e) $|\eta^{LeadLep}|$

(f) $|\eta^{SecondLeadLep}|$

(g) H_T

(h) N_{Jets}
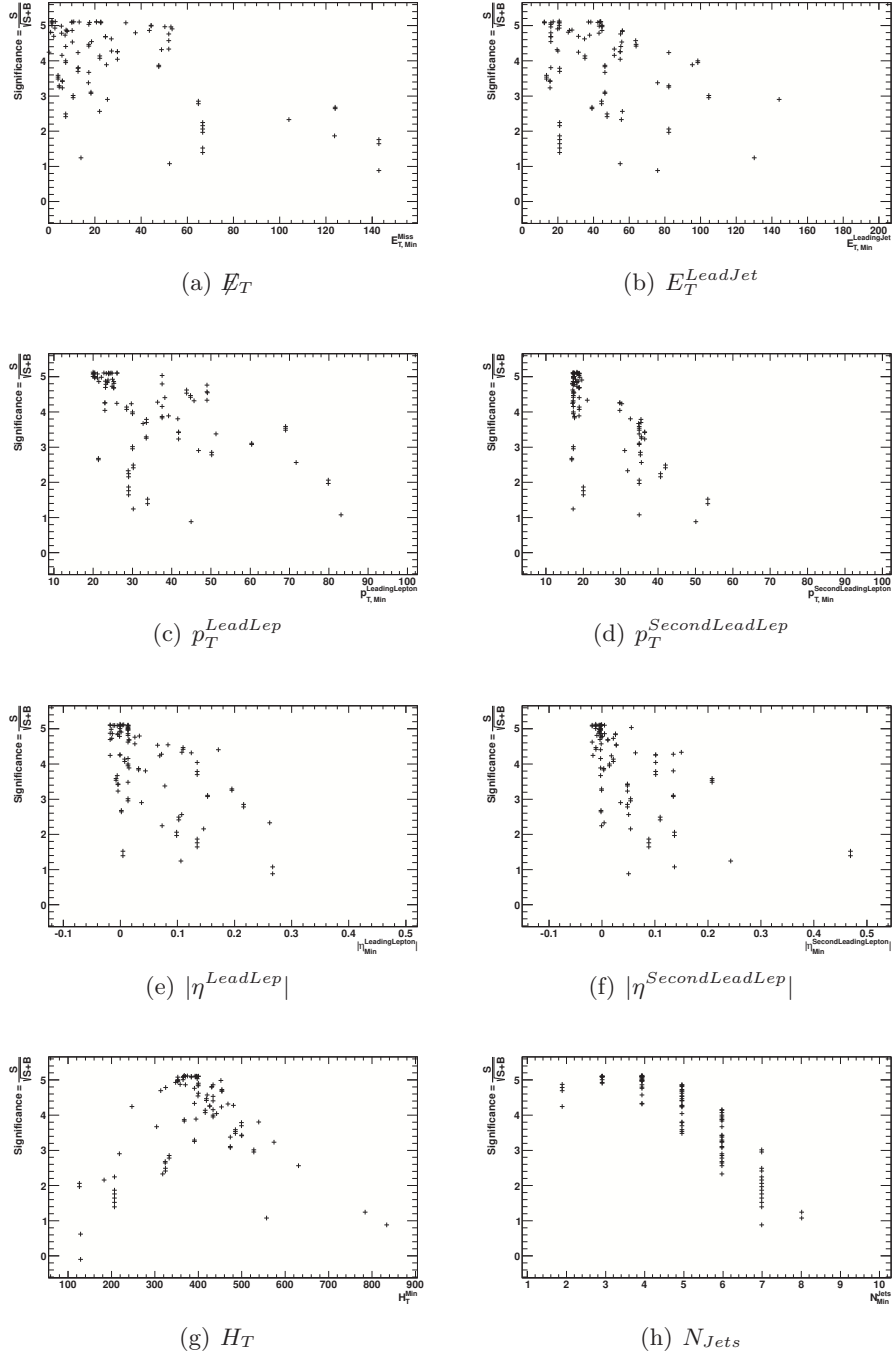
Figure 6.9.: Significance $S/\sqrt{S+B}$ as a function of the cut values for the input variables optimized with TMVA.

Sample	Generated events	Trigger	$N_{lepton} \geq 1$	$P_T^{LeadLep}$	$P_T^{2ndLeadLep}$
b' (400 GeV)	9.99×10^4	$0.39792^{+0.00155}_{-0.00154}$	$0.91602^{+0.00139}_{-0.00141}$	$0.88938^{+0.00164}_{-0.00166}$	$0.98893^{+0.00058}_{-0.00061}$
$t\bar{t}+jets$	8.79×10^5	$0.30840^{+0.00051}_{-0.00050}$	$0.94945^{+0.00043}_{-0.00044}$	$0.81407^{+0.00079}_{-0.00079}$	$0.99464^{+0.00016}_{-0.00017}$
$Z+jets$	2.55×10^7	$0.36774^{+0.00015}_{-0.00015}$	$0.98618^{+0.00982}_{-0.00982}$	$0.68339^{+0.00039}_{-0.00057}$	$0.99983^{+0.00001}_{-0.00035}$
$Z+b\bar{b}+jets$	1×10^6	$0.74409^{+0.00068}_{-0.00069}$	$0.97924^{+0.00028}_{-0.00035}$	$0.75461^{+0.00088}_{-0.00093}$	$0.99705^{+0.00012}_{-0.00030}$
$W+jets$	3.12×10^7	$0.45855^{+0.00021}_{-0.00021}$	$0.99470^{+0.00004}_{-0.00004}$	$0.57705^{+0.00029}_{-0.00029}$	$1.00000^{+0.00000}_{-0.00000}$
$W+b\bar{b}+jets$	1.65×10^4	$0.21197^{+0.00326}_{-0.00320}$	$0.96960^{+0.00285}_{-0.00340}$	$0.77031^{+0.00728}_{-0.00760}$	$0.99936^{+0.00044}_{-0.00152}$
$Single\ Top$	1.65×10^6	$0.46526^{+0.00070}_{-0.00070}$	$0.97321^{+0.00034}_{-0.00035}$	$0.77353^{+0.00091}_{-0.00092}$	$0.99826^{+0.00010}_{-0.00011}$
$Diboson+jets$	1.52×10^5	$0.39130^{+0.00131}_{-0.00130}$	$0.98042^{+0.00057}_{-0.00063}$	$0.77816^{+0.00177}_{-0.00181}$	$0.98834^{+0.00051}_{-0.00059}$
$Drell-Yan$	1.59×10^6	$0.04733^{+0.00028}_{-0.00027}$	$0.98164^{+0.00080}_{-0.00083}$	$0.70156^{+0.00275}_{-0.00277}$	$0.99968^{+0.00012}_{-0.00019}$

Sample	E_T^{Miss}	$E_T^{LeadJet}$	$\eta^{LeadLep}$	$\eta^{2ndLeadLep}$	H_T
b' (400 GeV)	$0.50842^{+0.00279}_{-0.00279}$	$0.98097^{+0.00107}_{-0.00113}$	$0.90338^{+0.00233}_{-0.00238}$	$0.94826^{+0.00184}_{-0.00190}$	$0.95064^{+0.00185}_{-0.00191}$
$t\bar{t}+jets$	$0.38342^{+0.00111}_{-0.00111}$	$0.81163^{+0.00138}_{-0.00140}$	$0.85898^{+0.00144}_{-0.00148}$	$0.97906^{+0.00061}_{-0.00065}$	$0.48918^{+0.00240}_{-0.00241}$
$Z+jets$	$0.03532^{+0.00083}_{-0.00046}$	$0.64018^{+0.00272}_{-0.00278}$	$0.68806^{+0.00362}_{-0.00370}$	$0.97964^{+0.00130}_{-0.00158}$	$0.39143^{+0.00606}_{-0.00609}$
$Z+b\bar{b}+jets$	$0.05300^{+0.00069}_{-0.00067}$	$0.61593^{+0.00514}_{-0.00531}$	$0.74738^{+0.00649}_{-0.00683}$	$0.96988^{+0.00291}_{-0.00375}$	$0.38282^{+0.01197}_{-0.01202}$
$W+jets$	$0.06374^{+0.00013}_{-0.00013}$	$0.53631^{+0.00111}_{-0.00113}$	$0.69979^{+0.00158}_{-0.00161}$	$0.99997^{+0.00001}_{-0.00028}$	$0.23435^{+0.00150}_{-0.00149}$
$W+b\bar{b}+jets$	$0.19664^{+0.00845}_{-0.00797}$	$0.53989^{+0.02344}_{-0.02426}$	$0.68373^{+0.03097}_{-0.03408}$	$1.00000^{+0.00000}_{-0.02051}$	$0.34385^{+0.04570}_{-0.04389}$
$Single\ Top$	$0.28703^{+0.00113}_{-0.00112}$	$0.57428^{+0.00227}_{-0.00228}$	$0.84720^{+0.00223}_{-0.00228}$	$0.99010^{+0.00063}_{-0.00070}$	$0.20839^{+0.00290}_{-0.00286}$
$Diboson+jets$	$0.33402^{+0.00232}_{-0.00230}$	$0.49865^{+0.00461}_{-0.00465}$	$0.75680^{+0.00627}_{-0.00662}$	$0.92737^{+0.00413}_{-0.00503}$	$0.38123^{+0.00943}_{-0.00933}$
$Drell-Yan$	$0.00262^{+0.00042}_{-0.00037}$	$0.48134^{+0.07946}_{-0.07863}$	$0.59108^{+0.11268}_{-0.12142}$	$1.00000^{+0.00000}_{-0.12003}$	$0.18270^{+0.15958}_{-0.10364}$

Sample	N_{Jets}	M_{inv}	$Z - Veto$	Total ϵ
b' (400 GeV)	$0.97841^{+0.00127}_{-0.00134}$	$0.99996^{+0.00004}_{-0.00016}$	$0.98537^{+0.00106}_{-0.00114}$	$0.12553^{+0.00105}_{-0.00104}$
$t\bar{t} + jets$	$0.92320^{+0.00170}_{-0.00179}$	$0.99993^{+0.00005}_{-0.00032}$	$0.99645^{+0.00044}_{-0.00061}$	$0.02998^{+0.00026}_{-0.00026}$
$Z + jets$	$0.72513^{+0.00882}_{-0.00948}$	$1.00000^{+0.00000}_{-0.00387}$	$0.88765^{+0.00804}_{-0.00963}$	$0.00769^{+0.00028}_{-0.00027}$
$Z + b\bar{b} + jets$	$0.76734^{+0.01465}_{-0.01696}$	$1.00000^{+0.00000}_{-0.00932}$	$0.89131^{+0.01356}_{-0.01801}$	$0.00929^{+0.00065}_{-0.00060}$
$W + jets$	$0.66787^{+0.00305}_{-0.00314}$	$1.00000^{+0.00000}_{-0.00112}$	$1.00000^{+0.00000}_{-0.00112}$	$0.01388^{+0.00019}_{-0.00018}$
$W + b\bar{b} + jets$	$0.74504^{+0.05377}_{-0.07853}$	$1.00000^{+0.00000}_{-0.10372}$	$1.00000^{+0.00000}_{-0.10372}$	$0.00690^{+0.00190}_{-0.00148}$
$Single\ Top$	$0.67122^{+0.00706}_{-0.00715}$	$1.00000^{+0.00000}_{-0.00150}$	$0.99535^{+0.00124}_{-0.00212}$	$0.00421^{+0.00008}_{-0.00008}$
$Diboson + jets$	$0.57318^{+0.01616}_{-0.01738}$	$1.00000^{+0.00000}_{-0.01249}$	$0.89977^{+0.01291}_{-0.01933}$	$0.01323^{+0.00069}_{-0.00063}$
$Drell - Yan$	$0.06529^{+0.49929}_{-0.06528}$	$1.00000^{+0.00000}_{-0.99998}$	$1.00000^{+0.00000}_{-0.99998}$	$0.00000^{+0.00000}_{-0.00000}$

Table 6.2.: Event selection efficiency for the signal b' with $m(b') = 400\,\text{GeV}$ and all used background categories. For the trigger selection the item EF_e20_medium is used. Optimized event selection cuts are applied. The number of generated events are scaled to a luminosity of $2.05\,\text{fb}^{-1}$.

6.3. Background fake estimation

Electroweak processes can produce real leptons passing the tight selection, which are used in this analysis. These processes are listed in the following:

- Semi leptonic *b*-hadron decays

- Long lived weakly decaying states such as $\pi^\pm$ or K mesons

- Reconstruction of a π^0 shower as an electron

- Reconstruction of electrons from conversion or direct photons

Fake leptons from processes like semi leptonic *b*-hadron decays can be studied with multijet events. But due to the event selection the probability of such QCD multijets events passing the event selection criteria is very low. Thus, data driven methods are applied for the fake estimation in the analysis and are add as the "Fake" contribution in the final histograms in chapter 6.4. The final results are discussed in events with one electron or muon and events with two leptons, which have the same or the opposite-sign charge. For every category one method for the fake estimation is presented. For the single lepton and the opposite-sign dilepton category the methods are developed by the *TopFake group* [76]. The estimation for the two same-sign leptons category is based on the ATLAS note "Search for Same-Sign Top Pairs and Fourth Generation Bottom-like Quarks in Same-Sign Dilepton Final States with $1\,\text{fb}^{-1}$ of Data" [97].fake sources are included like the reconstruction of electrons from conversion or direct photons or the reconstruction of leptons with the wrong charge.

Single electron category

The anti-electron method [76] is applied for the fake estimation in events with one electron[1] and with at least one jet. To determine the fake estimation events need to be selected which contain predominantly fake electrons. These electrons have to pass all criteria described in chapter 6.1.1 but with the medium quality criteria and without an isolation cut. This amount of events is called QCD template ($N^{dataevents}$). Due to the change of the electron selection the missing transverse energy is recalculated with these electrons. With this selection the data events can be contaminated with events of physics processes like $t\bar{t}$, $W^\pm + jets$ and $Z + jets$ and need to be removed: $N^{data\ events} - \sum_i^{MC_i}$ with i for the Monte Carlo sample. For the normalization of the QCD template a

---

[1]Positrons are also taken into account.

control region is chosen, for which the electrons have to pass an isolation criteria with $E_T^{cone20} > 3.5\,\mathrm{GeV}$ ($N_{E_T^{cone20}>3.5\,\mathrm{GeV}}^{QCD\ events}$). Then the QCD events in the signal region of one electron or positron are determined by an extrapolation with applying the isolation of $E_T^{cone20} < 3.5\,\mathrm{GeV}$ ($N_{E_T^{cone20}<3.5\,\mathrm{GeV}}^{QCD\ events}$). The final equation for the QCD fake prediction ($N^{QCD\ events}$) is given by:

$$N^{QCD\ events} = N_{E_T^{cone20}<3.5\,\mathrm{GeV}}^{QCD\ events} \cdot \frac{N^{data\ events} - \sum_i^{MC_i}}{N_{E_T^{cone20}>3.5\,\mathrm{GeV}}^{QCD\ events}} \tag{6.15}$$

The QCD event rate is calculated with a luminosity of $\mathcal{L} = 689\,\mathrm{pb}^{-1}$ and is presented in table 6.3 as a function of the jet multiplicity [76]. Then these yields are scaled to a luminosity, which is used for this thesis, and are added to the histograms for the single electron category (chapter 6.4). The error on the QCD yields is obtained by propagating the error on each term of the formula and is calculated with the square root of the number of events.

N_{jets}	$N^{QCD\ events} \cdot 100\,\% / N_{events}^{\mathcal{L}=689\,\mathrm{pb}^{-1}}$
2	(11.7 ± 1.3) %
3	(13.0 ± 1.7) %
4	(12.2 ± 2.8) %
≥ 5	(9.0 ± 3.2) %

Table 6.3.: Calculated QCD event rate as a function of the jet multiplicities for the single electron category with a luminosity of $\mathcal{L} = 689\,\mathrm{pb}^{-1}$ [76].

Single muon category

The fake estimation for events with one muon and at least one jet is calculated with the matrix method and is based on the selection of two categories of leptons: loose and tight lepton selection [76]. Generally for a single lepton analysis, the number of events, which contains one loose lepton can be written as:

$$N^{loose} = N_{real}^{loose} + N_{fake}^{loose} \tag{6.16}$$

where N_{real}^{loose} and N_{fake}^{loose} are the number of events containing real and fake leptons, which pass the loose lepton requirements. The ratio of events within the tight and loose lepton selection criteria can be expressed as an efficiency. The efficiency differs for real and fake lepton components. Therefore, the number of selected events with the tight lepton criteria are written as:

$$N^{tight} = \varepsilon_{real} N_{real}^{loose} + \varepsilon_{fake} N_{fake}^{loose} \tag{6.17}$$

where ε_{real} and ε_{fake} are the efficiencies of real and fake loose leptons being selected as tight leptons. These efficiencies are defined as:

$$\varepsilon_{real} = \frac{N_{tight}^{real}}{N_{loose}^{real}} \quad \text{and} \quad \varepsilon_{fake} = \frac{N_{tight}^{fake}}{N_{loose}^{fake}} , \tag{6.18}$$

where N_{tight}^{real} and N_{tight}^{fake} are the fractions of real and fake lepton events passing the tight selection criteria. Finally, the number of events with one fake lepton passing the tight selection criteria is calculated as follows:

$$N_{fake}^{tight} = \frac{\epsilon_{fake}}{\epsilon_{real} - \epsilon_{fake}} (N^{loose} \epsilon_{real} - N^{tight}) \tag{6.19}$$

This way of background estimation can only be used if the values of ε_{real} and ε_{fake} are significantly different. Generally, ε_{real} is measured from the signal region with the tag and probe method, while ε_{fake} is determined from a control region, where the contribution of the fake leptons is significantly higher than the real lepton contribution. ε_{fake} is determined with the ratio between loose and tight muons in this region.

Monte Carlo events with the process $Z \to \mu^+ \mu^-$ are applied for the measurement of the signal efficiencies with the tag and probe method. For the extraction of the fake efficiency a control region with the following criteria is used: $M_T(W) < 20\,\text{GeV}$ and $\not{E}_T + M_T(W) < 60\,\text{GeV}$, where $M_T(W)$ is calculated as follows:

$$M_T(W) = \sqrt{2 \cdot p_T^{lepton} \cdot \not{E}_T \cdot (1 - \cos(\Delta\phi))} \tag{6.20}$$

and describe the transverse W boson mass. Loose muons have to pass the same criteria as described in 6.1.2 but without an isolation criteria, while tight muons have to fulfill all of them. The muon contribution from $W^\pm + jets$ and $Z + jets$ events in the control region is determined from Monte Carlo and subtracted to obtain a purer QCD estimation. The final QCD yields are obtained with a luminosity of $\mathcal{L} = 697.9\,\text{pb}^{-1}$ and than scaled to

the luminosity used for this thesis. The QCD yield rate in the signal region as a function of the jet multiplicity is presented in table 6.4 [76]. The uncertainties are obtained by using a Gaussian with a 68 % CL interval.

N_{jets}	$N_{fake}^{tight} \cdot 100\,\% / N_{events}^{\mathcal{L}=689\,\mathrm{pb}^{-1}}$
1	$(5.5 \pm 0.4)\ \%$
2	$(9.4 \pm 0.8)\ \%$
3	$(10.4 \pm 0.8)\ \%$
4	$(9.3 \pm 0.7)\ \%$
≥ 1	$(9.6 \pm 0.7)\ \%$

Table 6.4.: Calculated QCD event rate as a function of the jet multiplicities for the single muon category with a luminosity of $\mathcal{L} = 689\,\mathrm{pb}^{-1}$ [76].

Opposite sign dilepton category

For the fake estimate in the opposite-sign dilepton category the matrix method is used as well. Generally, the number of selected events for the different lepton categories with two leptons is defined as follows:

$$
\begin{pmatrix} N^{tt} \\ N^{tl} \\ N^{lt} \\ N^{ll} \end{pmatrix} = M \times \begin{pmatrix} N_{rr}^{ll} \\ N_{rf}^{ll} \\ N_{fr}^{ll} \\ N_{ff}^{ll} \end{pmatrix}
\tag{6.21}
$$

with N^{tt} as the number of events with two tight leptons and N^{ll} with the number of event with two loose leptons, while N^{tl} and N^{lt} are the evens with one tight and one loose lepton. N_{rr}^{ll} is the number of events with two real leptons passing the loose selection and N_{ff}^{ll} is the number of events with two fake leptons passing the tight selection, while N_{rf}^{ll} and N_{fr}^{ll} is the counted number of events with one fake and one real lepton, where both leptons pass the loose selection. With equation (6.18) the updated matrix is given

by:

$$M = \begin{pmatrix} \varepsilon_{real}^1 \varepsilon_{real}^2 & \varepsilon_{real}^1 \varepsilon_{fake}^2 & \varepsilon_{fake}^1 \varepsilon_{real}^2 & \varepsilon_{fake}^1 \varepsilon_{fake}^2 \\ \varepsilon_{real}^1 (1 - \varepsilon_{real}^2) & \varepsilon_{real}^1 (1 - \varepsilon_{fake}^2) & \varepsilon_{fake}^1 (1 - r2) & \varepsilon_{fake}^1 (1 - \varepsilon_{fake}^2) \\ (1 - \varepsilon_{real}^1)r - 2 & (1 - \varepsilon_{real}^1)\varepsilon_{fake}^2 & (1 - \varepsilon_{fake}^1)\varepsilon_{real}^2 & (1 - \varepsilon_{fake}^1)\varepsilon_{fake}^2 \\ (1 - \varepsilon_{real}^1)(1 - \varepsilon_{real}^2) & (1 - \varepsilon_{real}^1)(1 - \varepsilon_{fake}^2) & (1 - \varepsilon_{fake}^1)(1 - \varepsilon_{real}^2) & (1 - \varepsilon_{fake}^1)(1 - \varepsilon_{fake}^2) \end{pmatrix} \tag{6.22}$$

The probability ε_{real} is determined for electrons and muons separately in $Z \to l^+ l^-$ event in data with the tag and probe method. ε_{fake} is measured in single loose lepton events in data and also in this case for electrons and muons separately. Tight leptons pass the selection criteria described in chapter 6.1.1 and 6.1.2. Loose electrons also fulfill the cut in chapter 6.1.1 but with the medium quality criteria, $E_T^{cone20} < 6\,\text{GeV}$ and a hit in the *b-layer*. Loose muons pass also the criteria in chapter 6.1.2 but without an isolation in the calorimeter and in the inner detector. The determined events contain leptons from physics processes like $t\bar{t}$, $W^\pm + jets$ and $Z + jets$, which are determined with Monte Carlo and subtracted from the data events. With the matrix M in equation (6.22) the final number of QCD events (N_{fake}^{tt}) can be calculated as follows:

$$N^{QCD\ events} = N_{rf}^{tt} + N_{fr}^{tt} + N_{ff}^{tt} \ , \tag{6.23}$$

where N_{rf}^{tt} and N_{fr}^{tt} is the number of events, in which one real lepton and fake lepton pass the tight selection and N_{ff}^{tt} is the measured number of events with two leptons passing the tight selection.

Table 6.5 shows the final fake lepton yields for the categories $e^+ e^-$, $e^+ \mu^-$ and $\mu^+ \mu^-$ as a function of the jet multiplicity [76]. In the case of same-flavour events ($e^+ e^-$ and $\mu^+ \mu^-$) a cut on the invariant mass is applied: $M_{l^+ l^-} > 15\,\text{GeV}$ and $|M_{l^+ l^-} - 91| > 10\,\text{GeV}$. For events with zero and one jet a systematic uncertainty of $100\,\%$ has been determined, while for events with two jets the systematic uncertainty is $50\,\%$. Further details are available in this ATLAS note [76].

Same-sign dilepton category

For the determination of the fakes in same-sign dilepton category the matrix method is used [97] as well. For the tight definition of an electron all selection criteria as described in 6.1.1 have to be passed. The electrons for the loose definition need to pass the medium *isEM* quality criteria and a b-layer hit. The real electron control region is created with the selection of one tight electron and one opposite loose electron. The invariant mass of both electrons has to be in the Z-mass range of $86 - 96\,\text{GeV}$. The fake control region

N_{jets}	$N_{e^+e^-}^{QCD\ events}$	$N_{e^+\mu^-}^{QCD\ events}$	$N_{\mu^+\mu^-}^{QCD\ events}$
0	3.3 ± 3.3	3.8 ± 3.8	0 ± 0
1	4.1 ± 4.1	19 ± 19	0.4 ± 0.4
2≥	4 ± 2	44 ± 22	6.3 ± 3.2

Table 6.5.: Measured QCD event yields as a function of the jet multiplicities for the opposite-sign dilepton category with a luminosity of $\mathcal{L} = 689\,\mathrm{pb}^{-1}$. For events with zero and one jet a systematic uncertainty of $100\,\%$ has been determined, while for events with two jets the systematic uncertainty is $50\,\%$ [76].

is obtained by requiring two loose electrons in the event and one of them has to pass the trigger selection criteria of the item *EF_e20_medium*. To reduce the real electrons from the W- and Z-decay in the fake control region the following additional cuts are applied:

- The distance in ϕ between any jet and the missing transverse energy has to be lower than 0.1, because the angle between the neutrino and the lepton from the W boson decay is very small if the W boson is boosted. In the other case it is a back-to-back decay of both particles.

- The transverse mass calculated from the electron and the missing transverse energy with equation (6.20) has to be lower than $30\,\mathrm{GeV}$. If there are W decays into electrons and neutrinos the distribution of the transverse mass has its maximum at the W boson mass ($m_W \approx 80\,\mathrm{GeV}$) and decreases sharply with lower values. The contributions at lower values are caused by fake electrons.

- The impact parameter d_0 needs to be greater than $|d_0| > 0.02\,\mathrm{mm}$ for the electron, because then the electron tracks from a W or a Z boson decay are very close to the primary vertex and have a very small value for d_0 in comparison to electrons from hadron decays inside jets.

The rate of produce faked electrons coming from hadron decays in a *b*-jet is higher than for light quark jets. With a *b-tagging* algorithm a jet can be identified as a *b*-jet and the electron fake estimation caused by a *b*-jet and a light quark jet can be done separately. For the identification of a *b*-jet the recommended *b-tagging* algorithm by the *ATLAS Top Group* is used and is called *JetProb* [76]. The requirement for a *b*-jet

is: $-\log_{10}(weight_{jetprob}) > 3.25$, while a light quark jet is identified with the criterion: $-\log_{10}(weight_{jetprob}) < 0.6$ [76]. The distinction between a b-jet and a light quark jet is done for a jet, which is closer than $\Delta R < 0.4$ to an electron. The measured probabilities ε_{real} (blue) and ε_{fake} (red with b-jets and green with light quark jets) are presented in Figure 6.10 as a function of p_T, η ϕ and H_T. ε_{real} shows in every histogram a flat behavior and has an efficiency of around 99 %. ε_{fake} measured with b-jets has a higher efficiency for lower values for the variables p_T and H_T and decreases with an increasing value of p_T and H_T. The behavior of all efficiencies as a function of ϕ is flat, while for η the efficiency is low in the region $1.3 \lesssim |\eta| \lesssim 1.5$.

(a) p_T

(b) η

(c) ϕ
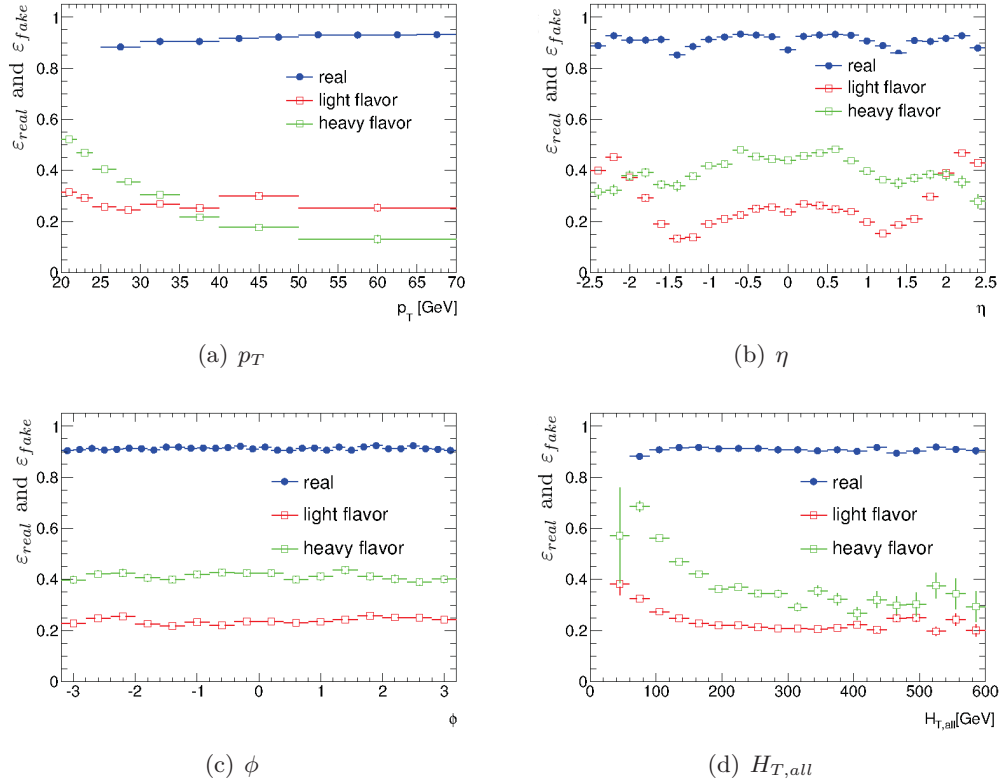
(d) $H_{T,all}$

Figure 6.10.: ε_{real} and ε_{fake} of real electrons and fake electrons from light flavor and heavy flavor jets, as a function of electron p_T, η, ϕ and $H_{T,all}$ [97].

Tight muons pass all criteria, which are described in chapter 6.1.2, while the loose muons have to pass all criteria like the tight ones except the isolation selection. As for the electrons the control samples with the real muons are filled with two leptons with the opposite-sign. One of these muons has to fulfill the tight selection and the other one the

loose selection. The invariant mass of both muons has to be in the range of the Z mass: $86 - 96\,\text{GeV}$. The fake control region is obtained by requiring one loose muon together with another muon, which passed the selection criteria of the trigger item *EF_mu18*. Additional requirements to reduce real muons from W and Z decays are the same as for electrons except the distance in ϕ between any jet and the missing transverse energy, which has to be lower than 0.5. To measure ε_{fake} near a b-jet and a light quark jet the same requirements are used as for a jet near an electron. Figure 6.11 shows ε_{real} (blue) and ε_{fake} (with b-jet in red and with a light quark in green) as a function of p_T, η ϕ and H_T. As for the electrons ε_{real} has a flat behavior in every histogram and an efficiency of $99\,\%$. Figure 6.11(a) and Figure 6.11(d) presents a high fake probability for lower values of p_T and H_T than for higher values. ε_{fake} as a function of η and ϕ with a light quark jet is very low, $\varepsilon_{fake} < 0.05$, while ε_{fake} measured near a b-jet is between 0.3 and 0.4 and has its minimum at $|\eta| \approx 0$.

(a) p_T

(b) η

(c) ϕ

(d) H_T
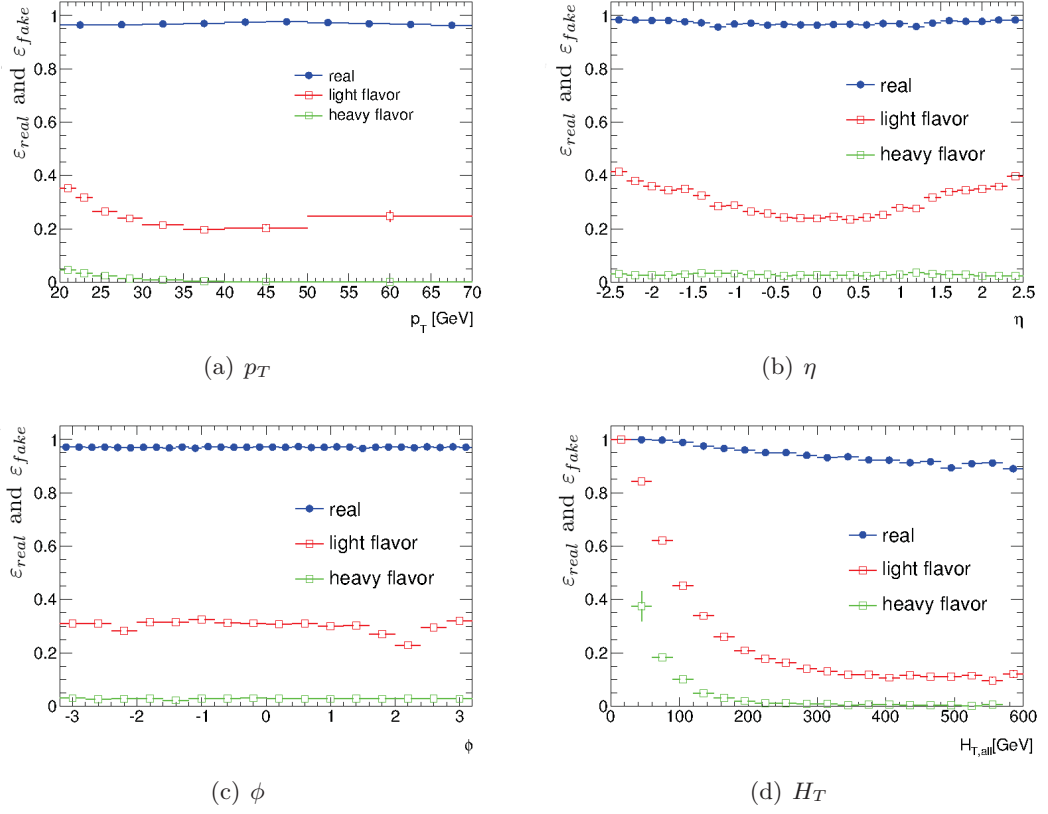
Figure 6.11.: Loose-to-tight rates of real muons and fake muons, as functions of muon p_T, η, ϕ and $H_{T,all}$(the p_T-sum for all jets, leptons) [97].

6.4. Data and Monte Carlo distributions

6.4.1. Top event selection

Figures 6.12 - 6.16 show the Monte Carlo prediction together with data from the egamma stream with exactly one electron or positron in every event. In these Figures and for the several following lepton categories, which are discussed below, the distributions $E\!\!\!/_T$, N_{Jets}, E_T^{Jets}, H_T and $p_T^{Leptons}$ are presented. The uncertainties of the Monte Carlo distributions are not shown, because the uncertainty calculation are not available yet. The uncertainty of the data are calculated with the square root of the entries in the corresponding bin, while in the case of zero entries the Feldman-Cousins method is used [100]. For every distribution the Monte Carlo processes $W + jets$ and $t\bar{t} + jets$ are the dominating contributions. The Monte Carlo together with the fakes describe the data very well as shown for the $E\!\!\!/_T$, H_T and $p_T^{Leptons}$. For the N_{Jets} and E_T^{Jets} the Monte Carlo underestimate the data, which can be caused by the missing correction factors for the $W + jets$ or by an overestimation of the fake contribution.

The distribution for events with exact two electron with the opposite-sign are presented in Figures 6.12 - 6.16. Here, the dominating background samples are $Z+jets$ and $t\bar{t}+jets$ and the Monte Carlo describe the data well, except $p_T^{Leptons}$ and H_T distribution.

For the category of exactly two leptons with the opposite-sign and different flavor the distributions are shown in Figures 6.22 - 6.26. In this case the dominating background process is $t\bar{t} + jets$. The disagreement between Monte Carlo and data for the $E\!\!\!/_T$ distribution can be caused by the underestimation of the fake contribution. Also the other distribution show a small disagreement between Monte Carlo and data, which can be also caused by an underestimation of the fake contribution in this category.

Figure 6.27 and 6.28 show the N_{Jets} distribution for exactly two same-sign electrons and exactly one electron and one muon with the same-sign, respectively. In both histograms the dominating background processes are $Diboson + jets$ and $t\bar{t} + jets$. The contribution of the process $t\bar{t} + jets$ can be caused by a wrong reconstructed charge or the identification of an electron coming from a hadron decay inside the jet, than the decay $t\bar{t}$ can produce only two leptons with the opposite-sign. The contribution of the process $Z + jets$ in Figure 6.27 is caused by the same reason as for the process $t\bar{t} + jets$. $Diboson + jets$ contains also the process $pp \rightarrow WZ \rightarrow l^{\pm}\nu_l l^{\pm}l^{\mp}$ and contribute via this process to this lepton category.

In the Figures A.1 - A.5 in Appendix A the distributions for exactly one muon and the data from the muons stream are plotted. Also in this case $W + jets$ and $t\bar{t}+jets$ are the dominated background samples. With the single muon category the agreement between

Monte Carlo and data is very well for the $\not{E}_T$ distribution. For the other distributions the Monte Carlo underestimate the data, which can be caused by an overestimation of the fake contribution or the missing correction factors for the $W + jets$ process.

The distributions for exactly two muon with the opposite-sign are presented in Figures A.6 - A.10 (Appendix A) and show a disagreement between Monte Carlo and data for few bins for every distribution. In these bins the Monte Carlo underestimate the data. As for two electrons with the opposite-sign $Z + jets$ and $t\bar{t} + jets$ are the dominated background samples.

Figures A.11 - A.15 in the Appendix A with events containing one electron and one muon with the opposite-sign show small discrepancies between Monte Carlo data. The dominating process is $t\bar{t} + jets$.

Events with two same-sign muons and one electron and one muon with the same-sing as a function of the jet multiplicity are plotted in Figure A.16 and A.17 (Appendix A), respectively. The dominated background sample is in the case of two same-sign muons only $Diboson + jets$, while for events one electron and one muon $Diboson + jets$ and $t\bar{t} + jets$ are the dominated ones. As already mentioned above $t\bar{t} + jets$ can contribute only due to a wrong charge of the reconstructed lepton or due to a reconstructed electron coming from a hadron decay inside the jet. In Figure A.16 also $W + jets$ contribute caused by the reconstruction of a muon from the hadron decay inside the jet.
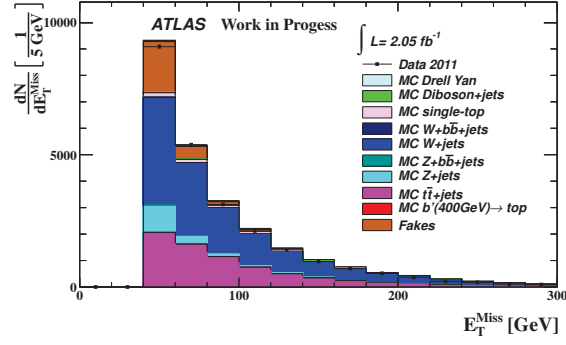
Figure 6.12.: $\displaystyle{\not}E_T$ for the category e^+/e^- with the top event selection cuts and the requirement of an electron trigger chain.
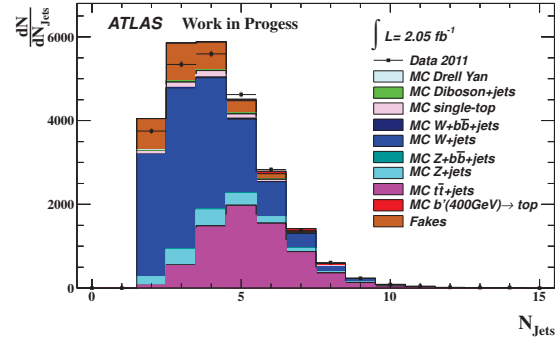
Figure 6.13.: N_{Jets} for the category e^+/e^- with the top event selection cuts and the requirement of an electron trigger chain.
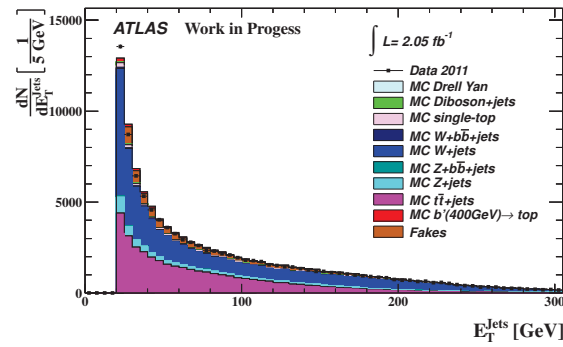
Figure 6.14.: E_T^{Jets} for the category e^+/e^- with the top event selection cuts and the requirement of an electron trigger chain.
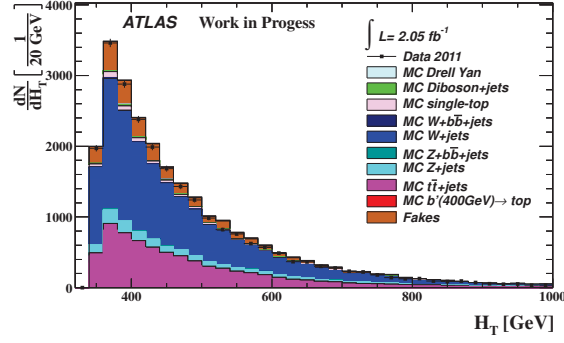
Figure 6.15.: H_T for the category e^+/e^- with the top event selection cuts and the requirement of an electron trigger chain.
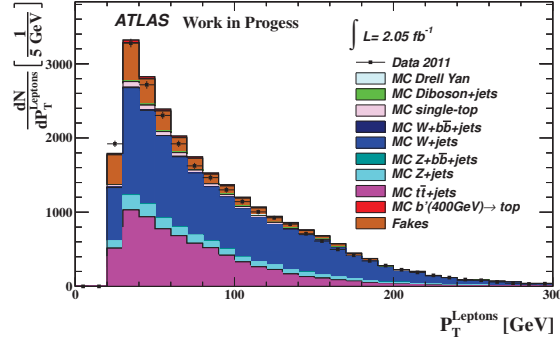
Figure 6.16.: $p_T^{Leptons}$ for the category e^+/e^- with the top event selection cuts and the requirement of an electron trigger chain.
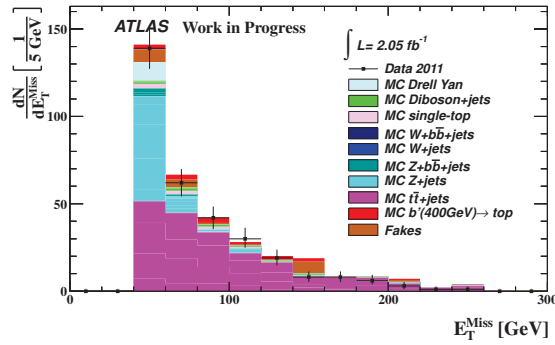
Figure 6.17.: $\not{E}_T$ for the category e^+e^- with the top event selection cuts and the requirement of an electron trigger chain.
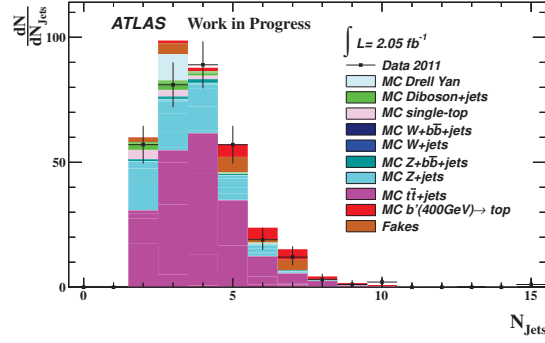
Figure 6.18.: N_{Jets} for the category e^+e^- with the top event selection cuts and the requirement of an electron trigger chain.
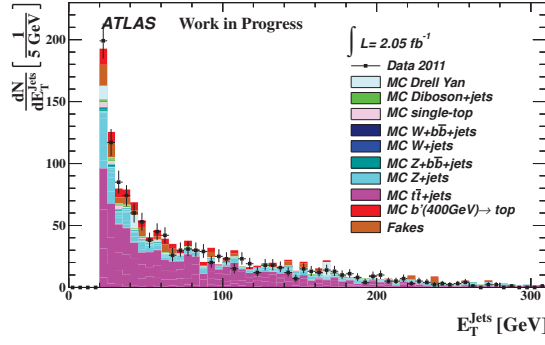
Figure 6.19.: E_T^{Jets} for the category e^+e^- with the top event selection cuts and the requirement of an electron trigger chain.
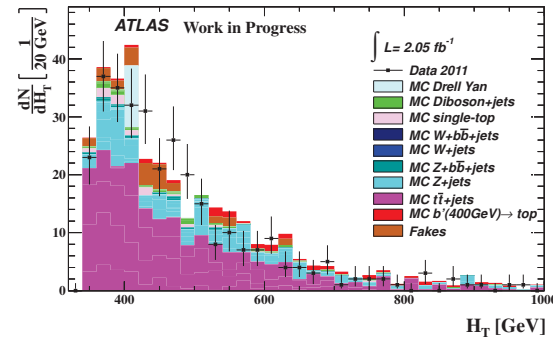
Figure 6.20.: H_T for the category e^+e^- with the top event selection cuts and the requirement of an electron trigger chain.
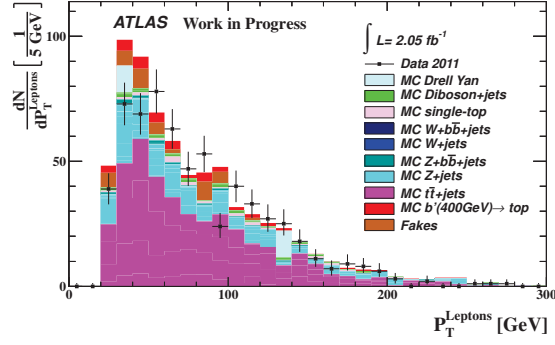
Figure 6.21.: $p_T^{Leptons}$ for the category e^+e^- with the top event selection cuts and the requirement of an electron trigger chain.
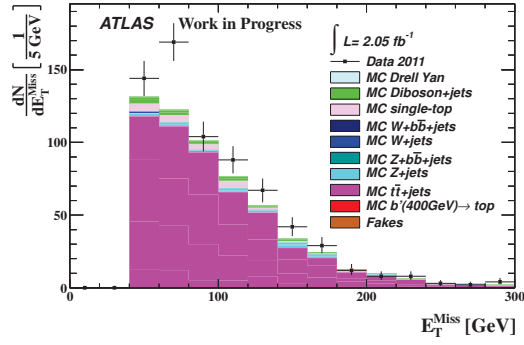
Figure 6.22.: $\not{E}_T$ for the category $e^+\mu^-/e^-\mu^+$ with the top event selection cuts and the requirement of an electron trigger chain.
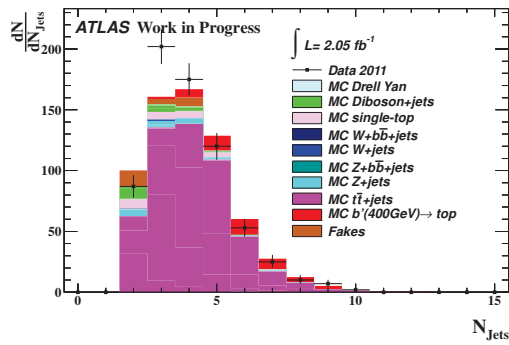
Figure 6.23.: N_{Jets} for the category $e^+\mu^-/e^-\mu^+$ with the top event selection cuts and the requirement of an electron trigger chain.
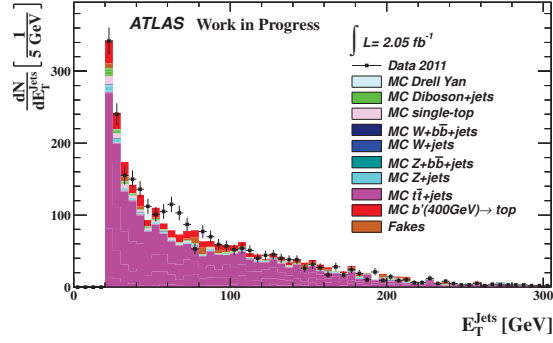
Figure 6.24.: E_T^{Jets} for the category $e^+\mu^-/e^-\mu^+$ with the top event selection cuts and the requirement of an electron trigger chain.
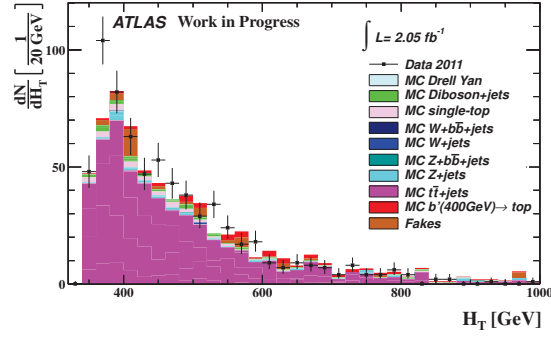
Figure 6.25.: H_T for the category $e^+\mu^-/e^-\mu^+$ with the top event selection cuts and the requirement of an electron trigger chain.
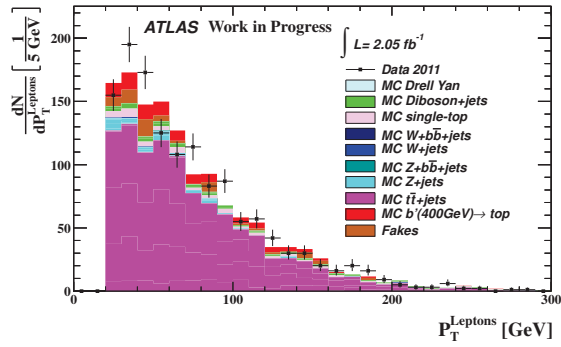
Figure 6.26.: $p_T^{Leptons}$ for the category $e^+\mu^-/e^-\mu^+$ with the top event selection cuts and the requirement of an electron trigger chain.
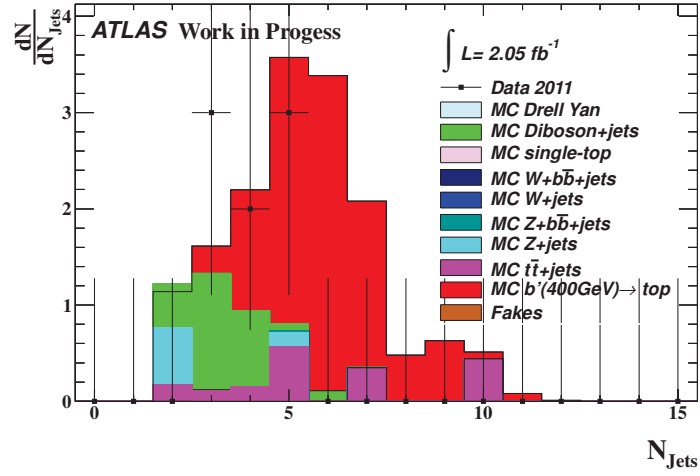
Figure 6.27.: N_{Jets} for the category e^+e^+/e^-e^- with the top event selection cuts and the requirement of an electron trigger chain.
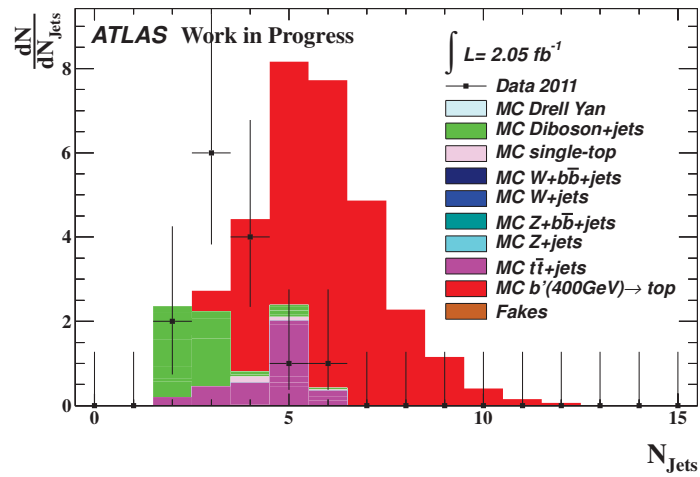
Figure 6.28.: N_{Jets} for the category $e^+\mu^+/e^-\mu^-$ with the top event selection cuts and the requirement of an electron trigger chain.

6.4.2. Optimized event selection

In this chapter the agreement between Monte Carlo and data with the used optimized event selection are discussed. Also in this case the uncertainties on the Monte Carlo prediction are not presented due to the missing implementation in the analyses framework. The uncertainty of the data are calculated with the square root of the entries in the corresponding bin, while in the case of zero entries the Feldman-Cousins method is used [100].

In the single electron/positron category (Figures 6.29 - 6.33) the dominating background processes are $W + jets$ and $t\bar{t} + jets$ as for the top event selection criteria. In this case the Monte Carlo underestimates the data. The reason for this underestimation could be the missing correction for the $W + jets$ contribution or the missing recalculation of the missing transverse momentum after applying the scale factors for the electrons.

With events containing exactly two opposite-sign electrons (Figure 6.34 - 6.38) there is a disagreement between Monte Carlo and data. Due to improved cut values for the event selection the contribution of $Z + jets$ is smaller than with the top event selection criteria.

Figure 6.29 - 6.33 show the distribution for events with one electron and one muon with the opposite-sign and a disagreement between Monte Carlo and data is visible.

When applying a muon trigger chain and when using the data from the muons stream the dominating background samples are the same as for the electron channels. Events with exactly one muon are presented in Figure A.18 - A.22 in the Appendix A. There, the Monte Carlo underestimates the data, which can also be caused by the missing correction for the $W + jets$ contribution or the missing recalculation of the missing transverse momentum after applying the scale factors for the electrons. In the case of two muons with the opposite-sign in every event the distributions are shown in Figure A.23 - A.27 in the Appendix A. For these distributions the agreement between Monte Carlo and data is good except for few bins, where the Monte Carlo underestimates or overestimates the data. The dominating Monte Carlo process is $t\bar{t} + jets$. In the Figures A.28 - A.22 in the Appendix A the distributions are plotted for events with one electron and one muon with the opposite-sign. Here, the agreement between Monte Carlo and data is good except for few bins.

With the improvement of the event selection cuts no data events passed the criteria when using the data from the muons stream for events with exactly two same-sign muons (Figure A.33 in the Appendix A), while three events pass the optimized event selection criteria for events, which contain one muon and one electron with the same-sign (Figure

A.34 in the Appendix A). Applying an egamma trigger chain and with the data from the egamma stream only one event passed the event selection criteria in events with exactly two same-sign electrons (Figure 6.44) and one electron and one muon with the same-sign(Figure 6.45). This shows that the improvement of the event selection cuts has a better background suppression, but also less data events pass these criteria.
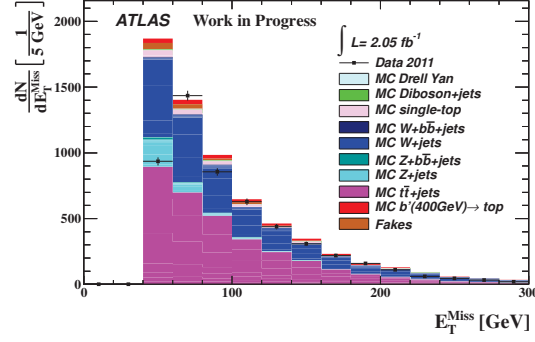
Figure 6.29.: $\displaystyle{\not}E_T$ for the category e^+/e^- with the optimized event selection cuts and the requirement of an electron trigger chain.
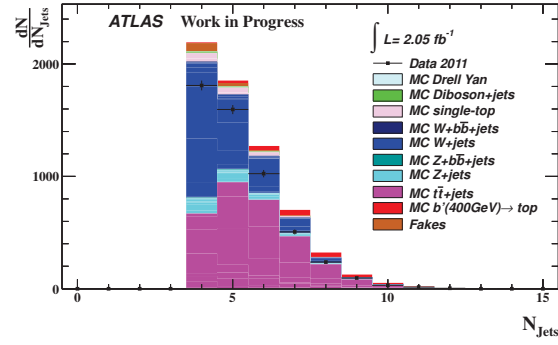
Figure 6.30.: N_{Jets} for the category e^+/e^- with the optimized event selection cuts and the requirement of an electron trigger chain.
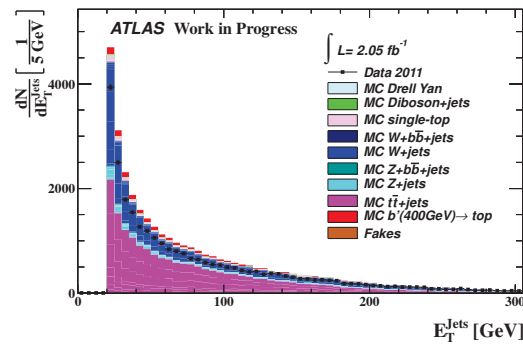
Figure 6.31.: E_T^{Jets} for the category e^+/e^- with the optimized event selection cuts and the requirement of an electron trigger chain.
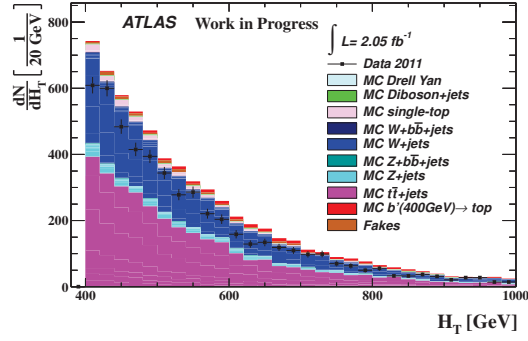
Figure 6.32.: H_T for the category e^+/e^- with the optimized event selection cuts and the requirement of an electron trigger chain.
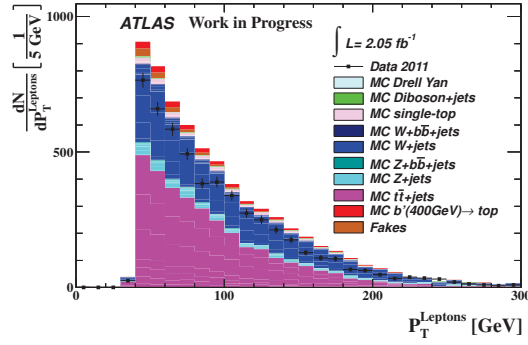
Figure 6.33.: $p_T^{Leptons}$ for the category e^+/e^- with the optimized event selection cuts and the requirement of an electron trigger chain.
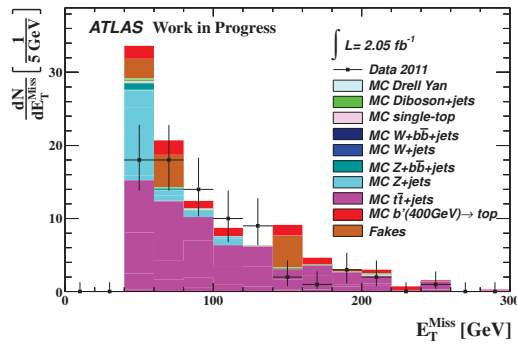
Figure 6.34.: $\not{E}_T$ for the category e^+e^- with the optimized event selection cuts and the requirement of an electron trigger chain.
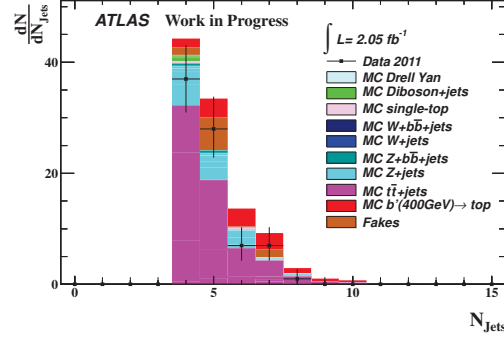
Figure 6.35.: N_{Jets} for the category e^+e^- with the optimized event selection cuts and the requirement of an electron trigger chain.
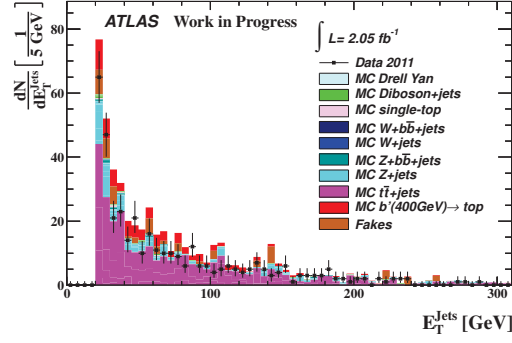
Figure 6.36.: E_T^{Jets} for the category e^+e^- with the optimized event selection cuts and the requirement of an electron trigger chain.
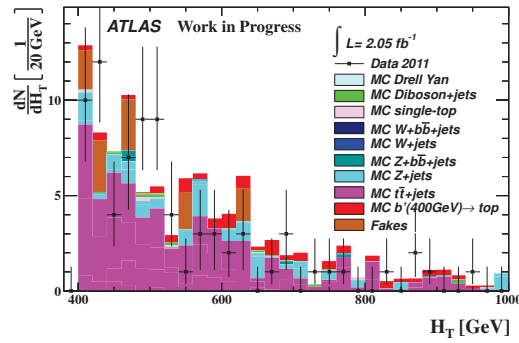
Figure 6.37.: H_T for the category e^+e^- with the optimized event selection cuts and the requirement of an electron trigger chain.
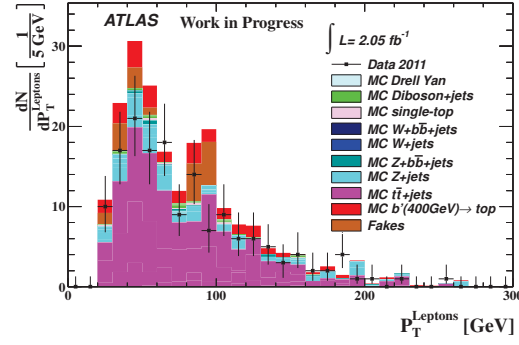
Figure 6.38.: $p_T^{Leptons}$ for the category e^+e^- with the optimized event selection cuts and the requirement of an electron trigger chain.
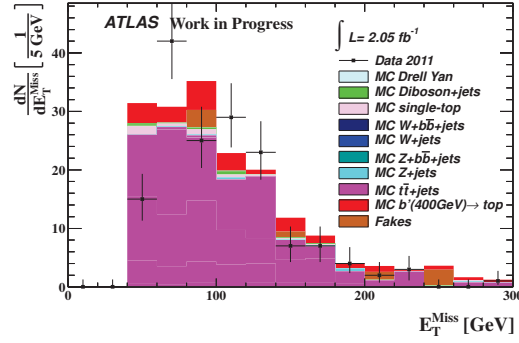
Figure 6.39.: $\not{E}_T$ for the category $e^+\mu^-/e^-\mu^+$ with the optimized event selection cuts and the requirement of an electron trigger chain.
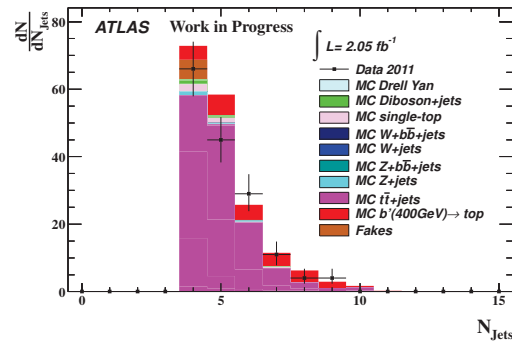
Figure 6.40.: N_{Jets} for the category $e^+\mu^-/e^-\mu^+$ with the optimized event selection cuts and the requirement of an electron trigger chain.
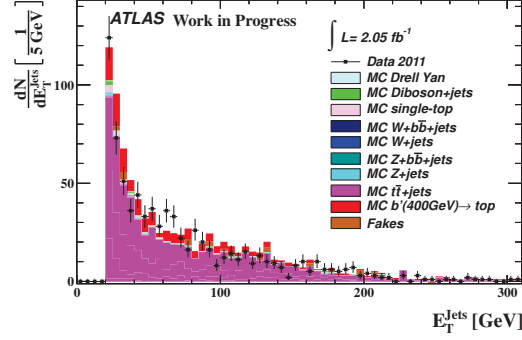
Figure 6.41.: E_T^{Jets} for the category $e^+\mu^-/e^-\mu^+$ with the optimized event selection cuts and the requirement of an electron trigger chain.
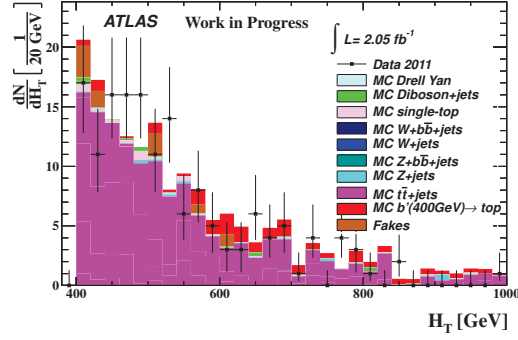
Figure 6.42.: H_T for the category $e^+\mu^-/e^-\mu^+$ with the optimized event selection cuts and the requirement of an electron trigger chain.
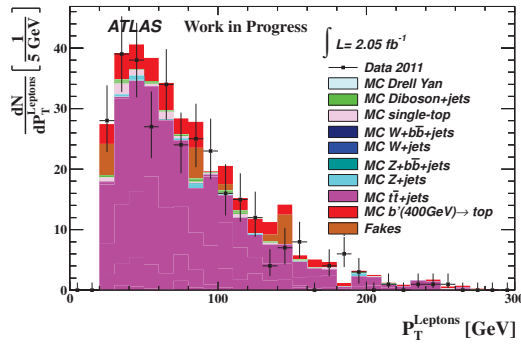
Figure 6.43.: $p_T^{Leptons}$ for the category $e^+\mu^-/e^-\mu^+$ with the optimized event selection cuts and the requirement of an electron trigger chain.
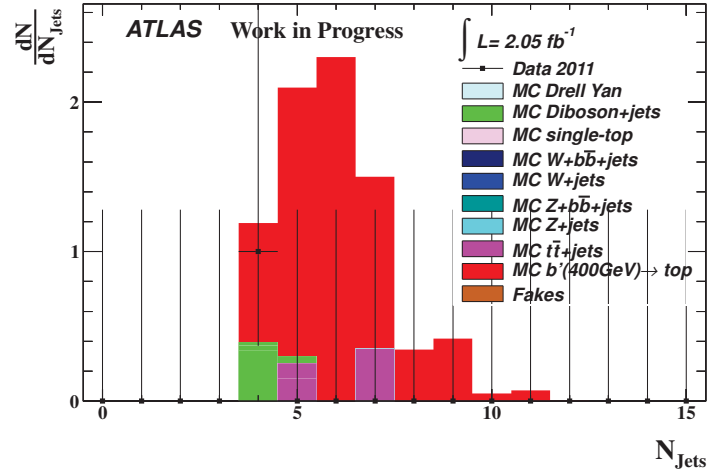
Figure 6.44.: N_{Jets} for the category e^+e^+/e^-e^- with the optimized event selection cuts and the requirement of an electron trigger chain.
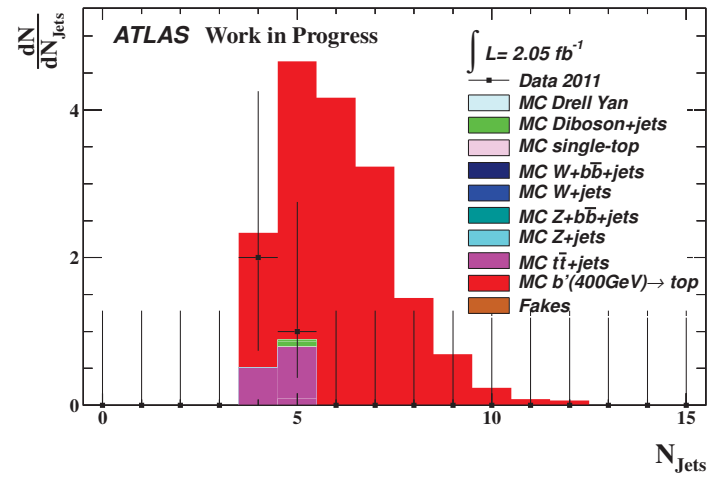
Figure 6.45.: N_{Jets} for the category $e^+\mu^+/e^-\mu^-$ with the optimized event selection cuts and the requirement of an electron trigger chain.

7. Systematic studies

The final yields in single and dilepton events with the top and optimized event selection criteria are discussed in the chapter 6. With the measured data and Monte Carlo yields in the signal region of two same-sign leptons the signal can be extracted (chapter 8). For the extracted of the signal and the lower mass limit determination it is necessary to consider the sources of the systematic uncertainties.

For example, systematic uncertainties are caused by the reconstruction algorithms used for the physical objects and by defects from the experiment itself. A list of the systematic uncertainties and their effect on the signal (b' with $m_{b'} = 400\,\mathrm{GeV}$) and the complete background contribution is given in Table 7.1. They were determined with the analysis in the ATLAS note [97]. For the systematic studies the top event selection criteria were used. The reconstruction efficiencies of the muons and electrons contains the uncertainties of the reconstruction algorithm as well as the uncertainties from the trigger object selection and scale factors. For the signal and background an upper and a lower bound of the uncertainty on the acceptance are listed in Table 7.1.

The effect of uncertainties from the jet energy scale were studied with a rescaling of the jet momentum as a function of its transverse momentum (p_T) and its pseudorapidity (η). The size of this uncertainty was determined with the relative difference between the acceptance with the jet energy rescaling and the acceptance without the jet energy rescaling.

The jet energy scale resolution was measured with dijet events. The effect on the signal and background was studied with a smearing based on a Gaussian distribution of the jet momentum depending on its transverse momentum and its pseudorapidity. The effect of this uncertainty is determined from the difference between the counted events with a smearing and the counted events without a smearing.

The effects on the counted events by the uncertainties coming from the reconstruction algorithm, which also takes into account the uncertainties from the trigger identification and the scale factors, were measured by varying the lepton selection inside the uncertainties.

Source	Uncertainty on signal acceptance (%)	Uncertainty on background acceptance (%)
Jet energy scale	+0.7, −0.8	+7.1, −5.5
Jet energy resolution	+0.7, −0.8	+4.1, −4.2
Jet reconstruction efficiency	+0.1, −0.1	+0.1, −0.1
Electron energy scale	+0.3, −0.4	+1.1, −1.2
Electron energy resolution	+0.1, −0.1	+0.8, −0.8
Muon energy scale	+0.1, −0.1	+0.1, −0.1
Muon energy resolution	+0.2, −0.3	+0.6, −0.7
Electron reconstruction efficiency	+3.4, −4.9	+1.8, −2.0
Muon reconstruction efficiency	+4.4, −5.3	+2.3, −3.0
Missing Transverse Momentum	+0.8, −0.8	+0.9, −0.9
Broken LAr Calorimeter modules	+2.0, −3.0	+1.0, −2.0

Table 7.1.: Sources of systematic uncertainties and their contributions to the uncertainty on signal and background acceptance. Lepton reconstruction efficiencies takes also into account the trigger and scale factor uncertainties. For these studies the top event selection criteria were used [97].

The energy scale uncertainty of the electrons was studied by rescaling the transverse energy of the cluster. With the relative difference between the selected events with an energy rescaling and the selected events without a rescaling is used for the determination of the effect on the signal and the background. This is also done for the muons, but in this case the transverse momentum of the muons is used. To study the effect coming from the energy resolution a smearing on the transverse momentum for the muons and on the transverse energy of the electron cluster is applied, which is based on a Gaussian distribution. The relative difference between the selected events with a smearing and

without a smearing gives the uncertainty.

If the energy or the momentum of any physical object in the event is modified by a smearing or rescaling the missing transverse energy needs to be recalculated. The uncertainty from the missing transverse energy can also be studied with a 1σ shift in the *CellOut* and *SoftJet* term in the $\not{E}_T$ calculation. Using the relative difference between the counted events with the recalculated $\not{E}_T$ and the events with the original $\not{E}_T$ the uncertainty is determined.

As shown in Table 7.1, the biggest uncertainties are coming from the jet energy scale and the jet energy resolution.

The signal extraction and the lower mass limit determination also depend on the the Monte Carlo estimation, which is affected by the configuration of the Monte Carlo generator. Changing the configuration can lead to an effect on the event selection efficiency. In the following, I discuss the effect on the event selection efficiency coming from replacing the PDF and from varying the parameters for the ISR and FSR simulation. For these systematic studies a b' signal samples is used generated with Pythia6.

7.1. PDF uncertainties

As already described in chapter 4.1.1 the parton distribution function defines the probability density for finding a parton (quark or gluon) in the proton with a certain longitudinal momentum fraction x at a squared momentum transfer q^2. Thus, changing the PDF can lead to an effect on the cross section for the simulated process or the simulation of the underlying event.

The underlying event in the Monte Carlo samples are dominated by multi-parton interactions (MPI) caused by the interaction of the partons beside the hard scattering. The MPI is modelled phenomenologically and a set of parameters in the generator can be used to optimize the Monte Carlo estimation for a comparison to experimental data, which is know as "tuning".

The calculation of the partonic cross section for the MPI can lead into divergences and, thus, for modeling the MPI a cuttoff parameter is needed, which is based on the scattering p_T and is called p_T^{min}. In Pythia6 this parameter is evolved as function of the center-of-mass energy and the calculation is given by [101]:

$$p_\perp^{min}(\sqrt{s}) = p_\perp^{min}(1800\,\text{GeV}) \cdot \left(\frac{\sqrt{s}}{1800\,\text{GeV}} \right)^{e/2} \ , \tag{7.1}$$

where $p_\perp^{min}(1800\,\text{GeV})$ is set to $1800\,\text{GeV}$ due to the parameter optimization with the Tevatron Run I data in the past. In ATLAS $p_\perp^{min}(1800\,\text{GeV})$ and the exponent e are used for the optimization of the parameters in Pythia6 labeled PARP(82) and PARP(90), respectively. For example, a higher value of e produce a higher $p_\perp^{min}(\sqrt{s})$ at LHC energies and reduce the MPI activity.

The MPI model also uses the color reconnection mechanism, which needs to be tuned to LHC data. The color reconnection mechanism modeled in Pythia6 is connected to the probability P_{keep} that a string does not participate in this process and is given by:

$$P_{keep} = (1 - PARP(78))^{n_{MPI}} \; , \tag{7.2}$$

where n_{MPI} is the number of additional parton-parton interactions, which occur in the event. It shows, that the probability for color reconnection goes up with an increasing of the interaction. Furthermore, the parameter PARP(77) in Pythia6 is used for the Pythia6 tuning, which is needed to suppress reconnections of high p_T strings.

The geometrical overlap of the colliding protons is modeled using a double Gaussian ("hot spot model") with parameters PARP(84) and PARP(83), which determine the inner radius and the outer radius for the master density. Both parameters were tuned to data.

With the parameters discussed above Pythia6 was tuned to set of data with a center-of-mass energy of $\sqrt{s} = 0.9\,\text{TeV}$ and $\sqrt{s} = 7\,\text{TeV}$ taken with ATLAS in 2010 [102]. Further data sets from the experiments D0 and CDF were included for the tuning. This tune is called *ATLAS Minimum Bias Tune 1* (AMBT1).

In AMBT1 the PDF MRST 2007LO* [103] is used, which is a modified leading-order PDF. The reason for using a modified leading-order PDF is that Pythia6 is a leading-order generator, which cannot take into account a next to leading-order loop correction for the event generation and the cross section calculation. For leading-order generators only corresponding leading-order PDFs can be applied. To get a more realistic description of the simulation of proton-proton collisions together with the gluon radiations a modified leading-order PDF is used in ATLAS for the MC10 production.

For the uncertainty study of the event selection efficiency coming from the PDF choice CTEQ6L [104] and CTEQ6LL [104] are used. CTEQ6LL is also a modified leading order PDF, while CTEQ6L is a leading-order PDF. Inside ATLAS studies have been shown that the agreement between the Monte Carlo estimation and the data is very sensitive to the PDF and the corresponding Pythia6 tune [102]. Thus, replacing the PDF requires a retune of the parameters. For the PDFs CTEQ6L and CTEQ6LL the parameters in

Pythia6 were optimized with the same data set used for AMBT1 [105] using the *Professor* [106] tool. The tool is based on a definition and minimization of a goodness of fit function between experimental data and parametrized generator responses. The generator response is obtained using Rivet [107], which mimics experimental data analysis with Monte Carlo generators. The final tuned parameter values for the new PDFs together with the values of the MC10 setup of Pythia6 are listed in Table 7.2.

Parameters	MC10	Retuned CTEQ6L	Retuned CTEQ6LL
Parp(77)	1.016	0.63	0.59
Parp(78)	0.538	0.33	0.31
Parp(82)	2.292	2.18	2.06
Parp(84)	0.651	0.40	0.45
Parp(90)	0.250	0.23	0.24

Table 7.2.: Tune parameters and values for MC10, CTEQ6L and CTEQ6LL [102], [105].

With these new PDFs and the corresponding tuned parameter values Monte Carlo samples were produced (labeled as "new tune") with the signal process and a b' mass, $m_{b'} = 350\,\text{GeV}$. Monte Carlo samples using the other PDFs but with the MC10 generator setup (labeled "no tune") were simulated as well. The idea of using the MC10 setup with a different PDF is to study the effect on the event selection efficiency coming from replacing the PDF without optimizing parameter values, then non optimized parameters can lead to an over- or underestimation of the MPI model with respect to the data. Every sample were produced with a different random seed start value and the configuration of the Monte Carlo generator filter as described in chapter 4.1.4. Table 7.3 presents the leading-order cross section, which were calculated by Pythia6 without the generator filter efficiency. The cross section calculated with the PDF in the MC10 setup for $m_{b'} = 350\,\text{GeV}$ is higher than calculated with CTEQ6L and CTEQ6LL. Figure 7.3(a) presents the gluon density function $f(x, Q^2 = 2 \times 10^5\,\text{GeV}^2)$ multiplied with the momentum fraction x for the PDFs MRST 2007LO* (MC10), CTEQ6L and CTEQ6LL as a function of the momentum fraction of the gluon. The distributions for the other type of partons are plotted in Figure B.1 in the Appendix B and all flavors together are plotted in Figure 7.3(b). Within a proton-proton collision $f(x, q^2)$ defines the probability that a parton

from the proton will interact in the hard scattering process with a parton from the other proton. For a low mass of the b' a low momentum fraction is needed. In Figure 7.3(b) at low values of x the gluon has the highest value for $f \cdot x$ and thus, the gluon fusion channel is dominating production channel. The differences of the cross section in Table 7.3 is caused by a higher $f \cdot x$ value for MRST 2007LO* than for CTEQ6L and CTEQ6LL. The cross sections calculated with CTEQ6L and CTEQ6LL are equal due to the similar behavior of $f \cdot x$ for both PDFs as a function of x.

PDF	$\sigma \ (m_{b'} = 350\,\mathrm{GeV})$ [pb]
MC10	1.122
CTEQ6L (new tune)	0.878
CTEQ6LL (new tune)	0.865
CTEQ6L (no tune)	0.861
CTEQ6LL (no tune)	0.886

Table 7.3.: The leading-order cross section σ is presented for the MC10 setup and for CTEQ6L and CTEQ6LL with the MC10 setup (no tune) and with the re-tuned parameter values (new tune).

Another way to study the PDF effect on the event selection efficiency is to use a "reweighting" method [109]. With this tool a new weight is calculated for the new PDF with respect to the PDF in MC10 for every event. This depends on the flavor f of the parton in the proton, which is used for the hard process, the momentum fraction of this parton x and the momentum transfer q^2. With the LHAPDF interface [110] the PDF momentum density f for for a given PDF, x and q are calculated and used in the following equation

$$c = \frac{f_1^{MRST\ 2007LO^*}(x_1, q) \cdot f_2^{MRST\ 2007LO^*}(x_2, q)}{f_1^i(x_1, q) \cdot f_2^i(x_2, q)}, \qquad (7.3)$$

where i is the new PDF, which is used for the reweighting with respect to MRST 2007LO* and 1 and 2 are the partons, which interacts in the hard scattering process. The multiplication of the initial event weight w and c results in the new weight: $w_{new} = w \cdot c$. Figure 7.2 presents the new weight w_{new} for the PDFs CTEQ6L and CTEQ6LL together with

(a) gluon   (b) all
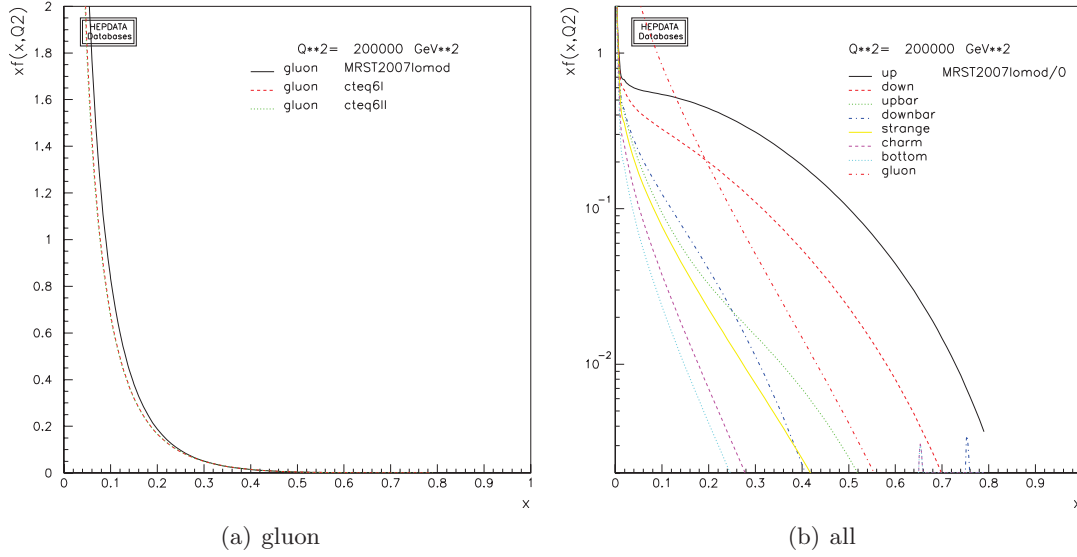
Figure 7.1.: Parton density function multiplied with the momentum fraction x as function of the momentum fraction for the gluon the PDF MRST 2007LO* (MC10), CTEQ6L and CTEQ6LL ((a)) and all partons for the PDF MRST 2007LO* ((b)) [108]

the weight of the simulated Monte Carlo samples with Pythia6 and the MC10 setup. The calculated weights with the reweighting method have values between 0.3 and 1.0, while the standard weight with the MC10 setup in the simulated samples has always the value 1.0.

Table 7.5, 7.7 and B.1 in the Appendix B present the event selection efficiencies for the produced samples with the different PDF setup and for the reweighted samples. The number of generated events are scaled to the available luminosity of $\mathcal{L} = 2.05\,\mathrm{fb}^{-1}$ and the event selection efficiencies and uncertainties are calculated with equation (6.7). For the determination of the lower and upper limit for the efficiency equation (6.9) is used. For the selection of the event the top event selection is applied.

As shown in Table 7.5 selecting events with a trigger requirement or a cut on $P_T^{LeadLep}$, $P_T^{2ndLeadLep}$ and N_{Jets} do not show any differences on the event selection efficiencies between the several samples. Applying exactly two same-sign electrons in every event shows very small differences, but these differences are within the upper and lower limit of the efficiencies. In Figure 7.4 the multiplicity and the transverse momentum of the electron and muon on generator level are plotted. For this no event selection criteria are used the distribution are normalized to $\mathcal{L} = 2.05\,\mathrm{fb}^{-1}$. The distribution coming
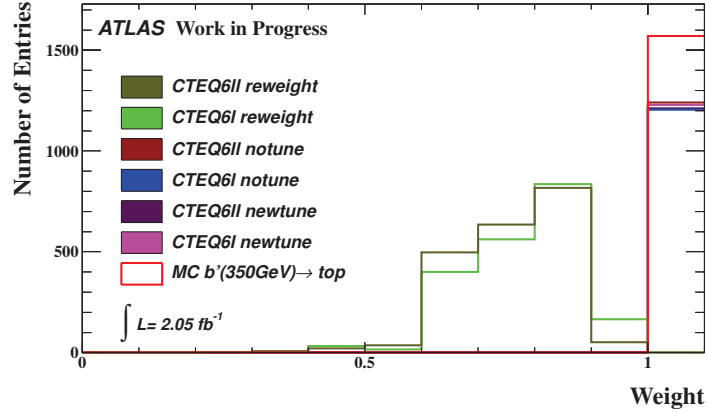
Figure 7.2.: Monte Carlo event weight of Pythia6 samples and the weight calculated by the reweighting method. All distributions are normalized to a luminosity of $\mathcal{L} = 2.05\,\mathrm{fb}^{-1}$.

from the sample with the default MC10 setup is higher than the other distributions, which is caused by the higher cross section of this sample. But the shape is for every samples the same and shows that replacing the PDFs does not have a visible effect on the leptons multiplicity and transverse momentum. Small differences on the event selection efficiencies are visible, but the differences are within the upper and lower limit of the efficiencies. It is similar for the missing transverse momentum requirement. The event selection efficiency for the PDF CTEQ6LL with the MC10 setup has the highest event selection efficiency, which is not understood yet and needs to be studied. The components for the $\not{E}_T$ calculation are not available in the analysis framework. Also the event selection efficiency for H_T is different between the default MC10 setup and the new PDFs, while the efficiencies for the samples with the new weight are similar. The differences are caused by the overlap removal between electron and jets. The overlap removal is made before the calculation of H_T. Table 7.4 shows the event selection efficiencies for H_T without applying the overlap removal and the event selection efficiencies are similar. With applying CTEQ6L more jets are removed than for the default MC10 setup, which results in a lower value for H_T, while using CTEQ6LL less jets jets were removed and H_T is higher. Without the overlap removal the differences in the total event selection efficiency is smaller than with the overlap removal. The small differences in total event selection are caused by the missing transverse momentum requirement.

In Table 7.6 the event selection efficiencies are listed requiring exactly two same-sign electrons in every event and the optimized event selection. The differences between

Sample	H_T
Default	$0.99341^{+0.00305}_{-0.00493}$
CTEQ6L new tune	$0.99440^{+0.00328}_{-0.00615}$
CTEQ6LL new tune)	$0.99814^{+0.00162}_{-0.00501}$
CTEQ6L no tune)	$0.99266^{+0.00402}_{-0.00717}$
CTEQ6LL no tune)	$0.99894^{+0.00103}_{-0.00479}$
CTEQ6L reweight)	$0.99145^{+0.00386}_{-0.00615}$
CTEQ6LL reweight	$0.99145^{+0.00390}_{-0.00626}$

Table 7.4.: Event selection efficiency after applying the cut on H_T for the samples with the different PDF setups. Events with two same-sign electrons and the top event selection cuts are used. No overlap removal is made.

the efficiencies are small and within the upper and lower limit of the efficiencies. The total event selection efficiencies are higher for "CTEQ6LL new tune" and "CTEQ6LL no tune" than for "Default", while for "CTEQ6L new tune" and "CTEQ6L no tune" the efficiencies are lower than for "Default". The behavior between the efficiencies are caused by a cut on H_T, but the event selection efficiencies for the other cuts, which are applied before H_T requirement like $\not{E}_T$, show a different behavior. A reason could be the small jet multiplicity between the different samples. Removing the overlap removal between electrons and jets in the analysis show a very small difference between the total event selection efficiencies of the different Monte Carlo samples and the efficiencies are within the upper and lower limit of the efficiency. In this case the event selection efficiency after applying the H_T requirement is ≈ 0.99. Figure 7.3 presents the N_{Jets} and the E_T^{Jets} distribution for events with two same-sign electrons. Both distributions are scaled $\mathcal{L} = 2.05\,\mathrm{fb}^{-1}$. Only the object selection criteria for jets are applied and the no event selection. The differences between the several samples are very small. The maximum of the N_{Jets} distribution for the default signal sample has a higher maximum than the other samples, but between the samples with the changed PDF the behavior of the distributions are the same. For the E_T^{Jets} distribution the behavior of the different samples with the replaced PDF are the same. But the distribution for the default

sample is higher than the other ones for $E_T^{Jets} < 100\,\text{GeV}$. In the case of the reweighting method the differences between the total event selection efficiencies ("Default", CTEQ6L reweight" and "CTEQ6LL reweight") are smaller than for using the top even selection cuts. This is caused by the calculated weight, than with the default weight value, which is one, event selection efficiencies are equal. The shape of the N_{Jets}, E_T^{Jets} and $p_T^{Leptons}$ in the Figures B.2 - B.4 (used top event selection) and in the Figures B.11 - B.13 (used optimized event selection) in the Appendix B are equal for "Default", CTEQ6L reweight" and "CTEQ6LL reweight".

(a) N_{Jets} (b) E_T^{Jets}
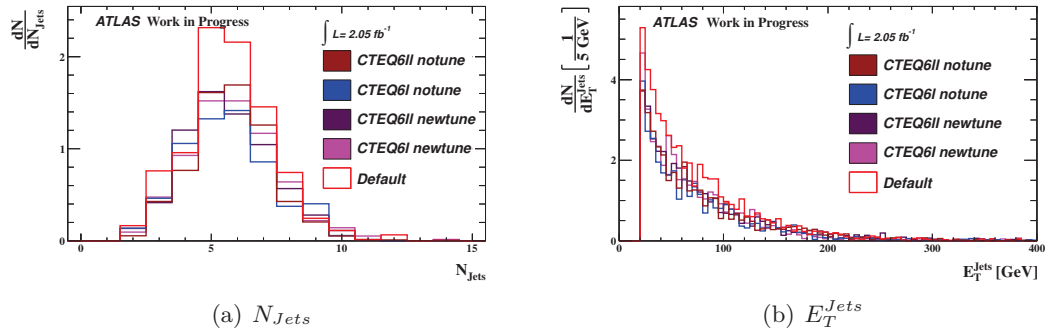
Figure 7.3.: N_{Jets} and E_T^{Jets} for events with two same-sign electrons. Only the jet selection criteria and no event selection criteria are applied. The distributions are scaled to a luminosity of $\mathcal{L} = 2.05\,\text{fb}^{-1}$.

requires further investigations.

The event selection efficiencies for events with two same-sign muons and the top event selection criteria are listed in Table 7.7. Also here, the efficiencies are small and within the upper and lower of the efficiencies. The total event selection efficiency for "CTEQ6L new tune" is lower than for "Default" and for "CTEQ6LL new tune" the total event selection efficiency is higher than "Default". Replacing the PDF and use the MC10 values for the parameters the behavior is the different. The efficiency for "CTEQ6L new tune" and "CTEQ6LL new tune" are higher than for "Default". These behaviors are visible with the requirement of two same-sign muons in the event, which can be caused by reconstructed muons coming from a hadron decays inside the jet. The efficiencies for the samples "CTEQ6L reweight" and "CTEQ6LL reweight" has a smaller difference between each other and also with respect to "Default". This effect is also caused by the new calculated for these samples, then with the default weight, for which the value is one, the event selection efficiencies are equal. Using the optimized event selection criteria in events with two same-sign muons (Table 7.8) the same behavior between the different

efficiencies are visible. In the Figures B.5 - B.7 in the Appendix B the N_{Jets}, E_T^{Jets} and $p_T^{Leptons}$ are plotted and do not any differences between the behaviors. In the case of the used optimized event selection criteria no differences are visible for the distributions in the Figures B.14 - B.16 in the Appendix B.

The event selection efficiencies for events with one electron and one muon and the used top event selection are listed in Table B.1 in the Appendix B. The total event selection efficiency for "CTEQ6LL new tune" is lower than for "Default", while for "CTEQ6L new tune" the efficiency is higher than for "Default". Using only a new PDF the opposite behavior is visible. The same effect already visible with requiring one electron and one muon. This can be caused by the different rate of reconstructed leptons near a jet. In the case of "CTEQ6L reweight" and "CTEQ6LL reweight" both efficiencies are similar, but higher than for "Default", caused by the new calculated weight, then also here with the default weight the event selection efficiencies are equal. In Table B.2 selected event with the optimized event selection criteria are listed. Requiring the optimized event selection the same behavior is visible as for using the top event selection. With using the top event selection criteria and the optimized event selection criteria no differences are visible for the distributions (N_{Jets}, E_T^{Jets} and $p_T^{Leptons}$) between the samples "Default", "CTEQ6L reweight" and "CTEQ6LL reweight" in the Figures B.8 - B.10 and Figures B.17 - B.19, respectively.

the jet multiplicity. The differences between the event selection efficiencies are also caused by overlap removal and the values are simialr without the overlap removal.

setup. The differences between total event selection efficiencies of the samples are smaller than with the applied event selection efficiencies.
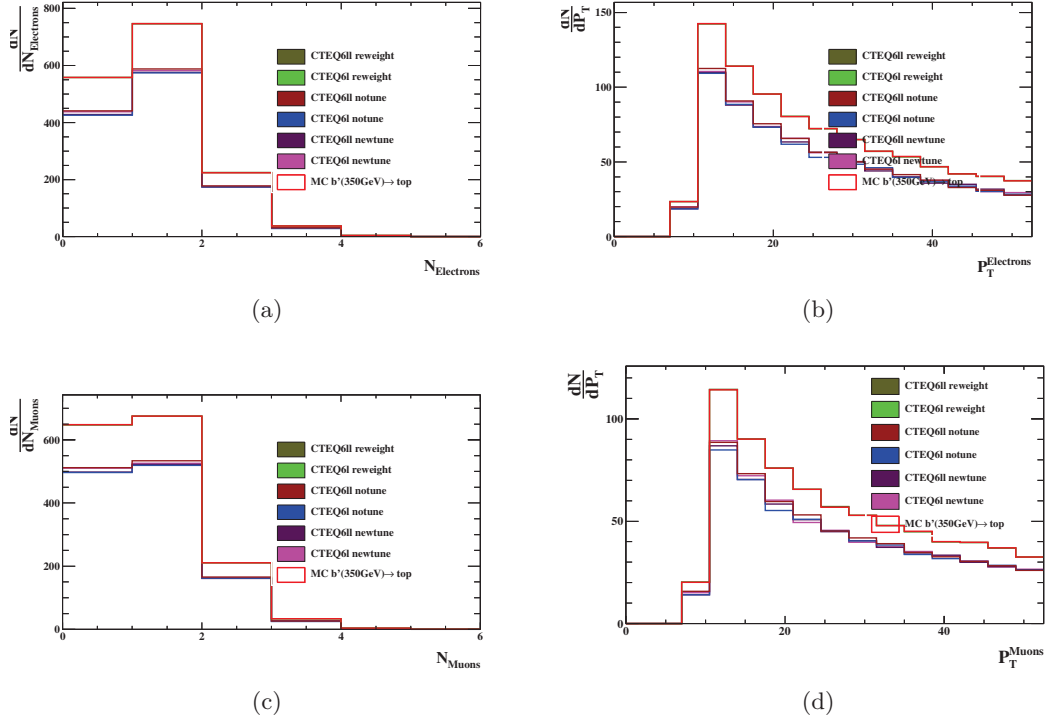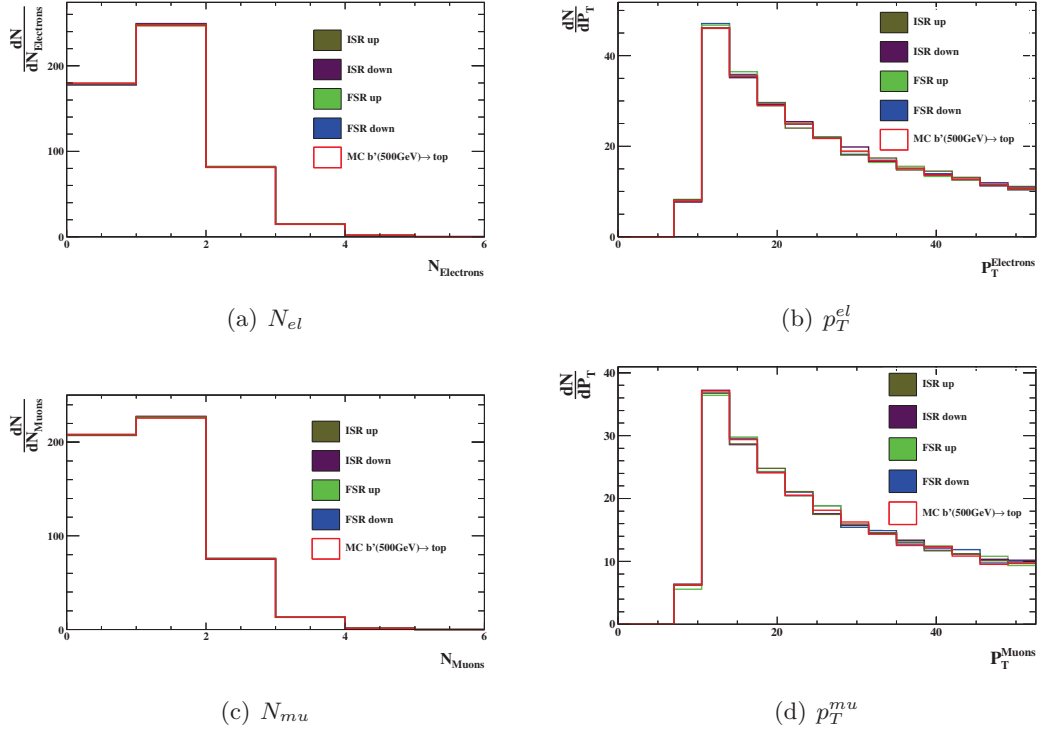
(a)

(b)

(c)

(d)

Figure 7.4.: N_{el} and N_μ on generator level together with their transverse momentum (p_T^{el} and p_T^{mu}) scaled to a luminosity of $\mathcal{L} = 2.05\,\mathrm{fb}^{-1}$. There are no requirements for the production channel of the electron and muons. The distributions are presented for the Monte Carlo samples with the several PDF configuration and the MC10 setup.

Sample	Generated events	Trigger	e^+e^+/e^-e^-	$P_T^{LeadLep}$	$P_T^{2ndLeadLep}$	E_T^{Miss}
Default	1.45×10^5	$0.99886^{+0.00009}_{-0.00010}$	$0.00615^{+0.00021}_{-0.00020}$	$1.00000^{+0.00000}_{-0.00206}$	$1.00000^{+0.00000}_{-0.00206}$	$0.76629^{+0.01435}_{-0.01497}$
CTEQ6L new tune	9.99×10^4	$0.99885^{+0.00011}_{-0.00012}$	$0.00596^{+0.00025}_{-0.00024}$	$1.00000^{+0.00000}_{-0.00308}$	$1.00000^{+0.00000}_{-0.00308}$	$0.79082^{+0.01692}_{-0.01794}$
CTEQ6LL new tune	9.86×10^4	$1.00055^{+-1.00055}_{-1.00055}$	$0.00613^{+0.00026}_{-0.00025}$	$1.00000^{+0.00000}_{-0.00302}$	$1.00000^{+0.00000}_{-0.00302}$	$0.77148^{+0.01732}_{-0.01826}$
CTEQ6L no tune	9.96×10^4	$0.99706^{+0.00017}_{-0.00018}$	$0.00546^{+0.00024}_{-0.00023}$	$1.00000^{+0.00000}_{-0.00338}$	$1.00000^{+0.00000}_{-0.00338}$	$0.78095^{+0.01804}_{-0.01912}$
CTEQ6LL no tune	9.99×10^4	$0.99864^{+0.00012}_{-0.00013}$	$0.00559^{+0.00024}_{-0.00023}$	$1.00000^{+0.00000}_{-0.00328}$	$1.00000^{+0.00000}_{-0.00328}$	$0.82640^{+0.01623}_{-0.01746}$
CTEQ6L reweight	1.16×10^5	$0.99850^{+0.00011}_{-0.00012}$	$0.00622^{+0.00024}_{-0.00023}$	$1.00000^{+0.00000}_{-0.00253}$	$1.00000^{+0.00000}_{-0.00253}$	$0.77186^{+0.01581}_{-0.01659}$
CTEQ6LL reweight	1.14×10^5	$0.99844^{+0.00012}_{-0.00013}$	$0.00622^{+0.00024}_{-0.00023}$	$1.00000^{+0.00000}_{-0.00259}$	$1.00000^{+0.00000}_{-0.00259}$	$0.77123^{+0.01603}_{-0.0168}$

Sample	H_T	N_{Jets}	M_{inv}	$Z-Veto$	Total ϵ
Default	$0.91862^{+0.01050}_{-0.01180}$	$1.00000^{+0.00000}_{-0.00292}$	$0.98926^{+0.00401}_{-0.00586}$	$0.94943^{+0.00878}_{-0.01035}$	$0.00406^{+0.00017}_{-0.00017}$
CTEQ6L new tune	$0.90374^{+0.01368}_{-0.01552}$	$1.00000^{+0.00000}_{-0.00431}$	$0.99993^{+0.00007}_{-0.00435}$	$0.92024^{+0.01319}_{-0.01533}$	$0.00391^{+0.00021}_{-0.00020}$
CTEQ6LL new tune	$0.93098^{+0.01175}_{-0.01375}$	$1.00000^{+0.00000}_{-0.00421}$	$0.99493^{+0.00314}_{-0.00614}$	$0.93584^{+0.01179}_{-0.01398}$	$0.00410^{+0.00021}_{-0.00020}$
CTEQ6Lnotune	$0.93148^{+0.01230}_{-0.01451}$	$1.00000^{+0.00000}_{-0.00464}$	$0.99261^{+0.00406}_{-0.00726}$	$0.92835^{+0.01306}_{-0.01545}$	$0.00365^{+0.00020}_{-0.00019}$
CTEQ6LL no tune	$0.94767^{+0.01036}_{-0.01249}$	$1.00000^{+0.00000}_{-0.00419}$	$0.99899^{+0.00098}_{-0.00470}$	$0.93532^{+0.01179}_{-0.01396}$	$0.00408^{+0.00021}_{-0.00020}$
CTEQ6L reweight	$0.91770^{+0.01167}_{-0.01327}$	$1.00000^{+0.00000}_{-0.00357}$	$0.99105^{+0.00400}_{-0.00635}$	$0.95226^{+0.00944}_{-0.01139}$	$0.00415^{+0.00020}_{-0.00019}$
CTEQ6LL reweight	$0.91754^{+0.01183}_{-0.01347}$	$1.00000^{+0.00000}_{-0.00366}$	$0.99105^{+0.00405}_{-0.00646}$	$0.94230^{+0.01048}_{-0.01242}$	$0.00410^{+0.00020}_{-0.00019}$

Table 7.5.: Event selection efficiency for the samples with the different PDF setups. Events with two same-sign electrons and the top event selection cuts are used.

Sample	Generated events	Trigger	e^+e^+/e^-e^-	$P_T^{LeadLep}$	$P_T^{2ndLeadLep}$
Default	1.45×10^5	$0.99886^{+0.00009}_{-0.00010}$	$0.00615^{+0.00021}_{-0.00020}$	$0.94896^{+0.00737}_{-0.00844}$	$0.98908^{+0.00351}_{-0.00485}$
CTEQ6L new tune	9.99×10^4	$0.99885^{+0.00011}_{-0.00012}$	$0.00596^{+0.00025}_{-0.00024}$	$0.97299^{+0.00659}_{-0.00837}$	$0.96897^{+0.00716}_{-0.00896}$
CTEQ6LL new tune	9.86×10^4	$1.00055^{+-1.00055}_{-1.00055}$	$0.00613^{+0.00026}_{-0.00025}$	$0.94523^{+0.00924}_{-0.01083}$	$0.99338^{+0.00323}_{-0.00538}$
CTEQ6L no tune	9.96×10^4	$0.99706^{+0.00017}_{-0.00018}$	$0.00546^{+0.00024}_{-0.00023}$	$0.95120^{+0.00923}_{-0.01105}$	$0.97953^{+0.00614}_{-0.00827}$
CTEQ6LL no tune	9.99×10^4	$0.99864^{+0.00012}_{-0.00013}$	$0.00558^{+0.00024}_{-0.00023}$	$0.96614^{+0.00761}_{-0.00947}$	$0.99400^{+0.00315}_{-0.0547}$
CTEQ6L reweight	1.16×10^5	$0.99850^{+0.00011}_{-0.00012}$	$0.00622^{+0.00024}_{-0.00023}$	$0.95230^{+0.00791}_{-0.00926}$	$0.99010^{+0.00368}_{-0.00536}$
CTEQ6LL reweight	1.14×10^5	$0.99844^{+0.00012}_{-0.00013}$	$0.00622^{+0.00024}_{-0.00023}$	$0.95182^{+0.00804}_{-0.00942}$	$0.99026^{+0.00369}_{-0.00542}$

Sample	E_T^{Miss}	$E_T^{LeadJet}$	$\eta^{LeadLep}$	$\eta^{2ndLeadLep}$	H_T
Default	$0.76060^{+0.01495}_{-0.01560}$	$0.95780^{+0.00795}_{-0.00952}$	$0.89758^{+0.01235}_{-0.01374}$	$0.85312^{+0.01529}_{-0.01665}$	$0.63551^{+0.02292}_{-0.02352}$
CTEQ6L new tune	$0.78996^{+0.01746}_{-0.01854}$	$0.94593^{+0.01073}_{-0.01294}$	$0.88097^{+0.01596}_{-0.01790}$	$0.86585^{+0.01794}_{-0.02006}$	$0.61523^{+0.02822}_{-0.02898}$
CTEQ6LL new tune	$0.78201^{+0.01758}_{-0.01861}$	$0.95142^{+0.01017}_{-0.01241}$	$0.92581^{+0.01278}_{-0.01496}$	$0.82425^{+0.01952}_{-0.02127}$	$0.65052^{+0.02742}_{-0.02840}$
CTEQ6L no tune	$0.78575^{+0.01854}_{-0.01972}$	$0.96392^{+0.00929}_{-0.01192}$	$0.89673^{+0.01567}_{-0.01790}$	$0.89572^{+0.01662}_{-0.01911}$	$0.63019^{+0.02853}_{-0.02942}$
CTEQ6LL no tune	$0.82343^{+0.01669}_{-0.01795}$	$0.95283^{+0.01007}_{-0.01233}$	$0.90478^{+0.01441}_{-0.01648}$	$0.88874^{+0.01626}_{-0.01846}$	$0.72055^{+0.02505}_{-0.02643}$
CTEQ6L reweight	$0.76666^{+0.01643}_{-0.01724}$	$0.96097^{+0.00843}_{-0.01038}$	$0.88651^{+0.01425}_{-0.01589}$	$0.85377^{+0.01693}_{-0.01861}$	$0.64017^{+0.02538}_{-0.02615}$
CTEQ6LL reweight	$0.76615^{+0.01665}_{-0.01748}$	$0.96061^{+0.00857}_{-0.01057}$	$0.88730^{+0.01439}_{-0.01607}$	$0.85440^{+0.01711}_{-0.01883}$	$0.63701^{+0.02575}_{-0.02652}$

Sample	N_{Jets}	M_{inv}	$Z-Veto$	Total ϵ
Default	$1.00000^{+0.00000}_{-0.00617}$	$0.99518^{+0.00354}_{-0.00819}$	$0.93256^{+0.01462}_{-0.01787}$	$0.00190^{+0.00012}_{-0.00011}$
CTEQ6L new tune	$1.00000^{+0.00000}_{-0.00929}$	$0.99985^{+0.00015}_{-0.00937}$	$0.93052^{+0.01814}_{-0.02309}$	$0.00183^{+0.00014}_{-0.00013}$
CTEQ6LL new tune	$1.00000^{+0.00000}_{-0.00870}$	$0.98950^{+0.00649}_{-0.01265}$	$0.92338^{+0.01850}_{-0.02306}$	$0.00194^{+0.00015}_{-0.00014}$
CTEQ6L no tune	$1.00000^{+0.00000}_{-0.00942}$	$0.98494^{+0.00826}_{-0.01466}$	$0.94521^{+0.01638}_{-0.02174}$	$0.00181^{+0.00014}_{-0.00013}$
CTEQ6LL no tune	$1.00000^{+0.00000}_{-0.00751}$	$1.00000^{+0.00000}_{-0.00751}$	$0.92540^{+0.01688}_{-0.02077}$	$0.00225^{+0.00016}_{-0.00015}$
CTEQ6L reweight	$1.00000^{+0.00000}_{-0.00750}$	$0.99545^{+0.00364}_{-0.00950}$	$0.93226^{+0.01615}_{-0.02014}$	$0.00194^{+0.00014}_{-0.00013}$
CTEQ6LL reweight	$1.00000^{+0.00000}_{-0.00772}$	$0.99499^{+0.00392}_{-0.00989}$	$0.93248^{+0.01636}_{-0.02047}$	$0.00193^{+0.00014}_{-0.00013}$

Table 7.6.: Event selection efficiency for the samples with the different PDF setups. Events with two same-sign electrons and the optimized event selection cuts are used.

141

Sample	Generated events	Trigger	$\mu^+\mu^+/\mu^-\mu^-$	$P_T^{LeadLep}$	$P_T^{2ndLeadLep}$	E_T^{Miss}
Default	1.45×10^5	$0.99886^{+0.00009}_{-0.00010}$	$0.00870^{+0.00025}_{-0.00024}$	$0.98920^{+0.00287}_{-0.00375}$	$1.00000^{+0.00000}_{-0.00147}$	$0.78935^{+0.01166}_{-0.01213}$
CTEQ6L new tune	9.99×10^4	$0.99885^{+0.00011}_{-0.00012}$	$0.00867^{+0.00030}_{-0.00029}$	$0.99097^{+0.00314}_{-0.00447}$	$1.00000^{+0.00000}_{-0.00214}$	$0.81245^{+0.01346}_{-0.01421}$
CTEQ6LL new tune	9.86×10^4	$1.00055^{+-1.00055}_{-1.00055}$	$0.00900^{+0.00031}_{-0.00030}$	$0.99141^{+0.00302}_{-0.00432}$	$1.00000^{+0.00000}_{-0.00208}$	$0.77726^{+0.01418}_{-0.01483}$
CTEQ6L no tune	9.96×10^4	$0.99706^{+0.00017}_{-0.00018}$	$0.00936^{+0.00031}_{-0.00030}$	$0.99428^{+0.00239}_{-0.00367}$	$1.00000^{+0.00000}_{-0.00198}$	$0.81584^{+0.01286}_{-0.01357}$
CTEQ6LL no tune	9.99×10^4	$0.99864^{+0.00012}_{-0.00013}$	$0.00936^{+0.00031}_{-0.00030}$	$0.99491^{+0.00224}_{-0.00353}$	$1.00000^{+0.00000}_{-0.00197}$	$0.79735^{+0.01332}_{-0.01398}$
CTEQ6L reweight	1.16×10^5	$0.99850^{+0.00011}_{-0.00012}$	$0.00866^{+0.00028}_{-0.00027}$	$0.98946^{+0.00316}_{-0.00427}$	$1.00000^{+0.00000}_{-0.00184}$	$0.78807^{+0.01307}_{-0.01367}$
CTEQ6LL reweight	1.14×10^5	$0.99844^{+0.00012}_{-0.00013}$	$0.00868^{+0.00028}_{-0.00027}$	$0.98946^{+0.00320}_{-0.00434}$	$1.00000^{+0.00000}_{-0.00188}$	$0.78856^{+0.01321}_{-0.01382}$

Sample	H_T	N_{Jets}	M_{inv}	$Z - Veto$	Total ϵ
Default	$0.89045^{+0.01000}_{-0.01083}$	$1.00000^{+0.00000}_{-0.00209}$	$0.99813^{+0.00131}_{-0.00287}$	$0.94161^{+0.00793}_{-0.00901}$	$0.00568^{+0.00020}_{-0.00020}$
CTEQ6L new tune	$0.86593^{+0.01300}_{-0.01410}$	$1.00000^{+0.00000}_{-0.00303}$	$0.99301^{+0.00325}_{-0.00527}$	$0.92880^{+0.01052}_{-0.01206}$	$0.00557^{+0.00024}_{-0.00023}$
CTEQ6LL new tune	$0.93233^{+0.00961}_{-0.01096}$	$1.00000^{+0.00000}_{-0.00287}$	$0.99426^{+0.00285}_{-0.00478}$	$0.93332^{+0.00991}_{-0.01138}$	$0.00600^{+0.00025}_{-0.00024}$
CTEQ6L no tune	$0.91905^{+0.00996}_{-0.01113}$	$1.00000^{+0.00000}_{-0.00264}$	$0.99911^{+0.00082}_{-0.00307}$	$0.90168^{+0.01136}_{-0.01259}$	$0.00627^{+0.00026}_{-0.00025}$
CTEQ6LL no tune	$0.88165^{+0.01194}_{-0.01302}$	$1.00000^{+0.00000}_{-0.00280}$	$0.99674^{+0.00205}_{-0.00407}$	$0.92918^{+0.01007}_{-0.01148}$	$0.00605^{+0.00025}_{-0.00024}$
CTEQ6L reweight	$0.89199^{+0.01113}_{-0.01218}$	$1.00000^{+0.00000}_{-0.00261}$	$0.99819^{+0.00138}_{-0.00340}$	$0.94066^{+0.00893}_{-0.01028}$	$0.00565^{+0.00023}_{-0.00022}$
CTEQ6LL reweight	$0.89155^{+0.01127}_{-0.01234}$	$1.00000^{+0.00000}_{-0.00267}$	$0.99818^{+0.00140}_{-0.00346}$	$0.94067^{+0.00903}_{-0.01041}$	$0.00566^{+0.00023}_{-0.00022}$

Table 7.7.: Event selection efficiency for the samples with the different PDF setups. Events with two same-sign muons and the top event selection cuts are used.

143

Sample	Generated events	Trigger	$\mu^+\mu^+/\mu^-\mu^-$	$P_T^{LeadLep}$	$P_T^{2ndLeadLep}$
Default	1.45×10^5	$0.99886^{+0.00009}_{-0.00010}$	$0.00870^{+0.00025}_{-0.00024}$	$0.90698^{+0.00821}_{-0.00888}$	$0.88996^{+0.00930}_{-0.01001}$
CTEQ6L new tune	9.99×10^4	$0.99885^{+0.00011}_{-0.00012}$	$0.00867^{+0.00030}_{-0.00029}$	$0.90422^{+0.01004}_{-0.01102}$	$0.86663^{+0.01224}_{-0.01321}$
CTEQ6LL new tune	9.86×10^4	$1.00055^{+-1.00055}_{-1.00055}$	$0.00900^{+0.00031}_{-0.00030}$	$0.92764^{+0.00870}_{-0.00972}$	$0.87427^{+0.01162}_{-0.01257}$
CTEQ6L no tune	9.96×10^4	$0.99706^{+0.00017}_{-0.00018}$	$0.00936^{+0.00031}_{-0.00030}$	$0.91854^{+0.00899}_{-0.00994}$	$0.89750^{+0.01042}_{-0.01140}$
CTEQ6LL no tune	9.99×10^4	$0.99864^{+0.00012}_{-0.00013}$	$0.00936^{+0.00031}_{-0.00030}$	$0.91363^{+0.00922}_{-0.01015}$	$0.87732^{+0.01129}_{-0.01222}$
CTEQ6L reweight	1.16×10^5	$0.99850^{+0.00011}_{-0.00012}$	$0.00866^{+0.00028}_{-0.00027}$	$0.90950^{+0.00906}_{-0.00991}$	$0.89132^{+0.01033}_{-0.01122}$
CTEQ6LL reweight	1.14×10^5	$0.99844^{+0.00012}_{-0.00013}$	$0.00868^{+0.00028}_{-0.00027}$	$0.90966^{+0.00916}_{-0.01003}$	$0.89077^{+0.01047}_{-0.01138}$

Sample	E_T^{Miss}	$E_T^{LeadJet}$	$\eta^{LeadLep}$	$\eta^{2ndLeadLep}$	H_T
Default	$0.78163^{+0.01310}_{-0.01367}$	$0.94963^{+0.00775}_{-0.00897}$	$0.86571^{+0.01250}_{-0.01352}$	$0.75785^{+0.01702}_{-0.01784}$	$0.60548^{+0.02262}_{-0.02307}$
CTEQ6L new tune	$0.81621^{+0.01504}_{-0.01601}$	$0.94372^{+0.00979}_{-0.01153}$	$0.88236^{+0.01420}_{-0.01575}$	$0.78732^{+0.01937}_{-0.02068}$	$0.63725^{+0.02605}_{-0.02684}$
CTEQ6LL new tune	$0.77416^{+0.01578}_{-0.01657}$	$0.95092^{+0.00913}_{-0.01089}$	$0.82825^{+0.01657}_{-0.01787}$	$0.75084^{+0.02104}_{-0.02224}$	$0.65255^{+0.02707}_{-0.02804}$
CTEQ6L no tune	$0.81595^{+0.01414}_{-0.01500}$	$0.95950^{+0.00785}_{-0.00946}$	$0.83945^{+0.01514}_{-0.01632}$	$0.76974^{+0.01908}_{-0.02019}$	$0.58568^{+0.02591}_{-0.02637}$
CTEQ6LL notune	$0.78225^{+0.01527}_{-0.01606}$	$0.95775^{+0.00828}_{-0.00999}$	$0.85316^{+0.01509}_{-0.01641}$	$0.77320^{+0.01947}_{-0.02067}$	$0.62801^{+0.02595}_{-0.02667}$
CTEQ6Lreweight	$0.78068^{+0.01465}_{-0.01536}$	$0.94745^{+0.00883}_{-0.01034}$	$0.86228^{+0.01414}_{-0.01540}$	$0.75832^{+0.01909}_{-0.02012}$	$0.61321^{+0.02531}_{-0.02591}$
CTEQ6LL reweight	$0.78118^{+0.01481}_{-0.01554}$	$0.94731^{+0.00893}_{-0.01049}$	$0.86272^{+0.01428}_{-0.01557}$	$0.75803^{+0.01931}_{-0.02036}$	$0.61146^{+0.02562}_{-0.02623}$

Sample	N_{Jets}	M_{inv}	$Z-Veto$	Total ϵ
Default	$1.00000^{+0.00000}_{-0.00610}$	$0.99841^{+0.00153}_{-0.00689}$	$0.97648^{+0.00858}_{-0.01234}$	$0.00202^{+0.00012}_{-0.00012}$
CTEQ6L new tune	$1.00000^{+0.00000}_{-0.00790}$	$1.00000^{+0.00000}_{-0.00790}$	$0.89596^{+0.02025}_{-0.02401}$	$0.00207^{+0.00015}_{-0.00014}$
CTEQ6LL new tune	$1.00000^{+0.00000}_{-0.00848}$	$0.98569^{+0.00766}_{-0.01340}$	$0.94006^{+0.01625}_{-0.02095}$	$0.00202^{+0.00015}_{-0.00014}$
CTEQ6L no tune	$1.00000^{+0.00000}_{-0.00804}$	$1.00000^{+0.00000}_{-0.00804}$	$0.85665^{+0.02360}_{-0.02701}$	$0.00195^{+0.00015}_{-0.00014}$
CTEQ6LL no tune	$1.00000^{+0.00000}_{-0.00786}$	$0.99692^{+0.00278}_{-0.00931}$	$0.92618^{+0.01721}_{-0.02132}$	$0.00215^{+0.00016}_{-0.00015}$
CTEQ6L reweight	$1.00000^{+0.00000}_{-0.00754}$	$0.99821^{+0.00174}_{-0.00844}$	$0.97646^{+0.00950}_{-0.01423}$	$0.00203^{+0.00014}_{-0.00013}$
CTEQ6LL reweight	$1.00000^{+0.00000}_{-0.00773}$	$0.99823^{+0.00173}_{-0.00862}$	$0.97623^{+0.00966}_{-0.01451}$	$0.00203^{+0.00014}_{-0.00013}$

Table 7.8.: Event selection efficiency for the samples with the different PDF setups. Events with two same-sign muons and the optimized event selection cuts are used.

7.2. ISR/FSR uncertainties

A higher FSR and ISR activity leads to more jets, while a lower FSR and ISR activity leads to a lower jet multiplicity. As this is important for the event selection. Monte Carlo samples with varying the ISR and FSR were produced following the ATLAS top group recommendation and with $m(b') = 500\,\text{GeV}$. Also a different start random seed value is used for the production of the several samples together with the Monte Carlo generator filter setup described in chapter 4.1.4. The recommended parameters by the *ATLAS Top group* with the updated parameters for higher and lower ISR and FSR activity are listed in Table 7.9 and 7.10, respectively [76].

Parameter	MC10	Less ISR activity	More ISR activity
PARP(64)	3.0	4.0	0.25
PARP(67)	1.0	0.5	6.0

Table 7.9.: Parameter values for more and less ISR on generator level.

Parameter	MC10	Less FSR activity	More FSR activity
PARP (72)	0.192	0.096	0.384
PARJ (82)	1.0	2.0	0.5

Table 7.10.: Parameter values for more and less FSR on generator level.

In general, the the gluon radiation depends on α_s and varying the scale for α_s changes the ISR activity in Pythia6. For the ISR evolution in Pythia6 the α_s scale is not modified directly, instead the energy scale of the process E is used and multiplied with a factor called PARP(64), which does not have any physical correspondence. Figure 7.5 presents schematically the evolution of α_s as a function of the energy E and with a high value of PARP(64) α_s has a low value. A high α_s value increases the ISR activity, while with a low α_s value the ISR activity decreases.

As introduced in chapter 4.1.1 the ISR evaluation starts at the hard scattering scale with q^2_{max} and ends at the cutoff parameter scale, where q^2_0 is defined. With varying the range between q^2_{max} and q^2_0 the ISR activity can be regulated. It is not recommended to move q^2_0 to lower values, than it is used for suppressing the divergences. Thus, q^2_{max}
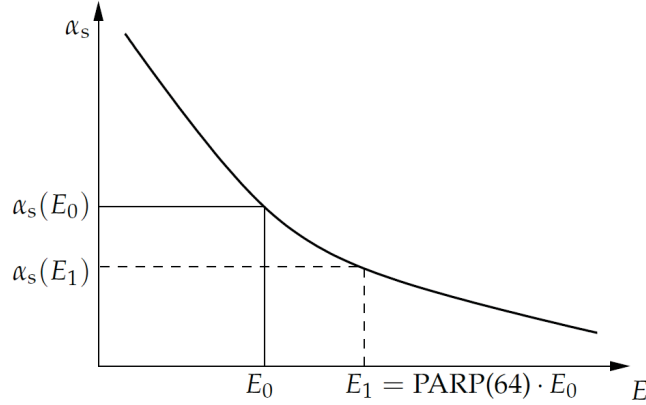
Figure 7.5.: Schematic α_s evolution as a function of the process energy E. In the Pythia6 model the energy is multiplied with the tune parameter PARP(64) for the α_s definition, instead of defining the energy scale directly for the ISR evolution [111].

is used for the regulating the ISR activity. With moving to higher values of q^2_{max} the ISR activity is higher than with a lower values of q^2_{max}. In the Pythia6 model q^2_{max} is multiplied with a factor labeled as PARP(67).

For the uncertainty studies coming from varying the corresponding FSR parameters the upper scale limit, from where the FSR evaluation started, is changed. For this the parameter PARP(72) in Pythia6 is used and is multiplied with q^2_{max} defined by the momentum of radiated gluon or created quark-anti-quark pair by the ISR evolution. A higher value of PARP(72) leads to a higher FSR activity than a smaller value.

The FSR activity in Pythia6 also depends on the invariant mass of the radiating parton and varying the value of the invariant mass changes the FSR activity. This parameter is implemented in Pythia6 in such a way that partons with a lower invariant mass than the defined value are not allowed to radiate. Thus, a low values leads to a high FSR activity, while a high value suppresses the FSR activity. The value of the parameter PARJ(82) represents the invariant mass cut in units of GeV.

In Figure 7.6 the electron and muon multiplicity together with their transverse momentum on generator level are plotted. Due to the generator filter only leptons with $p_T > 10\,\text{GeV}$ and $|\eta| < 2.7$ are selected. Every distribution is scaled to a luminosity of $\mathcal{L} = 2.05\,\text{fb}^{-1}$. It show that varying the values for ISR and FSR does not change the electron and muon multiplicity.

(a) N_{el} (b) p_T^{el}

(c) N_{mu} (d) p_T^{mu}

Figure 7.6.: N_{el} and N_{μ} on generator level together with their transverse momentum (p_T^{el} and p_T^{mu}) scaled to a luminosity of $\mathcal{L} = 2.05\,\text{fb}^{-1}$. There are no requirements for the production channel of the electron and muons. The distributions are presented for the Monte Carlo samples with varied ISR and FSR parameters and the MC10 setup.

In Table 7.11 the event selection efficiencies for applying the top selection criteria and requiring exactly two same-sign electrons in every event are listed. Default stands for the MC10 setup on generator level. In general, the differences between the event selection efficiencies are very small and are within the upper and lower limit of the efficiencies. The small differences for the total event selection efficiencies are caused by applying two same-sign electrons, because the same behavior of the differences are visible there. For the samples "FSR up" and "ISR up" the event selection efficiencies are higher than for the "Default" sample. The samples with "FSR down" and "ISR down" have a lower efficiency with respect to "Default" one. The reason for this are misidentified electrons near the jet, because a higher jet multiplicity leads to a higher number of misidentified electrons and thus a higher event selection efficiency. This is visible in the Figures B.20 and B.21 in the Appendix B. There, the N_{Jets} and the E_T^{Jets} distributions are plotted

with the applied object selection and no event selection criteria. The Figures show, that the jet multiplicity is higher for "ISR up" and "FSR up" than for the other samples. The same behavior between the efficiencies is also visible with the cut on H_T. With removing the overlap removal from the analysis the calculated H_T increases and due to that the event selection efficiencies are for every samples 1.00. In this case the difference between the total event selection efficiencies are the same as with an overlap removal in the analysis. Applying a $\not{E}_T$ cut leads to a higher efficiency for "FSR down" and "ISR down" with respect to "Default". For "FSR up" and "ISR up" the opposite behavior is visible. Higher FSR and ISR activity cause a higher value for $\not{E}_T{}^{CellOut}$, $\not{E}_T{}^{SoftJets}$, or $\not{E}_T{}^{Jets}$ in the event. This leads to a smaller calculated $\not{E}_T$ and a lower event selection efficiency than for the $\not{E}_T$ in the case of "Default".

Table 7.12 presents the event selection efficiencies for events with exactly two same-sign electrons and for the used optimized event selection criteria. The differences between the efficiencies are small and withing the upper and lower limit of the efficiency. For the total event selection efficiencies, the event selection efficiencies for applying same-sign electrons and a cut on the missing transverse energy are same as in Table 7.11, for which the top event selection criteria are used.

The efficiencies for events with two same-sign muons and with the top event selection cuts are listed in Table 7.13. The total event selection efficiencies for "ISR down" is lower than for "Default", while "FSR up", "FSR down" and "ISR up" has a higher total event selection efficiency than "Default". The same behavior is also visible without an overlap removal in the analysis. This is caused by the cut on the transverse momentum of the leading muon. A lower ISR activity leads to more reconstructed muons with a lower transverse momentum and a lower event selection efficiency with respect to "Default". This is supported by Figure B.23, where the the N_{Jets} distribution of "ISR down" has the highest maximum and a high jet multiplicity leads to a high number of misidentified leptons. For "FSR up", "FSR down" and "ISR up" more muons with a higher transverse momentum are reconstructed than for " Default". Using the optimized event selection efficiencies (Table 7.14) for "ISR down" the total event selection efficiency is the same as for "Default", while for the other samples the efficiencies are higher than for "Default" caused by the cut on the transverse momentum of the muon.

In the attachment B the event selection efficiencies for events with one electron and one muon are listed in Table B.3 and Table B.4 for the top event selection criteria and the optimized event selection criteria, respectively. For both event selection criteria the differences between the efficiencies are small and within the upper and lower limit of the efficiencies. Applying the top event selection criteria the total event selection efficiencies

for "ISR up" is higher than for "Default". For "FSR down", "FSR up" and "ISR down" the total event selection efficiencies are smaller than for "Default". The same behavior is visible for selecting events with one electron and one muon with the same-sign. The reason for this is that "ISR up" causes more electrons and muon, which passes the object selection, than "FSR up", "FSR down" and "ISR down". Using the optimized event selection criteria "FSR down", "FSR up" and "ISR up" has a higher total event selection efficiency than "Default", while for "ISR down" the efficiency is lower than "Default" caused by the same reason as in Table B.3. Figure B.26 in the Appendix shows the N_{Jets} distribution for events with one electron ane muon with the same-sign.

Sample	Generated events	Trigger	e^+e^+/e^-e^-	$P_T^{LeadLep}$	$P_T^{2ndLeadLep}$	E_T^{Miss}
Default	$1.45 \times 10^5 \pm 380$	$1.00000^{+0.00000}_{-0.00001}$	$0.00760^{+0.00023}_{-0.00023}$	$1.00000^{+0.00000}_{-0.00166}$	$1.00000^{+0.00000}_{-0.00166}$	$0.91000^{+0.00865}_{-0.00943}$
FSR down	$4.99 \times 10^4 \pm 223$	$1.00000^{+-1.00000}_{-1.00000}$	$0.00731^{+0.00040}_{-0.00038}$	$1.00000^{+0.00000}_{-0.00501}$	$1.00000^{+0.00000}_{-0.00501}$	$0.91781^{+0.01443}_{-0.01692}$
FSR up	$4.99 \times 10^4 \pm 223$	$1.00000^{+0.00000}_{-0.00004}$	$0.00809^{+0.00042}_{-0.00040}$	$1.00000^{+0.00000}_{-0.00453}$	$1.00000^{+0.00000}_{-0.00453}$	$0.91337^{+0.01406}_{-0.01626}$
ISR down	$4.99 \times 10^4 \pm 223$	$1.00000^{+-1.00000}_{-1.00000}$	$0.00737^{+0.00040}_{-0.00038}$	$1.00000^{+0.00000}_{-0.00497}$	$1.00000^{+0.00000}_{-0.00497}$	$0.92391^{+0.01386}_{-0.01637}$
ISR up	$4.99 \times 10^4 \pm 223$	$1.00000^{+-1.00000}_{-1.00000}$	$0.00827^{+0.00042}_{-0.00040}$	$1.00000^{+0.00000}_{-0.00443}$	$1.00000^{+0.00000}_{-0.00443}$	$0.90073^{+0.01480}_{-0.01688}$

Sample	H_T	N_{Jets}	M_{inv}	$Z - Veto$	Total ϵ
Default	$0.99201^{+0.00275}_{-0.00390}$	$0.99799^{+0.00130}_{-0.00264}$	$0.99697^{+0.00164}_{-0.00292}$	$0.95850^{+0.00633}_{-0.00732}$	$0.00654^{+0.00022}_{-0.00021}$
FSR down	$0.99403^{+0.00384}_{-0.00778}$	$1.00000^{+0.00000}_{-0.00549}$	$1.00000^{+0.00000}_{-0.00549}$	$0.95796^{+0.01092}_{-0.01402}$	$0.00639^{+0.00037}_{-0.00035}$
FSR up	$0.99729^{+0.00224}_{-0.00617}$	$1.00000^{+0.00000}_{-0.00497}$	$0.99728^{+0.00224}_{-0.00619}$	$0.95913^{+0.01027}_{-0.01307}$	$0.00705^{+0.00039}_{-0.00037}$
ISR down	$0.98529^{+0.00631}_{-0.00978}$	$1.00000^{+0.00000}_{-0.00546}$	$1.00000^{+0.00000}_{-0.00546}$	$0.94627^{+0.01229}_{-0.01525}$	$0.00635^{+0.00037}_{-0.00035}$
ISR up	$0.99462^{+0.00346}_{-0.00701}$	$1.00000^{+0.00000}_{-0.00494}$	$0.99730^{+0.00223}_{-0.00616}$	$0.94580^{+0.01176}_{-0.01443}$	$0.00699^{+0.00039}_{-0.00037}$

Table 7.11.: Event selection efficiency for the samples with the different ISR/FSR setups. Events with two same-sign electrons and the top event selection cuts are used.

Sample	Generated events	Trigger	e^+e^-/e^-e^-	$P_T^{LeadLep}$	$P_T^{2ndLeadLep}$
Default	1.45×10^5	$1.00000^{+0.00000}_{-0.00001}$	$0.00760^{+0.00023}_{-0.00023}$	$0.98000^{+0.00418}_{-0.00514}$	$0.99722^{+0.00151}_{-0.00269}$
FSR down	4.99×10^4	$1.00000^{+-1.00000}_{-1.00000}$	$0.00731^{+0.00040}_{-0.00038}$	$0.97808^{+0.00752}_{-0.01058}$	$0.99440^{+0.00361}_{-0.00731}$
FSR up	4.99×10^4	$1.00000^{+0.00000}_{-0.00004}$	$0.00809^{+0.00042}_{-0.00040}$	$0.98762^{+0.00531}_{-0.00824}$	$0.99749^{+0.00207}_{-0.00571}$
ISR down	4.99×10^4	$1.00000^{+-1.00000}_{-1.00000}$	$0.00737^{+0.00040}_{-0.00038}$	$0.98641^{+0.00583}_{-0.00904}$	$0.99449^{+0.00355}_{-0.00719}$
ISR up	4.99×10^4	$1.00000^{+-1.00000}_{-1.00000}$	$0.00827^{+0.00042}_{-0.00040}$	$0.98305^{+0.00620}_{-0.00896}$	$0.99507^{+0.00317}_{-0.00643}$

Sample	E_T^{Miss}	$E_T^{LeadJet}$	$\eta^{LeadLep}$	$\eta^{2ndLeadLep}$	H_T
Default	$0.90884^{+0.00880}_{-0.00959}$	$0.98874^{+0.00332}_{-0.00446}$	$0.91615^{+0.00894}_{-0.00984}$	$0.90169^{+0.01004}_{-0.01099}$	$0.92982^{+0.00905}_{-0.01019}$
FSR down	$0.91549^{+0.01482}_{-0.01737}$	$0.99692^{+0.00254}_{-0.00701}$	$0.88889^{+0.01761}_{-0.02020}$	$0.89583^{+0.01814}_{-0.02113}$	$0.94574^{+0.01405}_{-0.01794}$
FSR up	$0.91206^{+0.01426}_{-0.01649}$	$0.98898^{+0.00525}_{-0.00858}$	$0.94708^{+0.01179}_{-0.01455}$	$0.87941^{+0.01783}_{-0.02022}$	$0.95652^{+0.01171}_{-0.01517}$
ISR down	$0.92244^{+0.01412}_{-0.01667}$	$0.98198^{+0.00710}_{-0.01055}$	$0.87768^{+0.01830}_{-0.02078}$	$0.87456^{+0.01976}_{-0.02258}$	$0.90837^{+0.01832}_{-0.02189}$
ISR up	$0.89851^{+0.01512}_{-0.01724}$	$0.98898^{+0.00525}_{-0.00858}$	$0.93872^{+0.01265}_{-0.01534}$	$0.85460^{+0.01944}_{-0.02169}$	$0.92708^{+0.01535}_{-0.01862}$

Sample	N_{Jets}	M_{inv}	$Z - Veto$	Total ϵ
Default	$0.99865^{+0.00111}_{-0.00308}$	$0.99730^{+0.00174}_{-0.00353}$	$0.95940^{+0.00723}_{-0.00858}$	$0.00490^{+0.00019}_{-0.00018}$
FSR down	$1.00000^{+0.00000}_{-0.00748}$	$1.00000^{+0.00000}_{-0.00748}$	$0.97131^{+0.01048}_{-0.01503}$	$0.00475^{+0.00033}_{-0.00031}$
FSR up	$1.00000^{+0.00000}_{-0.00639}$	$0.99650^{+0.00289}_{-0.00796}$	$0.95789^{+0.01180}_{-0.01545}$	$0.00547^{+0.00035}_{-0.00033}$
ISR down	$1.00000^{+0.00000}_{-0.00801}$	$1.00000^{+0.00000}_{-0.00801}$	$0.93860^{+0.01587}_{-0.02020}$	$0.00429^{+0.00031}_{-0.00029}$
ISR up	$1.00000^{+0.00000}_{-0.00684}$	$1.00000^{+0.00000}_{-0.00684}$	$0.93258^{+0.01535}_{-0.01895}$	$0.00499^{+0.00033}_{-0.00031}$

Table 7.12.: Event selection efficiency for the samples with the different ISR/FSR setups. Events with two same-sign electrons and the optimized event selection cuts are used.

Sample	Generated events	Trigger	$\mu^+\mu^+/\mu^-\mu^-$	$P_T^{LeadLep}$	$P_T^{2ndLeadLep}$	E_T^{Miss}
Default	1.45×10^5	$1.00000^{+0.00000}_{-0.00001}$	$0.00967^{+0.00026}_{-0.00026}$	$0.99786^{+0.00116}_{-0.00207}$	$1.00000^{+0.00000}_{-0.00131}$	$0.90688^{+0.00779}_{-0.00840}$
FSR down	4.99×10^4	$1.00000^{+-1.00000}_{-1.00000}$	$0.01082^{+0.00048}_{-0.00046}$	$0.99815^{+0.00153}_{-0.00423}$	$1.00000^{+0.00000}_{-0.00339}$	$0.90167^{+0.01289}_{-0.01448}$
FSR up	4.99×10^4	$1.00000^{+0.00000}_{-0.00004}$	$0.00992^{+0.00046}_{-0.00044}$	$0.99798^{+0.00167}_{-0.00461}$	$1.00000^{+0.00000}_{-0.00370}$	$0.90688^{+0.01314}_{-0.01490}$
ISR down	4.99×10^4	$1.00000^{+-1.00000}_{-1.00000}$	$0.00992^{+0.00046}_{-0.00044}$	$0.99596^{+0.00260}_{-0.00528}$	$1.00000^{+0.00000}_{-0.00371}$	$0.89249^{+0.01404}_{-0.01573}$
ISR up	4.99×10^4	$1.00000^{+-1.00000}_{-1.00000}$	$0.01066^{+0.00048}_{-0.00046}$	$0.99248^{+0.00358}_{-0.00588}$	$1.00000^{+0.00000}_{-0.00346}$	$0.90152^{+0.01303}_{-0.01465}$

Sample	H_T	N_{Jets}	M_{inv}	$Z-Veto$	Total ϵ
Default	$0.97314^{+0.00452}_{-0.00532}$	$1.00000^{+0.00000}_{-0.00149}$	$0.99838^{+0.00105}_{-0.00213}$	$0.94390^{+0.00655}_{-0.00732}$	$0.00802^{+0.00024}_{-0.00023}$
FSR down	$0.95885^{+0.00897}_{-0.01105}$	$1.00000^{+0.00000}_{-0.00392}$	$1.00000^{+0.00000}_{-0.00392}$	$0.95708^{+0.00935}_{-0.01151}$	$0.00894^{+0.00044}_{-0.00042}$
FSR up	$0.97991^{+0.00651}_{-0.00899}$	$1.00000^{+0.00000}_{-0.00417}$	$1.00000^{+0.00000}_{-0.00417}$	$0.96355^{+0.00888}_{-0.01124}$	$0.00847^{+0.00043}_{-0.00041}$
ISR down	$0.96364^{+0.00886}_{-0.01122}$	$1.00000^{+0.00000}_{-0.00431}$	$0.99292^{+0.00383}_{-0.00680}$	$0.93587^{+0.01195}_{-0.01420}$	$0.00790^{+0.00041}_{-0.00039}$
ISR up	$0.97689^{+0.00679}_{-0.00908}$	$1.00000^{+0.00000}_{-0.00393}$	$0.99785^{+0.00178}_{-0.00490}$	$0.94828^{+0.01026}_{-0.01238}$	$0.00882^{+0.00044}_{-0.00042}$

Table 7.13.: Event selection efficiency for the samples with the different ISR/FSR setups. Events with two same-sign muons and the top event selection cuts are used.

Sample	Generated events	Trigger	$\mu^+\mu^+/\mu^-\mu^-$	$P_T^{LeadLep}$	$P_T^{2ndLeadLep}$
Default	1.45×10^5	$1.00000^{+0.00000}_{-0.00001}$	$0.00967^{+0.00026}_{-0.00026}$	$0.94996^{+0.00582}_{-0.00650}$	$0.87810^{+0.00901}_{-0.00959}$
FSR down	4.99×10^4	$1.00000^{+-1.00000}_{-1.00000}$	$0.01082^{+0.00048}_{-0.00046}$	$0.95185^{+0.00919}_{-0.01102}$	$0.88911^{+0.01394}_{-0.01555}$
FSR up	4.99×10^4	$1.00000^{+0.00000}_{-0.00004}$	$0.00992^{+0.00046}_{-0.00044}$	$0.95354^{+0.00943}_{-0.01144}$	$0.88983^{+0.01451}_{-0.01627}$
ISR down	4.99×10^4	$1.00000^{+-1.00000}_{-1.00000}$	$0.00992^{+0.00046}_{-0.00044}$	$0.94141^{+0.01055}_{-0.01249}$	$0.90129^{+0.01389}_{-0.01573}$
ISR up	4.99×10^4	$1.00000^{+-1.00000}_{-1.00000}$	$0.01066^{+0.00048}_{-0.00046}$	$0.95301^{+0.00915}_{-0.01101}$	$0.87179^{+0.01497}_{-0.01652}$

Sample	E_T^{Miss}	$E_T^{LeadJet}$	$\eta^{LeadLep}$	$\eta^{2ndLeadLep}$	H_T
Default	$0.90146^{+0.00875}_{-0.00946}$	$0.98669^{+0.00349}_{-0.00453}$	$0.85838^{+0.01088}_{-0.01160}$	$0.78900^{+0.01381}_{-0.01448}$	$0.90896^{+0.01089}_{-0.01212}$
FSR down	$0.90372^{+0.01387}_{-0.01576}$	$0.98547^{+0.00572}_{-0.00853}$	$0.86486^{+0.01712}_{-0.01903}$	$0.84659^{+0.01946}_{-0.02156}$	$0.91275^{+0.01643}_{-0.01945}$
FSR up	$0.90238^{+0.01457}_{-0.01662}$	$0.98945^{+0.00503}_{-0.00823}$	$0.85333^{+0.01849}_{-0.02049}$	$0.81250^{+0.02220}_{-0.02427}$	$0.92308^{+0.01657}_{-0.02017}$
ISR down	$0.87857^{+0.01607}_{-0.01800}$	$0.99187^{+0.00441}_{-0.00781}$	$0.86066^{+0.01831}_{-0.02041}$	$0.79365^{+0.02325}_{-0.02522}$	$0.90400^{+0.01876}_{-0.02230}$
ISR up	$0.89367^{+0.01476}_{-0.01666}$	$0.98987^{+0.00482}_{-0.00789}$	$0.86189^{+0.01764}_{-0.01961}$	$0.78338^{+0.02288}_{-0.02466}$	$0.90530^{+0.01814}_{-0.02150}$

Sample	N_{Jets}	M_{inv}	$Z-Veto$	Total ϵ
Default	$1.00000^{+0.00000}_{-0.00286}$	$1.00000^{+0.00000}_{-0.00286}$	$0.93584^{+0.00970}_{-0.01116}$	$0.00413^{+0.00017}_{-0.00017}$
FSR down	$1.00000^{+0.00000}_{-0.00671}$	$1.00000^{+0.00000}_{-0.00671}$	$0.95588^{+0.01236}_{-0.01617}$	$0.00521^{+0.00034}_{-0.00032}$
FSR up	$1.00000^{+0.00000}_{-0.00761}$	$1.00000^{+0.00000}_{-0.00761}$	$0.95833^{+0.01277}_{-0.01716}$	$0.00461^{+0.00032}_{-0.00030}$
ISR down	$1.00000^{+0.00000}_{-0.00808}$	$0.99558^{+0.00365}_{-0.01005}$	$0.92889^{+0.01715}_{-0.02141}$	$0.00419^{+0.00031}_{-0.00029}$
ISR up	$1.00000^{+0.00000}_{-0.00764}$	$1.00000^{+0.00000}_{-0.00764}$	$0.96653^{+0.01145}_{-0.01601}$	$0.00463^{+0.00032}_{-0.00030}$

Table 7.14.: Event selection efficiency for the samples with the different ISR/FSR setups. Events with two same-sign muons and the optimized event selection cuts are used.

8. Signal extraction and mass limit calculation

The signal is extracted in events with two same-sign leptons by a simple counting method developed in this master thesis [20]. With the extracted signal events a lower mass limit for the down-type fourth generation quark can be determined. In this chapter, the counting method is introduced briefly together with the method for the limit calculation as well.

8.1. Counting Analysis

For the extraction of the signal events in the signal region (SR) of two same-sing leptons with the counting method a distribution with a significant difference between the signal and the background needs to be chosen. Therefore, the distribution N_{Jets} is a good candidate. The counting method counts all observed data events, $N_{Data}^{Obs,\ SR}$, in the signal region and subtracts then the sum of all Monte Carlo background events $N_{MC}^{BG,\ SR}$. Finally, the remaining events N_{Sig} should be the number of measured signal events in the signal region:

$$N_{Sig} = N_{Data}^{Obs,\ SR} - N_{MC}^{BG,\ SR} \ . \tag{8.1}$$

However, equation (8.1) provides only an unbiased result if the background is well estimated. For this the background needs to be controlled. In the first step, the counted number of events of a Monte Carlo sample i with the integrated luminosity L_i is rescaled to the collected data luminosity L^* via:

$$w_i = \frac{L^*}{L_i} = \frac{\sigma_i}{N_i} \cdot L^* \tag{8.2}$$

with N_i being the total number of events in the sample and σ_i being the used cross section for the corresponding Monte Carlo process. For example, if the used cross section is not equal to the one in nature then the weight w_i is over- or underestimated by a factor c and changes to w_i/c. Therefore, the Monte Carlo estimation needs to be corrected by a

scaling factor R_i taken from data with the assumption $c \approx R_i$:

$$\frac{w_i}{c} \rightarrow \frac{w_i}{c} \cdot R_i \tag{8.3}$$

R_i is determined from the ratio of the measured data and the generated Monte Carlo events to correct the contribution from the background i:

$$R_i = \frac{N_{Data}}{N_{MC,i}}. \tag{8.4}$$

This is done in a region, where the corresponding background i is dominant.

Figure 6.27, 6.28 and A.17 (Appendix A) shows the N_{Jets} distribution for events with the lepton category e^+e^+/e^-e^-, $e^+\mu^+/e^-\mu^-$ and $\mu^+\mu^+/\mu^-\mu^-$ with the data of the egamma and muons stream, respectively. The background process $t\bar{t} + jets$ contributes in every histogram, while $Z \rightarrow e^+e^-$ is only significant visible in the histogram of the lepton category e^+e^+/e^-e^- with the top event selection criteria. Thus, only $t\bar{t}+jets$ and $Z \rightarrow e^+e^-$ are corrected and both background processes can be measured in a control region. For the correction of $t\bar{t}+jets$ the lepton region $e^+\mu^-/e^-\mu^+$ is used and with the lepton category e^+e^- the process $Z \rightarrow e^+e^-$ is corrected. Other background processes are not controlled and therefore are combined in the category "other".

To obtain the correction factor in equation 8.4 via comparing the measured data with the Monte Carlo prediction in the corresponding control region (CR) equation 8.1 needs to be modified to the form

$$N_{Sig} = N_{Data}^{Obs,SR} - \sum_i \left(N_{MC,i}^{BG,SR} \cdot R_i \right) - \sum_{i_{other}} N_{BG,MC}, i_{other}^{SR} \tag{8.5}$$

and the correction factor R_i is as follows:

$$R_i = \frac{N_{Data}^{CR,i}}{N_{MC,i}^{CR,i}} \tag{8.6}$$

calculated in the corresponding control region. The background summation is done for the sum over the controlled backgrounds i. The index i_{other} contains all other background processes.

The N_{Jets} distributions for the lepton categories e^+e^- (Figure 6.18) and $e^+\mu^-/e^-\mu^+$ (Figure 6.23) also show contributions from other background processes and the signal in this control regions. Due to that these contributions have to be taken into account for the calculation of the correction factor R_i. This is done by a subtraction of these

additional background processes and the signal. This estimation needs to be controlled as well and leads to an iterative procedure of the calculation. Thus, for the first iteration step equation (8.5) is applied for the calculation of the number of signal events together with the control ratios R_i. Then in the following iteration steps k, the correction factors are obtained using

$$R_i^k = \frac{N_{Data}^{CR,i} - \sum_{m \neq i} R_m^{k-1} \cdot N_{MC,m}^{CR}}{N_{MC,i}^{CR,i}} \ ,$$
(8.7)

with the ratios R_i^{k-1} of the previous iteration step, $k-1$. The index $m \neq i$ stands for the summation over all samples except the process for the correction. Due to the additional subtraction of the signal in the control region the correction factor R_i^k is calculated also in the signal region. The final equation for the determination of the number of signal events in the iteration step k is as follows

$$N_{Sig}^k = N_{Data}^{Obs,SR} - \sum_i \left(N_{MC,i}^{BG,SR} \cdot \frac{N_{Data}^{CR,i} - \sum_{m \neq i} R_m^{k-1} \cdot N_{MC,m}^{CR}}{N_{MC,i}^{CR,i}} \right) - \sum_{i_{other}} N_{MC,i_{other}}^{BG,SR}$$
(8.8)

In Table 8.1 the counted yields of the background processes without any correction are listed with the applied top event selection criteria with the data of the egamma and muons stream. For the counting method ten iteration steps are used. Figure 8.1 shows the scale factors for every iteration for the dominant background process ($t\bar{t}$ and $Z \to e^+e^-$) in the signal regions. The ratio for $Z \to e^+e^-$ are shown only for the lepton category e^+e^+/e^-e^- due to it being the only contribution in this category. At the iteration step zero the values are small and fluctuate around the final value with the second or third step. Then with the third or fourth iteration the method converges. The final extracted yields are listed in Table 8.2 together with the number of observed events. Here, the signal sample with a b' mass of $m_{b'} = 400\,\mathrm{GeV}$ is used. The extracted yields with other masses of the b' are listed in Appendix C. The corrected values of the background are higher than for the values in Table 8.1 caused by an underestimation of the Monte Carlo contribution in the signal region. The higher value of the expected signal yields in comparison to the final signal yields shows that more events are expected than measured.

Using the optimized event selection criteria the counted background yields are listed Table 8.3. The control ratios are plotted in Figure 8.2 and the extracted yields are presented in Table 8.4. The control ratios are smaller than one caused by an overestimation of the background contribution in the signal region. Also with the applied optimized event selection more signal events are expected than measured.

8. Signal extraction and mass limit calculation

For the ratios and the yields in Table 8.2 and 8.4 no errors are determined because the errors are not applied for the mass limit calculation (see chapter 8.2). A possible way for the error calculation is described in [20].
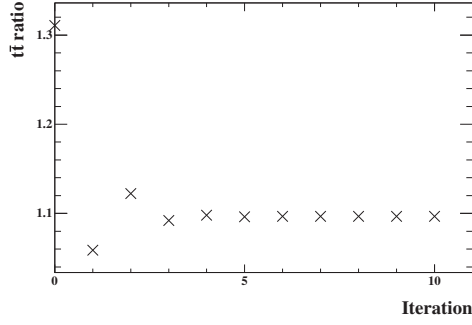
(a) $t\bar{t}$ ratios, e^+e^+/e^-e^-, Egamma stream.
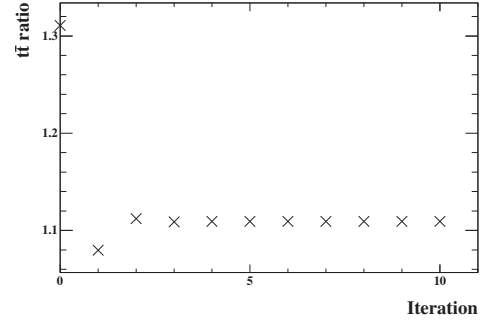
(b) $t\bar{t}$ ratios, $e^+\mu^+/e^-\mu^-$, Egamma stream.
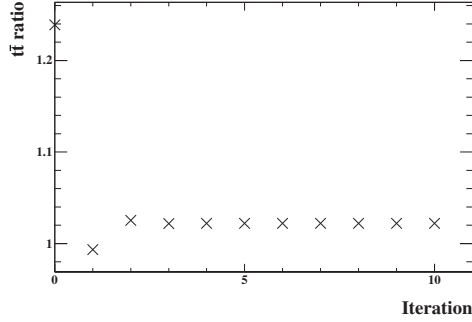
(c) $t\bar{t}$ ratios, $e^+\mu^+/e^-\mu^-$, Muons stream.
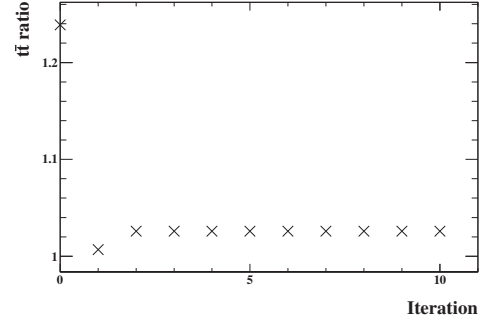
(d) $t\bar{t}$ ratios, $\mu^+\mu^+/\mu^-\mu^-$, Muons stream.
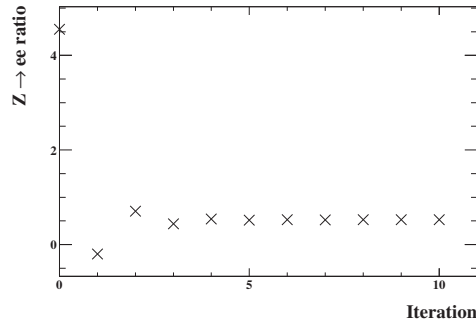
(e) $Z \to e^+e^-$ ratios, $e^+e'+e^-e^-$, Egamma stream.

Figure 8.1.: Control ratios depending on the iteration step for the different lepton categories with the egamma and the muons stream. The top event selection is applied.

162
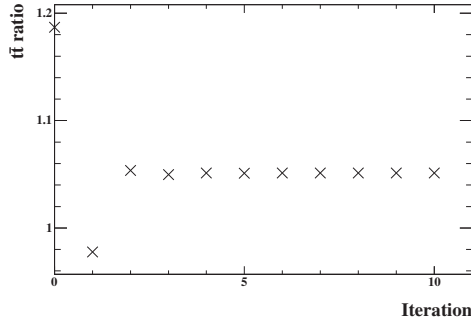
(a) $t\bar{t}$ ratios, $e^+\mu^+/e^-\mu^-$, Egamma stream.
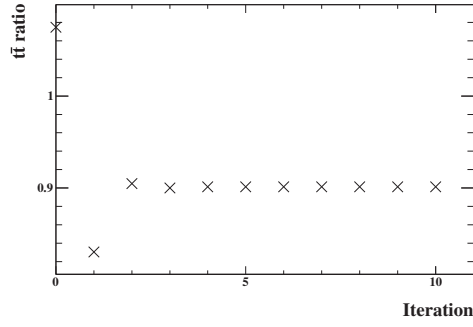
(b) $t\bar{t}$ ratios, $e^+\mu^+/e^-\mu^-$, Muons stream.
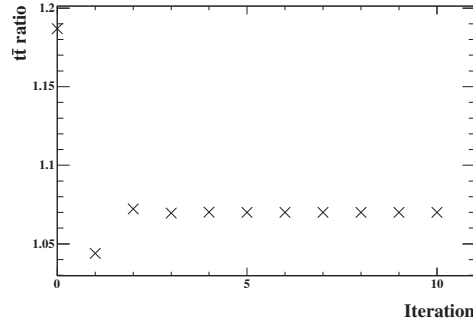
(c) $t\bar{t}$ ratios, e^+e^+/e^-e^-, Egamma stream.

Figure 8.2.: Control ratios depending on the iteration step for the different lepton categories with the egamma and the muons stream. The optimized event selection is applied.

	e^+e^+/e^-e^-	$e^+\mu^+/e^-\mu^-$	$e^+\mu^+/e^-\mu^-$	$mu^+\mu^+/mu^-\mu^-$
	Egamma stream		Muons stream	
Observed	8	14		6
$Z \to e^+e^-$	0.589314	0	0	0
$t\bar{t}$	1.78086	3.57763	2.81857	0
Other BG	1.82883	3.81874	2.91497	2.74957

Table 8.1.: Counted events of the dominated background in the signal region. The data of the egamma and muons stream are used separately and the top event selection criteria are applied.

	e^+e^+/e^-e^-	$e^+\mu^+/e^-\mu^-$	$e^+\mu^+/e^-\mu^-$	$mu^+\mu^+/mu^-\mu^-$
	Egamma stream		Muons stream	
Observed	8	14		6
$Z \to e^+e^-$	0.308712	0	0	0
$t\bar{t}$	1.953	3.96859	2.88094	0
Other BG	1.82883	3.81874	2.91497	2.74957
Final signal yields	3.90946	6.21266	5.20409	3.25043
Expected signal yields	10.955	26.7219	20.9909	15.3614

Table 8.2.: Measured events and determined final and expected signal yields in the dominated background in the signal region. The data of the egamma and muons stream are used separately and the top event selection criteria are applied. For the signal a b mass of $m_{b'} = 400\,\text{GeV}$ is used.

	e^+e^+/e^-e^-	$e^+\mu^+/e^-\mu^-$	$e^+\mu^+/e^-\mu^-$
		Egamma stream	Muons stream
Observed	1	3	3
$Z \to e^+e^-$	0	0	0
$t\bar{t}$	0.603296	1.29812	1.03722
Other BG	0.230059	0.0162672	-0.00552478

Table 8.3.: Counted events of the dominated background in the signal region. The data of the egamma and muons stream are used separately and the optimized event selection criteria are applied.

	e^+e^+/e^-e^-	$e^+\mu^+/e^-\mu^-$	$e^+\mu^+/e^-\mu^-$
		Egamma stream	Muons stream
Observed	1	3	3
$Z \to e^+e^-$	0	0	0
$t\bar{t}$	0.611614	1.29124	0.928771
Other BG	0.230059	0.0162672	-0.00552478
Final signal yields	0.158327	1.69249	2.07675
Expected signal yields	7.14418	15.5235	11.6977

Table 8.4.: Measured events and determined final and expected signal yields in the dominated background in the signal region. The data of the egamma and muons stream are used separately and the optimized event selection criteria are applied. For the signal a b mass of $m_{b'} = 400\,\text{GeV}$ is used.

8.2. Limit

With the extracted numbers of background, signal and observed events the lower mass limit of the b' can be determined. For this the modified frequentist method (or called CL_S method) [112] is used. This method is recommended by the *ATLAS Statistics Group* [97] and is optimal for excluding a signal even with an insufficient sensitivity. The CL_s method is based on a log-likelihood ratio (LLR), which is defined as a ratio of the probabilities p of a given experimental result with two alternative hypotheses: H_0 and H_1, and is given by [113]:

$$LLR = -2 \ln \frac{p(data|H_1)}{p(data|H_0)} \; . \tag{8.9}$$

H_1 is the test hypothesis, which describes the presence of the Standard Model background together with a signal of a fourth generation quark. H_0 is for the null hypothesis describing the Standard Model background without a signal. For both hypothesis the probability calculation is based on a best-fit value and uses a Poisson probability of observing the data multiplied by a Gaussian prior. This is done for each pseudo-experiment. With the CL_s method two p-values are calculated: CL_{s+b} and CL_b and are defined as follows:

$$1 - CL_b = p(LLR \leq LLR_{obs}|H_0) \; , \tag{8.10}$$

$$CL_{s+b} = p(LLR \geq LLR_{obs}|H_1) \; . \tag{8.11}$$

Observing signal and background without the presence of a signal is defined by the probability $1 - CL_b$ and is calculated with a value of a test statistic LLR_{obs} with usage of the data. The probability $1 - CL_b$ is determined as the upward fluctuation of the background, which is the signal-plus-background response as observed in data. CL_b itself can be seen as the confidence level for the background-only hypothesis. CL_{s+b} describe the downward fluctuation of the sum of the background together with the signal in data. In the case of no signal in data it is still possible to get a downward fluctuation. CL_{s+b} can also have small values even if it is difficult to test the results with the experiment. For a low sensitivity of the signal, the following equation is used:

$$CL_s = \frac{CL_{s+b}}{CL_b} \; . \tag{8.12}$$

From the frequentist point of view a mistake is being made at the rate of $5\,\%$ even

if there is no sensitivity for the experiment and the signal is excluded. Thus, the uncertainties of the exclusion potential of CL_{s+b} is $5\,\%$ even for very small signal rates. In this case CL_s is determined as $CL_s < 0.05$ for H_1 and this hypothesis is defined as excluded at $95\,\%$ confidence level.

Based on the CL_s method the final mass limits are calculated with the "MC Limits" tool [114] recommended by the *ATLAS Statistics Group* [97]. For this, the yields in the tables 8.2 - 8.4 and C.1 - C.12) are used. Figures 8.3 - 8.6 show the calculated values for the expected and observed limit at $95\,\%$ confidence level as a function of the b' mass, for every lepton category separately. For the limit calculation a branching ratio of $100\,\%$ for the decay $b' \to t + W$ is assumed. This limit is calculated with 5000 pseudo-experiments with variations in the model to account for the uncertainties. In this case only the uncertainty from the luminosity is used, which is $3.7\,\%$. Then the green and the yellow band represent the 1σ (yellow) and 2σ (green) range of the expected limit. The observed limit is measured with the data. In general, the observed limit should be inside the range of 1σ and 2σ, which demonstrates an agreement of the data with the Standard Model. In every histogram the observed limit is higher than the expected limit and shows a worse limit than expected due to a high fluctuation in the data. The point where the observed limit curve cross the line at $\sigma/\sigma_{SM} = 1$ defines the observed lower bound of the b' mass. $\sigma/\sigma_{SM} = 1$ implies the identification of one b' at $95\,\%$ confidence level. The final expected and observed mass limits in every lepton category are listed in Table 8.5 and 8.6, respectively. The highest observed mass limit is $461.161\,\text{GeV}$ for the category $e^+ \mu^+ / e^- \mu^-$ applying the optimized cut values, while the expected mass limit is $505.241\,\text{GeV}$. In general, an improvement of the limits is visible with the optimized selection criteria especially in the case of the egamma stream.
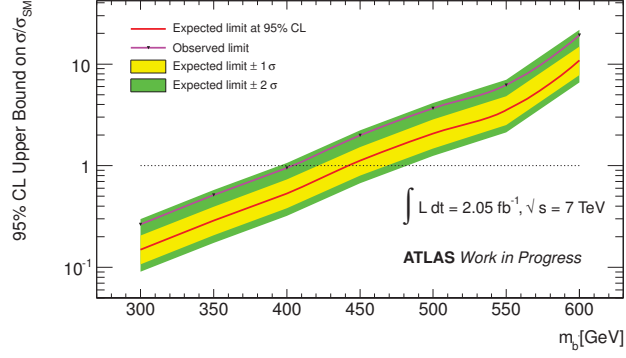
(a) e^+e^+/e^-e^-
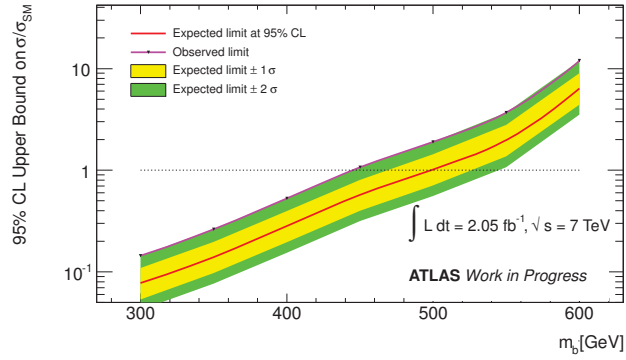
(b) $e^+\mu^+/e^-\mu^-$

Figure 8.3.: Expected and observed mass limit as a function of the b' mass. The green and the yellow band represent the 1σ (yellow) and 2σ (green) range of the expected limit. The point where the expected limit curve cross the line at $\sigma/\sigma_{SM} = 1$ defines the observed mass limit of the b'. The top event selection are applied for the lepton categories e^+e^+/e^-e^- and $e^+\mu^+/e^-\mu^-$. The data from the egamma stream is used.
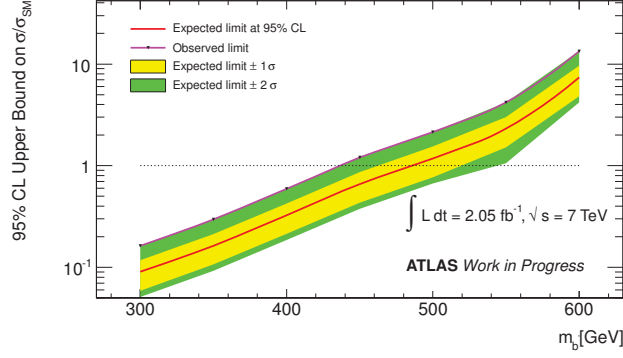
(a) $e^+\mu^+/e^-\mu^-$
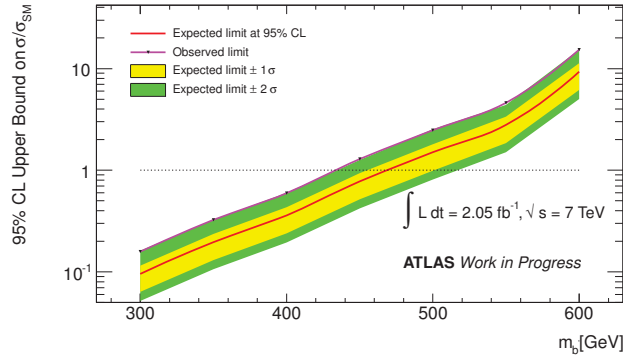
(b) $\mu^+\mu^+/\mu^-\mu^-$

Figure 8.4.: Expected and observed mass limit as a function of the b' mass. The green and the yellow band represent the 1σ (yellow) and 2σ (green) range of the expected limit. The point where the expected limit curve cross the line at $\sigma/\sigma_{SM} = 1$ defines the observed mass limit of the b'. The top event selection are applied for the lepton categories $\mu^+\mu^+/\mu^-\mu^-$ and $e^+\mu^+/e^-\mu^-$. The data from the muons stream is used.
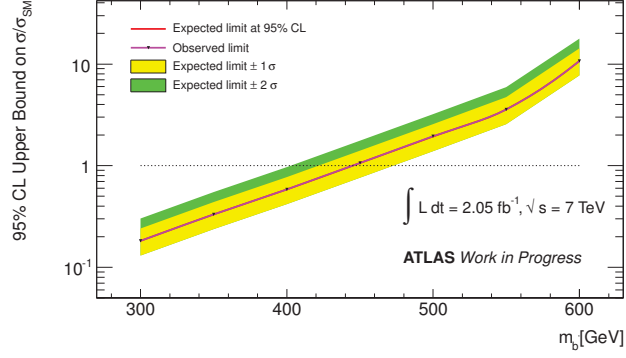
(a) e^+e^+/e^-e^-
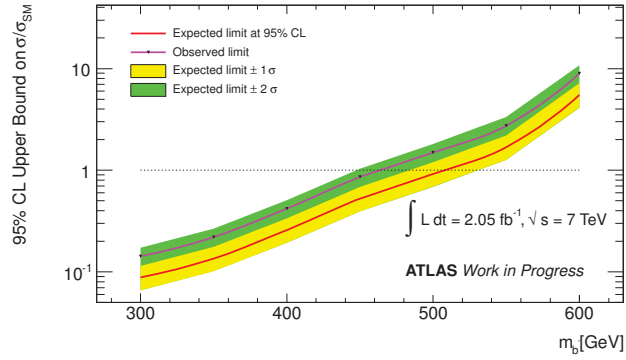
(b) e^+e^+/e^-e^-

Figure 8.5.: Expected and observed mass limit as a function of the b' mass. The green and the yellow band represent the 1σ (yellow) and 2σ (green) range of the expected limit. The point where the expected limit curve cross the line at $\sigma/\sigma_{SM} = 1$ defines the observed mass limit of the b'. The optimized event selection are applied for the lepton categories e^+e^+/e^-e^- and $e^+\mu^+/e^-\mu^-$. The data from the egamma stream is used.
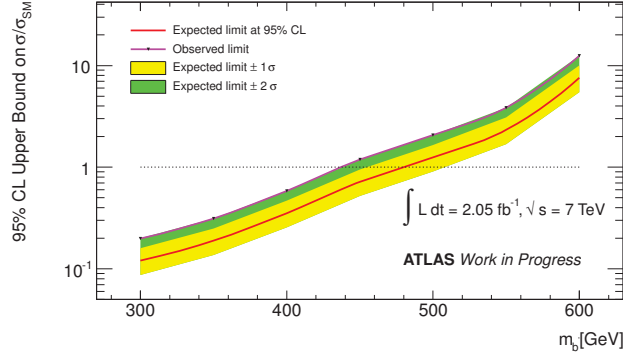
Figure 8.6.: Expected and observed mass limit as a function of the b' mass. The green and the yellow band represent the 1σ (yellow) and 2σ (green) range of the expected limit. The point where the expected limit curve cross the line at $\sigma/\sigma_{SM} = 1$ defines the observed mass limit of the b'. The optimized event selection are applied for the lepton category $e^+\mu^+/e^-\mu^-$. The data from the muons stream is used.

Lepton channel	Lower mass limit [GeV]	Lower mass limit [GeV]
	(Top evt cuts)	(Opt. evt. cuts)
$e + e + /e - e-$ (Egamma stream)	439.802	443.158
$e^+\mu^+/e^-\mu^-$ (Egamma stream)	497.921	505.241
$e^+\mu^+/e^-\mu^-$ Muons stream	483.007	476.307 GeV
$\mu^+\mu^+/\mu^-\mu^-$ Muons stream	465.357	

Table 8.5.: Expected lower mass limit calculated with the CL_s method for every same-sign dilepon category.

Lepton channel	Lower mass limit [GeV] (Top evt cuts)	Lower mass limit [GeV] (Opt. evt. cuts)
$e+e+/e-e-$ (Egamma stream)	402.504	443.141
$e^+\mu^+/e^-\mu^-$ (Egamma stream)	443.465	461.141
$e^+\mu^+/e^-\mu^-$ Muons stream	433.306	434.193
$\mu^+\mu^+/\mu^-\mu^-$ Muons stream	429.114	

Table 8.6.: Observed lower mass limit calculated with the CL_s method for every same-sign dilepon category.

9. Summary, conclusion and outlook

9.1. Summary and conclusion

With the start of the Large Hadron Collider (LHC) a new energy frontier in proton-proton collisions can be explored. This provides the possibility for the exclusion or discovery of new particles, which rules out or confirms new theories. In this thesis, a search of a down-type fourth generation quark is presented. The extension of the Standard Model with the model of a fourth generation leads to a possible ansatz for the generation of the baryogenesis or the unification of the three fundamental forces. From the theoretical point the model is not excluded. If the Higgs boson will be discovered with a mass of $m_H \approx 125 \, \mathrm{GeV}$, and with the same branching ratio as evidence was found for ATLAS and CMS, this model is excluded for many mass scenarios of the fourth generation particles [24], [25]. Searches at other experiments could only set a lower mass bound for these particles. The searches have been done with several assumptions for the decay channel.

Generally, the decay channel depends on the masses of the heavy quarks and the CKM matrix elements. With the assumption of a unitary V_{CKM}^{4x4} matrix many scenarios are possible inside the uncertainties of the V_{CKM}^{3x3} elements. As I discussed in chapter two a final state of four W bosons and two b quarks is available in all possible mass scenarios. This shows that this final state is independent on the mass scenario. With a pair production of the b' the decay channel and the assumption of a branching ratio of $100\,\%$ for the decay into $t + W$ is as follows:

$$pp \rightarrow b'\bar{b}' + X \rightarrow t\bar{t} + W^+ + W^- + X \rightarrow b\bar{b} + W^+ + W^- + W^+ + W^- + X$$

Assuming a leptonic decay of two W bosons into electrons and muons a search signature of two same-sign leptons with any flavor combination can be chosen. This is a rare Standard Model signature and provides the possibility for suppressing the background efficiently. The background suppression can be improved by exploiting the high jet multiplicity caused by the other two W decays into quarks in addition to the the b quarks. Furthermore, this is supported by applying a cut on the missing transverse energy.

Further requirements for the jet selection like b-tagging are not used for this analysis due to rather low identification efficiency and in order to suppress the uncertainties coming from this algorithm.

For the analysis in this thesis the top selection criteria developed by the *ATLAS Top Group* are used due to similar properties of this final state. To improve the background suppression and the signal selection the tool TMVA has been applied. This optimization leads to less background in the signal region with two same sign leptons. In chapter six it has been shown that applying the optimized event selection leads to less selected event in the signal region and in the lepton category $\mu^+\mu^+/\mu^-\mu^-$ no data events have passed these criteria. For a better optimization further studies are recommended and the optimization of the event selection should be done for every final state separately. For example, the optimization is done for the number of jets and transverse momentum of the leading lepton. Furthermore, the jet and lepton multiplicity is affected by the overlap removal between jets and leptons and can lead to different final states between events with two same-sign electrons or two same-sign muons.

The leptons, which pass the object selection, could also be coming from hadron decays inside the jets. Therefor, the fake estimation needs to be determined. In general, a Monte Carlo sample with QCD jets produced via gluon fusion or quark-anti-quark annihilation could be used for this study. Due to the tight object and event selection criteria the probability that such an event passes the event selection is very low, which leads to low statistics for the estimation and high uncertainties. To solve this problem a data driven method is applied for the determination of the fake estimation. This has been done for every lepton category separately by the *ATLAS Top Group* and for the publication in [97]. The results of these methods shows that the fake estimation in every lepton category is very low. The disagreement between data and Monte Carlo, which is discussed in chapter six, can be caused by an underestimation of the fake contribution.

In chapter six the object and event selection are introduced and with the requirements on $\not{E}_T$ and H_T the background could be suppressed very well. The total event selection efficiency ϵ for the signal with applying the top event selection criteria in every same-sign dilepton category is $\epsilon \approx 0.15$, while for the background $\epsilon \lesssim 0.05$. After applying the optimized event selection criteria both efficiencies are lower. In this chapter also the agreement between Monte Carlo and data has been discussed for several distribution like the transverse momentum of the leptons, transverse energy of the jets or the numbers of jets. It turns out that in events with one electron or positron for $p_T^{Leptons}$ and H_T the Monte Carlo describe the data very well, while for the N_{Jets} distribution the Monte Carlo is overestimated. In events with two opposite-sign electrons there is a agreement

between Monte Carlo and data. The distribution for events with one electron and one muon with the opposite-sign show small discrepancies between the Monte Carlo estimation and the data. With using the optimized event selection criteria, the Monte Carlo is underestimated. In events with two electrons or one electron and muon, both with the opposite sign, also show small discrepancies between the Monte Carlo and the data. This can be caused by the missing corrections for the missing transverse energy or the $W + jets$ Monte Carlo. Also a wrong estimation of the fake contribution can cause the disagreement. In the signal region of two same-sign leptons with any flavor combination $Diboson + jets$ and $t\bar{t} + jets$ are the dominating background processes. With using the optimized event selection criteria the Monte Carlo background is more suppressed than for the top event selection criteria, but also less signal and data events pass the event selection criteria.

In this thesis also the uncertainties on the event selection coming from changing the PDF and varying the Pythia6 parameters for the ISR and FSR activity are studied with signal Monte Carlo sample. In general, the Monte Carlo estimation depends on the setup of the generator. ATLAS studies have been shown that the data and Monte Carlo agreement depends on the tuning of the Pythia6 parameter for the MPI model. Monte Carlo samples have been produced with the PDFs (CTEQ6L and CTEQ6LL) and with the parameter values tuned for the corresponding PDF. Further samples have been used with a new PDF but with the default MC10 setup of the generator. The total event selection efficiencies are higher for the PDF CTEQ6LL with and without the optimized Pythia6 parameters with respect to the default MC10 Monte Carlo sample if two same-sign electrons are applied in every event. Replacing the PDF by CTEQ6L the total event selection efficiencies are smaller than for the Monte Carlo sample with the MC10 setup. This is caused by a higher electron fake rate for CTEQ6LL and lower electron fake rate for CTEQ6L than for the MC10 setup. Using events with two same-sign muons the behavior of the total event selection efficiencies is different. Here, the total event selection efficiencies is lower for CTEQ6L with the MC10 setup than for the sample with default MC10 setup. The efficiencies for all other configurations are higher than for the sample with default MC10 setup. When using optimized event selection criteria the sample with CTEQ6L and the MC10 setup has a lower event selection than the samples with the default MC10 setup, while for all other samples the efficiencies are higher. This can be caused by reconstructed fake muons coming from hadron decays inside the jet. Requiring one electron and one muon with the same-sign the total event selection efficiencies are higher for the PDF CTEQ6L with the tuned parameters and also for CTEQ6LL without the tunes parameters than for the default MC10 sample.

9. Summary, conclusion and outlook

For the other setups the efficiencies are smaller than for the default MC10 setup. This could also be caused by the different rates of reconstructed leptons coming from hadron decays. The uncertainties on the event selection efficiency have also been studied with Monte Samples, for which the event weight has been changed via a tool for the applied PDFs: CTEQ6L and CTEQ6LL. In every same-sign lepton leptons category differences are observed between the samples with the new PDF and the new event weight and with respect to the MC10 setup. This is caused by the new weight, than with the default weight the event selection efficiencies are equal. Changing the parameters values for the ISR and FSR leads to an effect on the total event selection efficiencies. Applying the top event selection or the optimized event selection and requiring two same-sign electrons in every event, the total event selection efficiencies decrease with a lower ISR and FSR activity with respect to the default MC10 generator setup. In events with two same-sign muons and the top event selection the total event selection efficiency is lower for "ISR down" than for the sample with the MC10 setup, while for the other ISR and FSR configurations the efficiencies are higher. In the case of the optimized event selection the efficiency for "ISR down" is similar with respect to the default MC10 setup and for all other configurations the efficiencies are higher. In events with one electron and one muon with the same-sign the event selection efficiency is higher for "ISR up" than for the default MC10 setup, while for the other ISR and FSR configuration the efficiencies are lower with repect to the default MC10 sample. The same behavior is also visible for applying the optimized event selection. These differences between the event selection efficiencies are caused by the misidentification rate for the reconstructed muons and electrons coming from hadron decays inside the jet.

With the passed data and Monte Carlo events in the signal region of two same-sign leptons the signal is extracted via a counting method [20]. With this method the Standard Model backgrounds in the signal region are also corrected with respect to a control region. It shows that for applying the top event selection criteria the Monte Carlo in the signal region is underestimated, while with the optimized event selection criteria the Monte Carlo is overestimated. Furthermore, the expected number of signal events is higher than for the measured events. With the extracted signal in every lepton category a lower mass bound is determined via a modified frequentist method [112]. The expected mass limit is higher than the observed limit and with the optimized event selection the mass limit could be improved. The highest observed mass limit for the b' of $m_{b'} = 461\,\text{GeV}$ is determined in the lepton category $e^+\mu^+/e^-\mu^-$ with the applied optimized event selection criteria, while the expected mass limit is $m_{b'} = 505\,\text{GeV}$. For this determination a branching ratio of $BR = 100\,\%$ for the decay $b' \to t + W$ is assumed.

9.2. Outlook

The determination of the mass limit is made with a luminosity of $\mathcal{L} = 2.05\,\mathrm{fb}^{-1}$. In the year 2012 the LHC is running with a center-of-mass energy of $\sqrt{s} = 7\,\mathrm{TeV}$, and it is planned to collect a luminosity of $\mathcal{L} \approx 15\,\mathrm{fb}^{-1}$. This provides the possibility to discover the fourth generation or to rule out a large mass range for the fourth generation quarks. For this analysis and the lower mass bound determination a branching ratio of $BR = 100\,\%$ for the decay $b' \rightarrow t + W$ is assumed. If the branching ratio is smaller in nature, less events would be expected for the signal and the observed mass limit will move to lower values. In addition, a short lifetime is assumed for the quark. With a longer lifetime the particle pass the cuts without detection. For this a different analysis needs to be done and can lead to a different mass limit.

The results of the analysis can be improved with a better method for the fake estimation, since one reason for the disagreement between Monte Carlo and data is an underestimation of the fakes contribution. The agreement between Monte Carlo and data can also be improved with the implementation of the missing correction like for the missing transverse energy or the $W + jets$

In the case of the uncertainty studies, there are further investigations required concerning the event selection efficiencies coming from PDF and ISR/FSR, since the behavior of some event selection is not yet fully understood.

In the case of the signal extraction, this can be improved by using a fit instead of a counting method. This is more precise due to the determination of the agreement between data and Monte Carlo via the shape of the distribution, which is used for the fit. A more precise signal extraction leads to a better mass limit. Furthermore, the mass limit is determined in this analysis without including any uncertainties and the implementation of the uncertainties leads to better sensitivity of the mass limit.

A. Additional information for the object and the event selection

A. Additional information for the object and the event selection

Sample	Generated events	Trigger	$N_{lepton} \geq 1$	$p_T^{LeadLep}$	$p_T^{2ndLeadLep}$
b' (400 GeV)	9.99×10^4	$0.99863^{+0.00012}_{-0.00013}$	$0.24463^{+0.00136}_{-0.00136}$	$0.94796^{+0.00142}_{-0.00145}$	$1.00000^{+0.00000}_{-0.00008}$
$t\bar{t} + jets$	8.79×10^5	$0.99830^{+0.00004}_{-0.00005}$	$0.21682^{+0.00047}_{-0.00047}$	$0.90824^{+0.00069}_{-0.00070}$	$1.00000^{+0.00000}_{-0.00003}$
$Z + jets$	2.55×10^7	$0.91648^{+0.00010}_{-0.00011}$	$0.73944^{+0.00025}_{-0.00025}$	$0.89772^{+0.00020}_{-0.00021}$	$1.00000^{+0.00000}_{-0.00000}$
$Z + b\bar{b} + jets$	1×10^6	$0.99835^{+0.00008}_{-0.00009}$	$0.68127^{+0.00079}_{-0.00080}$	$0.92079^{+0.00057}_{-0.00058}$	$1.00000^{+0.00000}_{-0.00007}$
$W + jets$	2.46×10^7	$0.49076^{+0.05594}_{-0.05594}$	$0.66612^{+0.00033}_{-0.00033}$	$0.86691^{+0.00030}_{-0.00030}$	$1.00000^{+0.00000}_{-0.00000}$
$W + b\bar{b} + jets$	1.65×10^4	$0.98819^{+0.00080}_{-0.00090}$	$0.17265^{+0.00306}_{-0.00299}$	$0.88599^{+0.00605}_{-0.00659}$	$1.00000^{+0.00000}_{-0.00143}$
$Single\ Top$	1.65×10^6	$0.99964^{+0.27211}_{-0.27211}$	$0.37673^{+0.00076}_{-0.00076}$	$0.88190^{+0.00081}_{-0.00081}$	$1.00000^{+0.00000}_{-0.00003}$
$Diboson + jets$	2.47×10^5	$0.99838^{+0.00010}_{-0.00013}$	$0.31845^{+0.00125}_{-0.00124}$	$0.93112^{+0.00117}_{-0.00123}$	$1.00000^{+0.00000}_{-0.00014}$
$Drell - Yan$	1.59×10^6	$1.00081^{+0.70768}_{-0.70768}$	$0.04835^{+0.00021}_{-0.00021}$	$0.48532^{+0.00227}_{-0.00227}$	$1.00000^{+0.00000}_{-0.00008}$

Sample	$\not{E}_T$	H_T	N_{Jets}	M_{inv}	$Z-Veto$	Total ϵ
b' (400 GeV)	$0.78491^{+0.00270}_{-0.00272}$	$0.95817^{+0.00148}_{-0.00153}$	$0.99942^{+0.00018}_{-0.00025}$	$0.99985^{+0.00009}_{-0.00016}$	$0.98954^{+0.00077}_{-0.00083}$	$0.17222^{+0.00120}_{-0.00119}$
$t\bar{t}+jets$	$0.67190^{+0.00117}_{-0.00117}$	$0.47067^{+0.00166}_{-0.00167}$	$0.99891^{+0.00017}_{-0.00025}$	$0.99994^{+0.00003}_{-0.00015}$	$0.99686^{+0.00029}_{-0.00036}$	$0.05485^{+0.00032}_{-0.00031}$
$Z+jets$	$0.14892^{+0.00029}_{-0.00029}$	$0.18355^{+0.00256}_{-0.00253}$	$0.96274^{+0.00208}_{-0.00254}$	$1.00000^{+0.00000}_{-0.00123}$	$0.79608^{+0.00517}_{-0.0544}$	$0.00921^{+0.00022}_{-0.00021}$
$Z+b\bar{b}+jets$	$0.10662^{+0.00091}_{-0.00126}$	$0.26606^{+0.00754}_{-0.00743}$	$0.98094^{+0.00335}_{-0.00548}$	$1.00000^{+0.00000}_{-0.00399}$	$0.76067^{+0.01071}_{-0.01189}$	$0.01331^{+0.00064}_{-0.00061}$
$W+jets$	$0.42062^{+0.00046}_{-0.00046}$	$0.13210^{+0.00067}_{-0.00066}$	$0.97266^{+0.00125}_{-0.00161}$	$1.00000^{+0.00000}_{-0.00107}$	$1.00000^{+0.00000}_{-0.00107}$	$0.02603^{+0.00016}_{-0.00016}$
$W+b\bar{b}+jets$	$0.44965^{+0.01034}_{-0.01028}$	$0.23207^{+0.02229}_{-0.02109}$	$1.00000^{+0.00000}_{-0.03191}$	$1.00000^{+0.00000}_{-0.03191}$	$1.00000^{+0.00000}_{-0.03191}$	$0.01828^{+0.00231}_{-0.00202}$
$Single\ Top$	$0.59001^{+0.00131}_{-0.00131}$	$0.11440^{+0.00128}_{-0.00126}$	$0.98724^{+0.00124}_{-0.00149}$	$1.00000^{+0.00000}_{-0.00053}$	$0.99912^{+0.00032}_{-0.00067}$	$0.01158^{+0.00013}_{-0.00013}$
$Diboson+jets$	$0.51436^{+0.00235}_{-0.00235}$	$0.25630^{+0.00426}_{-0.00415}$	$0.91750^{+0.00567}_{-0.00671}$	$0.99866^{+0.00079}_{-0.00427}$	$0.90607^{+0.00575}_{-0.00713}$	$0.03540^{+0.00084}_{-0.00080}$
$Drell-Yan$	$0.01192^{+0.00075}_{-0.00070}$	$0.02022^{+0.01229}_{-0.00818}$	$0.60872^{+0.23576}_{-0.28352}$	$1.00000^{+0.00000}_{-0.41238}$	$1.00000^{+0.00000}_{-0.41238}$	$0.00000^{+0.00000}_{-0.00000}$

Table A.1.: Event selection efficiency for the signal b' with $m(b') = 400\,\text{GeV}$ and all used background categories. For the trigger selection the item EF_mu18 is used. Top event selection cuts are applied. The number of generated events are scaled to a luminosity of 2.05 fb^{-1}.

181

Sample	Generated events	Trigger	$N_{lepton} \geq 1$	$P_T^{LeadLep}$	$P_T^{2ndLeadLep}$
b' (400 GeV)	9.99×10^4	$0.99863^{+0.00012}_{-0.00013}$	$0.24463^{+0.00136}_{-0.00136}$	$0.79245^{+0.00259}_{-0.00261}$	$0.97188^{+0.00118}_{-0.00123}$
$t\bar{t} + jets$	8.79×10^5	$0.99830^{+0.00004}_{-0.00005}$	$0.21681^{+0.00047}_{-0.00047}$	$0.63964^{+0.00114}_{-0.00115}$	$0.98292^{+0.00037}_{-0.00039}$
$Z + jets$	2.55×10^7	$0.90936^{+0.00011}_{-0.00012}$	$0.75438^{+0.00026}_{-0.00026}$	$0.55601^{+0.00036}_{-0.00036}$	$0.99310^{+0.00008}_{-0.00008}$
$Z + b\bar{b} + jets$	1×10^6	$0.99835^{+0.00008}_{-0.00009}$	$0.68127^{+0.00079}_{-0.00080}$	$0.66157^{+0.00101}_{-0.00101}$	$0.92986^{+0.00067}_{-0.00068}$
$W + jets$	3.12×10^7	$0.40881^{+0.00014}_{-0.00014}$	$0.69805^{+0.00034}_{-0.00034}$	$0.34895^{+0.00033}_{-0.00033}$	$1.00000^{+0.00000}_{-0.00001}$
$W + b\bar{b} + jets$	1.65×10^4	$0.98819^{+0.00080}_{-0.00090}$	$0.17265^{+0.00306}_{-0.00299}$	$0.53954^{+0.00962}_{-0.00971}$	$0.99915^{+0.00065}_{-0.00259}$
$Single\ Top$	1.65×10^6	$0.99964^{+0.27211}_{-0.27211}$	$0.37673^{+0.00076}_{-0.00076}$	$0.55999^{+0.00122}_{-0.00122}$	$0.99328^{+0.00025}_{-0.00027}$
$Diboson + jets$	1.52×10^5	$0.99838^{+0.00011}_{-0.00013}$	$0.32046^{+0.00126}_{-0.00126}$	$0.67619^{+0.00219}_{-0.00222}$	$0.94252^{+0.00137}_{-0.00146}$
$Drell - Yan$	1.59×10^6	$1.00081^{+0.70768}_{-0.70768}$	$0.04835^{+0.00021}_{-0.00021}$	$0.08015^{+0.00125}_{-0.00123}$	$0.93008^{+0.00409}_{-0.00431}$

Sample	E_T^{Miss}	$E_T^{LeadJet}$	$\eta^{LeadLep}$	$\eta^{2ndLeadLep}$	H_T
b' (400 GeV)	$0.77691^{+0.00303}_{-0.00306}$	$0.97823^{+0.00120}_{-0.00127}$	$0.83773^{+0.00308}_{-0.00313}$	$0.92763^{+0.00236}_{-0.00243}$	$0.94448^{+0.00217}_{-0.00225}$
$t\bar{t}+jets$	$0.64460^{+0.00143}_{-0.00144}$	$0.80563^{+0.00143}_{-0.00145}$	$0.77629^{+0.00178}_{-0.00181}$	$0.97203^{+0.00074}_{-0.00079}$	$0.46969^{+0.00263}_{-0.00264}$
$Z+jets$	$0.07733^{+0.00045}_{-0.00045}$	$0.56495^{+0.00309}_{-0.00315}$	$0.49338^{+0.00476}_{-0.00478}$	$0.93497^{+0.00324}_{-0.00374}$	$0.36040^{+0.00808}_{-0.00801}$
$Z+b\bar{b}+jets$	$0.09177^{+0.00113}_{-0.00112}$	$0.54393^{+0.00574}_{-0.00601}$	$0.62528^{+0.00876}_{-0.00910}$	$0.92951^{+0.00570}_{-0.00711}$	$0.39511^{+0.01568}_{-0.01580}$
$W+jets$	$0.20563^{+0.00061}_{-0.00060}$	$0.48287^{+0.00111}_{-0.00114}$	$0.55915^{+0.00191}_{-0.00192}$	$0.99995^{+0.00002}_{-0.00042}$	$0.24542^{+0.00200}_{-0.00196}$
$W+b\bar{b}+jets$	$0.37697^{+0.01328}_{-0.01301}$	$0.51967^{+0.02253}_{-0.02321}$	$0.63953^{+0.03134}_{-0.03425}$	$1.00000^{+0.00000}_{-0.02215}$	$0.29419^{+0.06329}_{-0.05693}$
$Single\ Top$	$0.52655^{+0.00167}_{-0.00167}$	$0.54135^{+0.00228}_{-0.00228}$	$0.76327^{+0.00271}_{-0.00274}$	$0.98455^{+0.00084}_{-0.00090}$	$0.17780^{+0.00293}_{-0.00287}$
$Diboson+jets$	$0.52526^{+0.00294}_{-0.00294}$	$0.46434^{+0.00462}_{-0.00464}$	$0.67220^{+0.00725}_{-0.00752}$	$0.89283^{+0.00553}_{-0.00652}$	$0.34325^{+0.01061}_{-0.01039}$
$Drell-Yan$	$0.02238^{+0.00273}_{-0.00245}$	$0.50781^{+0.06098}_{-0.06119}$	$0.50487^{+0.08844}_{-0.08871}$	$1.00000^{+0.00000}_{-0.08468}$	$0.15048^{+0.12130}_{-0.07906}$

Sample	N_{Jets}	M_{inv}	$Z-Veto$	Total ϵ
b' (400 GeV)	$0.97296^{+0.00158}_{-0.00167}$	$1.00000^{+0.00000}_{-0.00018}$	$0.98201^{+0.00131}_{-0.00141}$	$0.10027^{+0.00095}_{-0.00095}$
$\bar{t}+jets$	$0.92485^{+0.00184}_{-0.00195}$	$0.99997^{+0.00003}_{-0.00039}$	$0.99470^{+0.00060}_{-0.00079}$	$0.02400^{+0.00024}_{-0.00023}$
$Z+jets$	$0.67982^{+0.01232}_{-0.01356}$	$1.00000^{+0.00000}_{-0.00735}$	$0.80976^{+0.01280}_{-0.01556}$	$0.00311^{+0.00018}_{-0.00017}$
$Z+b\bar{b}+jets$	$0.72281^{+0.02098}_{-0.02469}$	$1.00000^{+0.00000}_{-0.01598}$	$0.76561^{+0.02476}_{-0.03126}$	$0.00543^{+0.00056}_{-0.00051}$
$W+jets$	$0.71722^{+0.00363}_{-0.00519}$	$1.00000^{+0.00000}_{-0.00385}$	$1.00000^{+0.00000}_{-0.00385}$	$0.01279^{+0.00020}_{-0.00019}$
$W+b\bar{b}+jets$	$0.96235^{+0.02557}_{-0.11559}$	$1.00000^{+0.00000}_{-0.11860}$	$1.00000^{+0.00000}_{-0.11860}$	$0.00536^{+0.00165}_{-0.00123}$
$Single\ Top$	$0.67051^{+0.00818}_{-0.00831}$	$1.00000^{+0.00000}_{-0.00197}$	$0.99633^{+0.00127}_{-0.00254}$	$0.00306^{+0.00007}_{-0.00007}$
$Diboson+jets$	$0.49256^{+0.01970}_{-0.02234}$	$1.00000^{+0.00000}_{-0.02076}$	$0.86000^{+0.01844}_{-0.02539}$	$0.00786^{+0.00055}_{-0.00049}$
$Drell-Yan$	$0.06508^{+0.44526}_{-0.06506}$	$1.00000^{+0.00000}_{-0.99988}$	$1.00000^{+0.00000}_{-0.99988}$	$0.00000^{+0.00000}_{-0.00000}$

Table A.2.: Event selection efficiency for the signal b' with $m(b') = 400\,\text{GeV}$ and all used background categories. For the trigger selection the item *EF_mu18* is used. Optimized event selection cuts are applied. The number of generated events are scaled to a luminosity of $2.05\,\text{fb}^{-1}$.

A.1. Data and Monte Carlo distributions
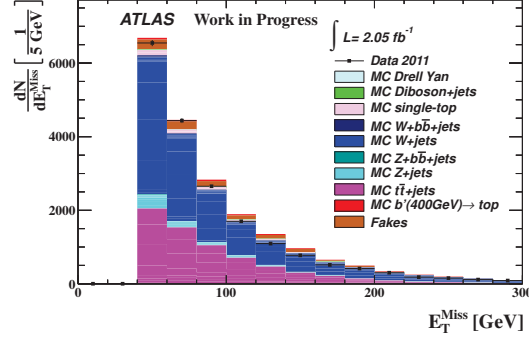
Figure A.1.: $\not{E}_T$ for the category μ^+/μ^- with the top event selection cuts and the requirement of an muon trigger chain.
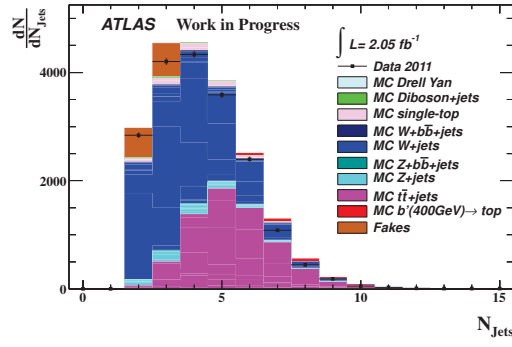
Figure A.2.: N_{Jets} for the category μ^+/μ^- with the top event selection cuts and the requirement of an muon trigger chain.
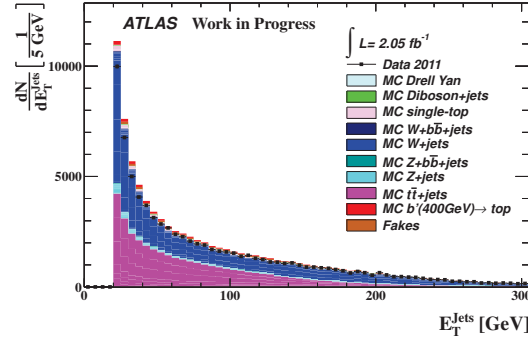
Figure A.3.: E_T^{Jets} for the category μ^+/μ^- with the top event selection cuts and the requirement of an muon trigger chain.
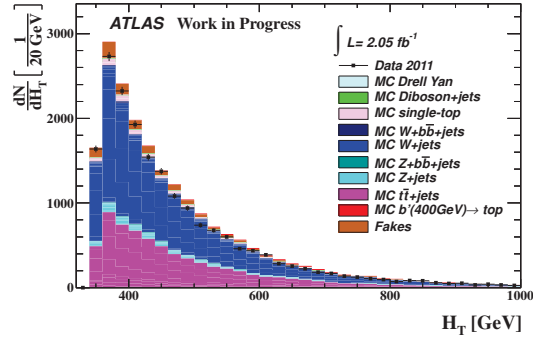
Figure A.4.: H_T for the category μ^+/μ^- with the top event selection cuts and the requirement of an muon trigger chain.
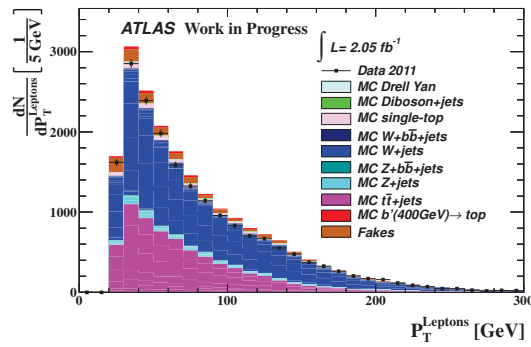
Figure A.5.: $p_T^{Leptons}$ for the category μ^+/μ^- with the top event selection cuts and the requirement of an muon trigger chain.
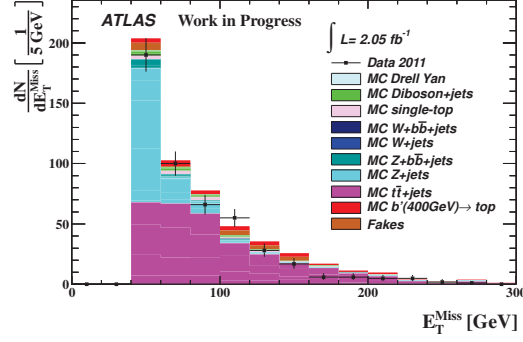
Figure A.6.: $\not{E}_T$ for the category $\mu^+\mu^-$ with the top event selection cuts and the requirement of an muon trigger chain.

Figure A.7.: N_{Jets} for the category $\mu^+\mu^-$ with the top event selection cuts and the requirement of an muon trigger chain.
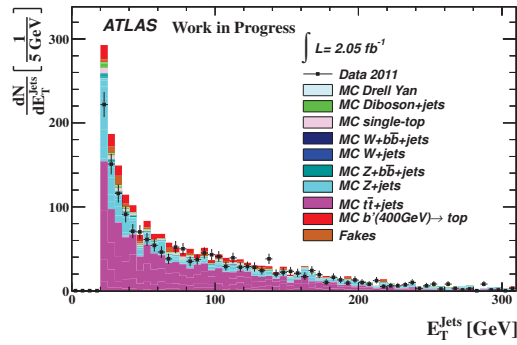
Figure A.8.: E_T^{Jets} for the category $\mu^+\mu^-$ with the top event selection cuts and the requirement of an muon trigger chain.

Figure A.9.: H_T for the category $\mu^+\mu^-$ with the top event selection cuts and the requirement of an muon trigger chain.
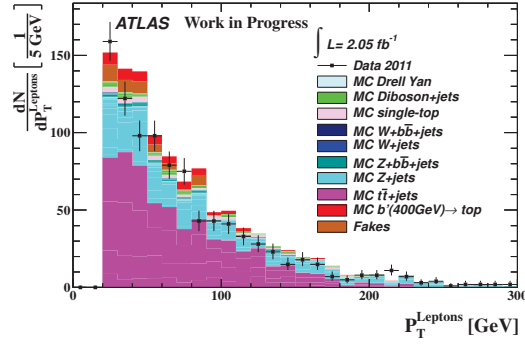
Figure A.10.: $p_T^{Leptons}$ for the category $\mu^+\mu^-$ with the top event selection cuts and the requirement of an muon trigger chain.
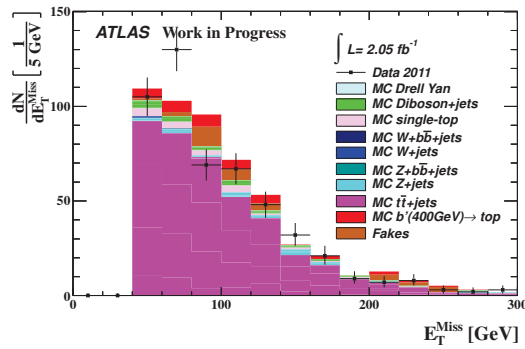
Figure A.11.: $\not{E}_T$ for the category $e^+\mu^-/e^-\mu^+$ with the top event selection cuts and the requirement of an muon trigger chain.
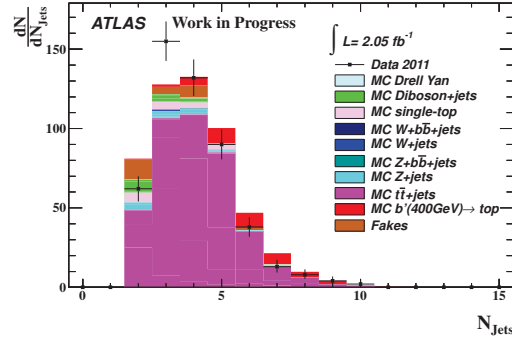
Figure A.12.: N_{Jets} for the category $e^+\mu^-/e^-\mu^+$ with the top event selection cuts and the requirement of an muon trigger chain.
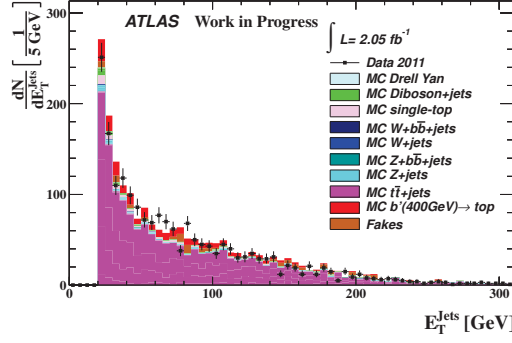
Figure A.13.: E_T^{Jets} for the category $e^+\mu^-/e^-\mu^+$ with the top event selection cuts and the requirement of an muon trigger chain.
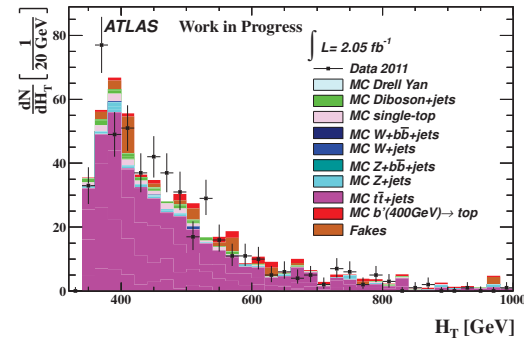
Figure A.14.: H_T for the category $e^+\mu^-/e^-\mu^+$ with the top event selection cuts and the requirement of an muon trigger chain.

Figure A.15.: $p_T^{Leptons}$ for the category $e^+\mu^-/e^-\mu^+$ with the top event selection cuts and the requirement of an muon trigger chain.
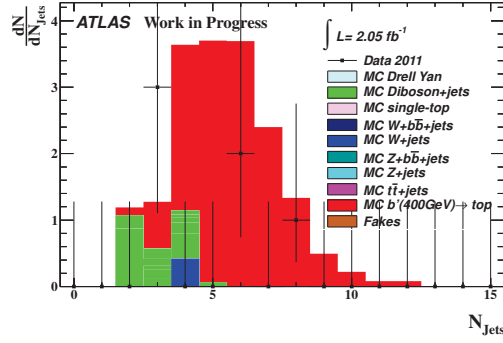
Figure A.16.: e^+e^+/e^-e^- for the category $e^+\mu^-/e^-\mu^+$ with the top event selection cuts and the requirement of an muon trigger chain.
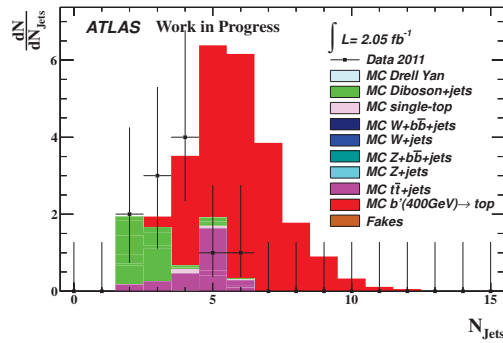
Figure A.17.: $e^+\mu^+/e^-\mu^-$ for the category $e^+\mu^-/e^-\mu^+$ with the top event selection cuts and the requirement of an muon trigger chain.
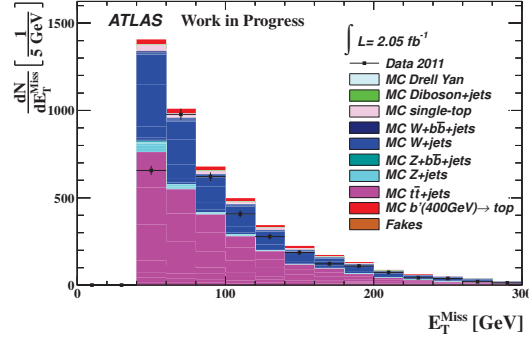
Figure A.18.: $\not{E}_T$ for the category μ^+/μ^- with the optimized event selection cuts and the requirement of an muon trigger chain.
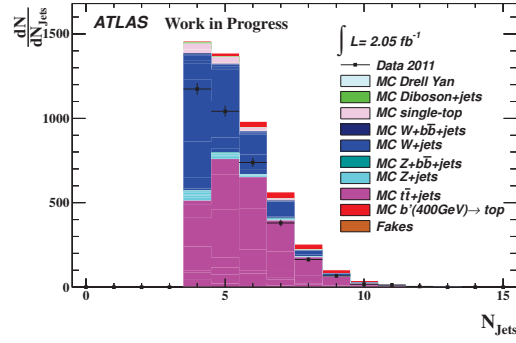
Figure A.19.: N_{Jets} for the category μ^+/μ^- with the optimized event selection cuts and the requirement of an muon trigger chain.
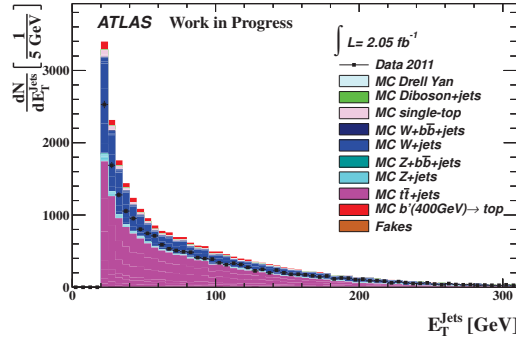
Figure A.20.: E_T^{Jets} for the category μ^+/μ^- with the optimized event selection cuts and the requirement of an muon trigger chain.

A. Additional information for the object and the event selection
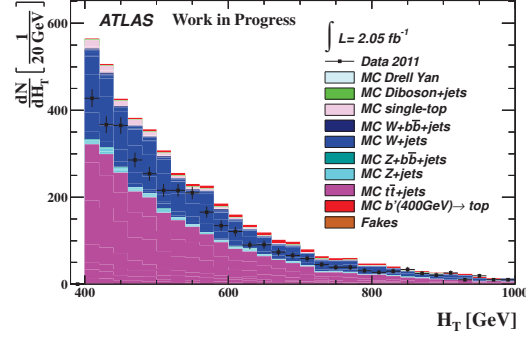
Figure A.21.: H_T for the category μ^+/μ^- with the optimized event selection cuts and the requirement of an muon trigger chain.
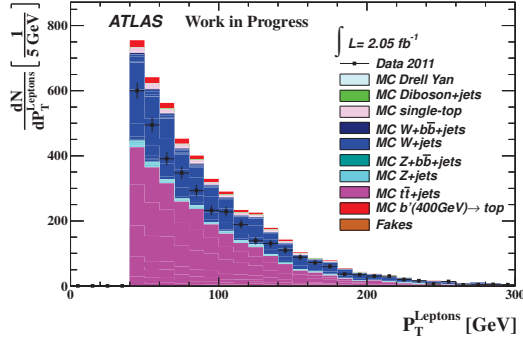
Figure A.22.: $p_T^{Leptons}$ for the category μ^+/μ^- with the optimized event selection cuts and the requirement of an muon trigger chain.
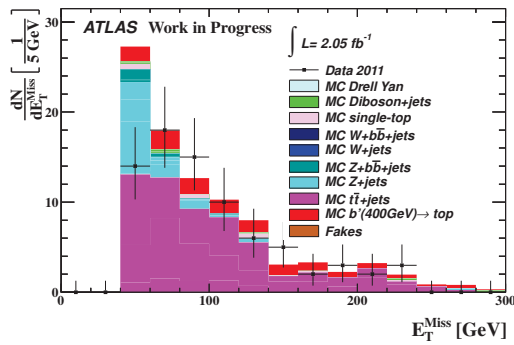
Figure A.23.: $\not{E}_T$ for the category $\mu^+\mu^-$ with the optimized event selection cuts and the requirement of an muon trigger chain.
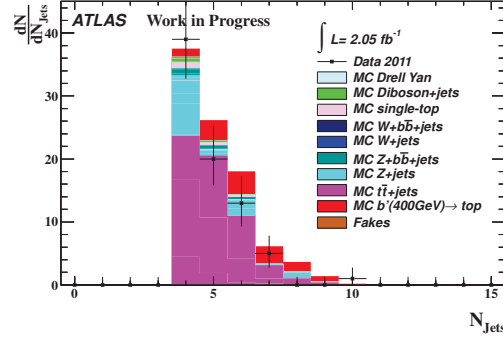
Figure A.24.: N_{Jets} for the category $\mu^+\mu^-$ with the optimized event selection cuts and the requirement of an muon trigger chain.
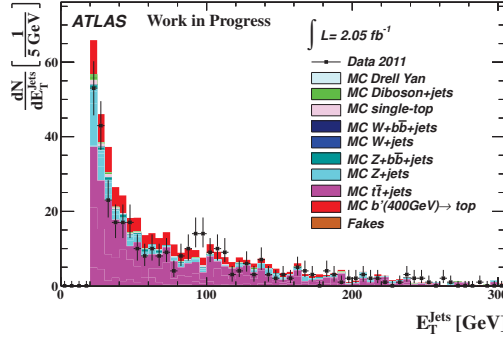
Figure A.25.: E_T^{Jets} for the category $\mu^+\mu^-$ with the optimized event selection cuts and the requirement of an muon trigger chain.
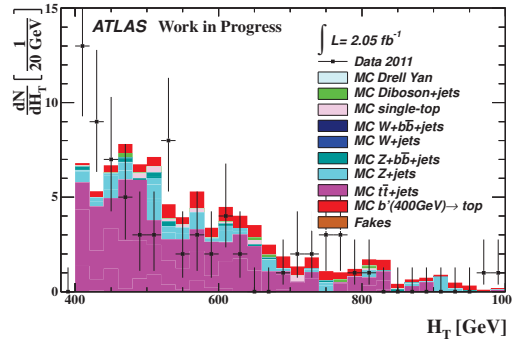
Figure A.26.: H_T for the category $\mu^+\mu^-$ with the optimized event selection cuts and the requirement of an muon trigger chain.

Figure A.27.: $p_T^{Leptons}$ for the category $\mu^+\mu^-$ with the optimized event selection cuts and the requirement of an muon trigger chain.
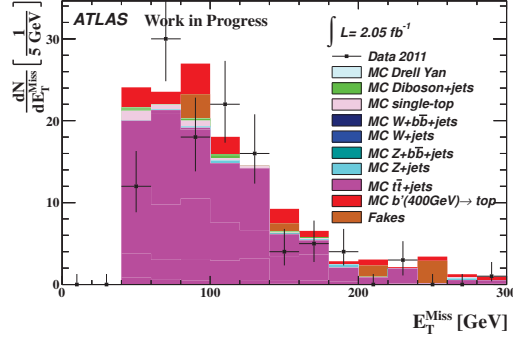
Figure A.28.: $\not{E}_T$ for the category $e^+\mu^-/e^-\mu^+$ with the optimized event selection cuts and the requirement of an muon trigger chain.
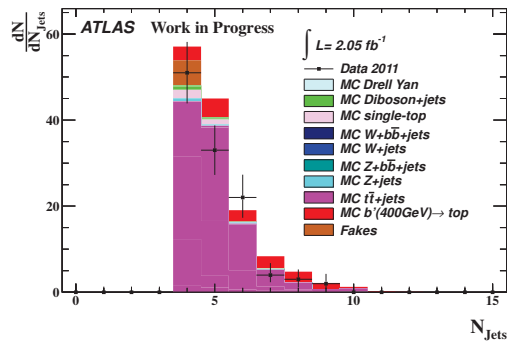
Figure A.29.: N_{Jets} for the category $e^+\mu^-/e^-\mu^+$ with the optimized event selection cuts and the requirement of an muon trigger chain.
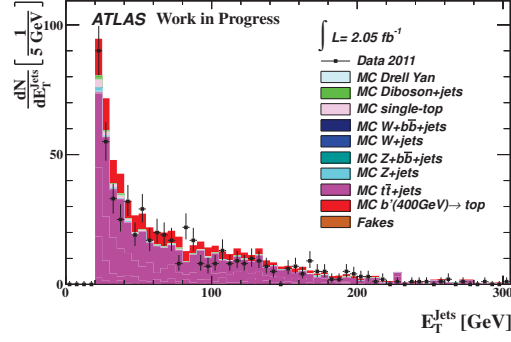
Figure A.30.: E_T^{Jets} for the category $e^+\mu^-/e^-\mu^+$ with the optimized event selection cuts and the requirement of an muon trigger chain.
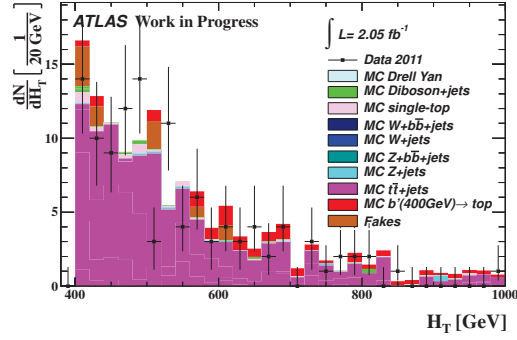
Figure A.31.: H_T for the category $e^+\mu^-/e^-\mu^+$ with the optimized event selection cuts and the requirement of an muon trigger chain.
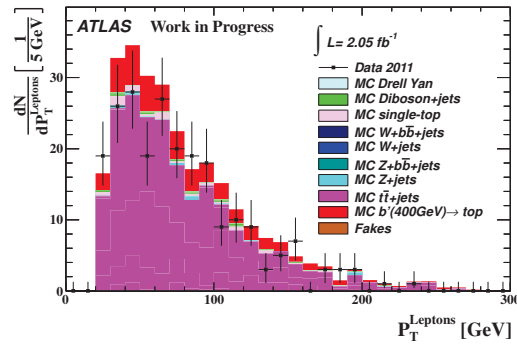
Figure A.32.: $p_T^{Leptons}$ for the category $e^+\mu^-/e^-\mu^+$ with the optimized event selection cuts and the requirement of an muon trigger chain.

Figure A.33.: N_{Jets} for the category $\mu^+\mu^+/\mu^-\mu^-$ with the optimized event selection cuts and the requirement of an muon trigger chain.
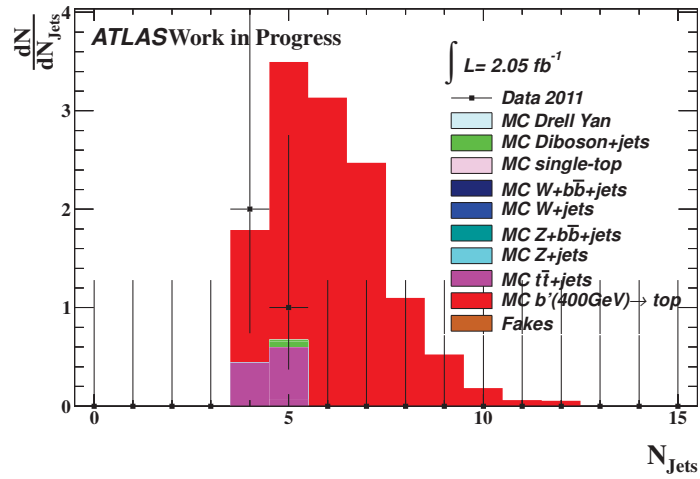
Figure A.34.: N_{Jets} for the category $e^+\mu^+/e^-\mu^-$ with the optimized event selection cuts and the requirement of an muon trigger chain.

B. Additional information for the systematic studies

B.1. PDF uncertainties
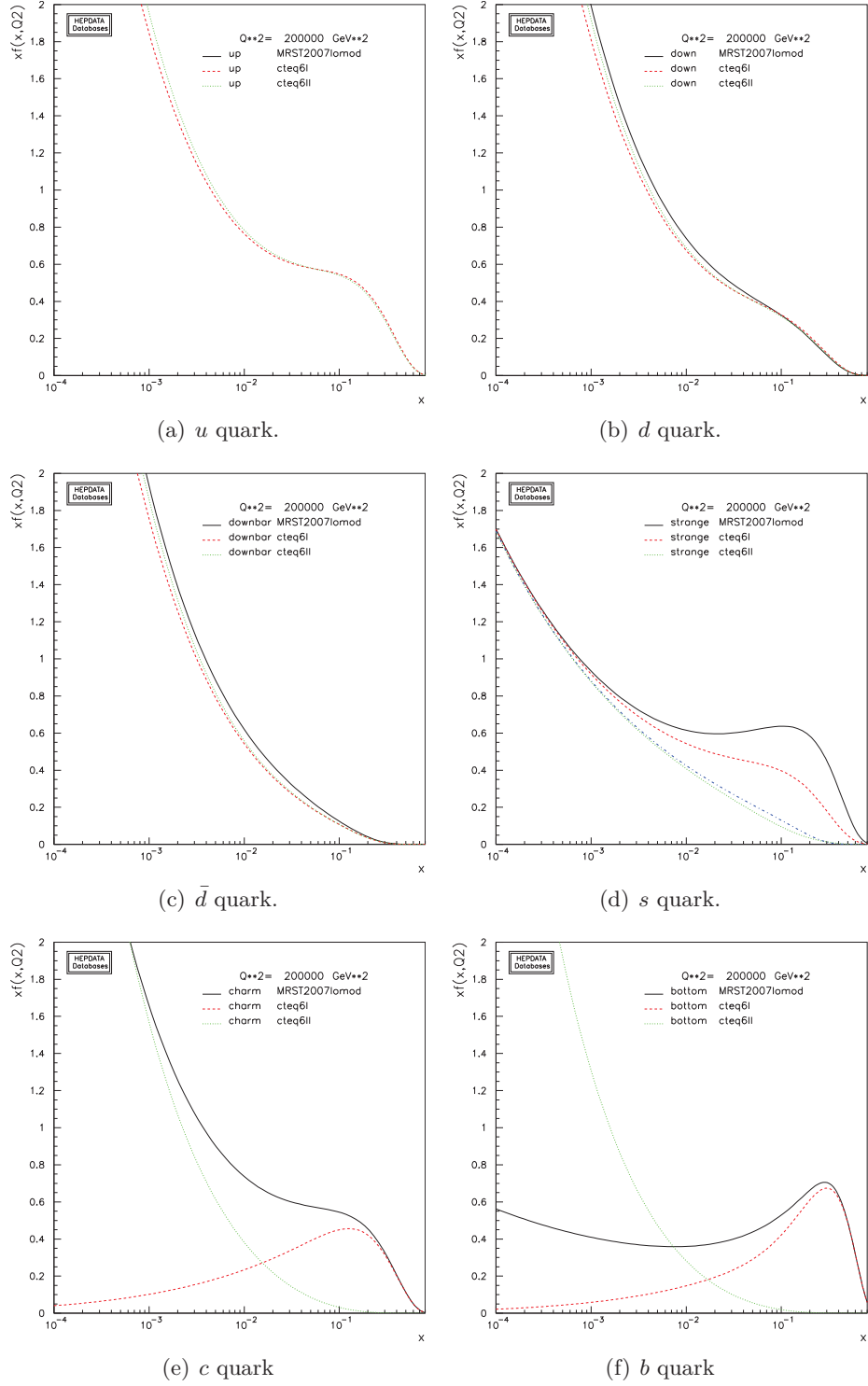
Figure B.1.: Parton density function multiplied with the momentum fraction x as function of the momentum fraction for the *up*, *down*, $\bar{d}$, *s*, *c*, *b* for the PDF MRST 2007LO* (MC10), CTEQ6L and CTEQ6LL [108].

Sample	Generated events	Trigger	$e^+\mu^+/e^-\mu^-$	$P_T^{LeadLep}$	$P_T^{2ndLeadLep}$	E_T^{Miss}
Default	1.45×10^5	$0.99886^{+0.00009}_{-0.00010}$	$0.01500^{+0.00032}_{-0.00032}$	$1.00000^{+0.00000}_{-0.00084}$	$1.00000^{+0.00000}_{-0.00084}$	$0.79293^{+0.00874}_{-0.00902}$
CTEQ6L new tune	9.99×10^4	$0.99885^{+0.00011}_{-0.00012}$	$0.01591^{+0.00040}_{-0.00039}$	$1.00000^{+0.00000}_{-0.00115}$	$1.00000^{+0.00000}_{-0.00115}$	$0.78373^{+0.01041}_{-0.01077}$
CTEQ6LL new tune	9.86×10^4	$1.00055^{+-1.00055}_{-1.00055}$	$0.01457^{+0.00039}_{-0.00038}$	$1.00000^{+0.00000}_{-0.00127}$	$1.00000^{+0.00000}_{-0.00127}$	$0.80149^{+0.01059}_{-0.01102}$
CTEQ6L no tune	9.96×10^4	$0.99706^{+0.00017}_{-0.00018}$	$0.01504^{+0.00039}_{-0.00038}$	$1.00000^{+0.00000}_{-0.00123}$	$1.00000^{+0.00000}_{-0.00123}$	$0.78877^{+0.01064}_{-0.01103}$
CTEQ6LL no tune	9.99×10^4	$0.99864^{+0.00012}_{-0.00013}$	$0.01560^{+0.00040}_{-0.00039}$	$1.00000^{+0.00000}_{-0.00118}$	$1.00000^{+0.00000}_{-0.00118}$	$0.77612^{+0.01065}_{-0.01101}$
CTEQ6L reweight	1.16×10^5	$0.99850^{+0.00011}_{-0.00012}$	$0.01509^{+0.00036}_{-0.00036}$	$1.00000^{+0.00000}_{-0.00104}$	$1.00000^{+0.00000}_{-0.00104}$	$0.79272^{+0.00974}_{-0.01008}$
CTEQ6LL reweight	1.14×10^5	$0.99844^{+0.00012}_{-0.00013}$	$0.01509^{+0.00037}_{-0.00036}$	$1.00000^{+0.00000}_{-0.00107}$	$1.00000^{+0.00000}_{-0.00107}$	$0.79240^{+0.00987}_{-0.01021}$

Sample	H_T	N_{Jets}	M_{inv}	$Z-Veto$	Total ϵ
b' (400 GeV)	$0.91266^{+0.00681}_{-0.00731}$	$1.00000^{+0.00000}_{-0.00117}$	$1.00000^{+0.00000}_{-0.00117}$	$1.00000^{+0.00000}_{-0.00117}$	$0.01084^{+0.00028}_{-0.00027}$
CTEQ6L new tune	$0.92037^{+0.00769}_{-0.00839}$	$1.00000^{+0.00000}_{-0.00160}$	$1.00000^{+0.00000}_{-0.00160}$	$1.00000^{+0.00000}_{-0.00160}$	$0.01146^{+0.00034}_{-0.00034}$
CTEQ6LL new tune	$0.91444^{+0.00825}_{-0.00900}$	$1.00000^{+0.00000}_{-0.00174}$	$1.00000^{+0.00000}_{-0.00174}$	$1.00000^{+0.00000}_{-0.00174}$	$0.01069^{+0.00034}_{-0.00033}$
CTEQ6L no tune	$0.89921^{+0.00879}_{-0.00950}$	$1.00000^{+0.00000}_{-0.00173}$	$1.00000^{+0.00000}_{-0.00173}$	$1.00000^{+0.00000}_{-0.00173}$	$0.01064^{+0.00033}_{-0.00032}$
CTEQ6LL no tune	$0.92809^{+0.00744}_{-0.00818}$	$1.00000^{+0.00000}_{-0.00163}$	$1.00000^{+0.00000}_{-0.00163}$	$1.00000^{+0.00000}_{-0.00163}$	$0.01122^{+0.00034}_{-0.00033}$
CTEQ6L reweight	$0.91657^{+0.00742}_{-0.00805}$	$1.00000^{+0.00000}_{-0.00144}$	$1.00000^{+0.00000}_{-0.00144}$	$1.00000^{+0.00000}_{-0.00144}$	$0.01095^{+0.00031}_{-0.00030}$
CTEQ6LL reweight	$0.91646^{+0.00752}_{-0.00816}$	$1.00000^{+0.00000}_{-0.00147}$	$1.00000^{+0.00000}_{-0.00147}$	$1.00000^{+0.00000}_{-0.00147}$	$0.01094^{+0.00032}_{-0.00031}$

Table B.1.: Event selection efficiency for the samples with the different PDF setups. Events with one electron and one muon with the same-sign and the top event selection cuts are used.

Sample	Generated events	Trigger	$e^+\mu^+/e^-\mu^-$	$P_T^{LeadLep}$	$P_T^{2ndLeadLep}$
Default	$1.45e+05$	$0.99886^{+0.00009}_{-0.00010}$	$0.01500^{+0.00032}_{-0.00032}$	$0.93200^{+0.00540}_{-0.00581}$	$0.93422^{+0.00551}_{-0.00595}$
CTEQ6L new tune	$9.99e+04$	$0.99885^{+0.00011}_{-0.00012}$	$0.01590^{+0.00040}_{-0.00039}$	$0.92924^{+0.00644}_{-0.00700}$	$0.93613^{+0.00637}_{-0.00698}$
CTEQ6LL new tune	$9.86e+04$	$1.00055^{+-1.00055}_{-1.00055}$	$0.01458^{+0.00039}_{-0.00038}$	$0.92372^{+0.00700}_{-0.00762}$	$0.93087^{+0.00696}_{-0.00764}$
CTEQ6L no tune	$9.96e+04$	$0.99706^{+0.00017}_{-0.00018}$	$0.01504^{+0.00039}_{-0.00038}$	$0.95136^{+0.00556}_{-0.00619}$	$0.93768^{+0.00641}_{-0.00705}$
CTEQ6LL no tune	$9.99e+04$	$0.99864^{+0.00012}_{-0.00013}$	$0.01560^{+0.00040}_{-0.00039}$	$0.93291^{+0.00634}_{-0.00692}$	$0.92906^{+0.00674}_{-0.00736}$
CTEQ6L reweight	$1.16e+05$	$0.99850^{+0.00011}_{-0.00012}$	$0.01509^{+0.00036}_{-0.00036}$	$0.93146^{+0.00603}_{-0.00654}$	$0.93471^{+0.00611}_{-0.00666}$
CTEQ6LL reweight	$1.14e+05$	$0.99844^{+0.00012}_{-0.00013}$	$0.01509^{+0.00037}_{-0.00036}$	$0.93118^{+0.00612}_{-0.00664}$	$0.93393^{+0.00622}_{-0.00679}$

B. *Additional information for the systematic studies*

Sample	E_T^{Miss}	$E_T^{LeadJet}$	$\eta^{LeadLep}$	$\eta^{2ndLeadLep}$	H_T
Default	$0.79178^{+0.00940}_{-0.00971}$	$0.94800^{+0.00573}_{-0.00636}$	$0.87974^{+0.00867}_{-0.00922}$	$0.84820^{+0.01021}_{-0.01079}$	$0.64531^{+0.01495}_{-0.01523}$
CTEQ6L new tune	$0.78387^{+0.01117}_{-0.01159}$	$0.94362^{+0.00701}_{-0.00787}$	$0.85449^{+0.01110}_{-0.01182}$	$0.83028^{+0.01282}_{-0.01360}$	$0.64672^{+0.01813}_{-0.01855}$
CTEQ6LL new tune	$0.79505^{+0.01157}_{-0.01206}$	$0.94964^{+0.00696}_{-0.00794}$	$0.86901^{+0.01110}_{-0.01193}$	$0.83063^{+0.01328}_{-0.01413}$	$0.64449^{+0.01884}_{-0.01929}$
CTEQ6L no tune	$0.78438^{+0.01136}_{-0.01180}$	$0.93367^{+0.00770}_{-0.00857}$	$0.85468^{+0.01135}_{-0.01211}$	$0.80507^{+0.01386}_{-0.01461}$	$0.62611^{+0.01911}_{-0.01949}$
CTEQ6LL no tune	$0.76950^{+0.01157}_{-0.01198}$	$0.95613^{+0.00634}_{-0.00728}$	$0.87783^{+0.01045}_{-0.01124}$	$0.83707^{+0.01261}_{-0.01342}$	$0.67944^{+0.01761}_{-0.01812}$
CTEQ6L reweight	$0.79091^{+0.01048}_{-0.01087}$	$0.95005^{+0.00626}_{-0.00704}$	$0.87540^{+0.00979}_{-0.01047}$	$0.84854^{+0.01138}_{-0.01210}$	$0.64767^{+0.01667}_{-0.01702}$
CTEQ6LL reweight	$0.79097^{+0.01062}_{-0.01102}$	$0.94979^{+0.00635}_{-0.00716}$	$0.87493^{+0.00994}_{-0.01063}$	$0.85046^{+0.01148}_{-0.01222}$	$0.64605^{+0.01690}_{-0.01726}$

Sample	N_{Jets}	M_{inv}	$Z-Veto$	Total ϵ
Default	$1.00000^{+0.00000}_{-0.00268}$	$0.99891^{+0.00098}_{-0.00320}$	$0.96825^{+0.00667}_{-0.00818}$	$0.00456^{+0.00018}_{-0.00018}$
CTEQ6L new tune	$1.00000^{+0.00000}_{-0.00391}$	$1.00000^{+0.00000}_{-0.00391}$	$0.96263^{+0.00871}_{-0.01091}$	$0.00451^{+0.00022}_{-0.00021}$
CTEQ6LL new tune	$1.00000^{+0.00000}_{-0.00421}$	$1.00000^{+0.00000}_{-0.00421}$	$0.95752^{+0.00963}_{-0.01197}$	$0.00422^{+0.00022}_{-0.00021}$
CTEQ6L no tune	$1.00000^{+0.00000}_{-0.00435}$	$1.00000^{+0.00000}_{-0.00435}$	$0.95708^{+0.00984}_{-0.01225}$	$0.00404^{+0.00021}_{-0.00020}$
CTEQ6LL no tune	$1.00000^{+0.00000}_{-0.00369}$	$1.00000^{+0.00000}_{-0.00369}$	$0.95693^{+0.00908}_{-0.01112}$	$0.00475^{+0.00023}_{-0.00022}$
CTEQ6L reweight	$1.00000^{+0.00000}_{-0.00331}$	$0.99888^{+0.00104}_{-0.00386}$	$0.95929^{+0.00838}_{-0.01021}$	$0.00455^{+0.00020}_{-0.00020}$
CTEQ6LL reweight	$1.00000^{+0.00000}_{-0.00340}$	$0.99888^{+0.00104}_{-0.00395}$	$0.95354^{+0.00906}_{-0.01090}$	$0.00451^{+0.00021}_{-0.00020}$

Table B.2.: Event selection efficiency for the samples with the different PDF setups. Events with one electron and one muon with the same-sign and the optimized event selection cuts are used.
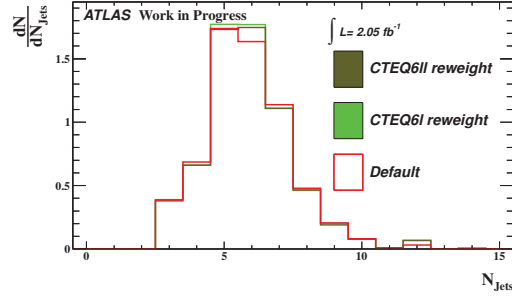
Figure B.2.: N_{Jets} distribution for the default signal sample and the reweighted samples with the PDFs: CTEQ6L and CTEQ6LL. Events with same-sign electrons and the optimized event selection are applied.
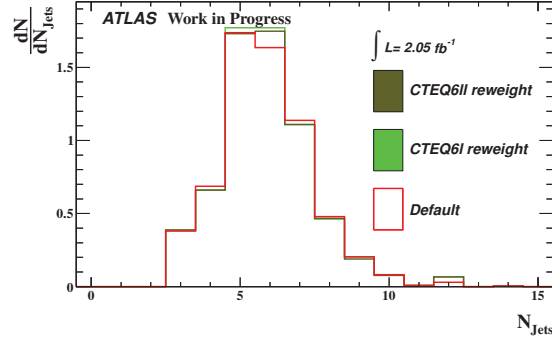
Figure B.3.: E_T^{Jets} distribution for the default signal sample and the reweighted samples with the PDFs: CTEQ6L and CTEQ6LL. Events with same-sign electrons and the optimized event selection are applied.
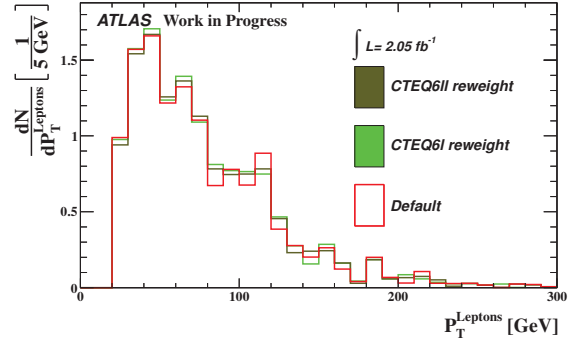
Figure B.4.: $p_T^{Leptons}$ distribution for the default signal sample and the reweighted samples with the PDFs: CTEQ6L and CTEQ6LL. Events with same-sign electrons and the optimized event selection are applied.
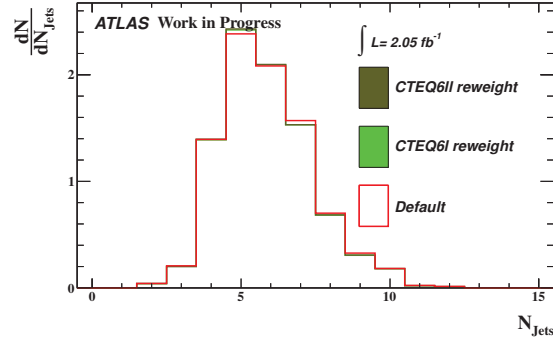
Figure B.5.: N_{Jets} distribution for the default signal sample and the reweighted samples with the PDFs: CTEQ6L and CTEQ6LL. Events with same-sign muons and the optimized event selection are applied.
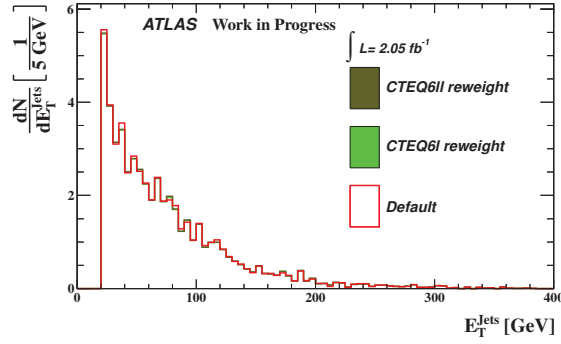
Figure B.6.: E_T^{Jets} distribution for the default signal sample and the reweighted samples with the PDFs: CTEQ6L and CTEQ6LL. Events with same-sign muons and the optimized event selection are applied.
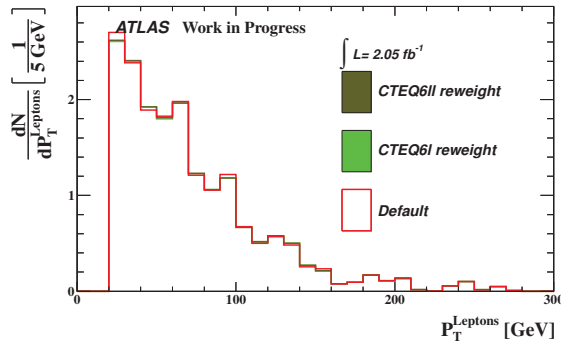
Figure B.7.: $p_T^{Leptons}$ distribution for the default signal sample and the reweighted samples with the PDFs: CTEQ6L and CTEQ6LL. Events with same-sign muons and the optimized event selection are applied.
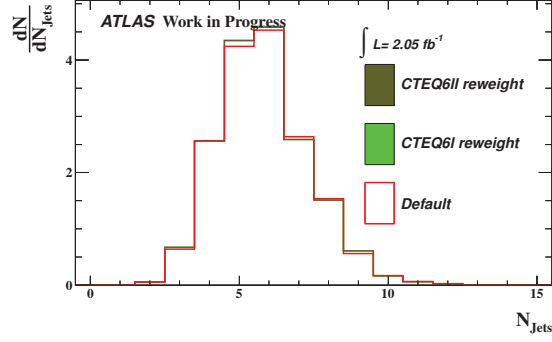
Figure B.8.: N_{Jets} distribution for the default signal sample and the reweighted samples with the PDFs: CTEQ6L and CTEQ6LL. Events with one electron and one muon with same-sign and the optimized event selection are applied.
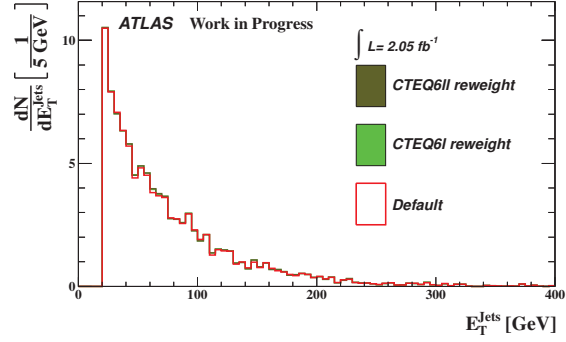
Figure B.9.: E_T^{Jets} distribution for the default signal sample and the reweighted samples with the PDFs: CTEQ6L and CTEQ6LL. Events with one electron and one muon with same-sign and the optimized event selection are applied.
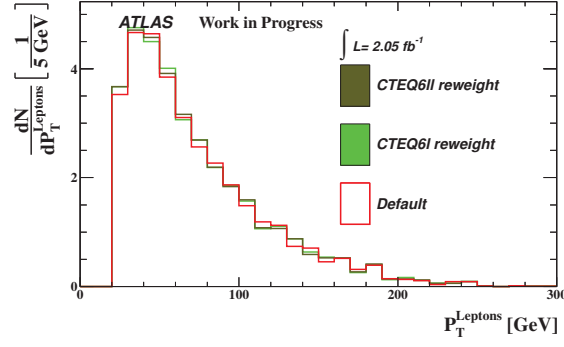
Figure B.10.: $p_T^{Leptons}$ distribution for the default signal sample and the reweighted samples with the PDFs: CTEQ6L and CTEQ6LL. Events with one electron and one muon with same-sign and the optimized event selection are applied.
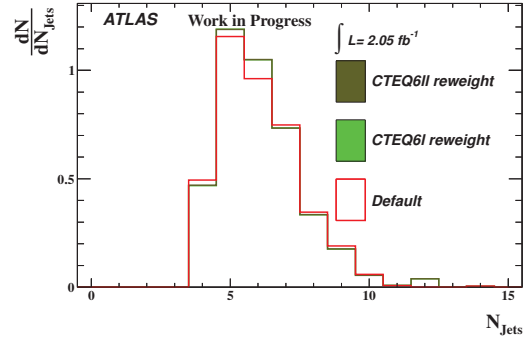
Figure B.11.: N_{Jets} distribution for the default signal sample and the reweighted samples with the PDFs: CTEQ6L and CTEQ6LL. Events with same-sign electrons and the optimized event selection are applied.
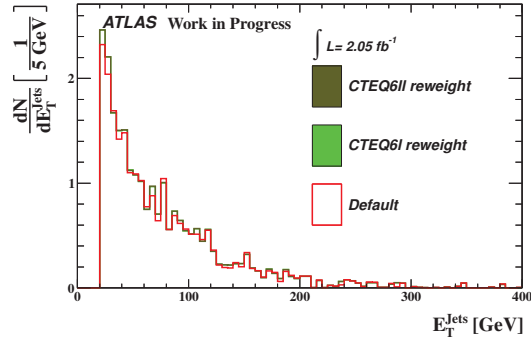
Figure B.12.: E_T^{Jets} distribution for the default signal sample and the reweighted samples with the PDFs: CTEQ6L and CTEQ6LL. Events with same-sign electrons and the optimized event selection are applied.
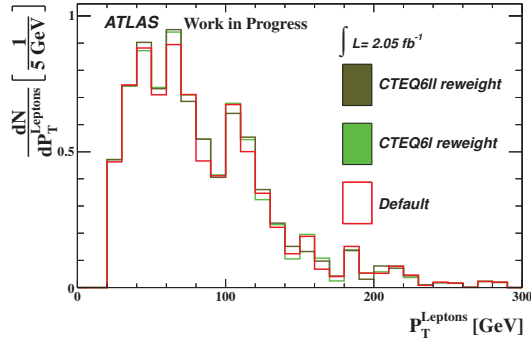
Figure B.13.: $p_T^{Leptons}$ distribution for the default signal sample and the reweighted samples with the PDFs: CTEQ6L and CTEQ6LL. Events with same-sign electrons and the optimized event selection are applied.
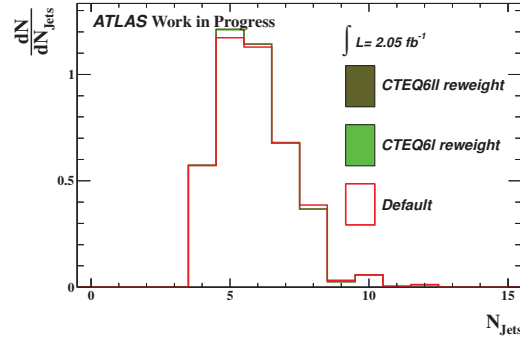
Figure B.14.: N_{Jets} distribution for the default signal sample and the reweighted samples with the PDFs: CTEQ6L and CTEQ6LL. Events with same-sign muons and the optimized event selection are applied.
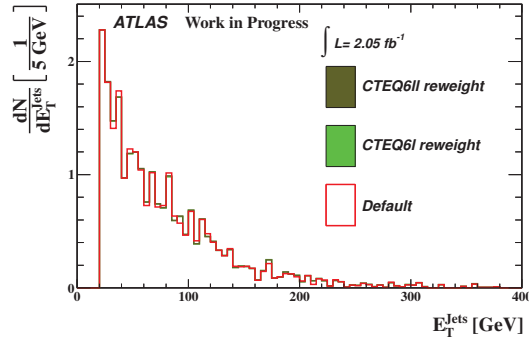
Figure B.15.: E_T^{Jets} distribution for the default signal sample and the reweighted samples with the PDFs: CTEQ6L and CTEQ6LL. Events with same-sign muons and the optimized event selection are applied.
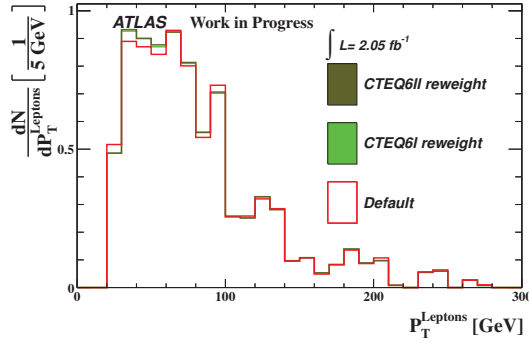
Figure B.16.: $p_T^{Leptons}$ distribution for the default signal sample and the reweighted samples with the PDFs: CTEQ6L and CTEQ6LL. Events with same-sign muons and the optimized event selection are applied.
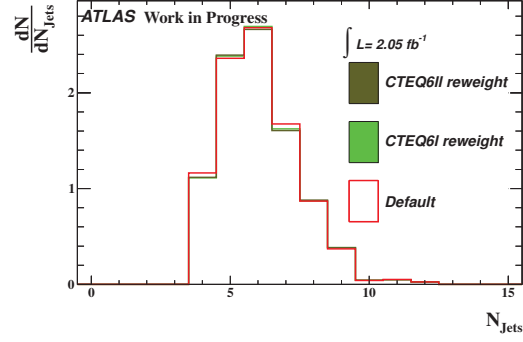
Figure B.17.: N_{Jets} distribution for the default signal sample and the reweighted samples with the PDFs: CTEQ6L and CTEQ6LL. Events with one electron and one muon with same-sign and the optimized event selection are applied.
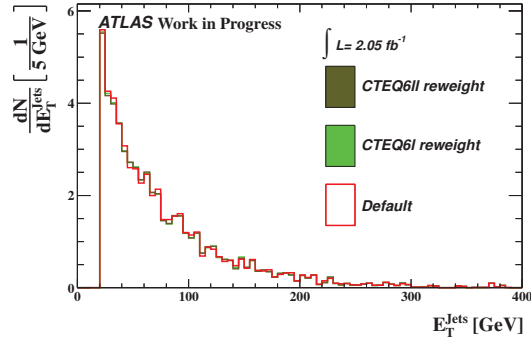
Figure B.18.: E_T^{Jets} distribution for the default signal sample and the reweighted samples with the PDFs: CTEQ6L and CTEQ6LL. Events with one electron and one muon with same-sign and the optimized event selection are applied.
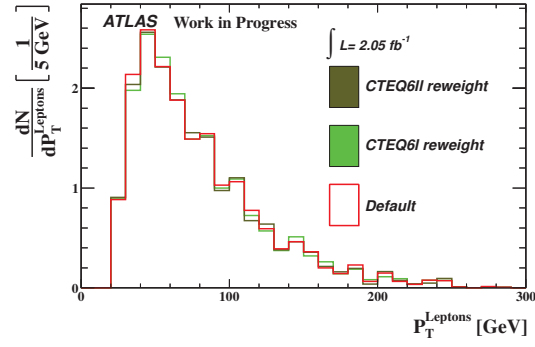
Figure B.19.: $p_T^{Leptons}$ distribution for the default signal sample and the reweighted samples with the PDFs: CTEQ6L and CTEQ6LL. Events with one electron and one muon with same-sign and the optimized event selection are applied.

B.2. ISR/FSR uncertainties

Sample	Generated events	Trigger	$e^+\mu^+/e^-\mu^-$	$P_T^{LeadLep}$	$P_T^{2ndLeadLep}$	E_T^{Miss}
Default	1.45×10^5	$1.00000^{+0.00000}_{-0.00001}$	$0.01791^{+0.00035}_{-0.00035}$	$1.00000^{+0.00000}_{-0.00071}$	$1.00000^{+0.00000}_{-0.00071}$	$0.92094^{+0.00530}_{-0.00563}$
FSR down	4.99×10^4	$1.00000^{+-1.00000}_{-1.00000}$	$0.01721^{+0.00060}_{-0.00058}$	$1.00000^{+0.00000}_{-0.00213}$	$1.00000^{+0.00000}_{-0.00213}$	$0.91036^{+0.00977}_{-0.01078}$
FSR up	4.99×10^4	$1.00000^{+0.00000}_{-0.00004}$	$0.01671^{+0.00059}_{-0.00057}$	$1.00000^{+0.00000}_{-0.00219}$	$1.00000^{+0.00000}_{-0.00219}$	$0.91487^{+0.00969}_{-0.01074}$
ISR down	4.99×10^4	$1.00000^{+-1.00000}_{-1.00000}$	$0.01769^{+0.00061}_{-0.00059}$	$1.00000^{+0.00000}_{-0.00207}$	$1.00000^{+0.00000}_{-0.00207}$	$0.90713^{+0.00980}_{-0.01076}$
ISR up	4.99×10^4	$1.00000^{+-1.00000}_{-1.00000}$	$0.01833^{+0.00062}_{-0.00060}$	$1.00000^{+0.00000}_{-0.00200}$	$1.00000^{+0.00000}_{-0.00200}$	$0.93005^{+0.00844}_{-0.00943}$

Sample	H_T	N_{Jets}	M_{inv}	$Z-Veto$	Total ϵ
Default	$0.98660^{+0.00233}_{-0.00277}$	$1.00000^{+0.00000}_{-0.00078}$	$1.00000^{+0.00000}_{-0.00078}$	$1.00000^{+0.00000}_{-0.00078}$	$0.01628^{+0.00034}_{-0.00033}$
FSR down	$0.98210^{+0.00468}_{-0.00607}$	$1.00000^{+0.00000}_{-0.00238}$	$1.00000^{+0.00000}_{-0.00238}$	$1.00000^{+0.00000}_{-0.00238}$	$0.01539^{+0.00057}_{-0.00055}$
FSR up	$0.99083^{+0.00336}_{-0.00488}$	$1.00000^{+0.00000}_{-0.00242}$	$1.00000^{+0.00000}_{-0.00242}$	$1.00000^{+0.00000}_{-0.00242}$	$0.01515^{+0.00056}_{-0.00054}$
ISR down	$0.98377^{+0.00440}_{-0.00577}$	$1.00000^{+0.00105}_{-0.00290}$	$1.00000^{+0.00000}_{-0.00233}$	$1.00000^{+0.00000}_{-0.00233}$	$0.01577^{+0.00057}_{-0.00055}$
ISR up	$0.98472^{+0.00415}_{-0.00543}$	$1.00000^{+0.00000}_{-0.00218}$	$1.00000^{+0.00000}_{-0.00218}$	$1.00000^{+0.00000}_{-0.00218}$	$0.01679^{+0.00059}_{-0.00057}$

Table B.3.: Event selection efficiency for the samples with the different ISR/FSR setups. Events with one electron and one muon with the same-sign and the top event selection cuts are used.

B. Additional information for the systematic studies

Sample	Generated events	Trigger	$e^+\mu^-/e^-\mu^-$	$P_T^{LeadLep}$	$P_T^{2ndLeadLep}$
Default	1.45×10^5	$1.00000^{+0.00000}_{-0.00001}$	$0.01791^{+0.00035}_{-0.00035}$	$0.97146^{+0.00326}_{-0.00364}$	$0.93767^{+0.00481}_{-0.00517}$
FSR down	4.99×10^4	$1.00000^{+-1.00000}_{-1.00000}$	$0.01721^{+0.00060}_{-0.00058}$	$0.95576^{+0.00700}_{-0.00814}$	$0.95372^{+0.00732}_{-0.00850}$
FSR up	4.99×10^4	$1.00000^{+0.00000}_{-0.00004}$	$0.01671^{+0.00059}_{-0.00057}$	$0.97002^{+0.00587}_{-0.00710}$	$0.93201^{+0.00886}_{-0.00999}$
ISR down	4.99×10^4	$1.00000^{+-1.00000}_{-1.00000}$	$0.01769^{+0.00061}_{-0.00059}$	$0.96829^{+0.00587}_{-0.00702}$	$0.94503^{+0.00779}_{-0.00890}$
ISR up	4.99×10^4	$1.00000^{+-1.00000}_{-1.00000}$	$0.01833^{+0.00062}_{-0.00060}$	$0.96066^{+0.00640}_{-0.00749}$	$0.94198^{+0.00788}_{-0.00895}$

Sample	E_T^{Miss}	$E_T^{LeadJet}$	$\eta^{LeadLep}$	$\eta^{2ndLeadLep}$	H_T
Default	$0.92083^{+0.00555}_{-0.00592}$	$0.98943^{+0.00217}_{-0.00266}$	$0.88569^{+0.00687}_{-0.00724}$	$0.83158^{+0.00861}_{-0.00896}$	$0.93375^{+0.00624}_{-0.00682}$
FSR down	$0.91060^{+0.01023}_{-0.01133}$	$0.99158^{+0.00332}_{-0.00497}$	$0.88402^{+0.01211}_{-0.01325}$	$0.85760^{+0.01410}_{-0.01530}$	$0.94963^{+0.00943}_{-0.01126}$
FSR up	$0.91777^{+0.01003}_{-0.01120}$	$0.98266^{+0.00489}_{-0.00648}$	$0.88088^{+0.01250}_{-0.01368}$	$0.84307^{+0.01501}_{-0.01621}$	$0.93465^{+0.01101}_{-0.01287}$
ISR down	$0.90470^{+0.01037}_{-0.01142}$	$0.98769^{+0.00400}_{-0.00554}$	$0.90443^{+0.01098}_{-0.01217}$	$0.81317^{+0.01543}_{-0.01643}$	$0.92090^{+0.01174}_{-0.01344}$
ISR up	$0.93116^{+0.00881}_{-0.00991}$	$0.99481^{+0.00247}_{-0.00406}$	$0.89700^{+0.01102}_{-0.01211}$	$0.83576^{+0.01426}_{-0.01528}$	$0.94435^{+0.00955}_{-0.01122}$

Sample	N_{Jets}	M_{inv}	$Z - Veto$	Total ϵ
Default	$1.00000^{+0.00000}_{-0.00124}$	$1.00000^{+0.00000}_{-0.00124}$	$0.94932^{+0.00569}_{-0.00633}$	$0.00971^{+0.00026}_{-0.00026}$
FSR down	$1.00000^{+0.00000}_{-0.00359}$	$1.00000^{+0.00000}_{-0.00359}$	$0.95481^{+0.00917}_{-0.01114}$	$0.00974^{+0.00046}_{-0.00044}$
FSR up	$1.00000^{+0.00000}_{-0.00388}$	$1.00000^{+0.00000}_{-0.00388}$	$0.94068^{+0.01087}_{-0.01290}$	$0.00890^{+0.00044}_{-0.00042}$
ISR down	$1.00000^{+0.00000}_{-0.00374}$	$1.00000^{+0.00000}_{-0.00374}$	$0.95910^{+0.00891}_{-0.01099}$	$0.00940^{+0.00045}_{-0.00043}$
ISR up	$1.00000^{+0.00000}_{-0.00337}$	$1.00000^{+0.00000}_{-0.00337}$	$0.96317^{+0.00804}_{-0.00992}$	$0.01048^{+0.00047}_{-0.00045}$

Table B.4.: Event selection efficiency for the samples with the different ISR/FSR setups. Events with one electron and one muon with the same-sign and the optimized event selection cuts are used.

215
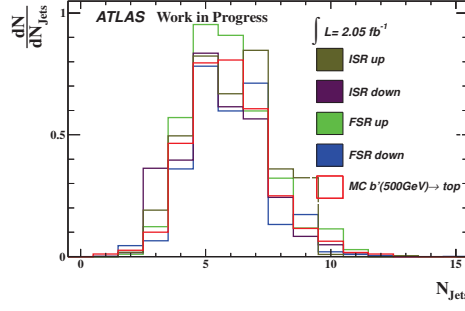
Figure B.20.: N_{Jets} distribution for the lepton category e^+e^+/e^-e^- for the "Default" and the different Monte carlo samples with the different ISR/FSR configuration. Only the opject selection are applied and no event selection criteria. The distribution are scaled to a luminosity of $\mathcal{L} = 2.05\,\mathrm{fb}^{-1}$
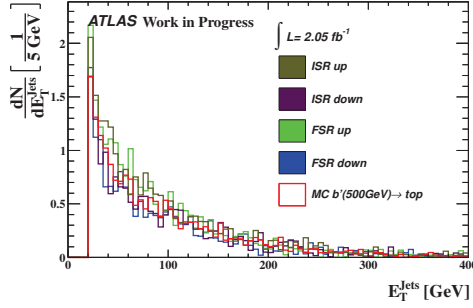
Figure B.21.: E_T^{Jets} distribution for the lepton category e^+e^+/e^-e^- for the "Default" and the different Monte carlo samples with the different ISR/FSR configuration. Only the opject selection are applied and no event selection criteria. The distribution are scaled to a luminosity of $\mathcal{L} = 2.05\,\mathrm{fb}^{-1}$
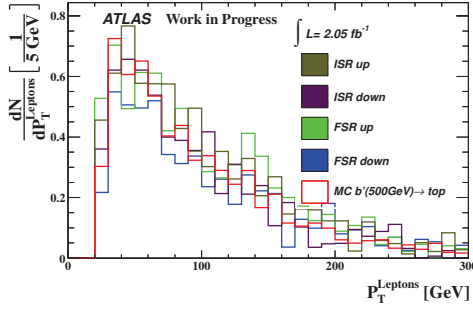
Figure B.22.: $p_T^{Leptons}$ distribution for the lepton category e^+e^+/e^-e^- for the "Default" and the different Monte carlo samples with the different ISR/FSR configuration. Only the opject selection are applied and no event selection criteria. The distribution are scaled to a luminosity of $\mathcal{L} = 2.05\,\mathrm{fb}^{-1}$
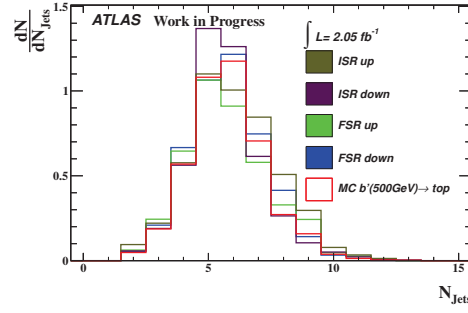
Figure B.23.: N_{Jets} distribution for the lepton category $\mu^+\mu^+/\mu^-\mu^-$ for the "Default" and the different Monte carlo samples with the different ISR/FSR configuration. Only the opject selection are applied and no event selection criteria. The distribution are scaled to a luminosity of $\mathcal{L} = 2.05\,\text{fb}^{-1}$
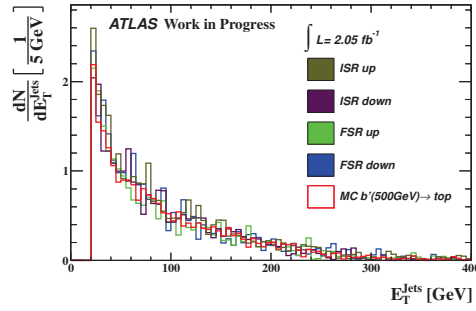
Figure B.24.: E_T^{Jets} distribution for the lepton category $\mu^+\mu^+/\mu^-\mu^-$ for the "Default" and the different Monte carlo samples with the different ISR/FSR configuration. Only the opject selection are applied and no event selection criteria. The distribution are scaled to a luminosity of $\mathcal{L} = 2.05\,\text{fb}^{-1}$
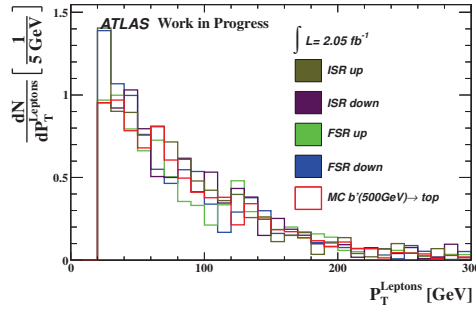
Figure B.25.: $p_T^{Leptons}$ distribution for the lepton category $\mu^+\mu^+/\mu^-\mu^-$ for the "Default" and the different Monte carlo samples with the different ISR/FSR configuration. Only the opject selection are applied and no event selection criteria. The distribution are scaled to a luminosity of $\mathcal{L} = 2.05\,\text{fb}^{-1}$
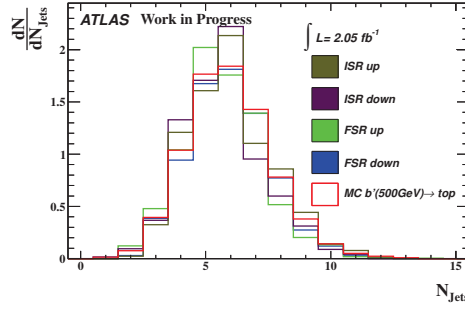
Figure B.26.: N_{Jets} distribution for the lepton category $e^+\mu^+/e^-\mu^-$ for the "Default" and the different Monte carlo samples with the different ISR/FSR configuration. Only the opject selection are applied and no event selection criteria. The distribution are scaled to a luminosity of $\mathcal{L} = 2.05\,\mathrm{fb}^{-1}$
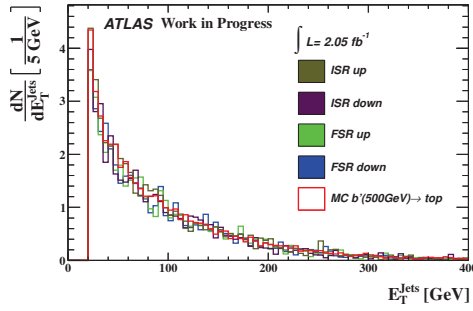
Figure B.27.: E_T^{Jets} distribution for the lepton category $e^+\mu^+/e^-\mu^-$ for the "Default" and the different Monte carlo samples with the different ISR/FSR configuration. Only the opject selection are applied and no event selection criteria. The distribution are scaled to a luminosity of $\mathcal{L} = 2.05\,\mathrm{fb}^{-1}$
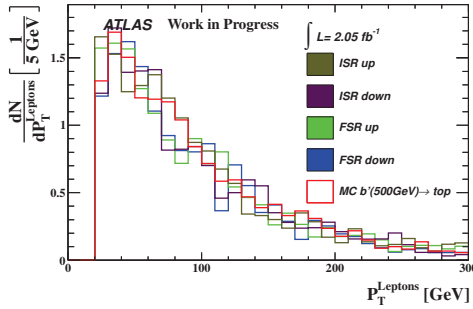
Figure B.28.: $p_T^{Leptons}$ distribution for the lepton category $e^+\mu^+/e^-\mu^-$ for the "Default" and the different Monte carlo samples with the different ISR/FSR configuration. Only the opject selection are applied and no event selection criteria. The distribution are scaled to a luminosity of $\mathcal{L} = 2.05\,\mathrm{fb}^{-1}$

C. Additional information for the signal extraction and mass limit calculation

	e^+e^+/e^-e^-	$e^+\mu^+/e^-\mu^-$	e^+mu^+/e^-mu^-	$mu^+\mu^+/mu^-\mu^-$
	Egamma stream		Muons stream	
Observed	8	14	11	6
$Z \to e^+e^-$	0.317445	0	0	0
$t\bar{t}$	1.94176	3.95611	2.86895	0
Other BG	1.82883	3.81874	2.91497	2.74957
Final signal yields	3.91197	6.22515	5.21608	3.25043
Expected	39.1598	97.8529	76.1663	57.7261

Table C.1.: Measured events and determined final and expected signal yields in the dominated background in the signal region. The data of the egamma and muons stream are used separately and the optimized event selection criteria are applied. For the signal a b mass of $m_{b'} = 300\,\text{GeV}$ is used.

	e^+e^+/e^-e^-	$e^+\mu^+/e^-\mu^-$	e^+mu^+/e^-mu^-	$mu^+\mu^+/mu^-\mu^-$
	Egamma stream		Muons stream	
Observed	8	11		6
$Z \to e^+e^-$	0.309807	0	0	0
$t\bar{t}$	1.94453	3.96564	2.87738	0
Other BG	1.82883	3.81874	2.91497	2.74957
Final signal yields	3.91683	6.21562	5.20766	3.25043
Expected	20.251	53.9163	41.8725	28.2287

Table C.2.: Measured events and determined final and expected signal yields in the dominated background in the signal region. The data of the egamma and muons stream are used separately and the top event selection criteria are applied. For the signal a b mass of $m_{b'} = 350\,\text{GeV}$ is used.

	e^+e^+/e^-e^-	$e^+\mu^+/e^-\mu^-$	e^+mu^+/e^-mu^-	$mu^+\mu^+/mu^-\mu^-$
	Egamma stream		Muons stream	
Observed	8	14	11	6
$Z \to e^+e^-$	0.306709	0	0	0
$t\bar{t}$	1.94832	3.96538	2.87842	0
Other BG	1.82883	3.81874	2.91497	2.74957
Final signal yields	3.91614	6.21588	5.20662	3.25043
Expected	5.2338	13.1748	10.3248	7.09934

Table C.3.: Measured events and determined final and expected signal yields in the dominated background in the signal region. The data of the egamma and muons stream are used separately and the top event selection criteria are applied. For the signal a b mass of $m_{b'} = 450$ GeV is used.

	e^+e^+/e^-e^-	$e^+\mu^+/e^-\mu^-$	e^+mu^+/e^-mu^-	$mu^+\mu^+/mu^-\mu^-$
	Egamma stream		Muons stream	
Observed	8	14	11	6
$Z \to e^+e^-$	0.306626	0	0	0
$t\bar{t}$	1.94978	3.97105	2.88283	0
Other BG	1.82883	3.81874	2.91497	2.74957
Final signal yields	3.91477	6.21021	5.2022	3.25043
Expected	2.81925	7.42322	5.81612	3.69279

Table C.4.: Measured events and determined final and expected signal yields in the dominated background in the signal region. The data of the egamma and muons stream are used separately and the top event selection criteria are applied. For the signal a b mass of $m_{b'} = 500$ GeV is used.

	e^+e^+/e^-e^-	$e^+\mu^+/e^-\mu^-$	e^+mu^+/e^-mu^-	$mu^+\mu^+/mu^-\mu^-$
	Egamma stream		Muons stream	
Observed	8	14	11	6
$Z \to e^+e^-$	0.30705	0	0	0
$t\bar{t}$	1.95592	3.96758	2.87891	0
Other BG	1.82883	3.81874	2.91497	2.74957
Final signal yields	3.90821	6.21368	5.20612	3.25043
Expected	1.65975	3.82127	2.95765	1.98625

Table C.5.: Measured events and determined final and expected signal yields in the dominated background in the signal region. The data of the egamma and muons stream are used separately and the top event selection criteria are applied. For the signal a b mass of $m_{b'} = 550$ GeV is used.

	e^+e^+/e^-e^-	$e^+\mu^+/e^-\mu^-$	e^+mu^+/e^-mu^-	$mu^+\mu^+/mu^-\mu^-$
	Egamma stream		Muons stream	
Observed	8	14	11	6
$Z \to e^+e^-$	0.305189	0	0	0
$t\bar{t}$	1.96023	3.96983	2.8822	0
Other BG	1.82883	3.81874	2.91497	2.74957
Final signal yields	3.90576	6.21142	5.20284	3.25043
Expected	0.537039	1.18135	0.926647	0.594124

Table C.6.: Measured events and determined final and expected signal yields in the dominated background in the signal region. The data of the egamma and muons stream are used separately and the top event selection criteria are applied. For the signal a b mass of $m_{b'} = 600\,\text{GeV}$ is used.

	e^+e^+/e^-e^-	$e^+\mu^+/e^-\mu^-$	e^+mu^+/e^-mu^-
	Egamma stream		Muons stream
Observed	1	3	3
$Z \to e^+e^-$	0	0	0
$t\bar{t}$	0.61149	1.28677	0.922748
Other BG	0.230059	0.0162672	-0.00552478
Final signal yields	0.158451	1.69696	2.08278
Expected	22.971	45.5686	34.3734

Table C.7.: Measured events and determined final and expected signal yields in the dominated background in the signal region. The data of the egamma and muons stream are used separately and the optimized event selection criteria are applied. For the signal a b mass of $m_{b'} = 300\,\text{GeV}$ is used.

	e^+e^+/e^-e^-	$e^+\mu^+/e^-\mu^-$	e^+mu^+/e^-mu^-
	Egamma stream		Muons stream
Observed	1	3	3
$Z \to e^+e^-$	0	0	0
$t\bar{t}$	0.611511	1.29253	0.929962
Other BG	0.230059	0.0162672	-0.00552478
Final signal yields	0.15843	1.69121	2.07556
Expected	12.59	29.4981	21.8968

Table C.8.: Measured events and determined final and expected signal yields in the dominated background in the signal region. The data of the egamma and muons stream are used separately and the optimized event selection criteria are applied. For the signal a b mass of $m_{b'} = 350\,\text{GeV}$ is used.

	e^+e^+/e^-e^-	$e^+\mu^+/e^-\mu^-$	e^+mu^+/e^-mu^-
	Egamma stream		Muons stream
Observed	1	3	3
$Z \to e^+e^-$	0	0	0
$t\bar{t}$	0.611798	1.28953	0.927131
Other BG	0.230059	0.0162672	-0.00552478
Final signal yields	0.158143	1.6942	2.07839
Expected	3.92254	7.58935	5.74744

Table C.9.: Measured events and determined final and expected signal yields in the dominated background in the signal region. The data of the egamma and muons stream are used separately and the optimized event selection criteria are applied. For the signal a b mass of $m_{b'} = 450\,\text{GeV}$ is used.

	e^+e^+/e^-e^-	$e^+\mu^+/e^-\mu^-$	e^+mu^+/e^-mu^-
	Egamma stream		Muons stream
Observed	1	3	3
$Z \to e^+e^-$	0	0	0
$t\bar{t}$	0.611815	1.2911	0.929225
Other BG	0.230059	0.0162672	-0.00552478
Final signal yields	0.158126	1.69264	2.0763
Expected	2.15296	4.34397	3.30531

Table C.10.: Measured events and determined final and expected signal yields in the dominated background in the signal region. The data of the egamma and muons stream are used separately and the optimized event selection criteria are applied. For the signal a b mass of $m_{b'} = 500\,\text{GeV}$ is used.

	e^+e^+/e^-e^-	$e^+\mu^+/e^-\mu^-$	e^+mu^+/e^-mu^-
	Egamma stream		Muons stream
Observed	1	3	3
$Z \to e^+e^-$	0	0	0
$t\bar{t}$	0.6118	1.29111	0.928191
Other BG	0.230059	0.0162672	-0.00552478
Final signal yields	0.158141	1.69262	2.07733
Expected	1.16777	2.36993	1.77802

Table C.11.: Measured events and determined final and expected signal yields in the dominated background in the signal region. The data of the egamma and muons stream are used separately and the optimized event selection criteria are applied. For the signal a b mass of $m_{b'} = 550\,\text{GeV}$ is used.

	e^+e^+/e^-e^-	$e^+\mu^+/e^-\mu^-$	e^+mu^+/e^-mu^-
	Egamma stream		Muons stream
Observed	1	3	3
$Z \to e^+e^-$	0	0	0
$t\bar{t}$	0.61204	1.29135	0.928912
Other BG	0.230059	0.0162672	-0.00552478
Final signal yields	0.157901	1.69238	2.07661
Expected	0.388648	0.726695	0.546675

Table C.12.: Measured events and determined final and expected signal yields in the dominated background in the signal region. The data of the egamma and muons stream are used separately and the optimized event selection criteria are applied. For the signal a b mass of $m_{b'} = 600\,\text{GeV}$ is used.

Bibliography

[1] S.L. Glashow. Partial Symmetries of Weak Interactions. *Nucl.Phys.*, 22:579–588, 1961. doi: 10.1016/0029-5582(61)90469-2.

[2] S. Weinberg. A model of leptons. *Phys. Rev. Lett.*, 19:1264–1266, Nov 1967. doi: 10.1103/PhysRevLett.19.1264. URL `http://link.aps.org/doi/10.1103/PhysRevLett.19.1264`.

[3] A. Salam. *in Elementary Particle Theory, p. 367*. Almqvist and Wiksell, Stockholm, 1968.

[4] G.'t Hooft. Renormalizable lagrangians for massive yang-mills fields. *Nuclear Physics B*, 35(1):167 – 188, 1971. ISSN 0550-3213. doi: 10.1016/0550-3213(71)90139-8. URL `http://www.sciencedirect.com/science/article/pii/0550321371901398`.

[5] G. 't Hooft and M. Veltman. Regularization and renormalization of gauge fields. *Nuclear Physics B*, 44(1):189 – 213, 1972. ISSN 0550-3213. doi: 10.1016/0550-3213(72)90279-9. URL `http://www.sciencedirect.com/science/article/pii/0550321372902799`.

[6] H. Fritzsch, M. Gell-Mann, and H. Leutwyler. Advantages of the Color Octet Gluon Picture. *Phys.Lett.*, B47:365–368, 1973. doi: 10.1016/0370-2693(73)90625-4.

[7] D. J. Gross and F. Wilczek. Ultraviolet behavior of non-abelian gauge theories. *Phys. Rev. Lett.*, 30:1343–1346, Jun 1973. doi: 10.1103/PhysRevLett.30.1343. URL `http://link.aps.org/doi/10.1103/PhysRevLett.30.1343`.

[8] P. W. Higgs. Broken symmetries, massless particles and gauge fields. *Phys.Lett.*, 12:132–133, 1964. doi: 10.1016/0031-9163(64)91136-9.

[9] P. W. Higgs. Broken symmetries and the masses of gauge bosons. *Phys. Rev. Lett.*, 13:508–509, Oct 1964. doi: 10.1103/PhysRevLett.13.508. URL `http://link.aps.org/doi/10.1103/PhysRevLett.13.508`.

Bibliography

[10] P. W. Higgs. Spontaneous symmetry breakdown without massless bosons. *Phys. Rev.*, 145:1156–1163, May 1966. doi: 10.1103/PhysRev.145.1156. URL `http://link.aps.org/doi/10.1103/PhysRev.145.1156`.

[11] F. Englert and R. Brout. Broken symmetry and the mass of gauge vector mesons. *Phys. Rev. Lett.*, 13:321–323, Aug 1964. doi: 10.1103/PhysRevLett.13.321. URL `http://link.aps.org/doi/10.1103/PhysRevLett.13.321`.

[12] G. S. Guralnik, C. R. Hagen, and T. W. B. Kibble. Global conservation laws and massless particles. *Phys. Rev. Lett.*, 13:585–587, Nov 1964. doi: 10.1103/PhysRevLett.13.585. URL `http://link.aps.org/doi/10.1103/PhysRevLett.13.585`.

[13] A. D. Sakharov. Violation of cp in variance, c asymmetry, and baryon asymmetry of the universe. *Soviet Physics Uspekhi*, 34(5):392, 1991. `http://stacks.iop.org/0038-5670/34/i=5/a=A08`.

[14] W. Hou. Source of CP Violation for Baryon Asymmetry of the Universe. Technical report, 2008. `http://arxiv.org/abs/0803.1234v3`.

[15] P.Q. Hung and C. Xiong. Dynamical Electroweak Symmetry Breaking with a Heavy Fourth Generation. *Nucl.Phys.*, B848:288–302, 2011. doi: 10.1016/j.nuclphysb.2011.02.018.

[16] B. Holdom. The discovery of the fourth family at the lhc: what if? *Journal of High Energy Physics*, 2006(08):076, 2006. URL `http://stacks.iop.org/1126-6708/2006/i=08/a=076`.

[17] G. D. Kribs, T. Plehn, M. Spannowsky, and T. M.P. Tait. Four generations and Higgs physics. *Phys.Rev.*, D76:075016, 2007. doi: 10.1103/PhysRevD.76.075016.

[18] J. Holt. Beyond the Standard Model. *Scientific American*, 2006.

[19] K. Nakamura and Particle Data Group. *Review of Particle Physics*, volume 37. 2010. `http://stacks.iop.org/0954-3899/37/i=7A/a=075021`.

[20] D. Wendland. Master thesis: Search for a signal of quarks of a fourth generation in same-sign dilepton final states with ATLAS. Humboldt University Berlin, 2010.

[21] V.A. Bednyakov, N.D. Giokaris, and A.V. Bednyakov. On the higgs mass generation mechanism in the standard model. *Physics of Particles and Nuclei*, 39:

13–36, 2008. ISSN 1063-7796. doi: 10.1134/S1063779608010024. URL `http://dx.doi.org/10.1134/S1063779608010024`.

[22] Search for the Standard Model Higgs boson at LEP. *Physics Letters B*, 565(0): 61 – 75, 2003. ISSN 0370-2693. doi: 10.1016/S0370-2693(03)00614-2. URL `http://www.sciencedirect.com/science/article/pii/S0370269303006142`.

[23] Combined CDF and D0 Search for Standard Model Higgs Boson Production with up to 10.0 fb-1 of Data. *hep-ex/1203.3774*, 2012. Preliminary results prepared for the Winter 2012 Conferences.

[24] G. Aad et al. An update to the combined search for the Standard Model Higgs boson with the ATLAS detector at the LHC using up to 4.9 fb-1 of pp collision data at $\sqrt{s} = 7$ TeV. Technical Report ATLAS-CONF-2012-019, CERN, Geneva, Mar 2012.

[25] S. Chatrchyan et al. Combined results of searches for the standard model Higgs boson in pp collisions at $\sqrt{s} = 7$ TeV. *Physics Letters B*, 710(1):26 – 48, 2012. ISSN 0370-2693. doi: 10.1016/j.physletb.2012.02.064. URL `http://www.sciencedirect.com/science/article/pii/S0370269312002055`.

[26] S. Kortner. SM scalar boson search with ATLAS at Rencontres de Moriond EW 2012. `http://indico.in2p3.fr/conferenceOtherViews.py?view=standard&confId=6001`.

[27] C. Jarlskog. Commutator of the quark mass matrices in the standard electroweak model and a measure of maximal CP nonconservation. *Phys. Rev. Lett.*, 55:1039–1042, Sep 1985. doi: 10.1103/PhysRevLett.55.1039. URL `http://link.aps.org/doi/10.1103/PhysRevLett.55.1039`.

[28] W. S. Hou. CP Violation and Baryogenesis from New Heavy Quarks. *Chin. J. Phys.*, 47:134, 2009.

[29] G. Hinshaw et al. Five-Year Wilkinson Microwave Anisotropy Probe (WMAP) Observations:Data Processing, Sky Maps, & Basic Results. *Astrophys. J. Suppl.*, 180:225–245, 2009. doi: 10.1088/0067-0049/180/2/225.

[30] NASA. COBE: Cosmic Background Explorer. `http://lambda.gsfc.nasa.gov/product/cobe/`.

[31] S. P. Martin. A Supersymmetry Primer. *hep-ph/9709356*, Sep 1997.

Bibliography

[32] S. Dittmaier, S. Dittmaier, C. Mariotti, G. Passarino, R. Tanaka, et al. Handbook of LHC Higgs Cross Sections: 2. Differential Distributions. *hep-ph/1201.3084*, 2012.

[33] P.Q. Hung. Minimal SU(5) resuscitated by longlived quarks and leptons. *Phys.Rev.Lett.*, 80:3000–3003, 1998. doi: 10.1103/PhysRevLett.80.3000.

[34] M.S. Chanowitz, M.A. Furman, and I. Hinchliffe. Weak interactions of ultra heavy fermions (II). *Nuclear Physics B*, 153(0):402 – 430, 1979. ISSN 0550-3213. doi: 10.1016/0550-3213(79)90606-0. `http://www.sciencedirect.com/science/article/pii/0550321379906060`.

[35] M. E. Peskin and T. Takeuchi. New constraint on a strongly interacting Higgs sector. *Phys. Rev. Lett.*, 65(8):964–967, Aug 1990. doi: 10.1103/PhysRevLett.65.964.

[36] H. J. He, N. Polonsky, and S. Su. Extra families, Higgs spectrum and oblique corrections. *Phys.Rev.*, D64:053004, 2001. doi: 10.1103/PhysRevD.64.053004.

[37] Precision electroweak measurements on the Z resonance. *Phys. Rept.*, 427:257–454, 2006. doi: 10.1016/j.physrep.2005.12.006.

[38] B. Adeva et al. The construction of the L3 experiment. *Nuclear Instruments and Methods in Physics Research Section A: Accelerators, Spectrometers, Detectors and Associated Equipment*, 289(1-2):35 – 102, 1990. ISSN 0168-9002. doi: DOI:10.1016/0168-9002(90)90250-A. `http://www.sciencedirect.com/science/article/B6TJM-470F3FY-4B/2/6a007b800a0bfaf46838e6b33386fc3e`.

[39] L3 Collaboration. Search for Heavy Neutral and Charged Leptons in e^+e^- Annihilation at LEP. *Phys. Lett. B.*, 517(CERN-EP-2001-046):75–85, 2001.

[40] L. M. Carpenter and A. Rajaraman. Revisiting Constraints on Fourth Generation Neutrino Masses. *Phys.Rev.*, D82:114019, 2010. doi: 10.1103/PhysRevD.82.114019.

[41] The CDF collaboration. Search for Heavy Top $t' \to Wq$ in Lepton Plus Jets Events in $\int \mathcal{L}dt = 4.6\,\mathrm{fb}^{-1}$. *Conf. Note 10110*, 2010. `http://www-cdf.fnal.gov/physics/new/top/confNotes/tprime_CDFnotePub.pdf`.

[42] T. Aaltonen et al. Search for New Bottomlike Quark Pair Decays $Q\bar{Q} \rightarrow (tW^{\mp})(\bar{t}W^{\pm})$ in Same-Charge Dilepton Events. *Phys. Rev. Lett.*, 104(9):091801, Mar 2010. doi: 10.1103/PhysRevLett.104.091801.

[43] S. Chatrchyan et al. Search for heavy, top-like quark pair production in the dilepton final state in pp collisions at $\sqrt{s} = 7$ TeV. *Phys.Lett.*, B716:103–121, 2012. doi: 10.1016/j.physletb.2012.07.059.

[44] I. Bertram et al. A Recipe for the construction of confidence limits. FERMILAB-TM-2104.

[45] S. Chatrchyan et al. Search for heavy bottom-like quarks in 4.9 inverse femtobarns of pp collisions at $\sqrt{s} = 7$ TeV. *hep-ex/1204.1088*, 2012.

[46] G.s Aad et al. Search for down-type fourth generation quarks with the ATLAS detector in events with one lepton and high transverse momentum hadronically decaying W bosons in $\sqrt{s} = 7$ TeV pp collisions. *Phys. Rev. Lett.*, 109:032001, Jul 2012. doi: 10.1103/PhysRevLett.109.032001. URL `http://link.aps.org/doi/10.1103/PhysRevLett.109.032001`.

[47] G. Aad et al. Search for pair production of a heavy quark decaying to a W boson and a b quark in the lepton+jets channel with the ATLAS detector. *Phys. Rev. Lett.*, 108:261802, Jun 2012. doi: 10.1103/PhysRevLett.108.261802. URL `http://link.aps.org/doi/10.1103/PhysRevLett.108.261802`.

[48] P. Q. Hung and M. Sher. Experimental constraints on fourth generation quark masses. *Phys. Rev.*, D77:037302, 2008. doi: 10.1103/PhysRevD.77.037302.

[49] H. Lacker and A. Menzel. Constraints on CKM matrix elements within a fourth generation. January 14-16 2010, Taipei, Second Workshop on Beyond 3 Generation Standard Model.

[50] A. Menzel. Diploma thesis: Constraints on Matrix Elements of the Quark and Neutrino Mixing Matrix within a Four Generation Standard Model with CKMfitter, Humboldt University Berlin, 2010.

[51] M. Aliev, Lacker H., U. Langenfeld, S. Moch, P. Uwer, and W. Wiedermann. – HATHOR – HAdronic Top and Heavy quarks crOss section calculatoR. Technical Report DESY 10-091, HU-EP-10-33, SFB/CPP-10-60, DESY, 2010. `http://arxiv.org/abs/1007.1327v1`.

Bibliography

[52] S. Moch and P. Uwer. Theoretical status and prospects for top-quark pair production at hadron colliders. *Phys.Rev.*, D78:034003, 2008. doi: 10.1103/PhysRevD. 78.034003.

[53] S. Moch and P. Uwer. Heavy-quark pair production at two loops in QCD. *Nucl.Phys.Proc.Suppl.*, 183:75–80, 2008. doi: 10.1016/j.nuclphysbps.2008.09.085.

[54] O. Eberhardt. Diploma thesis: Constraints on Matrix Elements of the Quark and Neutrino Mixing Matrix within a Four Generation Standard Model with CKMfitter., University Regensburg, 2010.

[55] O. S. Brüning, P. Collier, P. Lebrun, S. Myers, R. Ostojic, J. Poole, and P. Proudlock. *LHC Design Report.* Geneva, 2004. CERN-2004-003-V-1.

[56] G. Aad et al. The ATLAS Experiment at the CERN Large Hadron Collider. *JINST*, 3(S08003), 2008. `http://iopscience.iop.org/1748-0221/3/08/S08003`.

[57] S. Chatrchyan et al. The CMS Experiment at the CERN LHC. *JINST*, 3(S08004), 2008. `http://iopscience.iop.org/1748-0221/3/08/S08004`.

[58] K. Aamodt et al. The ALICE Experiment at the CERN LHC. *JINST*, 3(S08002), 2008. `http://iopscience.iop.org/1748-0221/3/08/S08002`.

[59] A. Augusto Alves Jr. et al. The LHCb Detector at the LHC. *JINST*, 3(S08005), 2008. `http://iopscience.iop.org/1748-0221/3/08/S08005`.

[60] CERN. Overview of CERN's acclerator layout. `http://ps-div.web.cern.ch/ ps-div/LHC-PS/LHC-PS.html`.

[61] G. Aad et al. Commissioning of the ATLAS high-performance b-tagging algorithms in the 7 TeV collision data. ATLAS-CONF-2011-102.

[62] J. Haller, A. Dos Anjos, N. Ellis, M. Landon, R. Spiwoks, T. Wengler, W. Wiedenmann, and H. Zobernig. Configuration of the ATLAS trigger. oai:cds.cern.ch:849080. Technical Report ATL-DAQ-CONF-2005-024, CERN, Geneva, 2005.

[63] Sjöstrand, T. and Mrenna, S. and Skands, P. PYTHIA 6.4 physics and manual. *Journal of High Energy Physics*, 2006(05):026, 2006. `http://arxiv.org/abs/ hep-ph/0603175`.

[64] M. L. Mangano, F. Piccinini, A. D. Polosa, M. Moretti, and R. Pittau. ALPGEN, a generator for hard multiparton processes in hadronic collisions. *Journal of High Energy Physics*, 2003(07):001, 2003. `http://arxiv.org/abs/hep-ph/0206293`.

[65] G. Corcella, I.G. Knowles, G. Marchesini, S. Moretti, K. Odagiri, et al. HERWIG 6.5 release note. 2002.

[66] T. Przedzinski. Software for physics of tau lepton decay in LHC experiments. *hep-ph/1009.3877*, 2010. MS Thesis.

[67] P. Golonka and Z. Was. PHOTOS Monte Carlo: A Precision tool for QED corrections in *Z* and *W* decays. *Eur.Phys.J.*, C45:97–107, 2006. doi: 10.1140/epjc/s2005-02396-4.

[68] R. Keith Ellis, W. James Stirling, and B. R. Webber. *QCD and Collider Physics*, volume 8. Cambridge University Press, 1996.

[69] J. M. Campbell, J. W. Huston, and W. J. Stirling. Hard Interactions of Quarks and Gluons: A Primer for LHC Physics. *Rept. Prog. Phys.*, 70:89, 2007. doi: 10.1088/0034-4885/70/1/R02.

[70] CDF. Top analysis. `http://www-cdf.fnal.gov/physics/new/top/2007/topProp/KA_Afb/`.

[71] J. Alwall, P. Demin, S. de Visscher, R. Frederix, Michel H., et al. MadGraph/MadEvent v4: The New Web Generation. *JHEP*, 0709:028, 2007. doi: 10.1088/1126-6708/2007/09/028.

[72] M. L. Mangano, M. Moretti, F. Piccinini, and M. Treccani. Matching matrix elements and shower evolution for top-quark production in hadronic collisions. *JHEP*, 0701:013, 2007. doi: 10.1088/1126-6708/2007/01/013.

[73] J. M. Butterworth, J. R. Forshaw, and M. H. Seymour. Multiparton interactions in photoproduction at HERA. *Z.Phys.*, C72:637–646, 1996. doi: 10.1007/s002880050286.

[74] S. Frixione and B. R. Webber. Matching NLO QCD computations and parton shower simulations. *JHEP*, 0206:029, 2002.

[75] S. Agostinelli and others. Geant4 — a simulation toolkit. *Nuclear Instruments and Methods in Physics Research*, A(506):250–303, 2003.

Bibliography

[76] G. Aad et al. Measurement of the top quark pair cross section with ATLAS in pp collisions at $\sqrt{s} = 7$ TeV using final states with an electron or a muon and a hadronically decaying τ lepton. *hep-ex/1205.2067*, 2012.

[77] Non-collision backgrounds as measured by the ATLAS detector during the 2010 proton-proton run. Technical Report ATLAS-CONF-2011-137, CERN, Geneva, Sep 2011.

[78] Data-Quality Requirements and Event Cleaning for Jets and Missing Transverse Energy Reconstruction with the ATLAS Detector in Proton-Proton Collisions at a Center-of-Mass Energy of $sqrts = 7$ TeV. Technical Report ATLAS-CONF-2010-038, CERN, Geneva, Jul 2010.

[79] S van der Meer. Calibration of the effective beam height in the isr. Technical Report CERN-ISR-PO-68-31. ISR-PO-68-31, CERN, Geneva, 1968.

[80] G. Aad et al. Luminosity Determination in pp Collisions at $\sqrt{s} = 7$ TeV Using the ATLAS Detector at the LHC. *Eur.Phys.J.*, C71:1630, 2011. doi: 10.1140/epjc/s10052-011-1630-5.

[81] Luminosity determination in pp collisions at sqrt(s) = 7 tev using the atlas detector in 2011. Technical Report ATLAS-CONF-2011-116, CERN, Geneva, Aug 2011.

[82] The ATLAS Collaboration. ATLAS: Detector and physics performance technical design report. Volume 1. Technical Report CERN-LHCC-99-14, CERN, 1999.

[83] G. Aad et al. Expected Performance of the ATLAS Experiment - Detector, Trigger and Physics. *hep-ex/0901.0512*, 2009.

[84] Muon reconstruction efficiency in reprocessed 2010 LHC proton-proton collision data recorded with the ATLAS detector. Technical Report ATLAS-CONF-2011-063, CERN, Geneva, Apr 2011.

[85] G.Z. Blazey et al. Run II Jet Physics: Proceedings of the Run II QCD and Weak Boson Physics Workshop. `http://arxiv.org/abs/hep-ex/0005012`.

[86] S.n D. Ellis and D. E. Soper. Successive combination jet algorithm for hadron collisions. *Phys.Rev.*, D48:3160–3166, 1993. doi: 10.1103/PhysRevD.48.3160.

[87] Y. L. Dokshitzer, G. D. Leder, S. Moretti, and B. R. Webber. Better Jet Clustering Algorithms. *JHEP*, 08:001, 1997.

[88] M. Cacciari, Gavin P. S., and G. Soyez. The anti-k_t jet clustering algorithm. *JHEP*, 04:063, 2008. doi: 10.1088/1126-6708/2008/04/063.

[89] G. Aad et al. Electron performance measurements with the ATLAS detector using the 2010 LHC proton-proton collision data. *Eur.Phys.J.*, C72:1909, 2012. doi: 10.1140/epjc/s10052-012-1909-1.

[90] G. Aad et al. Performance of the electron and photon trigger in p-p collisions at $\sqrt{s} = 7$ tev. Technical Report ATLAS-CONF-2011-114, CERN, Geneva, Aug 2011.

[91] G. Aad et al. Performance of the ATLAS Electron and Photon Trigger in p-p Collisions at $\sqrt{s} = 7$ TeV in 2011. Technical Report ATLAS-CONF-2012-048, CERN, Geneva, May 2012.

[92] G. Aad et al. Jet energy measurement with the ATLAS detector in proton-proton collisions at $\sqrt{s} = 7$ TeV. *hep-ex/1112.6426*, 2011.

[93] G. Aad et al. Reconstruction and Calibration of Missing Transverse Energy and Performance in Z and W events in ATLAS Proton-Proton Collisions at 7 TeV. Technical Report ATLAS-CONF-2011-080, CERN, Geneva, Jun 2011.

[94] G. Aad et al. Performance of Missing Transverse Momentum Reconstruction in Proton-Proton Collisions at 7 TeV with ATLAS. *Eur.Phys.J.*, C72:1844, 2012. doi: 10.1140/epjc/s10052-011-1844-6.

[95] G. Aad et al. Non-collision backgrounds as measured by the ATLAS detector during the 2010 proton-proton run. Technical Report ATLAS-CONF-2011-137, CERN, Geneva, Sep 2011.

[96] G. Aad et al. Performance of primary vertex reconstruction in proton-proton collisions at $\sqrt{s}$ =7 TeV in the ATLAS experiment. Technical Report ATLAS-CONF-2010-069, CERN, Geneva, Jul 2010.

[97] G. Aad et al. Search for same-sign top-quark production and fourth-generation down-type quarks in *pp* collisions at $\sqrt{s} = 7$ TeV with the ATLAS detector. *JHEP*, 1204:069, 2012. doi: 10.1007/JHEP04(2012)069.

[98] P. Speckmayer, A. Höcker, J. Stelzer, and H. Voss. The toolkit for multivariate data analysis, TMVA 4, http://tmva.sourceforge.net/. *Journal of Physics: Conference Series*, 219(3):032057, 2010. `http://stacks.iop.org/1742-6596/219/i=3/a=032057`.

Bibliography

[99] Yong-Sheng Zhu. On Statistical Significance of Signal. *High Energy Phys. Nucl. Phys.*, 30:331–334, 2006.

[100] G. J. Feldman and R. D. Cousins. Unified approach to the classical statistical analysis of small signals. *Phys. Rev. D*, 57:3873–3889, Apr 1998. doi: 10.1103/ PhysRevD.57.3873. `http://link.aps.org/doi/10.1103/PhysRevD.57.3873`.

[101] A. Buckley. Soft QCD in ATLAS: Measurements and modelling of multi-parton interactions. *Acta Phys.Polon.*, B42:2669–2696, 2011. doi: 10.5506/APhysPolB. 42.2669. 33 pages, Proceedings of the 51st Cracow School of Theoretical Physics, June 2011.

[102] G. Aad et al. Charged particle multiplicities in p p interactions at $\sqrt{s} = 0.9$ and 7 tev in a diffractive limited phase-space measured with the atlas detector at the lhc and new pythia6 tune. Technical Report ATLAS-CONF-2010-031, CERN, Geneva, Jul 2010.

[103] A. Sherstnev and R. S. Thorne. Parton Distributions for LO Generators. *Eur.Phys.J.*, C55:553–575, 2008. doi: 10.1140/epjc/s10052-008-0610-x.

[104] J. Pumplin, D.R. Stump, J. Huston, H.L. Lai, Pavel M. Nadolsky, et al. New generation of parton distributions with uncertainties from global QCD analysis. *JHEP*, 0207:012, 2002.

[105] M. Aliev. PYTHIA6 retune for CTEQ6L and CTEQ6LL. `https://indico.cern. ch/contributionDisplay.py?contribId=15&confId=145994`.

[106] A. Buckley, H. Hoeth, H. Lacker, H. Schulz, and J. von Seggern. Systematic event generator tuning for the lhc. *The European Physical Journal C - Particles and Fields*, 65:331–357, 2010. ISSN 1434-6044. `http://dx.doi.org/10.1140/epjc/ s10052-009-1196-7`.

[107] A. Buckley, J. M. Butterworth, L. Lonnblad, H. Hoeth, J. Monk, et al. Rivet user manual. 2010.

[108] The Durham HepData Project. Online pdf plotting and calculation. `http:// hepdata.cedar.ac.uk/pdf/pdf3.html`.

[109] G. Aad et al. Search for gluinos in events with two same-sign leptons, jets and missing transverse momentum with the ATLAS detector in pp collisions at $\sqrt{s} = 7$ TeV. *Phys.Rev.Lett.*, 108:241802, 2012. doi: 10.1103/PhysRevLett.108.241802.

[110] M. R. Whalley, D. Bourilkov, and R. C. Group. The Les Houches Accord PDFs (LHAPDF) and Lhaglue. *hep-ph/0508110*, 2005.

[111] H. Schulz. Diploma thesis: Systematic Event Generator Tuning with Professor, Humboldt University Berlin, 2009.

[112] A. L. Read. Presentation of search results: the cls technique. *Journal of Physics G: Nuclear and Particle Physics*, 28(10):2693, 2002. `http://stacks.iop.org/0954-3899/28/i=10/a=313`.

[113] The TEVNPH Working Group. Combined CDF and D0 Upper Limits on Standard Model Higgs-Boson Production with 2.1 - 5.4 fb-1 of Data. *hep-ex/0911.3930*, 2009.

[114] T. Junk. MC Limits. *CDF 8128, CDF 7904, CDF 7578*. `http://www-cdf.fnal.gov/~trj/mclimit/production/mclimit.html`.

[115] S. Weinberg. Non-abelian gauge theories of the strong interactions. *Phys. Rev. Lett.*, 31:494–497, Aug 1973. doi: 10.1103/PhysRevLett.31.494. URL `http://link.aps.org/doi/10.1103/PhysRevLett.31.494`.

List of Figures

List of Tables

250

Selbständigkeitserklärung

Ich erkläre, dass ich die vorliegende Arbeit selbständig und nur unter Verwendung der angegebenen Literatur und Hilfsmittel angefertigt habe.

Berlin, den 03. Mai 2012   Rocco Mandrysch